Developing Optical Coherence Tomography for the Quantitative Study of Erosive and Carious Lesions in Dental Enamel in vitro

Abdirahman Aden

Submitted in partial fulfilment of the requirements for the degree of

Doctor of Philosophy in the

Faculty of Medicine and Dentistry, University of London

Clinical and Diagnostic Oral Sciences

Barts and The London School of Medicine and Dentistry

Institute of Dentistry

Queen Mary University of London, UK

Supervisor: Dr Pete Tomlins

Advisors: Prof Paul Anderson, Dr Gary Burnett and Prof Richard Lynch

Statement of Originality

I, Abdirahman Aden, confirm that the research included within this thesis is my own work or that where it has been carried out in collaboration with, or supported by others, that this is duly acknowledged below and my contribution indicated. Previously published material is also acknowledged below.

I attest that I have exercised reasonable care to ensure that the work is original, and does not to the best of my knowledge break any UK law, infringe any third party's copyright or other Intellectual Property Right, or contain any confidential material.

I accept that the College has the right to use plagiarism detection software to check the electronic version of the thesis.

I confirm that this thesis has not been previously submitted for the award of a degree by this or any other university.

The copyright of this thesis rests with the author and no quotation from it or information derived from it may be published without the prior written consent of the author.

Examination: Thesis submitted for the degree of Doctor of Philosophy, University of London.

Signature: Date: September, 2016.

Acknowledgements

I commence in the name of Allah the most Gracious and most Merciful to whom I owe all gratitude and praise.

I am sincerely grateful to Dr. Pete Tomlins, my supervisor and mentor, to whom I owe so much for his guidance, support and engaging conversations. I would also like to acknowledge his exceptional levels of patients (May God bless you). It has been a privilege to have him as my supervisor.

I would also like to thank Prof Paul Anderson, Dr. Gary Burnett and Prof Richard Lynch for their sound advice and probing questions.

I would also like to thank BBSRC and GSK for supporting my studies financially (BBSRC Industrial CASE award BB/K501190/1). This work would not have been carried out without their funding.

I would also like to acknowledge all those that have helped me during my research; special thanks to Arthi Anthony, Carel Brigi, Muhammad Sabih Merchant, Saqlain Gilani and Huda Siraj. I would also like to thank David Mills and Graham Davis for their help with the XMT.

Last and foremost I wish to thank my family for their unconditional love and support and my wife, Hiba (perhaps the best outcome of this PhD).

This is for you Mr Abdulkadir Anod Dhore.

Abstract

Optical Coherence Tomography (OCT) is an imaging technique that uses near infra-red light to non-invasively form cross-sectional images of specimens, in a similar way to ultrasound and RADAR. A number of research groups have used OCT to study natural and artificial carious lesions and to some extent erosive lesions. For this, a variety of *in vitro* models have been used. However, the exact mechanism by which these demineralised enamel lesions affect the OCT measurements is not fully understood. This remains a barrier to its adoption as both an analytical laboratory tool and a widespread technique in clinical dentistry.

Therefore, the aim of this thesis was to develop an understanding of how different demineralised enamel lesions manifest in OCT measurements. This is necessary for the technique to become useful as an *in vivo* clinical measurement and imaging system.

Consequently, this study was carried out in a controlled laboratory environment for which a novel specimen holder was designed. This mitigated against specimen movement and maintained specimen hydration, which can be a source of uncertainty in the measurements. A custom-built OCT microscope was used for this work, which enabled automation of experiments and continuous time-lapse OCT imaging over time periods of hours to several days. This enabled bovine enamel demineralisation dynamics to be captured during *in vitro* caries and erosion formation. The stability of the system also enabled direct comparison between the OCT measurements of the optical properties of different demineralisation models.

To achieve these measurements, the OCT system was carefully characterised and compared to established profilometry measurements. Interestingly, this revealed that the experimental protocol used to obtain lesions for profilometry was not to be representative of the lesions formed and measured by OCT. This is an important point when interpreting OCT data in light of other techniques.

A novel method of analysis was developed that uses longitudinal OCT image correlation to quantify early stage surface softening during erosion. By using OCT volumetric data, this technique was able to measure sub-resolution changes at the specimen surface. Early results also indicate sensitivity to remineralisation.

This thesis shows that OCT is sensitive to different demineralisation models produced and measured under controlled conditions. New method of handling the data can observe changes not previously seen in OCT. However, further work is still required to understand the underlying physical changes that lead to this sensitivity in OCT.

CONTENTS

Glossary of Terms

$CaCl_2$	Calcium Chloride
CAT or CT	Computerized Axial Tomography
CCD	Charge Coupled Device
CEJ	Cemento-Enamel Junction
CLSM	Confocal Laser Scanning Microscopy
CMOS	Complementary Metal Oxide Semiconductor
CSF	Calibration Scale Factor
DEJ	Dentine- Enamel Junction
ESEM	Environmental SEM
FD-OCT	Fourier Domain OCT
FOTI	Fibre Optic Trans-illumination
FWHM	Full-Width at Half-Maximum
HAp	Hydroxyapatite
ISE	Ion Selective Electrodes
KH_2PO_4	Monopotassium Phosphate
NaF	Sodium Flouride
NaOH	Sodium Hydroxide
OCA	Optical Coherence Angiography
OCE	Optical Coherence Elastography
OCT	Optical Coherence Tomography
PBS	Polarising Beam-Splitter
PLM	Polarised Light Microscopy
PMMA	Polymethyl Methacrylate
PSF	Point-Spread Function
QLF	Quantitative Light-Induced Florescence
ROI	Region Of Interest
SCF	Self-Coherence Function
SD-OCT	Spectral Domain OCT
SEM	Scanning Electron Microscopy
SLD	Super Luminescent Diode

SS-OCT	Swept-Source Optical Coherent Tomography
TD-OCT	Time Domain OCT
TiO_2	Titanium Dioxide
TMR	Transverse Microradiography
UCSF	(University of California, San Francisco)
VH	Vickers Hardness
XMT	X-ray Micro-Tomography
UHR-OCT	Ultrahigh Resolution OCT

List of Figures

List of Tables

1 Introduction

The oral cavity may be viewed as a potential diagnostic window into the body. It comprises both epithelial soft tissue and exposed hard tissue. Consequently, the mouth is subject to many of the disease processes that affect similar tissues elsewhere in the body and perhaps diagnostic advances made in the mouth have the potential to impact on systemic disease.

The oral environment is subject to both chemical and physical challenges through intrinsic and extrinsic sources. Intrinsic sources are from gastro-oesophageal reflux and extrinsic sources are from the regular consumption of food and drink. These factors expose the oral hard tissue to multiple risks such as erosion, abrasion and attrition. Furthermore, the oral environment is the location of some of the most common human maladies, namely caries and dental erosion. These are the most prevalent chronic diseases worldwide, with an estimated global figure of around 5 billion people suffering from tooth decay (World Health Organisation [WHO] – Oral Health Fact Sheet 2003) (Petersen, 2003).

The recent international outlook in dental disease management is to move away from the surgical model, i.e. excision and restoration, towards a preventive approach (Pitts, 2004, Ten Bosch and Angmar-Mansson, 2004). Under this paradigm, the aim is to control the initiation and progression of dental disease over a patient's lifetime. To do this however requires suitable diagnostic techniques with the capability to support such preventative strategies.

New methods are needed for the non-destructive measurement of tooth demineralisation and remineralisation to monitor the progression of incipient caries lesions (tooth decay) for effective nonsurgical intervention and to evaluate the performance of anti-caries treatments such as chemical treatments or laser irradiation. A non-destructive, quantitative method of monitoring demineralisation and remineralisation "*in vivo*" with high sensitivity would be invaluable for use particularly in high-risk areas of the tooth such as the pits and fissures of the occlusal surfaces (Chan et al., 2015) and also for short-term clinical trials for various anti-caries agents such as fluoride dentifrices and antimicrobials.

Due to its non-invasive and non-destructive nature, and its ability to produce real-time three-dimensional images, Optical Coherence Tomography (OCT) has been identified as a potential technique that can be adopted clinically. However, OCT has been used for numerous studies for dental hard tissue. However, it is yet to gain widespread adoption either in dental clinical practice or as a laboratory technique. This is partly because it remains under-developed as a quantitative tool and little has been done to validate it against accepted methodologies. Furthermore, measurements based upon OCT have received little attention in terms of characterising its repeatability and reproducibility.

Therefore, the aim of this project was to develop OCT as a quantitative technique for measuring dental enamel and characterise its performance. Furthermore, this study aimed to develop an enhanced understanding of dental enamel lesion development dynamics under OCT imaging. To do this, a clear understanding of how physical changes in enamel during the demineralisation process are manifested in OCT images. Furthermore, different analysis techniques will be used to quantify these changes. An understanding of the challenges and limitations associated with this technique will accelerate its development and evaluation for potential use in a clinical setting.

1.1 Aims and Objectives

The studies presented in this thesis aimed to evaluate and develop an understanding of OCT in order to facilitate its transition from a largely *in vitro* based technique into a real-time *in vivo* system.

This objectives of the project are as follows:

1. To use OCT to image and real-time characterisation of erosion measurements by measuring changes of enamel thickness during surface erosion mineral loss.

2. To characterise different demineralisation dynamics on dental enamel. Evaluating the subsurface lesion depth dynamics in artificial caries models and also comparing the optical properties of three demineralisation models.

3. Use of volumetric data for characterisation of demineralised lesions by evaluating surface characteristics using *en face* OCT images. This will involve evaluating longitudinal correlation analysis of 3D OCT images to detect early stage erosion in dental enamel, and evaluation subsurface demineralisation and to monitor remineralisation.

This thesis is split into multiple chapters, each covering some of the multi-disciplinary background to this work: The first six chapters are related to the background knowledge focussing on the dental enamel structures, the two main disease processes (dental caries and dental erosion) and the techniques used to detect and monitor them will be introduced. In chapter 5, a discussion of the OCT concepts and principles that are relevant to this study will be made. The subsequent chapters will be results chapters which will be divided to four main studies. Chapter 7 is a validation study evaluating OCT measurements of erosive lesion depths, chapter 8 is an evaluation of subsurface caries-like lesions, chapter 9 is comparison the optical properties of three demineralisation models and chapter 10 is an introduction and assessment of a new OCT analysis technique that uses longitudinal image correlation analysis. A general discussion of the studies will be summarised in chapter 12 with suggestions for future work.

2 Dental Enamel

In order to address the dental hard tissue diseases, it is important to develop an appropriate understanding of tooth microstructure, chemistry and the associated diseases. This study is mainly focused on enamel and so the structure, physiology, and chemical characteristics of enamel will be discussed.

2.1 Enamel microstructure

Enamel is the most highly mineralised tissue in the body, consisting of more than 96% inorganic material in the form of apatite crystals and traces of organic material. In the inter-prismatic space of enamel is protein, which occupies as much as 2% of the volume (Wang et al., 1999).

Dental enamel comprises almost entirely of arranged arrays of densely packed hydroxyapatite (HAp) crystals, which are organised into rods known as enamel prisms. The crystals are organized in keyhole-shaped prisms and are 4 to 6 µm wide and extend from the dentin-enamel junction to the outer surface of the tooth (Zijp et al., 1995).

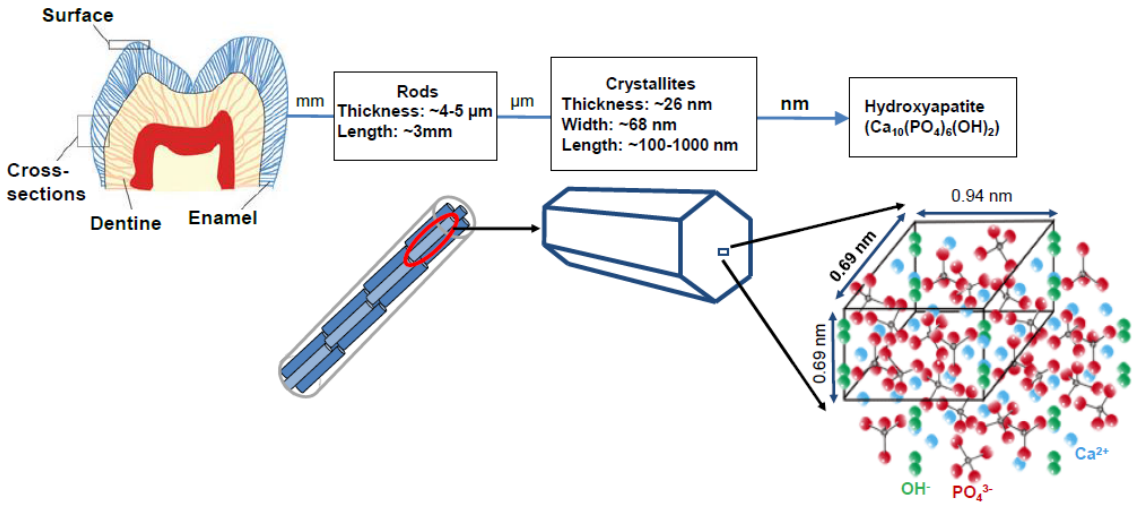

Figure 1 Structure of dental enamel showing different hierarchical levels. Hydroxyapatite are packed into crystals that are organised into rods. Image adapted from (Wang and Nancollas, 2008, Hannig and Hannig, 2010).

Figure 1 Structure of dental enamel showing different hierarchical levels. Hydroxyapatite are packed into crystals that are organised into rods. Adapted from (Wang and Nancollas, 2008, Hannig and Hannig, 2010).

The apatite crystals within the enamel pack together differentially to create a structure of enamel rods separated by inter-rod substance Figure 1. Therefore, each crystal is separated from its neighbours by tiny inter-crystalline spaces. In the inter-prismatic area, the crystal orientation is random, leading to a lower mineral content and a higher content of water and organic material (Zijp et al., 1995). The packing of crystals is slightly looser along the rod periphery than in the rod and inter-rod enamel. The rather low mineral and high protein content, is indicative of a higher porosity, and is probably due to a poorer prismatic packing (Robinson et al., 1971, Robinson et al., 1983). Furthermore, at the periphery of each prism, the crystals deviate somewhat from this orientation. The inter-crystalline spaces are filled with water and organic material which forms a fine network and offer diffusion pathways within the tissue. These are often referred to as micropores (or simply pores), and are regarded as an important feature with respect to caries onset (Carlström et al., 1963).

The enamel rods are orientated perpendicular to the Dentine-Enamel Junction (DEJ), and the enamel crystallites arranged within the rods run from the DEJ toward the tooth surface (Robinson et al., 2000). At the edge of the cusps and occasionally at the cervical area, the prisms are aligned perpendicular to the surface (Fernandes and Chevitarese, 1991). Near the crown, the outer surface is covered by a thin and transparent layer of enamel that consists almost entirely of calcium salts in the form of large apatite crystals (Wang et al., 1999).

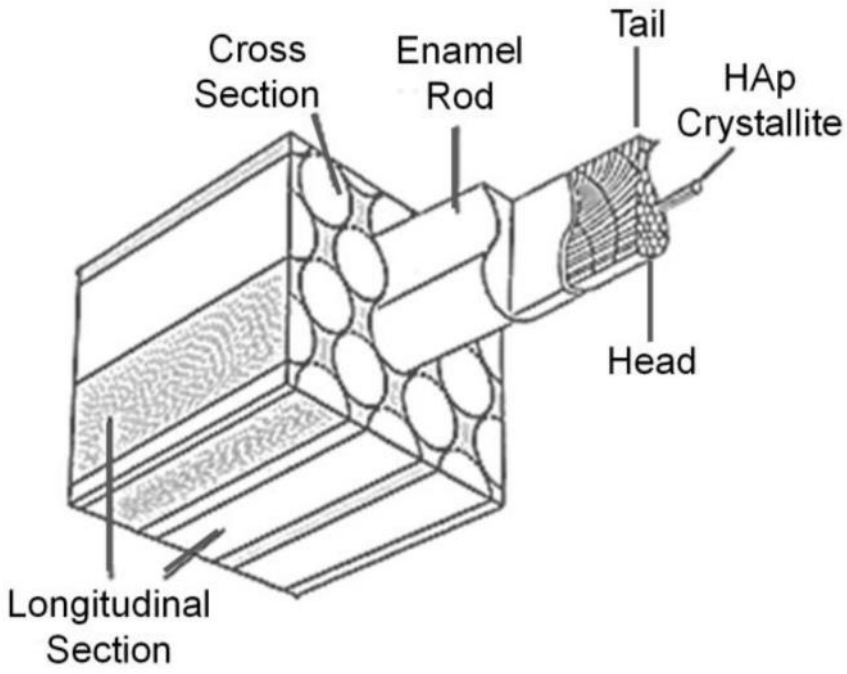

Figure 2 Cross-section of dental enamel revealing the "key-hole" shaped structure of the enamel rod (head and tail) packed with elongated HAp crystallites.

Cross-section of the crystallites are seen to be in the form of elongated, irregular hexagons. Each individual rod has a "key-hole" shape, in which the component parts are referred to as the head and the tail Figure 2. Throughout the enamel, most of the rods are arranged so that their heads are directed toward the crown of the tooth, and their tails toward the Cemento-Enamel Junction (CEJ) (Scott et al., 1974).

Although enamel is mostly inorganic, it is permeable; ionic exchange can occur between the enamel and the environment of the oral cavity, in particular the saliva (Nanci, 2007). However, when enamel is destroyed, by means of mechanical wear or disease, it cannot be replaced or regenerated. To compensate for this inherent limitation, enamel has acquired a high degree of mineralisation and a complex organisation.

2.2 Enamel physical properties

Enamel possesses exceptional mechanical properties that combine high hardness with remarkable resilience, largely due to its high mineral content and unique structural organization. The hardness enables enamel to withstand heavy masticatory forces. However, enamel is very brittle due to its low tensile strength. One characteristic feature that is a prevalent physical property of the enamel is the presence of pores in

its structure. Quantitative microradiography studies have demonstrated that the mineral content, and hence the porosity, varies markedly with enamel (Weidmann et al., 1967). Mineral content decreases from the outer surface towards the DEJ. The inner enamel rather comprises of more protein and water, due to the increase in enamel permeability to ions, water and small organic molecules (LOWE et al., 1971).

The number of available pores, the pore size and the inter-connectivity between the pores influence the diffusion of ions, water and small organic molecules. The charge of the diffusing ion also affects the partial acceptance or rejection of the transport of ion through the enamel pores. Although to a lesser extent, the organic matrix also controls the permeability and transport processes through enamel, for example, ionic diffusion is limited in the presence of proteins (Teaford et al., 2007).

2.3 Enamel chemical properties

The natural variability in chemical composition in enamel occurs both between teeth and within the same tooth, not only as a result of environmental exposure, but also as a consequence of developmental factors (Dowker et al., 1999). Mature enamel is mostly inorganic material containing hydroxyapatite crystals and various ions such as magnesium, carbonate and fluoride (Elliott, 2013).

Chemical gradients exist in enamel extending from the surface towards the DEJ. For example, the concentration gradients of carbonate and magnesium ions increases from the enamel surface towards the DEJ, whereas, the concentration of fluoride is generally higher at the surfaces and decreases towards the DEJ (Robinson et al., 2000). Furthermore, the gradients in porosity occurring in the enamel tissue allows for the entry of material into and out of the apatite structure. Between the inorganic substances, there is a fine network of organic protein content (LOWE et al., 1971). Proteins play an important role in the process of enamel formation and also in the process of remineralisation.

3 Enamel Caries and Erosion

3.1 Destruction of Dental Enamel

Caries and erosion are characterised by loss of mineral from oral hard tissue. Though the chemical process of dental erosion is similar to that of caries, i.e., dissolution of hydroxyapatite by acids, the clinical manifestations and management of dental erosion are fundamentally different from caries because the erosive process does not involve acid of bacterial origin. Clinically they are differentiated by the location from which they occur, with erosion being a surface phenomenon and caries occurring beneath the surface leading to eventual cavity formation.

3.2 Caries

Dental caries remains the most common oral disease affecting the majority of the world's population (Featherstone, 2000, Pitts and Stamm, 2004). The term dental caries is used to describe the results, signs and symptoms of a localized chemical dissolution of the tooth surface caused by acidic by-products from bacterial fermentation of dietary carbohydrates taking place in the biofilm covering the affected area (Kidd et al., 2000).

Streptococcus mutans has been shown to be the major cariogenic bacterium (Loesche, 1982). The bacterial cells of *S mutans* and other organisms colonize the surfaces of the teeth and form a complex biofilm commonly called dental plaque. When provided a suitable metabolic substrate, this infection produces organic acids (primarily lactic acid). These acids are capable of dissolving the mineral calcium from the crystalline enamel matrix as this causes the local pH to fall below a critical value resulting in demineralisation of dental tissues (Caufield and Griffen, 2000, Featherstone, 2004). Continued and repeated dissolution leads to cavitation and the subsequent need for repair (Featherstone, 2000).

Cavities are the clinical manifestation of a chronic bacterial infection dependent on a limited number of species of cariogenic bacteria, susceptible individuals and specific dietary patterns (such as sugar ingestion).

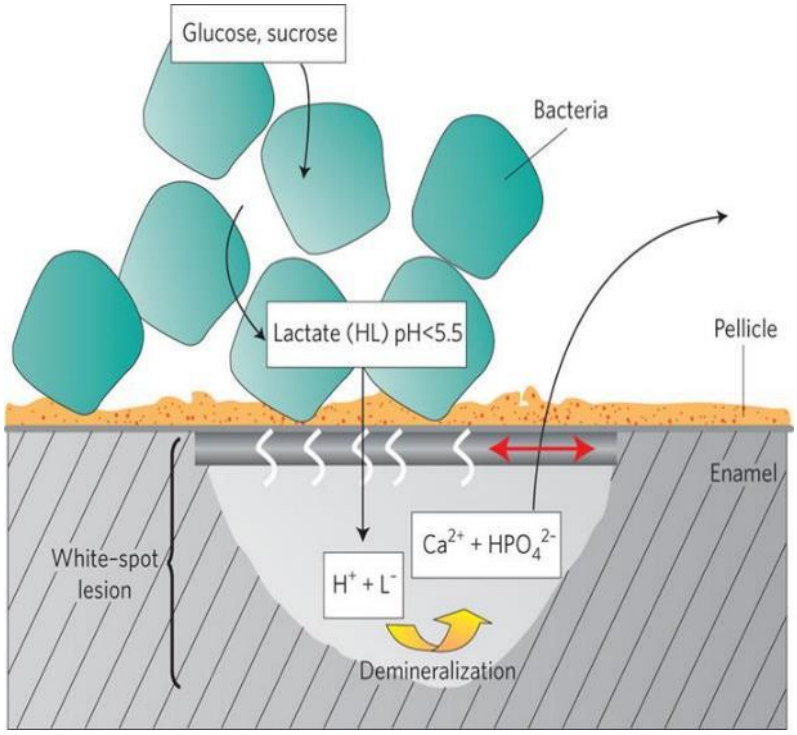

Figure 3 Early stages of tooth decay caused by bacterial biofilm. Bacteria metabolize sugar and other carbohydrates to produce lactate and other acids that, in turn, dissociate to form Hydroxide ions that demineralise the enamel beneath the surface of the tooth; calcium and phosphates are consequently dissolved. Image from (Hannig and Hannig, 2010)

3.2.1 The Process of Carious Lesion Formation

The initial stages of the carious lesion are characterized by a partial demineralisation of the enamel tissue. Figure 3 shows a developing subsurface lesion body with a preserved surface layer. The surface layer is preserved so long as it remains supported by subsurface structures (Fejerskov and Kidd, 2009). One of the histological features of the lesion is the presence of a relatively sound surface layer of enamel (2–50 μm thick) overlying the demineralised zone, which is where the bulk of the mineral loss occurs. Clinically, the lesion appears to the human eye as a "white spot" and is recognized as an early sign of dental caries, yet by this time the process has been going on for months (Featherstone, 2008).

The partial demineralisation of both surface and subsurface renders the enamel softer by further demineralisation (Fejerskov and Kidd, 2009). At this stage in the process, prior to cavitation, therapeutic intervention can reverse or arrest the process by remineralisation (Featherstone, 2000).

3.2.2 Histological Features of Carious Lesions

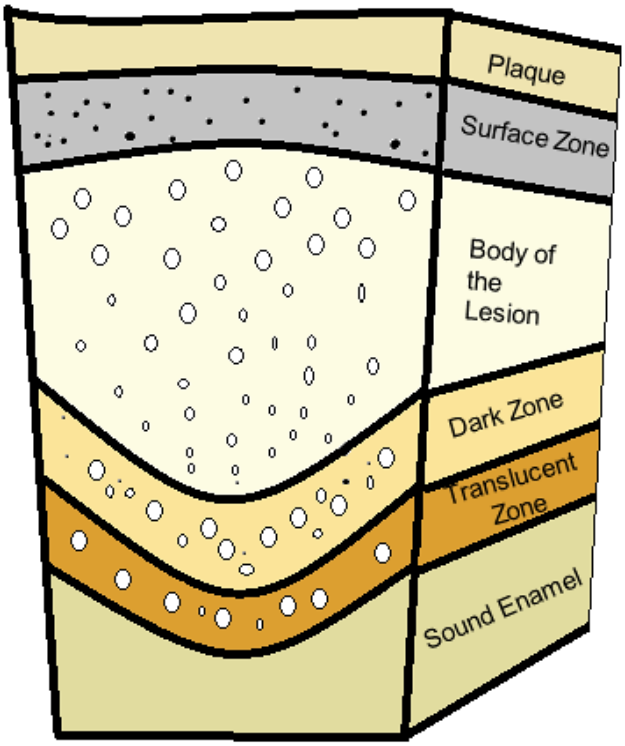

Figure 4 An illustration of the four zones starting from the outer enamel surface layer towards the DEJ. These zones are: surface, body of the lesion, dark and translucent (Darling, 1956).

The histological changes in the enamel carious lesion have been categorized into zones that are in accordance to the porosity levels and amount of mineral lost. These zones are: translucent, dark, body of the lesion and surface Figure 4 (Darling, 1956, Silverstone, 1968)

TRANSLUCENT ZONE

The first detectable carious changes in the enamel are in the translucent zone, and are thought to precede the formation of a surface layer. This zone shows the presence of a small number of relatively large pores, and accounts for approximately 1-2% mineral loss; minerals abundant in carbonate and magnesium. Much of this first loss also appears to derive from inter-prismatic areas and from the prism peripheries, in part due to an easier flux of ions through these regions (Darling, 1961, Arends and Ten Cate, 1981).

DARK ZONE

Similar to the translucent zone, the dark zone also shows porosity and mineral loss. Although, in the dark zone there is approximately 5-10% loss of mineral and the pore sizes appear to be smaller. This is a characteristic feature observed in this zone. It has been speculated that there are some remineralisation occurring in this region, which could be a possible explanation for the occlusion of some of the larger pores in the translucent zone (Silverstone, 1967). Therefore the dark zone could represent the region where both demineralisation and remineralisation occur.

BODY OF THE LESION

The body of the lesion is formed when there is continuous enlargement of the pores, which ultimately leads to the collapsing of the enamel structure. This is therefore the final stage of enamel destruction (Darling, 1961).

SURFACE ZONE

The surface layer is the outermost layer in the lesion with a thickness of approximately 40 μm. The porosity of the surface zone is 1-2%, which is similar to sound tissue (Darling, 1961). This is mainly due to the re-deposition of a fluoride-enriched mineral occurring after the initial dissolution of carbonate and magnesium components in the enamel surfaces. The accumulation of fluoride results in the surface to become more resistant to acid attack. Quite often, the surface zone is described as the relatively intact layer of enamel as less than 1 % mineral loss occurs in this region.

The presence of the pellicle (organic material) on the enamel surface may act as a perm-selective barrier, which reduces mineral loss at the surface(Lussi and Jaeggi, 2008). However, preferential demineralisation of deeper enamel layers can continue below the surface zone, resulting in the formation of a "subsurface" lesion. The diffusion of acids into the porous enamel microstructure to deeper more soluble layers would result in the removal of interior mineral in preference to the outer less soluble enamel tissue. If the surface zone remains intact, then sub-surface remineralisation can be facilitated through this surface layer and deeper in the main body of the lesion. However, if the surface layer collapses, than there is a permanent loss in the enamel structural integrity (Robinson et al., 1983).

3.3 Erosion

Tooth wear of multifactorial aetiology (erosion, attrition and abrasion) is a well-recognised problem in dentistry. Its increase in prevalence and severity is a major concern for the dental profession (Bardsley et al., 2004). Generally, dental erosion is more commonly evident during late adolescence and early adulthood. Tooth wear that involves the wear processes of erosion, abrasion and attrition has been found to be clinically common and positively associated with age (Spijker et al., 2009).

Clearly, its occurrence can be a serious problem especially if the process of erosion continues throughout adulthood resulting in cumulative loss of considerable amounts of tooth structure where preventive measures are not successful. Treatment of eroded teeth is commonly not possible in the advanced stages.

Early identification of patients with erosion is therefore important in order to stop its progression. Consequently, it is important to monitor whether an eroded surface is stabilized or is still being eroded (Jaeggi and Lussi, 2006).

Clinically, making casts and taking photographs of lesions are preferable, although there needs to be a considerable removal of enamel to be able to identify erosive activity.

Epidemiological studies have been published but the results are not easily comparable because of the wide range of indices used to measure and record tooth wear or erosion and the inevitable variation in diagnostic criteria. Further difficulty arises from clinical examination in distinguishing between wear caused primarily by acid erosion as opposed to that caused mainly by abrasion and/or attrition (Addy and Shellis, 2006).

Dental erosion is caused by sustained direct contact between tooth surfaces and acidic substances. The loss of dental hard tissue during erosion is associated with extrinsic and/or intrinsic acids that are not produced by bacteria.

3.3.1 Enamel Dissolution during Erosion

Erosion is characterized by dissolution and removal of an ultrathin layer of enamel each time it is exposed to an acidic challenge (Fejerskov and Kidd, 2009). The initial acid attacks on the tooth surface result in a superficial partial dissolution of mineral. This is normally referred to as early-stage surface softening(Arends and Ten Cate,

1981). This partly demineralised surface is prone to wear or remineralisation (Attin et al., 2003).

If the challenge is more prolonged, the outermost layer of the softened surface will eventually be completely dissolved, resulting in permanent loss of tooth structure (in depth) (Cheng et al., 2009b). This loss of enamel volume is characterized by a persistent softened layer at the surface of the remaining tissue.

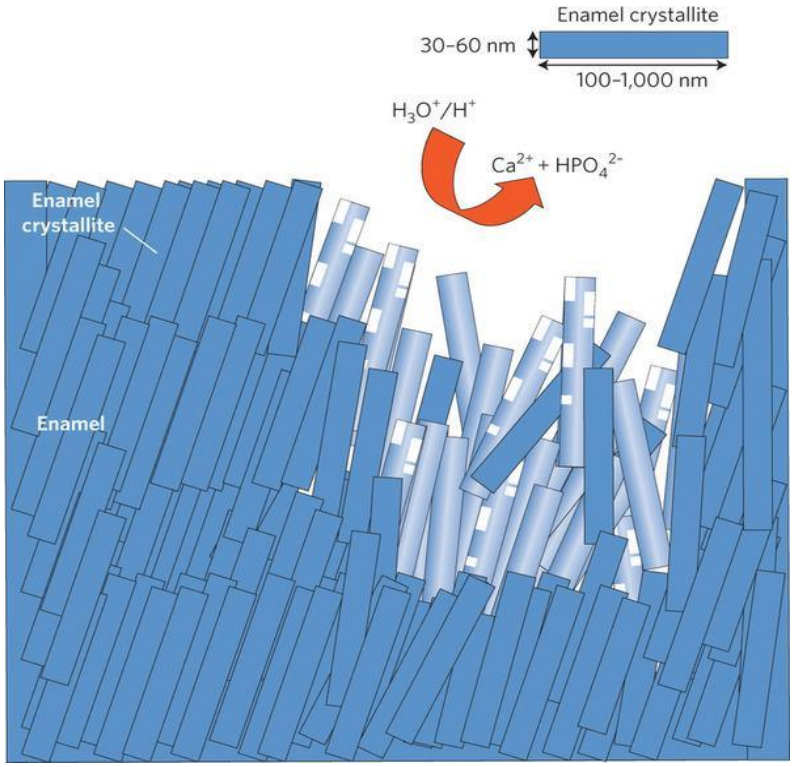

Figure 5Dental erosion caused by acidic beverages, acidic food and gastric juices in the oral cavity. The enamel surface undergoes partial and complete dissolution of the enamel crystallites, resulting in the release of Calcium (Ca2+) and Phosphate (HPO42−) ion which loosens the microstructure. Image from (Hannig and Hannig, 2010)

Figure 5 shows an illustration of enamel rods under acid attack during erosion. Low pH (pH 1–4) caused by acidic sources in the oral cavity, destroys the enamel surface by partial and complete dissolution of the enamel crystallites, resulting in the release of Calcium and Phosphate ions which loosens the microstructure.

3.4 Factors Influencing Enamel Dissolution

Factors influencing tooth erosion may be categorised into intrinsic (from within the body) and extrinsic factors (from external sources).

3.4.1 Intrinsic Factors

Intrinsic factors are characterised by voluntary and non-voluntary human action that results in the release of acid from the gastrointestinal tract into the oral cavity. Such intrinsic acids may reach the oral cavity by a variety of ways namely vomiting, regurgitation and reflux. This can be as a result of eating disorders that are associated with vomiting such as anorexia nervosa and bulimia nervosa (Scheutzel, 1996). These conditions permits internal acids to come into contact with tooth structure causing enamel dissolution.

3.4.2 Extrinsic Factors

Different extrinsic factors might act either singly or in combination.

I) Extrinsic factors: Dietary

A wide variety of soft drinks have been associated with the development of dental erosion; namely carbonated drinks, still and dilutable drinks, fruit juices, smoothies and sports and energy drinks(Ehlen et al., 2008). A recent systematic review (Salas et al., 2015) concluded that consumption of soft drinks, acidic snacks/sweets and acidic fruit juices increases the susceptibility of an individual developing dental erosion. The acid content in these drinks is important for flavour, taste perception, product stability and shelf life (Kilcast and Subramaniam, 2011). In recent years there has been a considerable increase in the sales of soft drinks, which has led to a higher risk of dental erosion associated with their excessive consumption.

II) Extrinsic factors: Environmental

Several occupations have been known to pose risks of dental erosion. Occupations such as industrial and mining have been traditionally linked to risk of dental erosion. These risks are decreasing dramatically with time as a result of the stricter Health and Safety regulations that now govern mines and factories (Bartlett et al., 1994). Similarly, other professions that are still at risk of dental erosion is professional wine and tea tasters. This is mainly due to the prolonged time of acidic exposure to teeth (Wiegand et al., 2007).

III) Extrinsic factors: Behavioural

Behavioural factors are entirely associated with habits and preference of each individual. For example, people with healthier lifestyles associated with increased physical activity, leads to increased fluid consumption to maintain fluid balance (Casa et al., 2005). Unfortunately, these drinks can be acidic and potentially erosive such as citrus flavoured drinks high-in-electrolyte and high-caffeine energy drinks. Therefore the frequency of carbonated beverage intake is an important factor to consider for better understanding of dental erosion caused by such drinks.

Similarly, the preferred method of drinking (i.e. sipping, gulping, using a straw) has been shown to influence acidic clearance patterns and thus which teeth are affected by dental erosion(Lussi et al., 2011). Keeping the drink in the oral cavity for a prolonged period of time before swallowing is associated with a higher incidence of erosion as a result of increased the exposure time. Frothing the drink and holding it in the mouth also affects its reactive potential with the dentition (Johansson et al., 2002).

Inappropriate brushing methods or excessive tooth brushing, usually by health conscious individuals, can lead to removal of the protective pellicle in turn aggravating dental erosion. The protective pellicle can minimize the effect of acidic exposure for it is believed that the presence of plaque delays tooth acid contact (Amaechi et al., 1999).

IV) Extrinsic factors: Biological

When it comes to the prevention of erosion, saliva is the most important biological component to be considered. Saliva dilutes and clears erosive substances from the oral cavity. This clearing and neutralizing effect is usually referred to as “salivary clearance” or “oral clearance capacity” (Bashir et al., 1995). The higher the salivary flow rate the better the buffering capacity and the faster the clearance (Ongole and Praveen, 2014).

Saliva also buffers and neutralizes acids whose presence may hamper the process of remineralisation. During remineralisation, saliva repairs the affected tooth structure by providing the required organic and inorganic material to compensate the loss caused by erosion. It provides a unique reservoir of calcium and phosphate ions to aid

remineralisation. The remineralisation eventually "re-hardens" the softened tooth structure (Lussi et al., 2011).

3.4.3 Critical pH

The critical pH can be referred to as the acidity level at which a bathing solution or saliva becomes saturated with respect to the tooth structure's ionic constituents. Generally, pH value of 5.5 has been suggested as a threshold above which it is considered safe with regard to loss of enamel mineral and below which demineralisation of enamel occurs (Larsen and Pearce, 2003).

When the pH of the oral cavity drops below the critical pH, as a result of acidic intake, recovery can be initiated via compensatory mechanisms including saliva. As long as the bathing solution or saliva is supersaturated with respect to enamel apatite, repair of enamel will occur. In contrast, if saliva is undersaturated with respect to enamel apatite it will start losing its ionic constituents upon acid attack.

Likewise, demineralisation occurs when tooth structure is exposed to an aqueous phase of acid that is under-saturated with respect to enamel apatite minerals. Initially, when an acidic beverage is consumed, plaque pH level may not drop as low as the pH of the drink (Honório et al., 2008) perhaps indicating that a covering of plaque protects against erosion. However, prolonged periods of low pH levels or frequent pH fluctuations below the critical pH can result in more rapid tooth structure dissolution.

4 *In vivo* and *In vitro* Detection of Enamel Caries and Erosion

4.1 Detection and Imaging *in vivo*

Dental erosion and caries are both fundamentally characterised by mineral loss. Hence, this is a critical factor in the diagnosis and management of the consequent lesions. In the clinic the diagnosis of carious lesions has been primarily by visual examination, based principally on clinical inspection and review of radiographs (Bader et al., 2001). In general dental practice today, probably the most widely applied technique clinically is dental X-ray imaging. This technique is used routinely to image dental structures and cavities within the oral cavity. Bitewing radiographs are commonly used to examine interdental caries and recurrent caries. However, dental X-ray imaging has poor sensitivity for detecting early carious lesions since the lesions are too shallow and do not provide enough contrast. Current clinical practice has been found to have limited sensitivity and specificity to all stages of dental lesion progression and thus presents an obstacle to the effective practice of preventative dentistry (Gomez, 2015). X-ray radiographic methods are also not ideal due to the continual exposure to X-rays concentrated onto a small area, which may be harmful to patients over a prolonged period.

4.2 Techniques for Detection of Lesions *in vitro*

Several analytical techniques have found utility for measuring dental mineralisation (Ten Bosch and Angmar-Månsson, 1991). Most of the techniques employed are *in vitro* techniques. These laboratory techniques have contributed to both the understanding of dental lesions and the development of oral healthcare treatments. However, they are not readily translated directly into the clinic for *in vivo* patient examination.

Additionally, none of the techniques currently used are suitable for the detection of all stages of the dental lesion progression. Each methodology has its limitations and important considerations. For example, most of the conventional methods used to measure caries do not establish the caries depth and severity accurately *in vivo*

(Huysmans and Longbottom, 2004). This is important because in dentistry, the restorative method for the treatment of an advanced caries lesion depends on the depth of the lesion inside the tooth (Amaechi et al., 2003b).

Some of the most prevalent techniques used in current dental research will be discussed below.

4.2.1 Microhardness Testing

Material hardness is typically measured by the size of penetration of a diamond indenter forced into a sample under low loads (typically < 200 g). The degree of loss of hardness "softening" can be measured by assessing how resistant a substrate is to the penetrating diamond indenter. The indenter can be a Knoop, Vickers or Berkovich nano-indenter (Schlueter et al., 2011).

Microhardness provides useful information that allows prediction of other physical properties of the material. Therefore, this technique has been widely used for assessment of surface softening in dental erosion models especially for enamel hardness testing, using either the Knoop or Vickers indenters (Figure 6) (Attin, 2006).

Indentations produced using micro-indenters usually yield indentation depths ranging from a few micrometres to tens of micrometres, while the ones produced by nano-indenters have much lesser depths of a few hundred nanometres (typically 200 nm)(Barbour and Rees, 2004). The size and depth of an indentation is affected by the physical characteristics of the material, not only in the immediate vicinity of the indentation but also up to a distance of ten times the dimensions of the indentation itself. Furthermore, microhardness techniques require the specimens to be flat. This can be achieved by polishing the surface of the substrate prior to the erosive attack. This procedure affects the end hardness value owing to the fact that the superficial layer of enamel contains considerably higher concentrations of fluoride and lower concentrations of carbonate and magnesium relative to deeper layers of enamel (Featherstone et al., 1983, Kielbassa et al., 1999). Thus, a deeper layer is usually more susceptible to erosion compared to a more superficial layer (Barbour and Rees, 2004)

Typical Knoop hardness values for dental hard tissues range from 272 to 440 KHN (Knoop Hardness Number) for enamel and from 50 to 70 KHN for dentine (Meredith et al., 1996). However, enamel hardness values usually have an increased standard

deviation owing to the differences in the degree of mineralisation of enamel from site to site and throughout its thickness (Devlin et al., 2006). It is also observed that enamel specimens will give higher hardness values if they were allowed to dry out after acidic exposures (Staines et al., 1981).

Figure 6 A commercial Vickers HMV microhardness tester (Shimadzu, Japan) comprising of the eyepiece, indenter translation stage and display screen.

Hardness measurements cannot quantify the amount of surface loss in advanced dental erosion cases; therefore they are mainly used to assess the degree of early surface softening (Schlueter et al., 2011). A further application for microhardness testing is for assessing the potential for remineralisation of eroded enamel by solutions that promote remineralisation. This potential can be measured either by the surface microhardness recovery test or the relative erosion resistance test (Hara and Zero, 2008).

4.2.2 Surface Profilometer

Profilometry is one of the most reliable techniques for quantifying dental tissue loss in dentistry. Surface profilometry involves surface measurement directly using a contacting stylus or indirectly, using a non-contact profilometer Figure 7. For contact

profilometry the stylus tip contacts the sample surface while for non-contact profilometry the optical beam indirectly scans the sample surface. Non-contacting surface profilometry utilises an optical stylus to quantify bulk tooth surface loss by producing a topograph of its surface.

The assessment of tooth tissue loss as a result of erosion using profilometry has been proved both suitable and reliable as a method to evaluate the extent of the erosive lesion extent (Hughes et al., 2000, Attin, 2006). This technique measures the amount of loss relative to a non-affected reference area (West et al., 2011). For erosion studies, Profilometer has been referred to as the 'gold standard' (Hall et al., 1997) and can be used *in vitro* and in situ. The principle in using profilometry for monitoring erosion progression is to measure a step between an unchangeable reference area and an experimental area that is exposed to the erosive impacts. An increasing step height in sequential measurements indicates a progression of substance loss (Schlueter et al., 2005).

Only advanced stages of erosion are usually assessed using this method (Barbour and Rees, 2004). It is widely used *in vitro* and in situ for the measurement of losses greater than 2 μm (Attin, 2006). Therefore, measuring the degree of softening is unfeasible using this technique (Schlueter et al., 2011).

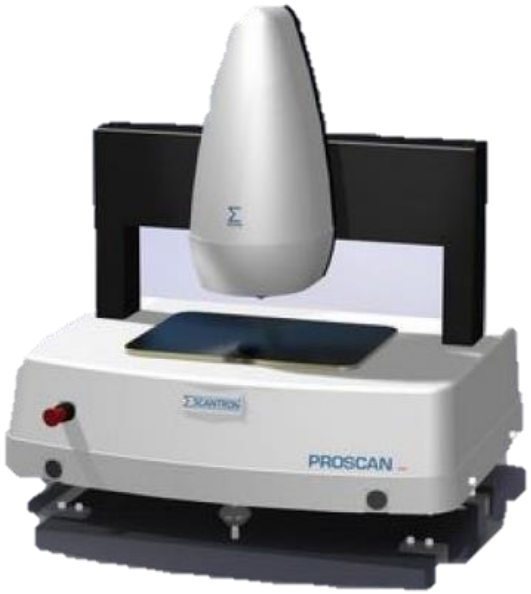

Figure 7 Commercial non-contact optical profilometer used for high accuracy high precision surface profilometry measurement (Scantron Industrial Products Ltd, Taunton, England, UK).

With profilometry, a relatively large area of enamel can be assessed fairly rapidly and data can be collected on the volume, as well as the vertical depth of enamel loss (Azzopardi et al., 2001). However, flat specimens are preferred for optimum sensitivity and accuracy of measurement (Schlueter et al., 2011).

4.2.3 Chemical Analysis

Other means of assessing the extent of dental erosion include chemical analysis of the dissolved minerals. The amount of dental enamel dissolution can be determined by measuring the amount of calcium and phosphate dissolved from the apatite crystals of dental hard tissue.

The technique of calcium analysis employs use of Ion Selective Electrodes (ISE) (Hara and Zero, 2008). An advantage of this methodology is that preparation of the specimen surfaces is not required in *in vitro* studies. A disadvantage of this method is that it does not provide information about physical and morphological changes of the lesions in the specimen, and that it is most suited for *in vitro* and *in situ* studies using extra-oral erosive challenge (Schlueter et al., 2011).

Atomic Absorption Spectrophotometry techniques have also been used. With this method, quantitative determination of chemical elements is done by employing the absorption of optical (light) radiation. An advantage of the spectrophotometry technique is that analysis of very small volumes of demineralisation solution; 10 µl is possible (Attin et al., 2005)

4.2.4 Microradiography

Microradiography is a technique that quantifies mineral loss according to the attenuation of X-ray radiation passing through enamel and/or dentine(Attin, 2006). The number of X-ray photons that transmit a dental hard tissue sample can be recorded either by photo counting-ray detectors or X-ray sensitive photographic plates/films. The detectors allow the mineral mass to be calculated by knowing the appropriate mass attenuation coefficient. Alternatively X-ray sensitive photographic plates or films record the grey values from which the mineral mass can be calculated by determining photographic density measurements calibrated using an aluminium step wedge (De Jong et al., 1987, Anderson et al., 1998).

Microradiography has been used in dental research since the mid-1970s (Groeneveld et al., 1974). For instance, Transverse Microradiography (TMR) has been developed for analysing transversely cut sections of enamel (50-200 μm) in order to assess lesion depth and mineral loss of carious lesions density (Amaechi et al., 2004, Fontana et al., 1996, Karlsson, 2010). TMR has been widely used in research for determining mineral changes in demineralised and remineralised dental caries and has more recently been adapted for dental erosion studies. Hall et al. found that TMR had a strong correlation with profilometry for measuring mineral loss for detection of early erosive lesions (Hall et al., 1997). The main advantage of TMR for assessing *in vitro* tooth wear is that it can simultaneously determine wear and demineralisation. However, the technique is rather time consuming and destructive (Arends and Ten Bosch, 1992). Despite the potential for disruption of the specimen, microradiography has been recognised as a useful and acceptable tool for assessing early tooth tissue loss from thin sections of tissue (Anderson et al., 1998).

4.2.5 X-Ray Micro-tomography

X-ray micro tomography (XMT), which is also called Micro CT is a miniaturized form of the well-known medical CT. XMT gives quantitative 3D information on linear attenuation coefficients at a scale of 2 to 100 μm (Davis et al., 2002, Wong et al., 2004). Micro CT shares its basic function with Computerized Axial Tomography (CAT or CT) scans, which have been used in the field of medicine for the last thirty to forty years (Landis and Keane, 2010).

In conventional radiography, X-rays pass through the investigated object, and the transmitted intensity is recorded as a two-dimensional image. The information contained in this radiograph is a projection of the absorption density in the sample onto the plane perpendicular to the X-ray beam direction. If the sample is imaged several times in different orientations then three-dimensional (volume) information on the sample structure can be obtained. A series of such radiographic images is reconstructed to form 3D tomographic cross-sections using computer algorithms. This is called a tomographic reconstruction. The data can be registered both in two or three dimensions and used for qualitative or quantitative analyses (Dowker et al., 1997)

Micro-CT is a variation of X-ray attenuation methods. Attenuation means the graduate diminution of radiation flux through a particular feature due to the process of scattering

and absorption of the radiation. The amplitude of voxels in an XMT image is proportional to the linear attenuation coefficient in the corresponding object voxels (neglecting artefacts), which are determined by the voxel densities and elemental compositions (Davis et al., 2013).

In dentistry, XMT provides 3D images that clearly distinguish the different tissues of the teeth. Thus it has been used to study demineralised lesions by providing quantitative high resolution 3D mapping of dental lesions (Choudhury and Jacques, 2012) mineral density (Elliott et al., 1998, Cochrane et al., 2012, Davis et al., 2013, Anderson et al., 1996). The technique is desirable because it is non-destructive so does not require sectioning or preparation of the samples. Hence changes in the microscopic structure can be repeatedly studied under different conditions i.e. between successive applications of externally induced changes by either mechanical or chemical processes (demineralisation or remineralisation).

4.2.6 Scanning Electron Microscopy

The Scanning Electron Microscope (SEM) was one of the first techniques described for assessing the structural changes of dental hard tissues (Boyde and Lester, 1967). SEM is widely used in dental erosion research (Cheng et al., 2009b, Faber et al., 2004). It is the most commonly used method for qualitative study of erosion in both enamel and dentine (Schlueter et al., 2011).

The SEM uses a very fine beam of electrons, which is scanned across the surface of the sample. Upon hitting the sample surface the electrons are either reflected as backscattered electrons or secondary electrons are generated by the interaction of the primary electrons with the sample surface. The resulting image resembles that seen through an optical lens but at a much higher resolution and a greater depth of field (Goodhew et al., 2000). The large depth of field is due to all parts of the image being in focus, despite being at different depths. Resolution of up to 1 nm is achievable with a field emission system and an in-lens detector.

For conventional SEM, the sample surface must be coated with a material that is electrically conductive in order to prevent accumulation of negative electrostatic charge. These charging effects result in artefacts that appear on microscope images as irregular, featureless bright patches, or streaks, which results in loss in resolution

(Shaffner and Van Veld, 1971). However, the coating is a disadvantage of this technique as the samples are irreversibly altered during the desiccation and sputtering process (Field et al., 2010). Therefore, conventional SEM cannot study the effects of treatments, such as remineralisation as serial measurements are not possible.

The development of Environmental SEM (ESEM) has allowed imaging in low vacuum and wet conditions making it suitable for imaging biological samples without the need for coating (Barbour and Rees, 2004). However, to date few studies have used ESEM to investigate *in vitro* or *in situ* tooth wear.

4.2.7 Optical Measurements Technique

Biomedical optics describes a range of technologies that utilise the interaction of light with biological tissue to convey some diagnostic information. Light primarily interacts with tissue by either being scattered or absorbed, characteristics that are described by the refractive index. Scattering occurs due to microscopic variations in refractive index. In soft tissue this can be attributed to the presence of cells, nuclei and extra cellular components. In dental hard tissue refractive index variations are assumed to occur at the interface between enamel prisms and the inter-prismatic structure. It is this scattering that gives enamel its white appearance. Therefore, any disease process that changes the physical tissue structure is likely to lead to some change in the way the light scatters.

The focus for a number of current studies in alternative techniques has been directed toward research, although with the ultimate goal of the applicability in the clinical situation. Caries has been studied using laser techniques such as Quantitative Light-Induced Florescence (QLF) (Pretty et al., 2002), Fibre Optic Trans-illumination (FOTI) (Côrtes et al., 2003), Polarised Light Microscopy (PLM)(White, 1995) and Confocal Laser Scanning Microscopy (CLSM)(Fontana et al., 1996).

Currently, the two most promising methods of assessing the surface characteristics of enamel are QLF (Stookey and González-Cabezas, 2001) and OCT (Pretty, 2006) that can be used for both laboratory-based *in vitro* experiments and *in vivo* clinical research.

QLF is a non-invasive optical technique developed for *in vivo* measurement of early caries (De Josselin de Jong et al., 1995). QLF is based on the principle that auto-

fluorescence of the enamel alters as the mineral content of the dental hard tissue changes (Karlsson, 2010), for example during the demineralisation and remineralisation process of dental enamel. The changes of optical parameters of carious tissue will lead to the emergence of dark-spot due to the increase in the scattering coefficient. The measurement reading from QLF gives a measure of the extent and severity of the lesion (Gomez, 2015). Changes in fluorescence radiance and lesion area can also be tracked over time, to monitor lesion development.

QLF has been used to assess tooth demineralisation *in vitro*. It has been used to longitudinally monitor, very early carious lesions of artificially demineralised enamel as soon as 24 hours after exposure(Pretty et al., 2002).

In vitro studies have also attempted to validate the use of QLF for quantifying acid erosion of enamel (Pretty et al., 2004). Pretty et al. demonstrated the ability of QLF to detect and longitudinally monitor erosion on unpolished enamel surfaces subjected to 30-min intervals of erosion for up to 15 hours. However, the main barrier for assessing surface changes with QLF is that it can only really determine trends rather than actually quantify tooth loss. Further studies of correlations with established methods are required to corroborate that the method measures what it purports to measure and to test their accuracy, reliability and reproducibility as QLF is strongly influenced by enamel porosity. Elton et al concluded that QLF is reliable for shallow erosive lesions but becomes less consistent as erosion advances (Elton et al., 2009).

5 Optical Coherence Tomography (OCT)

5.1 Introduction

Optical coherence tomography has been developed since the beginning of the 1990s as a non-invasive tool for biomedical imaging of human tissue with resolution on the order of 10 μm (Huang et al., 1991). OCT is analogous to ultrasound imaging except that infrared light waves rather than acoustic waves are used (Tearney et al., 1997). OCT is an attractive technique for clinical adoption as it is non-invasive and non-destructive and capable of producing cross-sectional images through inhomogeneous samples, such as biological tissue (Tomlins and Wang, 2005) without using ionising radiation.

Whilst predominantly used to provide two or three-dimensional images for visual evaluation, OCT can also provide quantitative information about local tissue density (Tomlins and Wang, 2005). Typically, OCT is used to image with a spatial resolution of around 1-15 μm although this varies between implementations. The maximum imaging depth in most tissues is limited by optical absorption and scattering to approximately 1–3 mm (Fujimoto, 2003b). The main disadvantage of OCT compared to alternative imaging modalities is its limited penetration depth in scattering media (Fercher et al., 2003).

5.2 OCT Basic Operation Principles

The functional principle behind OCT imaging is light scattering. OCT is based upon optical interferometry; whereby a broadband low coherence signal is split and later recombined by a Michelson interferometer. The split fields travel in a reference path, reflecting from a reference mirror, and also in a sample path where it is reflected from multiple layers within a sample (Schmitt, 1999). The light wave returning from the sample is a superposition of waves arriving with different delays to form interference fringes Figure 8.

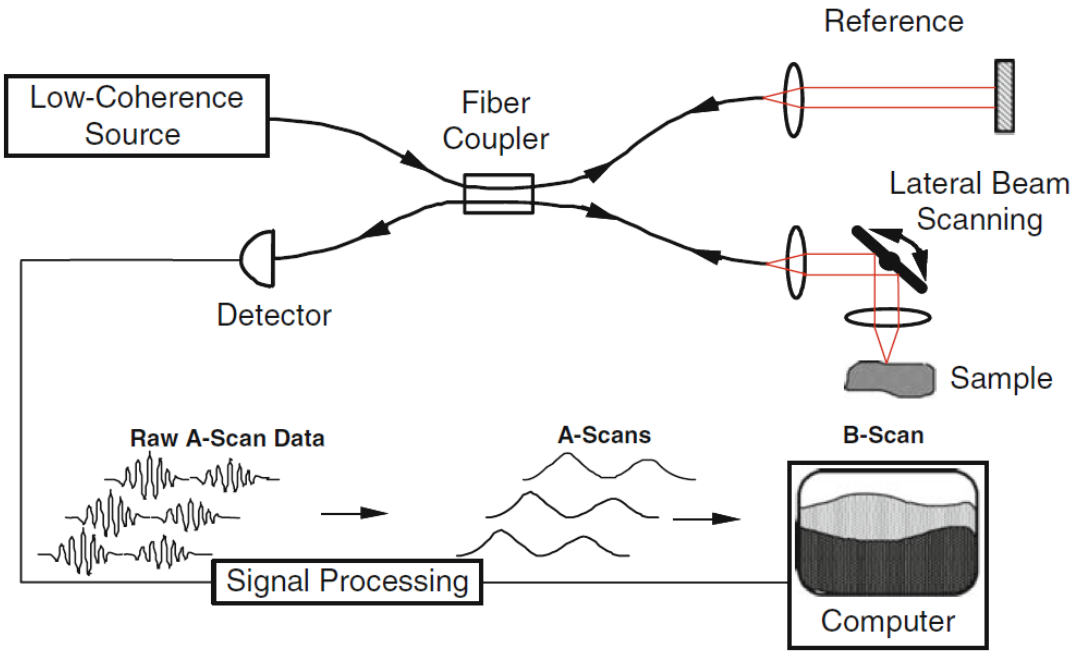

Figure 8 Schematic diagram of general fibre-optic OCT system. The red lines represent free-space optical paths, the bold lines represent fibre-optic paths, and the thin lines represent electronic signal paths. Image from (Izatt and Choma, 2008)

Interference between the optical fields is only observed when the reference and sample arm optical path lengths are matched to within the coherence length of the light (Fercher et al., 1993). The magnitude of these reflective signals is determined by the optical scattering properties of the tissue (Otis et al., 2000). The scattering is caused by microscopic spatial variations in refractive index (Tomlins and Wang, 2005). Thus, image contrast on an OCT image is determined by the optical properties of the tissue.

Basic OCT imaging discards the phase component of the interference signal, instead using its envelope to form images. The corresponding intensity peaks in the interference pattern envelope are collected as axial scans known as A-scans. These are recorded by OCT as changes in the detected light intensity. The intensity value is coded by grayscale or false color on a logarithmic scale to obtain optimal image contrast (Otis et al., 2000). By collecting many A-scans measured at adjacent positions of the sampling beam, the final graphical representation of a cross-sectional image can be constructed by displaying the value of the back-reflected intensity in depth, z, and in one of the transverse directions, x or y (Wojtkowski, 2010).

5.3 OCT Concepts

The general operation of different OCT modalities has been discussed extensively in the literature, including detailed theoretical descriptions of its operation (Fercher et al., 2003, Fujimoto, 2003a, Brezinski, 2006).

However, the interpretation of OCT images relies more critically upon understanding how light interacts with specimens. Therefore, this section will briefly introduce some key concepts required to interpret OCT images. Mathematical treatment is left to the specific chapters in this thesis where applicable.

5.3.1 Refractive Index

Each A-Scan represents scattering along the optical path travelled by light through the specimen. In the OCT image this is represented along a straight, vertical, line in the OCT B-Scan. However the optical path travelled by light propagating within the specimen is not guaranteed to follow a straight line. The path taken by the light depends upon the spatial refractive index distribution $n(x,y,z)$, where x, y and z represent a Cartesian coordinate system. Furthermore, the optical length, τ, of an arbitrary path, C, is integrated over $n(x,y,z)$,

$$\tau = \int_C n \mathrm{d}s$$

where ds is an infinitesimal step along the path. So, OCT produces images along an unknown physical path, of unknown physical distance due to an unknown spatial distribution of refractive index. To obviate this problem, a number of simplifications and assumptions are made. Generally, C is assumed to be approximately straight, following the direction of the incident light. The refractive index is represented by a constant average refractive index. Under these assumptions, the optical path length within a material having mean refractive index n_{ave} and thickness, Δz, is:

$$\tau = n_{\mathrm{ave}} \Delta z$$

Nevertheless, specimen refractive indices and layer thicknesses are often not known exactly, leading to potential errors when making measurements from OCT images.

Furthermore, refraction from off-normal illumination of the specimen and curved surface topography can lead to errors with physical measurements.

5.3.2 Scattering

An OCT image (B-Scan) is comprised of individual A-Scans, each representing the intensity of light backscattered along its path as it propagates through a specimen.

When a specimen is illuminated with light it scatters, either directionally or isotropically (in all directions equally). Optical scattering occurs when there is a variation in the refractive index of the specimen. At the limit of planar layers with different refractive indices, the interaction can be described fully by Fresnel's equations, with the directionality resulting in Snell's Law (Novotny and Hecht, 2012). However, when the specimen is described by a spatial function of refractive index, varying on a length scale much shorter than the wavelength of light, then Rayleigh scattering describes the interaction. A random spatial function of refractive index can be approximated by a distribution of spherical particles. The interaction of electromagnetic radiation with spheres can be solved exactly (Born and Wolf, 2000) and is called Mie Theory. Mie theory is often used to approximate the scattering behaviour of biological tissue where the spatial refractive index variations occur on a length scale similar to the wavelength of light, ~1 μm (Prahl, 1989).

Critically, Mie theory also describes the probability distribution of light scattering in any given direction. Light scattering back towards the incident direction is called backscatter and that continuing away from the light source is called forward scatter. Tissue scattering models in OCT have been previously discussed by (Schmitt, 1999). However, perhaps the most widely accepted is based upon the extended Huygens-Fresnel principle (Thrane et al., 2000), which has recently been experimentally validated in the single scattering regime (Almasian et al., 2015). Under the assumption of single scattering, this model resembles the Beer-Lambert law such that the backscattered intensity of light, *I*, decreases exponentially with depth, *z*, at a rate determined by the scattering coefficient of the medium, μ_s:

$$I(z) = \mu_B \mathrm{e}^{-\mu_s z}$$

Biological specimens are often represented conceptually and mathematically as a series of layers each having its own refractive index *n*, scattering coefficient μ_s and

backscattering coefficient μ_B. Furthermore, OCT imaging wavelengths are often chosen such that absorption can be assumed to be negligible to maximise the optical signal available for image formation. Therefore, the scattering coefficient accounts for signal attenuation as light propagates into the specimen and the backscattering coefficient accounts for the intensity of light detected by the OCT instrumentation and thus the contrast between tissue types. This idea is shown in Figure 9 where the specimen is comprised of three layers, each having distinct optical properties. Incident light is backscattered from different depths within the specimen. OCT A-Scans can therefore be considered as a spatial map of the backscattering coefficient, attenuated by the scattering coefficient.

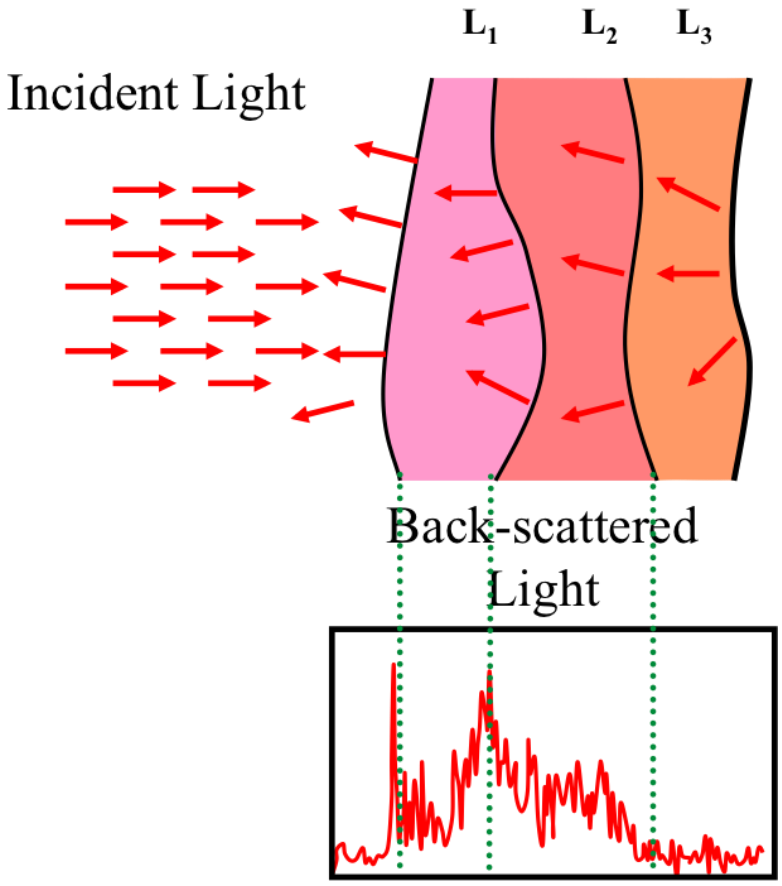

Figure 9 OCT images are formed when the illuminating light interacts with the specimen such that some light backscatters and is collected by the OCT optics. As light travels deeper into the specimen it is attenuated by the scattering coefficient of each layer. An OCT A-Scan is a depth map of the backscattering coefficient attenuated by the scattering coefficient.

5.3.3 Shadowing

OCT detects light that has survived a return path from the OCT objective and into the specimen without being absorbed or scattered outside of the objective numerical aperture. Consequently, the OCT signal detected from within the specimen is influenced by the attenuation of the light above it. Therefore, strong attenuation at the surface persists throughout the image, casting a shadow.

5.3.4 Signal Averaging

As described above, the OCT signal in tissue is typically considered to follow an exponential attenuation. Therefore, OCT images are usually presented on a logarithmic intensity scale, such that the signal loss with depth becomes linear.

Logarithmic compression of the intensity scale is beneficial for visualisation, but fundamentally limits the signal to noise ratio of the image data when only log. Scaled B-Scans are available for processing. This is shown below.

Assume a signal *S* and an additive Gaussian noise process, characterised by a zero mean and standard deviation σ. Thus, any discrete measurement of *S* can be written (the subscript *m* denoting that this is a measured value with noise)

$$S_m = S \pm \sigma$$

Now, assume that a set of M measurements is obtained such that each independent measurement *m* is indexed over *m*=1...M, i.e.

$$S_{m=1..M} = \{S_1, S_2 \ldots S_M\}$$

In this case, the mean Signal, $\overline{S}$, can be written:

$$\overline{S} = S \pm \frac{\sigma}{\sqrt{M}}$$

where the error term is equivalent to the standard error of the mean, i.e. the estimate of the true signal improves by taking more measurements. In other words, the noise term reduces as a factor of 1 over the square root of the number of measurements.

Therefore, the signal to noise ratio is

$$SNR = \sqrt{M}\frac{S}{\sigma}$$

Expressed in the log domain, this is

$$SNR_{log} = 10\,log_{10}(SNR) = 10\left[log_{10}\left(\sqrt{M}S\right) - log_{10}(\sigma)\right]$$

This is true of linear averaging.

However, taking the log of the measured signal, prior to averaging, assessment whether the same SNR enhancement is observed:

First, express the set of log signal measurements, s, as

$$s_{m=1..M} = \{10log_{10}(S_1), 10log_{10}(S_2) \ldots 10log_{10}(S_M)\}$$

The mean of this set of log measurements, $\overline{s}$, is therefore

$$\overline{s} = \frac{1}{M}10[log_{10}(S_1) + log_{10}(S_2) \ldots log_{10}(S_M)]$$

and is equivalent to

$$\overline{s} = \frac{1}{M}10[log_{10}(S_1 \times S_2 \ldots \times S_M)]$$

Using the definition above for S_m, this expands further to

$$\overline{s} = \frac{1}{M}10[log_{10}([S \pm \sigma]^M)]$$

In the presence of only noise, when no signal is present ((S=0)) we can express the noise component η as

$$\eta = \frac{1}{M}10[log_{10}(\sigma^M)]$$

Which simplifies to

$$\eta = 10log_{10}(\sigma)$$

Similarly, when noise is negligible (its standard deviation approaches zero, σ=0), the log average signal, s, is

$$s = \frac{1}{M} 10[log_{10}(S^M)]$$

which, applying log simplification becomes

$$s = 10log_{10}(S)$$

Since these are already in the log domain, the signal to noise ratio is the difference

$$SNR_{logave} = s - \eta$$

$$SNR_{logave} = 10[log_{10}(S) - log_{10}(\sigma)]$$

$$SNR = \frac{S}{\sigma}$$

Therefore, log domain averaging does not make any change to the signal to noise ratio.

5.4 Dental OCT

5.4.1 Light Scattering by Dental Enamel

Owing to the complex and anisotropic nature of biological tissues, optical properties such as absorption and scattering distributions generally depend on tissue orientation relative to the irradiating light source (Fried et al., 1995, Zimnyakov and Tuchin, 2002). In an attempt to clarify quantitatively the relation between the structure of enamel and light scattering, it is useful to understand the source of the scattering. Both demineralisation and remineralisation of dental enamel have been investigated by measuring changes in the backscattering of light by dental enamel. This optical process can be better understood if the scattering effects are explained on the basis of the structure of enamel. Scattering in dental enamel is caused by the combination of three effects: (Darling et al., 2006).

1. Prismatic crystallites scatter light because their refractive index is slightly higher than that of the surrounding medium

2. Inter-prismatic crystallites do the same but stronger because the index of refraction of the surrounding medium is lower

3. The periodic arrangement of prisms and inter-prismatic material causes diffraction of light waves. Due to processes 1 and 2 no diffraction pattern is formed but diffracted light is observed as scattered light.

Studies have shown that the scattering processes in enamel can be described by a linear combination of forward-directed and diffuse isotropic components (Altshuler et al., 1991). In these studies it has been shown that enamel HAp crystals are the main components responsible for the scattering process in enamel (Zijp et al., 1995) and therefore light scattering is relatively more isotropic (Fried et al., 1995).

At the dentin–enamel junction, dentinal tubules are oriented nearly perpendicularly to the propagation direction, which produce strong attenuation of backscattered light with increasing depth (Wang et al., 1999).

5.4.2 Previous Dental OCT Studies

OCT is a 3D microscopic investigation technique that has been used in both laboratory research and in clinics. This technique can provide structural information by detecting the light that is scattered from internal microstructures. The demineralisation during caries and erosion are characterised by changes within tissue structures (Feldchtein et al., 1998). These tissue changes modulate the intensity of the detected signal in the OCT images.

In recent years, OCT as an imaging technique has been widely applied in the study of hard tissue diseases. Structural changes during dental hard tissue disease process modulate the intensity of the detected signal in the OCT images. Reflectivity variation detected by OCT following demineralisation is expected to be related to the amount of mineral lost during the demineralisation process (Amaechi et al., 2003a). For example, during the caries process, micro-pores are formed in the lesions due to partial dissolution of the individual mineral crystals. Such small pores behave as scattering centres that strongly scatter visible and near-infrared (near-IR) light (Darling et al., 2006). OCT visualises this as a change in the signal intensity showing the depth of the lesion into the tissue.

This physical link between the demineralisation process and OCT image contrast is promising for quantitative evaluation of the degree of demineralisation (Amaechi et al., 2001). Furthermore, in previous studies, it appeared that increased reflectivity

from the superficial enamel in the case of lesions limited to enamel resulted in a low backscatter signal from the underlying sound enamel, therefore, the examiners could estimate the extent of lesion according to the border which appeared between the brighter and darker parts of enamel (Nakagawa et al., 2013).

Moreover, if caries progresses and results in the formation of cavities, the backscatter signal intensity in the margin of the defect increases, resulting in appearance of bright cavity borders that can readily be distinguished from a non-cavitated demineralised lesion (Shimada et al., 2013).

Amaechi et al. observed that various limiting factors that interfere with other imaging techniques based on the principles of fluorescence and diffraction were demonstrated to have no major effect on the application of OCT to detect caries. Factors specific to the oral cavity, such as the saliva and the presence of plaque or food debris did not affect the OCT results. Early caries detection can be obscured in the presence of bacterial plaque. Similarly, staining of the caries lesion influences the fluorescence of the lesion, thereby affecting the imaging and analysis of the lesion with the fluorescence devices presently used in clinic (Amaechi et al., 2001).

In general, demineralisation of enamel results in an increase in porosity because of mineral loss in the body of the lesion, which should be detectable with OCT. Small changes in volume % mineral cause large changes in light scattering/reflectivity.

Additionally, OCT systems can provide multiple views of the tooth tissue in 3D space, adding further versatility to tooth diagnosis. The A-scan mode can be used for quantitative analysis of the activity; demineralisation or remineralisation of the caries lesion over time. This could also therefore be exploited in the determination of the effect of caries therapeutic agents (e.g., fluoride mouth rinses, fluoride dentifrice) or laboratory testing of new oral healthcare products (Pretty, 2006).

OCT is not only valuable as a non-destructive tool for the assessment of anti-caries agents *in vivo* but is also valuable for *in vitro* studies as well since it does not require thin sectioning, and it can be carried out rapidly.

5.4.3 *In vivo*

Most of the research done so far using OCT in dental studies has been geared towards *in vivo* use. In some cases in situ appliances have been used to place these samples in the oral environment during *in situ* measurements (Amaechi et al., 2003a). Nevertheless, some researchers have attempted to image teeth *in vivo* with a combination of a designed and built hand piece for intraoral imaging of human dental tissue (Baumgartner et al., 1999, Colston et al., 1998) and OCT coupled stereo surgical microscope (Brandenburg et al., 2003)

Colston et al managed to identify hard tissue structures of the tooth in the OCT images. They also noted that imaging depth of the OCT system in enamel was higher than in the dentin, with the dentine-enamel junction (DEJ) visible in all the images. Likewise, several structural components of the gingival tissue including the sulcus, the epithelium, and the connective tissue layer were visible in their OCT images.

Their conclusive remarks suggested the need to modify their existing OCT system to improve image acquisition time, eliminate artefacts due to tissue birefringence and infection control, and improve registration of the hand piece against the tissue surface (Colston et al., 1998). Motion artefacts were present in 5% of the images. Motion artifacts that did occur were primarily low frequency modulations between adjacent A-scans due to patient breathing. Brandenburg et al., experienced difficulty in that not all teeth or soft tissue surfaces were equally accessible *in vivo* (Brandenburg et al., 2003). With a surgical microscope, access was best in the anterior parts of the oral cavity whereas posterior parts of the oral cavity were only accessible by use of a mirror (Brandenburg et al., 2003). Most significantly, Brandenburg et al observed that *in vivo* images showed a higher penetration depth than *in vitro* results obtained from imaging extracted teeth that were kept in saline solution.

The authors reported to observe some difficulty in that the relative position of the probing beam and the tissue affected the image. Similarly while trying to image inter-proximal regions, the authors found that typical dimensions of such contact sites were too large to be completely visualised.

Positive results showed however, that visualisation of carious lesions was possible. These appeared as bright band of high backscattering. Visualisation was affected

beneath the demineralised areas of the imaged extracted molar. The demineralised areas were apparent extending approximately 200 µm into enamel but this obscured the enamel–dentin junction underneath. The challenges faced by these researchers express the need for preceding laboratory research that is necessary in order to validate the OCT technique before implementation in clinics.

5.4.4 In vitro

Various influencing factors during demineralisation need to be taken into consideration. In order to study the nature of progression of the caries lesions, it has been necessary to establish and define all the factors suspected to play a role in the aetiology. To obtain such a standard platform with controlled parameters, focussing attention on desired specific factors, most of the research has been carried out in laboratories in *in vitro* models (Featherstone, 2000). In the laboratory setting, these factors can be controlled and characterised. For erosion studies, for example; time, volume, flow rate of solutions and consumption habits can be controlled. These factors have been suggested to be the main source of variation among *in vitro* and in situ models evaluating initial erosion (Young and Tenuta, 2011b)

In vitro measurements have been favoured in the vast amount of published work especially in validating OCT for dental studies (Amaechi et al., 2003a, Fried et al., 2002, Lee et al., 2009, Manesh et al., 2008, Sadr et al., 2013) Most of the studies carried out so far have been done on human dental samples extracted from patients for orthodontic reasons. Consequently, in most of the laboratory studies, researchers have used artificial demineralisation models to mimic the phenomena in the oral environment. Similarly in erosion studies, various models have been used to induce acidic challenges on the tooth surface (Barbour et al., 2003, Barbour and Rees, 2004). Most of the studies reviewed in this literature have used *in vitro* methods. Similar manifestation and characterisation of caries as observed on OCT images in *in vivo* have been reported.

Recent focus using OCT technique has been an attempt to quantify remineralisation. A study used OCT to image the remineralisation of subsurface lesions in bovine teeth (Mandurah et al., 2013). To obtain a standard platform with controlled parameters, focussing attention on desired specific factors with each experiment, it is ideally necessary to produce artificial caries like lesions *in vitro*. In order to objectively study

the multi-factorial nature of dental hard tissue lesions, simplified *in vitro* models have been adopted.

Artificial caries lesions allow for the control of the extension of the lesion among other factors including pH, severity and exposure time (Amaechi et al., 1999). For the purpose of laboratory studies, it is common to produce artificial lesions by using demineralising solution at pH levels lower than the critical pH. This model is used to define all the factors suspected to play a role in a simple acidic demineralisation process. Thus mimicking a simplistic model of artificial caries without taking into considerations of other oral environment factors.

Numerous studies have observed demineralisation induced by artificial lesions produced in teeth (Ten Cate et al., 1988, Argenta et al., 2003) and more recently using OCT (Sadr et al., 2013, Nazari et al., 2013, Nakajima et al., 2014). These studies have shown favourable results while observing a carefully controlled artificial demineralisation model. OCT images from these studies have confirmed demineralised lesions manifesting as regions of high back scattering underneath the enamel surfaces similar to natural caries images under OCT (Manesh et al., 2008).

Studies attempting to visualise carious lesions on different tooth morphology have been carried out. These were not only limited to the crowns of the teeth samples. Occlusal surfaces, pits and fissures, proximal surfaces and teeth roots were also scanned and examined for demineralisation and then OCT was used to determine the extent of the spread of the lesions.

5.4.5 Imaging of different tooth morphology & Challenges

The character of dental decay has changed dramatically with the majority of newly discovered caries lesions being highly localized to the occlusal pits and fissures of the posterior dentition and the interproximal contact sites between teeth.

Developing instruments that can quantify subtle surface changes, such as early demineralisation and erosive softening *in vivo*, are extremely challenging (Amaechi et al., 2003a). Such instruments need to be able to assess the natural enamel surface with its intrinsic curvature and the natural dentine surface with its persistent demineralised organic matrix. Tooth surface change is a complex process that can be measured in a variety of ways. No single technique provides a comprehensive assessment of the

varying tooth surfaces, and different techniques suffer different drawbacks. Some sections of the oral environment are difficult to access and assess. When exposed to demineralising solutions, the varied response in enamel solubility of different teeth may be associated with the developmental features of enamel, as well as the hierarchical microstructure of the prisms (Hariri et al., 2012b). The orientation of these rods and prisms may show variation among different teeth or different parts of the same tooth.

Several reports have investigated the application of OCT technology for direct imaging of caries, including smooth enamel surfaces as well as pits and fissure caries and approximal caries the latter being not directly accessible for imaging by other conventional techniques.

Imaging smooth surfaces

Chong et al, have showed successful cross-sectional imaging of the natural caries lesions on smooth enamel surface by OCT (Chong et al., 2007). The OCT images showed enamel caries as highlighted zone in tomograms which enabled efficient diagnosis of the lesion type, extent and dentin involvement. The aim of the study was to assess the inhibition of demineralisation in an *in vitro* simulated caries model by different fluoride agents using PS-OCT on smooth enamel surfaces. The mean integrated reflectivity (ΔR (dB x mm)) measured with PS-OCT between the control group and the groups treated with fluoride was found to be significantly different. Hence the OCT system was shown to be able to non-destructively measure the inhibition of artificial demineralisation on smooth surfaces by fluoride.

For the detection and distinction of caries from sound enamel, Nakagawa et al also noted a zone with increased brightness on SS-OCT images that appeared to correspond well with the demineralised zone in CLSM results (Nakagawa et al., 2013). The scanning light appeared to penetrate through the whole thickness of sound enamel, and the presence of the DEJ up to 3 mm underneath the intact enamel surface Figure 10. Furthermore, the researchers noted that enamel and dentin caries were outlined by a visible boundary on the cross- sectional OCT images.

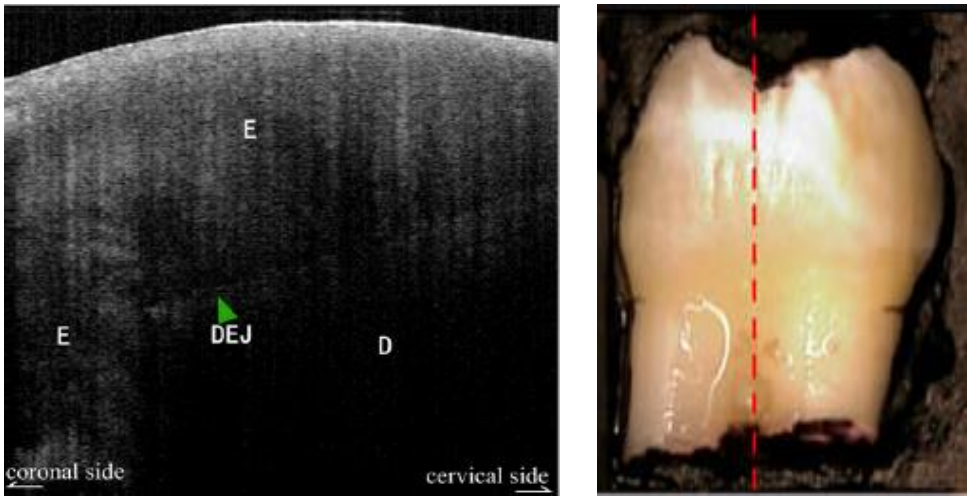

Figure 10 OCT image of smooth surfaces of extracted posterior tooth (Nakagawa et al., 2013). Enamel (E), Dentine (D) and DEJ. Red dotted line indicates location of OCT B-Scan.

The study was done to compare the effectiveness of OCT as compared to visual inspection and it was found that OCT had higher sensitivity for caries detection than visual inspection. Nakagawa et al. observed that signal intensity and attenuation patterns were both affected by caries. The effective imaging depth of OCT on tooth depends on the structure being imaged (Nakagawa et al., 2013). The extent of demineralisation was not quantitatively measured in the carious lesions. The challenges faced was that it appeared that increased reflectivity from the superficial enamel in the case of lesions limited to enamel resulted in a low backscatter signal from the underlying sound enamel, therefore, the examiners could only estimate the extent of lesion according to the border which appeared between the brighter and darker parts of enamel.

Imaging Interproximal

Shimada et al. carried out studies to determine the diagnostic accuracy of swept-source optical coherent tomography (SS-OCT) in detecting and estimating the depth of proximal caries in posterior teeth *in vivo* (Shimada et al., 2013). SS-OCT appeared to be a more reliable and accurate method compared to bitewing radiographs for the detection and estimation of the depth of proximal lesions in the clinical environment.

The SS-OCT system could detect the presence of proximal caries in tomograms that were synthesized based on the backscatter signal obtained from the proximal carious lesion through occlusal enamel Figure 11. SS-OCT showed significantly higher

sensitivity and larger area under the receiver operating characteristic curve than radiographs for the detection of cavitated enamel lesions and dentin caries. Since the optical characteristics of the enamel and dentin differ due to the structural and compositional factors, the two structures can be distinguished from each other with DEJ appearing as a dark borderline. The depth of demineralisation and caries penetration into dentin can be estimated by taking the location of the DEJ as a reference point.

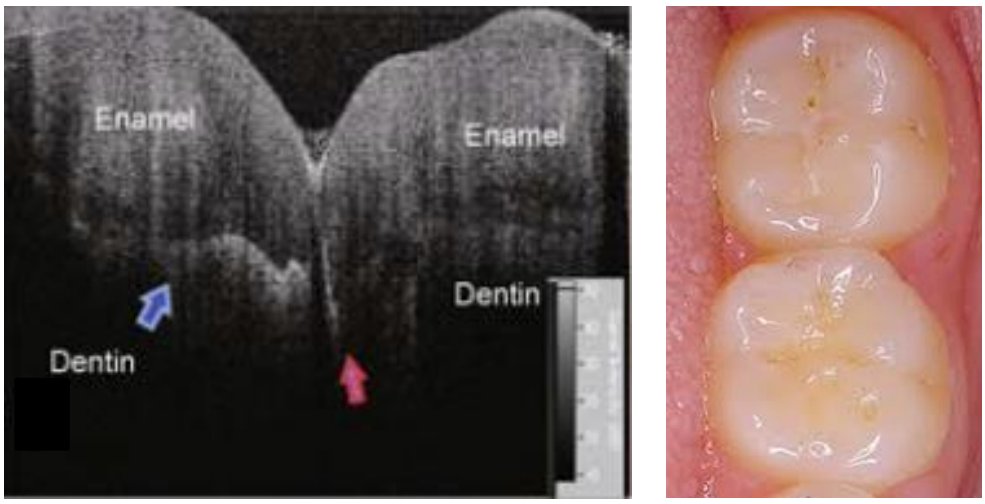

Figure 11 OCT images of inter-proximal surfaces of lower first and second molars of posterior teeth in vivo (Shimada et al., 2013). Red arrow indicates the proximal surface.

One major limitation was the measurements suffered from signal attenuation through the tooth, as a result of the SS-OCT probe having to be placed on the occlusal aspect of the posterior tooth, as the probe cannot be used through the side cheeks. Ngaotheppitak et al. showed that the integrated reflectivity in the perpendicular polarisation channel of PS-OCT could be used to represent the severity of demineralisation of the interproximal natural early caries lesions. They were unable to correlate the visual appearance, namely the lesion optical discoloration or pigmentation to either the lesion internal structure or severity when imaging proximal lesions (Ngaotheppitak et al., 2005).

Imaging occlusal surfaces

Jones et al. demonstrated that PS-OCT could image and quantify artificial caries progression on occlusal surfaces of posterior teeth (Jones et al., 2006a). The objective of their work was to investigate the relationship between the magnitude of

backscattered light and depolarisation recorded by PS-OCT with changes in the volume percent mineral of enamel obtained from high-resolution digital microradiography upon demineralisation.

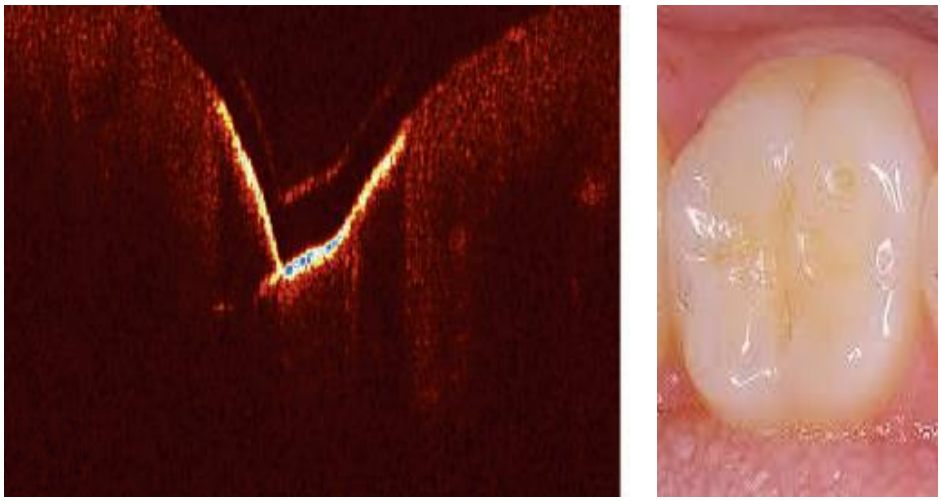

Figure 12 False colour images of occlusal surfaces imaged in vitro (Jones et al., 2013). High backscattering observed at site of artificial carious lesions.

The authors found that the penetration depth varied with the topography of the tooth, as the linearly polarised light had un-uniformly penetration within the tissue from 1 to 1.5 mm. Despite the possibility of increase in surface reflection and detector saturation, the researchers showed that PS-OCT was insensitive to the confounding effects of the intense Fresnel reflection at the surface of the tooth. One of the limitations in the study was that there was variability in occlusal lesion severity measured from the technique due to varying optical penetration and surface reflectivity. Images of sound occlusal surfaces did not show uniform penetration, as represented in the images because of the varying occlusal topography Figure 12.

Similarly, Staninec et al. had difficulty focusing on the lesions due to the topography of the occlusal surfaces and the limited depth of focus of their optical system (Staninec et al., 2011) but crucially the authors noted that although polarisation sensitive OCT systems did provide an apparent improvement in contrast, most of the benefit is near the tooth surface. Polarisation sensitivity also helps differentiate subsurface artefacts from lesions. However, the authors concluded that PS-OCT systems are more expensive and difficult to use and their study suggested that it is not absolutely necessary to have polarisation sensitivity to image deep occlusal lesions.

Imaging cracks

In a recent study, a (Swept Source system) SS-OCT was used for the detection of naturally formed enamel cracks *in vitro*. OCT images were compared against visual inspection results and CLSM observation was performed as a diagnostic validation to examine the presence and extent of tooth cracks on the investigation sites

This non-invasive method was capable of providing clear imaging of enamel cracks including information on the penetration depth Figure 13. Even when cracks extended beyond the DEJ, OCT was capable of imaging the whole feature, determining crack penetration depth (Imai et al., 2012).

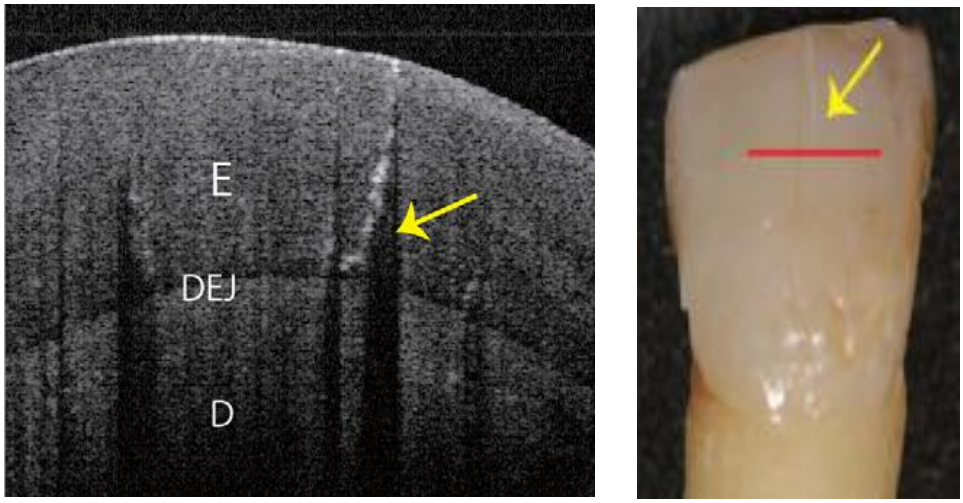

Figure 13 OCT visualisation of cracks within the enamel of anterior tooth (Imai et al., 2013). Enamel (E), Dentine (D) and DEJ. Red line indicates location of B-Scan. Yellow arrow shows the crack.

The enamel cracks on the images were clearly distinguished as a bright increase signal intensity. However, some of the intensified signals from deeper enamel cracks may have overlapped with enamel tufts, and this combined image appeared similar to a whole-thickness enamel crack on the image.

Furthermore, Imai et al. noted that their SS-OCT setup had limitations for the detection of root fracture at the sub gingival zone both through an open root canal because of the probe design and through the gingival because of the attenuation of the signal in the soft tissue and bone (Imai et al., 2012). The authors suggested a combinational usage of SSOCT for coronal fracture and radiograph for root fracture to improve clinical diagnosis.

Imaging roots

Lee et al. conducted experiments on artificial demineralisation on exposed root surfaces (Lee et al., 2009). The purpose of the study was to determine whether PS-OCT could be used to non-destructively assess artificial demineralisation on root surfaces and image the remaining thickness of the cementum layer. Another aim was to demonstrate that PS-OCT could be used to measure the inhibition of demineralisation on the surfaces of tooth roots by fluoride.

The OCT instrument was shown to detect and distinguish different layers of the root distinctly, namely the enamel, dentine and cementum. The authors observed that the cementum layer presented lower reflectivity as compared to the underlying dentin that caused a rapid change in reflectivity at the interface. The strong reflections from the root surface and the underlying cementum-dentin junction also enabled the calculation of the cementum thickness. This was proposed in estimate the severity of early non-cavitated root caries lesions by measuring the shrinkage in the lesion area using PS-OCT. However one of the challenges the authors faced was that this was easy to accomplish for *in vitro* studies where a stable level of hydration could be maintained, but stable hydration of the lesion was more difficult for *in vivo* measurements. Shrinkage and the lack of optical changes in the outer transparent cementum layers after demineralisation confounded analysis of lesion depth and severity. The most significant discovery in this study was the lack of optical changes in cementum as a result of demineralisation. It was concluded that the apatite crystallites are very small, on the order of tens of nm, to effect visible light or near-IR light and upon demineralisation may not produce as dramatic a change in light scattering as is observed for dentin and enamel.

5.4.6 Quantifying Dental OCT Systems Measurements

Numerous authors have demonstrated the potential of OCT for quantitative measurement of dental caries (Fried et al., 2002, Amaechi et al., 2001, Colston et al., 1998).

Amaechi et al. used OCT to analyse the change in mineral content as a function of the depth of penetration of light through the layers of enamel. For quantitative assessment, the researchers used A-scans to show the depth (mm) resolved reflectivity (dB) of the

tooth tissue in order to calculate the degree of reflectivity (R) of the tissue at any depth (Amaechi et al., 2003a). The result showed that ΔR (dB mm) decreased with increasing demineralisation time. The study showed that ΔR could be correlated with the integrated mineral loss (volume % mineral × microns) called ΔZ in Transverse Microradiography techniques. A linear correlation (Pearson correlation coefficient *r* = 1.00) was observed between the mineral loss, Δ*Z* (vol % μm), measured and the percentage reflectivity loss, $R^{\%}$. The authors concluded that with the above procedure, OCT could quantitatively monitor the mineral changes in a caries lesion on a longitudinal basis.

Other studies have assessed lesion depths in OCT images in order to quantify lesion severity. Lesion depths have been taken by measuring the distance between the ($1/e^2$) points in the lesion line profile to the point corresponding to the peak intensity (Can et al., 2008).

Similarly, signal attenuation measurements have been used to express the degree of decay in backscattered intensity between the exposed and non-exposed areas (Chew et al., 2014). The OCT-attenuation coefficient (μ_t) parameter derived from Beer-Lambert law has been used to calculate average signal intensity profile based on the exponential decay of irradiance from the surface of the specimen(Mandurah et al., 2013).

5.5 Current Limitations in Dental OCT Studies

In laboratory examination, exposure of specimens to ionising radiation is not a concern. Instead the focus of attention is on measurement accuracy, repeatability and data quality. But when shifting the focus to clinical based measurements, there is a need for further development, evaluation and validation of new methods. Important factors such as acquisition time, control of variables such as the environment need to be addressed. For clinical measurements, acquisition times are greatly important and patients' movement and accuracy needs to be taken into consideration. The sensitivity of any methodology towards patients' movement also has to be controlled and thus faster acquisition times are necessary. For accurate measurement of tissue properties *in vivo*, motion artifacts should be minimized (Kholodnykh et al., 2003).

5.5.1 Repeatability and Standardisation

There have been a wide variety of techniques used in previous OCT studies of dental hard tissue. Some researchers have used laboratory techniques combined with clinical techniques to image different aspects of dental disease. As a consequence, it has been difficult to establish a standardized system or protocol of measurement. Furthermore, previous studies have been affected by:

a) Poor characterization of OCT instrumentation and sample preparation resulting in unknown and un-quantified implications on measurements.

b) Previous results have not been reproducible.

c) Lack of standardization of approach to study design leading to inability to adequately compare results from different studies.

d) Inaccuracy in sample repositioning during repeat measurements

e) Difficulty in co-locating OCT images and histological tooth sections in studies that compare OCT images with other techniques

f) Challenges associated with varied surface topography of the teeth. Various tooth surfaces have different degrees of difficulty in imaging; inter-proximal and occlusal surfaces, for example, have varying optical penetration and surface reflectivity. These factors have not been well accounted for and not well characterized.

5.5.2 Uncertainty Analysis

The OCT instrument produces data of the object being imaged. All measurements, including those of OCT, are subject to noise and uncertainty. The observations of any specimen under OCT instrument may produce many possible data sets because of randomness introduced by the measurement process (Drexler and Fujimoto, 2008). Therefore OCT results need to be interpreted with caution (Gomez et al.). Standardised techniques for characterisation of OCT instrumentation are required. Measurement calibration phantom could perhaps be used to describe systems specification and performance during dental OCT studies.

5.5.3 Real-time Imaging

It is widely believed that OCT can be used as a tool for early detection of caries at initial stages (Amaechi et al., 2001). The early detection of tooth demineralisation hence offers a chance to impede the disease at its inception. Time-lapse imaging of the demineralisation as it takes place could yield invaluable information, reinforcing current caries treatment strategies and help design novel anti-caries agents that can address caries at different stages of advancement. Moreover, the effectiveness of these therapeutic agents, both marketed and experimental formulations can only be determined with a diagnostic method that can quantitatively monitor the periodical change in the mineral status of the caries lesion on a longitudinal basis (Amaechi et al., 2003a).

To apply improved remineralising and caries-arresting agents, and assess their efficacy and mode of action, it is important to closely monitor the cycles of demineralisation and remineralisation at regular time intervals. This could assist in determining the gradual phases of lesion activity and suggest the best stage for implementation of preventive and restorative treatment methods. Similarly, erosion studies and the dynamics of the erosion process would also benefit from real-time monitoring of lesion activity especially in the laboratory setting. For these studies, evaluation of the earliest time points that erosive lesion observations can be measured using OCT is imperative. Real-time imaging of lesions in order to validate *in vitro* studies has not been done. OCT measurements of samples under investigation without movement and drying are needed in order to monitor disease process longitudinally.

5.5.4 Stability of Measurements *in-vitro*

In vitro measurements have been favoured in the vast amount of published work especially in validating OCT for dental studies (Le et al., 2009, Manesh et al., 2008, Sadr et al., 2013).

Various influencing factors during *in vitro* demineralisation need to be taken into consideration. In order to study the nature of progression of the caries lesions, it has been necessary to establish and define all the factors suspected to play a role in the aetiology. In the laboratory setting, these factors can be controlled and characterised.

To obtain such a standard platform with controlled parameters, focussing attention on desired specific factors, most of the research has been carried out in laboratories use *in vitro* models (Featherstone, 2000). For erosion studies, for example; exposure time, volume, flow rate of solutions and can be controlled. These factors have been suggested to be the main source of variation among *in vitro* and in situ models evaluating initial erosion (Young and Tenuta, 2011a). Consequently, in most of the laboratory studies, researchers have used artificial demineralisation models to mimic the phenomena in the oral environment. Similarly in erosion studies, various models have been used to induce acidic challenges on the tooth surface.

Similar manifestation and characterisation of carious lesions observed on OCT images *in vitro* have been reported. Carious lesions have been observed as to exhibit high back scattering in enamel. However some researchers have failed to mention the loss of sub surface structures that is also seen, which makes analysis problematic.

Repositioning of the samples for accurate imaging has been one of the major confounding factor in lab-based studies (Chew et al., 2014). The samples are constantly moved between demineralisation solution and imaging apparatus in order to image them during the experimentation process, introducing errors in repositioning. This is significant as most studies used a single B-scan for analysis. For example, the slice thickness of the PS-OCT images reported by Jones et al. which were used for comparative analysis to microradiography, were 30 μm compared to the 200 μm section for microradiography (Jones and Fried, 2006, Kielbassa et al., 1999). This suggests that micrometre differences in section matching in those comparable studies have the potential to introduce errors in the correlation of the images and the quantification.

Specimen surfaces are also prone to strong Fresnel Reflections. To avoid this effects during experimentation, researchers have attempt to reduce the reflection from the tooth surface by deliberately imaging the sample at an angle, or by producing an artificial displacement covering the surface with a thick layer of water or a high refractive index liquid with a refractive index similar to enamel. Imaging the sample at an angle is a simple and effective method of reducing the specular reflection of the surface. However, it is only effective for flat samples. Applying a liquid to the surface is more problematic since it is difficult to control the thickness of the layer, and

beading of the liquid cause distortion of the optical path length, distorting the image of the lesion (Chan et al., 2013, Chan et al., 2015).

The irresolute results in OCT studies add to the undetermined confidence that surrounds OCT in dental study. In addition, when small amounts of mineral loss are to be monitored, the tooth surface should be placed in as reproducible position as possible for measurement, because surfaces are often inhomogeneous.

5.5.5 Hydration effects on the OCT measurements

Recent studies, using conventional OCT without polarisation sensitivity, have pointed out possible effects of hydration of samples on OCT images (Fried et al., 2002, Natsume et al., 2011, Shimamura et al., 2011). This study has shown that the hydration state affects the OCT signal intensity from enamel lesions in proportion to the demineralisation extent.

Nazari et al. carried out a study comparing the reflectivity of sound and demineralised enamel under hydrated and dry conditions (Nazari et al., 2013). The study found that sound enamel showed very similar images regardless of the hydration state of the specimens. On the other hand, demineralised enamel at hydrated and dry conditions showed different images. Under dry conditions, higher brightness was observed at enamel surface as well as enamel bulk for longer periods of demineralisation, but generally a clear boundary was not observed. In other words, a visual border between the brighter and darker parts of enamel could not be found. Likewise, on hydrated specimens, demineralised enamel appeared to be brighter as the demineralisation period increased; however, a boundary could be observed in some specimens. Control groups showed no change, hence confirming that the longitudinal changes observed were actually due to demineralisation, and not a systematic drift in the measurement (Nazari et al., 2013).

Significant differences were found between sound and demineralised enamel, and between different periods of demineralisation evaluation of the OCT signals at hydrated and dry conditions. Hydration was found to affect reflectivity in direct proportion to the lesion extent.

Recent study looked at the influence of several high refractive index fluids on the performance of polarization sensitive optical coherence tomography (PS-OCT). The

study showed effective imaging depth and lesion contrast improvements using the liquids which further enhanced the detection of hidden occlusal caries lesions (Kang et al., 2014).

6 Materials and Methods

6.1 Bovine Enamel Samples

Bovine enamel samples from one-year-old calf incisors were sectioned into 5-10mm diameter discs, sliced and polished in the coronal plane to a thickness of 3 mm such that they comprised both dentine and enamel. The samples were then embedded into a 25mm diameter clear resin substrate as shown in Figure 14. The enamel surface was prepared by polishing to a flat specular finish, leaving a residual enamel thickness of approximately 0.5 mm on top of the underlying dentine. Modus Laboratories Ltd, Reading, UK, undertook preparation and mounting of the discs.

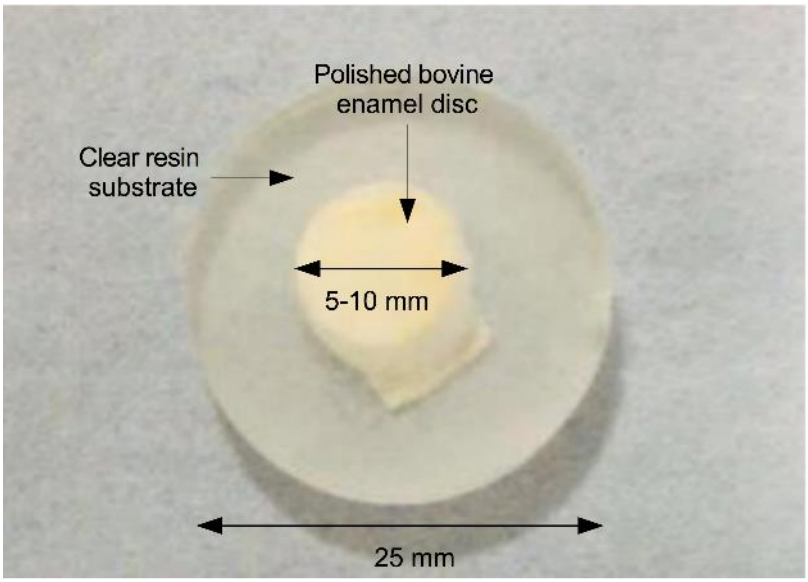

Figure 14 Bovine enamel disc measuring approximately 10 mm in diameter, embedded in a clear resin substrate having a diameter of 25 mm.

6.2 *In vitro* Erosive Model

A diluted citric acid model previously used for erosion studies (Hughes et al., 2000, Barbour et al., 2003, Young and Tenuta, 2011b) was prepared as 0.05 M citric acid solution. This was prepared by adding 10.6 grams w/v of anhydrous citric acid powder (PHR1071, Sigma Aldrich, UK) to 250 ml deionised water and stirred using a magnetic stirrer. After complete dissolution of the powder in the deionised water, the final volume of solution was adjusted to 1000 mL by adding deionized water while on the stirrer. The solution was buffered to pH 3.8 by the addition of 1 M Sodium

Hydroxide NaOH standard solution (71395, Sigma Aldrich, UK). The stock solution was stored at 25°C for a period of 2 hours prior to use. The pH of the solution was monitored throughout the experiments using SenTix® 41 electrode pH-meter (WTW GmbH, Germany).

6.3 *In vitro* Caries Models

Two acetic acid demineralising models were used in these experiments. The solution were prepared as follows:

A diluted acetic acid model, previously reported for demineralisation studies (Anderson and Elliott, 1992, Margolis and Moreno, 1992), was prepared as 0.17 M acetic acid. The solution was prepared by adding 10 ml acetic acid (A6283 Sigma Aldrich, UK) to 990 ml deionised water stirring using a magnetic stirrer. The solution was buffered to pH 4.0 by the addition of 1 M Sodium Hydroxide NaOH standard solution (71395, Sigma Aldrich, UK). The pH of the solutions was monitored using a SenTix® 41 electrode pH-meter (WTW GmbH, Germany).

A caries model that typically contains a source of Calcium and Phosphate, enabling sub-surface lesion to form whilst maintaining an in-tact surface (Ten Cate et al., 1988, Damen et al., 1998, Chan et al., 2013). The caries-like model solution was prepared as 2.2 mM $CaCl_2$, 2.2 mM KH_2PO_4 and 0.05 M acetic acid (comprising 2.871 ml of acetic acid in a stock solution of 1000 ml). The pH was adjusted to 4.4 with 1 M Sodium Hydroxide NaOH standard solution (71395, Sigma Aldrich, UK). The pH of the solutions was monitored using a SenTix® 41 electrode pH-meter (WTW GmbH, Germany).

6.4 *In vitro* Remineralisation Model

Both acidic and neutral remineralisation solutions adapted from previous studies (Jones et al., 2006b, Yamazaki and Margolis, 2008) were used. A 1 litre solution was prepared by adding 2mmol $CaCl_2$, 1.2mmol KH_2PO_4, 150mmol NaCl and 2 ppm NaF in deionised water. The pH of the remineralisation solution was adjusted to pH 4.9 for the acidic remineralisation model and pH 7 for the neutral remineralisation model. The pH of the solution was monitored throughout the experiments using SenTix® 41 electrode pH-meter (WTW GmbH, Germany).

6.5 Sample Holder

A custom multiple specimen holder was used for this study. The holder comprised 6 isolated flow-cell chambers into which individual specimens were placed. The entire holder was constructed from transparent Perspex (polymethyl methacrylate-PMMA), comprising approximately cuboid chambers measuring 24x24x4 mm (width x height x depth) and having an actual volume of 2.3 ml Figure 15. The true volume was slightly less than the cuboid volume due to rounded chamber edges. A single piece PMMA lid covered the compartments with each being isolated by a rubber O-ring (RS Components, Corby, UK). These were placed in semi-recessed grooves around each compartment such that a watertight seal was formed between the sample holder and its cover once screw fastened.

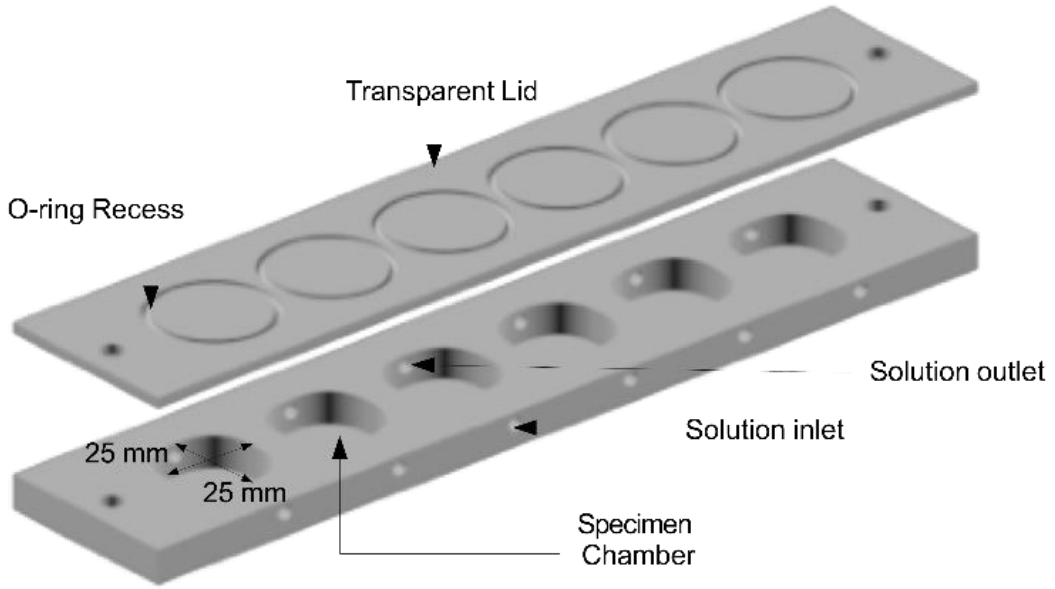

Figure 15 Specimen holder constructed from transparent PMMA, comprising 6 independent flow cell chambers. The total volume of each chamber = 2.3 ml. O-rings are incorporated to stop leakage.

The design of the chambers was such that they could accommodate approximately 0.8 mL of solution with the specimen and resin disc occupying the remaining volume (1.5 mL). The side walls of the holder were drilled to give inlet and outlet holes in order to deliver the demineralisation and remineralisation solutions.

6.6 OCT Configuration

The OCT system used was custom designed and built in-house at Queen Mary University of London. The instrument incorporated a fibre optic Michelson (Rollins and Izatt, 1999) interferometer design utilising a super-luminescent light emitting diode (SLD) optical source (SLD1325, Thorlabs Ltd, Cambridge, UK), operating with a nominal central wavelength of 1325 nm and bandwidth of approximately 100 nm. The axial and transverse resolutions were nominally 8 and 10 μm in air respectively. The emitted infrared radiation from the source is coupled into a single-mode fiber-optic Michelson interferometer along with an aiming beam of a continuous wave laser diode with the wavelength of 640 nm. The light was split into a sample and reference arms by a 50/50 beam splitter. The backscattered signal was collected back through the beam splitter and interference fringes were detected by a high-speed spectrometer, comprising an InGaAs linear detector array (SU-LDH2, Sensors Unlimited, USA), a reflective diffraction grating and focussing/collimating achromatic doublet lenses.

Images were obtained by raster scanning the probe beam over the tissue surface using a two-dimensional galvanometer configuration (GVS012, Thorlabs, Ltd, Cambridge, UK). The light was focussed beneath the sample surface by low numerical aperture scan lens (LSM03, Thorlabs, Ltd, Cambridge, UK). The system acquired, processed and displayed 3D OCT data in real-time, with a 2D B-Scan rate of approximately 100 frames per second using a general-purpose graphics processing unit (NVIDIA C2070) (Rasakanthan et al., 2011). Three-dimensional OCT volumes were acquired as a series of 500 B-Scan images, each comprising 500 A-Scans, of length 512 pixels.

The system point-spread function was measured using the method and phantoms described by (Tomlins, 2009). The axial and transverse resolutions in air respectively are described in Table 6.1.

Parameter	**Setting**
B-Scan Width (x × y)	3.5 × 3.5 mm
A-Scans per B-Scan	500
Number of B-Scans	500

Volume acquisition time	5 seconds
Axial PSF FWHM	8 um
Lateral PSF FWHM	10 um

Table 6.1 OCT system parameters. The system acquired, processed and displayed 3D OCT data in real-time, with a 2D frame rate of 100 frames per second.

Repeatable measurement of multiple specimens was facilitated by mounting the OCT imaging probe onto a two-dimensional motorised linear translation stage (LTS300, Thorlabs, Ltd, Cambridge, UK). The stages were mounted in an orthogonal (x,y) configuration, such that the samples could be arranged in a 2D matrix. The (x,y) coordinates of the light beam on the sample was recorded for accurate repositioning. The linear stages were operated automatically under computer control to achieve up to 2.0±1.7 μm positional repeatability in each dimension (Thorlabs, Ltd, Cambridge, UK).

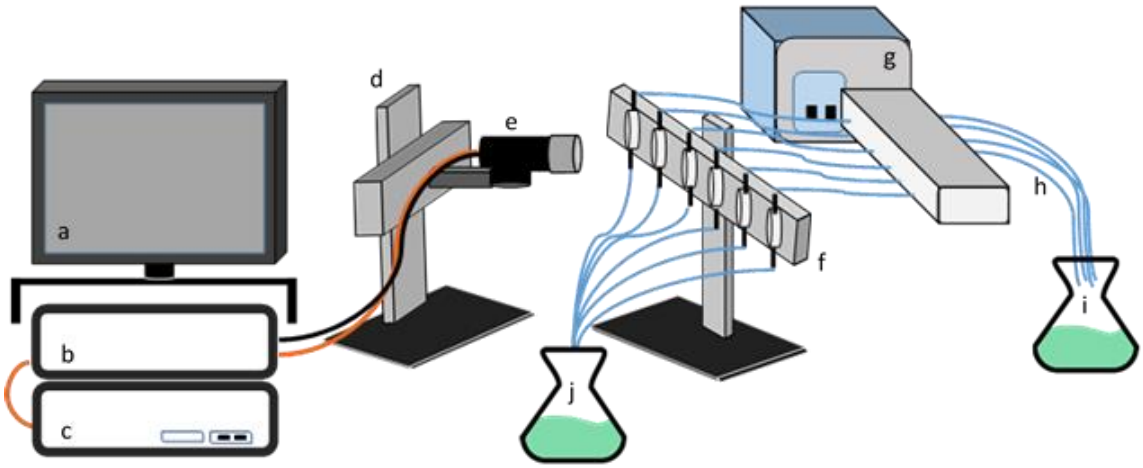

Figure 16 The OCT configuration used in the experiments. a) PC monitor, b) Continuous-wave red laser diode source (640 nm wavelength), c) Infra-red Light Source, d) Linear translation stage, e) Objective lens, f) Sample holder, g) Pump, h) Tubing and connectors, i) Acid solution reservoir and j) Solution drain.

6.7 Demineralisation Protocol

In order to produce uniform thickness across all samples, specimens were ground and polished to a thickness of 3mm with a p180 abrasive paper (3M PLC, Bracknell, U.K.).

The grinding and polishing stage were completed using a Kemet 40 automatic lapping unit (Kemet International Ltd. Maidstone, UK).

This was done in order to avoid optical path length mismatch by ensuring all samples were in the same imaging plane when placed in the sample holder. A micrometre gauge (RS Pro Micrometre, RS Components, Corby, UK) was used to confirm the specimen thickness.

The specimen surfaces were painted with a thin layer of acid-resistant varnish in the form of nail polish, Revlon (570, New York, USA) to prevent demineralisation except on a 3x3 mm region of interest.

The bovine samples were then immersed in 100 ml of deionised water for 24 hours prior to exposure to the demineralising agent. After the 24-hour hydration period, the samples were placed in isolated compartments within the sample holder, orientated with the enamel surface perpendicular to the OCT probe beam. A maximum of six samples were placed in the sample holder for each experiment. Each chamber was isolated by use of a rubber O-ring placed in the semi-recessed grooves around each compartment such that a watertight seal was formed. A transparent lid was placed over the sample holder, leaving a 1 mm gap between the enamel surface and its inner surface.

The demineralisation solution was introduced into each chamber of the holder through an inlet channel located below each specimen and ejected through an outlet channel located above. The solution was continuously refreshed at a rate of 5 mL/minute by a multi-channel pump (323Du/D, Watson Marlow, UK), drawing fresh solution from a 1 litre reservoir and ejecting used solution into a separate container. Both the inlet and outline channels were connected to different channels of the pump using clear PVC tubing having a 3 mm bore and 1 mm wall (01-94-1580, Altec Ltd, UK). The tubing was connected to the chamber inlet and outlet channels using winged 21 gauge winged infusion set syringes (SURFLO®, Terumo Medical, Belgium) and plastic connectors (05-44-5515, Altec Ltd, UK).

Experimentally, the specimen holder was mounted vertically such that the enamel surface was perpendicular to the bench. This configuration was chosen following experiments whereby bubbles formed on the enamel surface and prevented clear OCT images to be acquired. The vertical orientation allowed the bubbles to rise away from

the field of view. However, by operating in this regime, bottom of the specimen was exposed to the acid challenge a few seconds before the top. This was assumed to have a negligible impact upon the results. Baseline images of the samples were taken and the x,y positional information was then recorded and programmed at each sample position for automation.

The demineralisation process was then initiated by pumping the acidic solution through the samples. Filling of the sample compartments with 0.8 mL solution took less than 10 seconds. Once all sample holders were full, OCT imaging commenced.

For the artificial caries model and long-term erosive model, the OCT system was set to acquire hourly images for a total of 40, 48 - 72 Hours. For short-term (< 2Hours) erosive models, the OCT system was set to acquire rapid data in order to image early stage erosion. For remineralisation studies, the OCT imaging was acquired at hourly intervals for a total of 7 - 14 days.

6.8 Techniques

The main validation techniques with relevance to this thesis are surface microhardness, profilometry and X-ray Micro-Tomography and therefore the use of these will be reviewed below.

6.8.1 Microhardness Measurement Protocol

A Vickers micro-indenter (HMV Microhardness Tester, Shimadzu, Japan) was used to assess the surface hardness of the bovine tooth samples. The enamel blocks were placed flat on the translation stage of the indenter so that surface of the enamel was perpendicular to the direction of the load of the indenter. A surface area of approximately 1 mm × 1 mm window of the unvarnished sections of the bovine enamel was identified for indentation. The identification was done by firstly ensuring that the aiming beam of the micro-indenter was in focus before the loading was performed. Indentations were then made using a Vickers diamond indenter, with a load of 200 g applied for 10 s. Six indentations approximately 100 μm apart were made at the identified area during each measurement time point. All the indentation, and indent dimension measurements were performed manually. The horizontal lengths were measured, and the Vickers hardness numbers were calculated and averaged. This was repeated for all samples at 5, 10, 15, 30, 45 and 60 minutes of acid challenge.

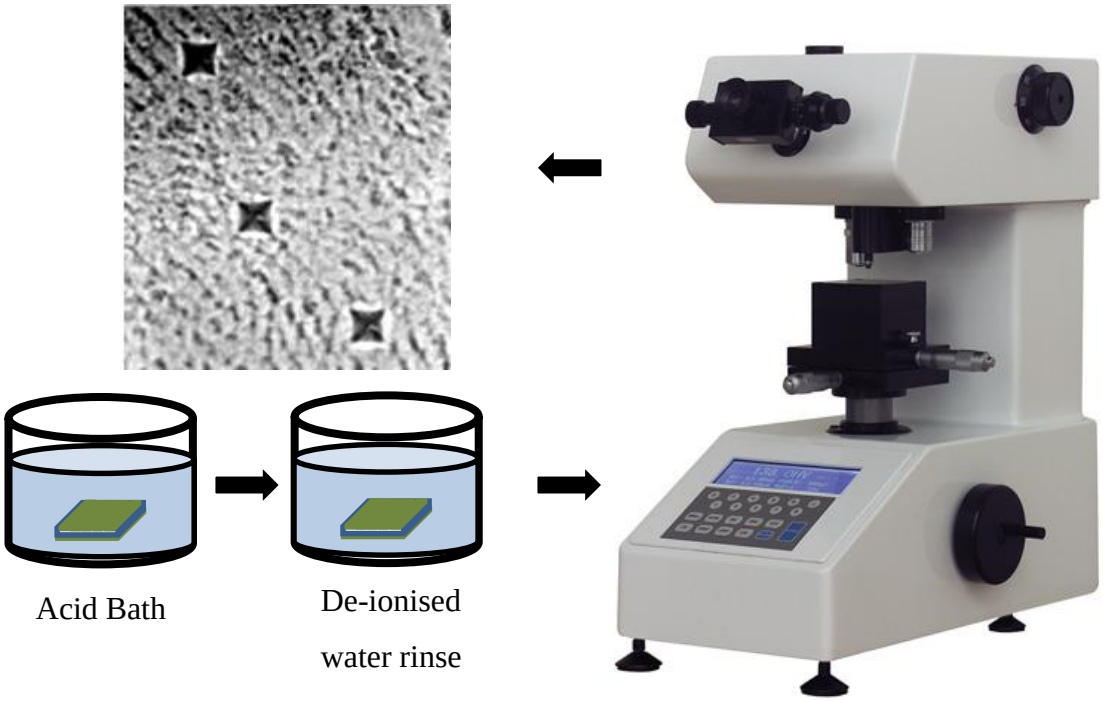

Figure 17 Microhardness Measurement setup. The samples are firstly dipped in acid solution for the erosive challenge then rinsed with deionised water and left to dry in room temperature. After the drying, hardness measurements are acquired by indentations with a Vickers indenter.

6.8.2 Profilometry Measurements

A Proscan 2000 non-contact surface profilometer S13/1.1 scan-head with resolution 25 nm (Scantron Industrial Products Ltd, Taunton, England, UK), was used to acquire topographs of the eroded bovine samples. The samples were placed flat on the translation stage of the profilometer with the enamel surface perpendicular to the beam. The sample surface was brought into focus by adjusting the height of the stage. The scanning was done using a step size of 20 μm in both x and y directions with the number of step being 400 (x-axis) and 200 (y-axis) in order to cover the whole range of steps. The resultant topographs (8 x 4 mm) were interpreted using propriety Proscan software.

From the topographs images, 5 line profiles were selected at spacing of approximately 1mm for each sample. Measurements were made at each step height after each erosive period. The mean step height of each model represented an actual substance loss. In sequential models, the difference in mean step height was defined as the erosive loss. The mean values were then averaged for all specimens and mean rate of erosion was determined.

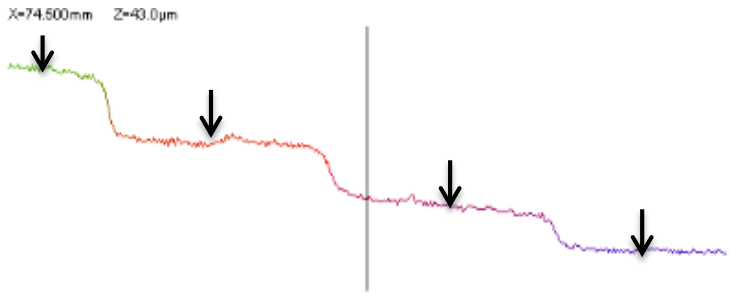

Figure 18 An illustration of one line profile of the erosive step height measured using the optical profilometer. Measurement is made at each step height for each sample. The mean step height of each model represented the physical loss due to the acid challenge.

6.8.3 X-Ray Micro-Tomography Measurements

Whole bovine samples blocks were scanned before and after demineralisation with a small-angle-cone-beam micro-CT (µCT40; Scanco Medical AG, Bassersdorf, Switzerland) with 15 µm voxel size at 90 kV X-ray generator voltage.

X-ray generator voltage calibration was performed, prior to scanning, with a 99.999% aluminium three-dimensional step wedge that allowed for accurate beam-hardening correction (Davis et al., 2002).

The samples were mounted kinematically on the rotation stage. The stage was computer-controlled in order to synchronise rotation and axial shift. The kinematic stage ensures that the samples can be removed and accurately repositioned.

A 50 µm thick amorphous scintillator projected the image onto a CCD array detector with 2048 x 252 elements and 24 µm pitch. The signal was digitized by means of an analogue digital converter (ADC). Reconstructions of the images were carried out by cone-beam algorithms and stored to computer hard-drive as DICOM images for evaluation. Acquisition times for each sample was approximately 24-hours.

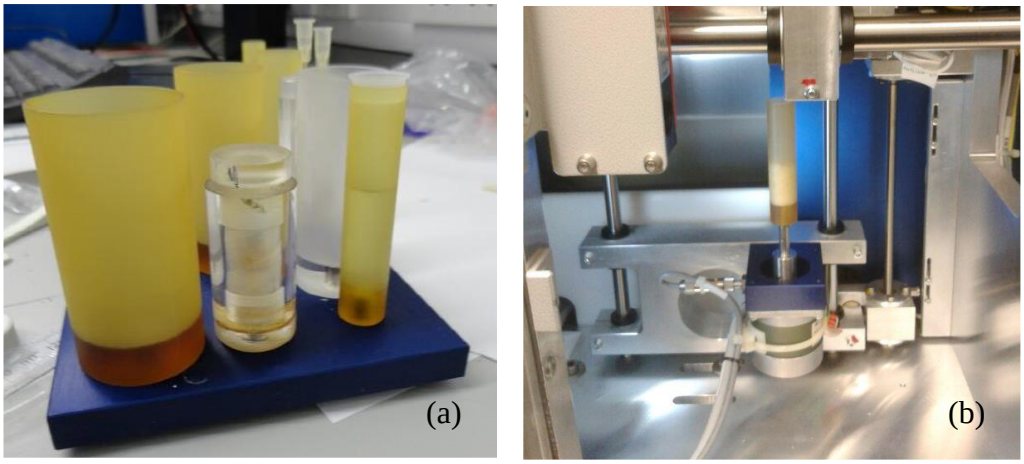

Figure 19 (a) Sample containers used for holding the bovine specimen during the XMT scanning. (b) Kinematic stage for mounting the sample holder.

7 Validation and Characterisation of OCT for Measuring Surface Demineralisation during Erosion

Presented at the 63rd Congress of the European Organisation for Caries Research (ORCA)

ATHENS, Greece 6-9 July 2016

7.1 Introduction

Detection of demineralisation and quantification of tooth substance loss by dental clinicians currently relies on visual and tactile examination, supported by radiographic data. However, with these subjective, semi-quantitative techniques, dental erosion is usually diagnosed when substantial enamel loss has already occurred (Wilder-Smith et al., 2009). Dental erosion starts by initial softening of the enamel surface followed by loss of volume with a softened layer persisting at the surface of the remaining tissue (Lussi et al., 2011). As erosion progresses the outermost layer of the softened surface is eventually completely dissolved, resulting in permanent loss of tooth structure (Addy and Shellis, 2006, Cheng et al., 2009a). This softened layer however has the potential to be remineralised (Eisenburger et al., 2001, Amaechi and Higham, 2001). None of the current existing techniques discussed in chapter 4.2 have been successfully used to detect and quantify this early stage of erosion *in vivo* (Schlueter et al., 2011).

OCT is a non-invasive technique that has potential to quantify tooth substance loss at early stages (Chan et al., 2013). Studies using OCT to assess dental erosion have proposed measuring the remaining enamel thickness once bulk loss of minerals is lost from the enamel surface (Wilder-Smith et al., 2009).

However, to date, the accuracy and sensitivity of this technique has not been fully characterized in a laboratory setting where the conditions are standardised. Therefore, no comparison with other studies was possible. Furthermore, to the author's knowledge no research has been done to evaluate the earliest time point at which OCT can be used to detect and monitor tooth loss using direct physical thickness measurements from OCT B-Scans. Consequently, no consensus exists for the minimum detection threshold criteria for measuring erosive lesions.

The primary aim of this chapter was to validate the use of OCT to measure real-time enamel erosion in a lab-based model environment. The secondary aim was to evaluate the OCT based measurement reproducibility.

7.2 Theory section

During advanced stages of erosion, bulk loss of mineral is exhibited from the enamel prisms (Lussi and Jaeggi, 2008). With time this causes dissolution of enamel structures in depth. With regards to OCT images of dental enamel cross-sections, this

bulk loss can potentially be observed as a receding enamel surface. OCT B-Scans provide a cross-sectional view of the enamel, from which surface mineral loss should be observable as an axial displacement of the surface. Direct measurement of axial displacement of the surface is therefore expected to be equal to the erosive lesions depth.

OCT B-scan images are produced from a collection of acquired axial scans (A-Scans) (Podoleanu, 2014). The A-Scan is a depth resolved function of the backscattered light intensity. Scattering objects along the A-Scan are resolvable in OCT because the broadband OCT light source centred at a wavelength of λ_0 has a finite coherence length (l_c) that is a function of its spectral width ($\Delta\lambda$).

$$l_c = \frac{4\ln(2)}{\pi}\frac{\lambda_0^2}{\Delta\lambda} \approx 0.88\frac{\lambda_0^2}{\Delta\lambda} \qquad \text{Equation 7.1}$$

The minimum distance between two objects for them to be 'resolved' is defined as the axial resolution (R_{OCT}) of the OCT system through the well-known relation (Tomlins and Wang, 2005).

$$R_{\mathrm{OCT}} \approx 0.44\frac{\lambda_0^2}{\Delta\lambda}, \qquad \text{Equation 7.2}$$

which describes the width of an assumed Gaussian axial point-spread function (PSF).

In order to measure the displacement of a single interface, i.e. the enamel surface, it is theoretically possible to localise the PSF to much less than the instrument resolution. This principle is the basis for super-resolution techniques such as PALM and STORM (Henriques et al., 2011). For PSF localisation, what is more important than PSF width is the spatial sampling frequency.

For a spectral domain OCT system, the A-Scan (and therefore the PSF) is not directly sampled in the spatial domain. Rather, each A-Scan is obtained from the Fourier transform of a detected spectral interference pattern. The interferometer output is projected onto a spectrometer and detected by *M* discrete pixels, as shown in Figure 20.

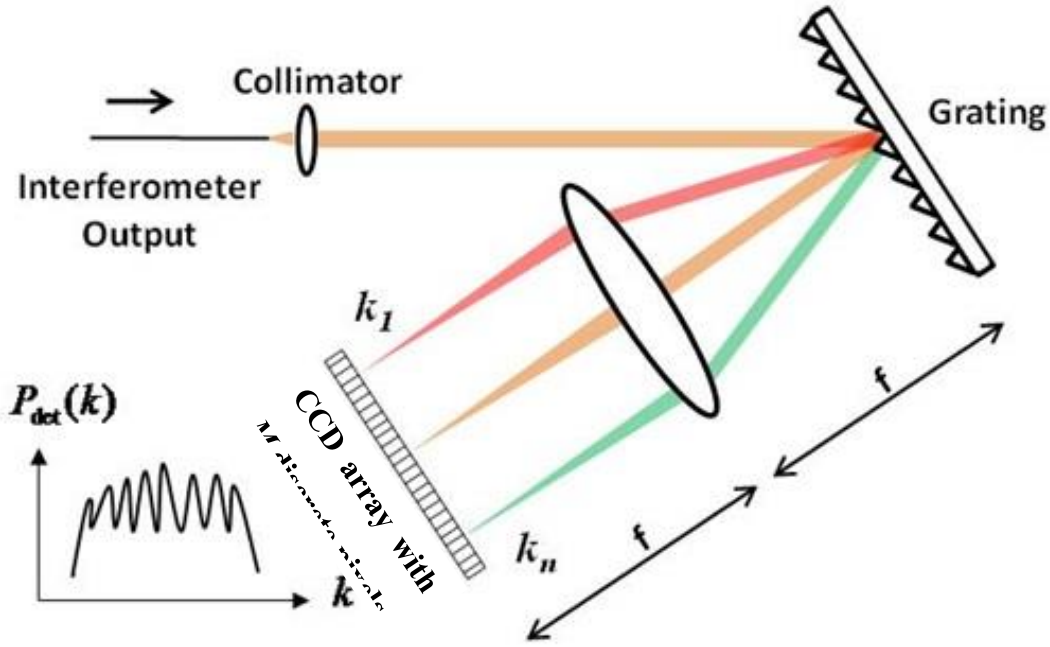

Figure 20 Schematic of a FD-OCT detection system using a CCD array line detector. A cone of collimated beams of different wavelengths emerges from the grating plane and each spectral slice is mapped to an individual pixel in the linear CCD array. The resulting spectrum shown is the depth-dependent scattering information (Image modified from Biophotonics Imaging Laboratory: OCT Technology". Biophotonics.illinois.edu. N.p., 2016. Web. 21 Sept. 2016)

This spectrally detected signal is transformed into a spatially resolved A-Scan by using a discrete Fourier transform. Consequently, there is a reciprocal relationship between the source bandwidth, $\Delta f = c\lambda_0^{-2}\Delta\lambda$, and the discrete spacing of points axially, δz.

$$\delta z \propto \frac{1}{\Delta f} \qquad \text{Equation 7.3}$$

Thus, the axial pixel spacing in a spectral domain OCT system is a function of the source bandwidth detected by the spectrometer. If the spectral bandwidth projected onto the spectrometer is increased, then the axial pixel size decreases. However, the maximum spectral bandwidth is limited by the finite bandwidth of the OCT light-source, limiting the minimum axial sampling frequency. Therefore, the ability to measure enamel erosion is expected to be primarily determined by the axial pixel size of the OCT system, which for Fourier domain OCT is limited by the spectrometer bandwidth. When erosion is small compared to the pixel size, then it will likely be difficult to detect any change.

Furthermore, axial displacements recorded by OCT are optical, being the product of the physical displacement and the group refractive index, n_g, of the medium through which the measurement is made (as briefly discussed in chapter 5). The group refractive index (or group index) is the consequence of the wavelength dependence of the phase index (or conventional refractive index n), related by Equation 7.4.

$$n_g = n - \lambda \frac{dn}{d\lambda} \qquad \text{Equation 7.4}$$

The effect of refractive index is to reduce the physical depth range of a single A-Scan. Therefore, the axial pixel size in a medium is inversely proportional its group index,

$$\delta z_{\text{medium}} = \frac{1}{4n_g} \frac{\lambda_0^2}{\Delta\lambda}. \qquad \text{Equation 7.5}$$

The dependence of OCT pixel size on the group index of the specimen and surrounding medium complicates its use as a physical measurement tool. Media having different group indices have different axial pixel sizes. The axial pixel size is effectively a calibration scale factor in units of micrometres per pixel (μm pix^{-1}) translating between pixel counts obtained from OCT images and physical units. Therefore, depending upon whether erosion is measured in terms of change in the enamel thickness or change in the surface position, a different calibration factor will be required.

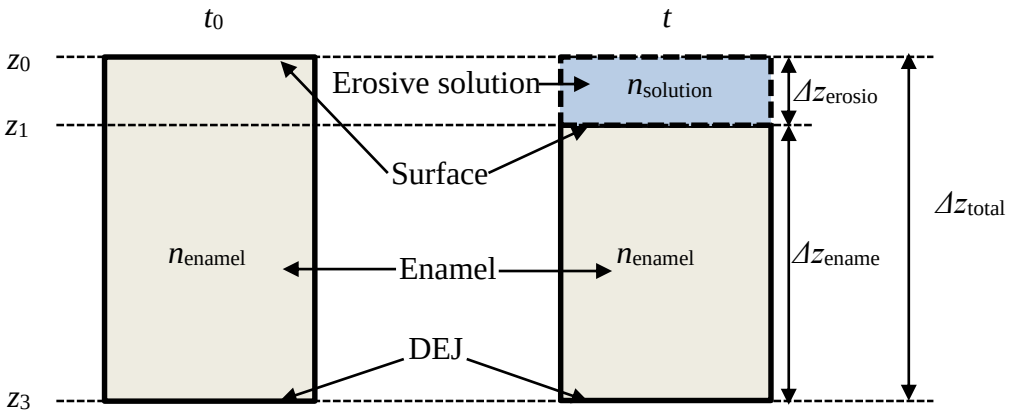

Figure 21 Schematic showing a cross-section of enamel at baseline, t0, and at some later time, t. At t0 the enamel has a total physical thickness Δz_{total}. The enamel is surrounded by some erosive solution such that after time t the total enamel thickness is reduced by $\Delta z_{erosion}$. The enamel has a group index n_{enamel} and the solution has a group index $n_{solution}$

Figure 21 shows a schematic of an enamel cross-section at baseline, t_0, and at some later time, *t*. At any given time *t* the enamel has a physical thickness $\Delta z_{\text{enamel}}(t)$. The total physical thickness $\Delta z_{\text{total}} = \Delta z_{\text{enamel}}(t_0)$ is constant in time, being the sum of both the remaining enamel thickness, $\Delta z_{\text{enamel}}(t)$, and the erosive lesion depth, $\Delta z_{\text{erosion}}(t)$,

$$\Delta z_{\text{total}} = \Delta z_{\text{enamel}}(t) + \Delta z_{\text{erosion}}(t). \qquad \text{Equation 7.6}$$

The enamel is surrounded by some erosive solution such that after time, *t*, the enamel thickness is reduced by $\Delta z_{\text{erosion}}(t)$. However, OCT makes measurements of optical, not physical, enamel and erosion thicknesses, $\Delta\tau_{\text{enamel}}$ and $\Delta\tau_{\text{erosion}}$ respectively. Optical thickness is the product of the physical thickness and the mean group index of the specimen such that,

$$\Delta\tau_{\text{enamel}}(t) = n_{\text{enamel}}\Delta z_{\text{enamel}}(t) \qquad \text{Equation 7.7}$$

and

$$\Delta\tau_{\text{erosion}}(t) = n_{\text{erosion}}\Delta z_{\text{erosion}}(t) \qquad \text{Equation 7.8}$$

where the enamel has a mean group index n_{enamel} and the solution a group index n_{erosion}.

As noted above, until calibrated, OCT optical thickness measurements are made in arbitrary units of 'pixels', denoted Δp,

$$\Delta p_{\text{enamel}}(t) = \delta z^{-1}\Delta\tau_{\text{enamel}}(t) \qquad \text{Equation 7.9}$$

and

$$\Delta p_{\text{erosion}}(t) = \delta z^{-1}\Delta\tau_{\text{erosion}}(t) \qquad \text{Equation 7.10}$$

where δz is the calibration scale factor in µm per pixel (µm pix^{-1}) that converts from OCT 'pixels' to physical units in air, assuming the group index of air $n_{\text{air}} \approx 1$. Defining the medium specific pixel calibrations, $\delta z_{\text{enamel}}^{-1} = \delta z^{-1} n_{\text{enamel}}$ and $\delta z_{\text{erosion}}^{-1} = \delta z^{-1} n_{\text{erosion}}$ and substituting Equation 7.7 into Equation 7.9 and for $\Delta z_{\text{enamel}}(t)$ from Equation 7.6, both $\Delta p_{\text{enamel}}(t)$ and $\Delta p_{\text{erosion}}(t)$ can be expressed in terms of $\Delta z_{\text{erosion}}(t)$.

$$\Delta p_{\text{enamel}}(t) = \delta z_{\text{enamel}}^{-1}[\Delta z_{\text{total}} - \Delta z_{\text{erosion}}(t)] \qquad \text{Equation 7.11}$$

$$\Delta p_{\text{erosion}}(t) = \delta z_{\text{erosion}}^{-1}\Delta z_{\text{erosion}}(t) \qquad \text{Equation 7.12}$$

Therefore, if δz, n_{enamel} and n_{erosion} are known, then the physical extent of lesions can be measured (Uhlhorn et al., 2008) (Hariri et al., 2012b). However, in biological

materials, exact values of the group index are generally not well known due to both natural variation and the difficulty with making such measurements. To obviate this problem, a statistical calibration can be obtained from an established, validated, technique such as profilometry, where the loss of enamel, $\Delta z_{\text{erosion}}(t)$, for an acid challenge duration, *t*, can be measured directly. However, Δz_{total} in Equation 7.11 remains unknown. This can be overcome by differentiating both Equation 7.11 and Equation 7.12 with respect to time and solving for the calibration coefficients in enamel and solution. This yields expressions that can be evaluated in terms of experimentally measurable quantities,

$$\delta z_{\text{enamel}} = -\frac{\dot{\Delta z}_{\text{erosion}}(t)}{\dot{\Delta p}_{\text{enamel}}(t)} \qquad \text{Equation 7.13}$$

and

$$\delta z_{\text{erosion}} = \frac{\dot{\Delta z}_{\text{erosion}}(t)}{\dot{\Delta p}_{\text{erosion}}(t)} \qquad \text{Equation 7.14}$$

where the dot represents the first derivative with respect to time. The physical rate of erosion, $\dot{\Delta z}_{\text{erosion}}(t)$, is directly measurable using profilometry. Optical measurements of the rate of enamel optical thickness change, $\dot{\Delta p}_{\text{enamel}}(t)$, and optical rate of surface loss, $\dot{\Delta p}_{\text{erosion}}(t)$, can be obtained directly from OCT images. The calibration factors, δz_{enamel} and $\delta z_{\text{erosion}}$ are in units of μm pix^{-1} and are related by

$$\frac{\gamma_{\text{erosion}}}{\gamma_{\text{enamel}}} = \frac{n_{\text{enamel}}}{n_{\text{erosion}}}. \qquad \text{Equation 7.15}$$

Therefore, calibration factors can be obtained that enable conversion of arbitrary optical units measured by OCT to physical units, under the assumption that profilometry measurements of $\dot{\Delta z}_{\text{erosion}}(t)$ are representative of the optical changes being measured using OCT.

The statistical calibration approach utilises profilometry as a reference technique to measure the mean rate of erosion over *N* specimens. The natural variation between enamel specimens yields differences in each, quantified by the standard deviation, σ_{ref}. The uncertainty, or degree to which the mean erosion rate is representative of the population of enamel specimens, is then estimated by the 95% confidence interval, $\varepsilon_{ref} = 2\sigma_{ref}/\sqrt{N}$.

Similarly, using OCT, a separate batch of *N* specimens can be measured. The mean rates of erosion and change in enamel thickness can be determined from OCT B-Scan images, measured in terms of the number of pixels with the corresponding uncertainty, $\varepsilon_{OCT} = 2\sigma_{OCT}/\sqrt{N}$.

7.3 Materials and methods

7.3.1 Sample preparation

A total of 16 bovine enamel specimens were used in this study. These were randomly allocated to two groups each of sample size *N*=8. One group for OCT imaging and the second for profilometry measurements. Specimens of 10 mm diameter bovine enamel discs were embedded into a 25mm diameter clear resin substrate with enamel thickness of approximately 0.5 mm on top of underlying dentine.

The specimens were initially stored dry in sealed containers at a temperature of 25°C**.** The OCT group of specimen surfaces were painted with varnish (Revlon, Boots, UK) to prevent erosion except on a small 3x3 mm region as described in Chapter 6.1. The samples were immersed in de-ionised water for a minimum of 2 hours prior to initiation of demineralisation and measurement in order to mitigate against hydration effects influencing the experiment.

7.3.2 Acidic Preparation and Challenge

Both sample groups were subjected to a citric acid challenge that was prepared as 0.05 M citric acid (Sigma Aldrich, UK). The solution was buffered to pH 3.8 using 1 M Sodium Hydroxide (NaOH). The pH of the solution was monitored using a SenTix® 41 electrode pH-meter (WTW GmbH, Germany). Whilst the two groups were subject to challenge from the same solution, the acid challenge was administered to the two groups differently. For the OCT sample group, the acid was pumped through the sample holder as described in Chapter 6.7. Samples used for the profilometry study, were placed in individual glass beakers for the acid challenge.

7.3.3 Reference Profilometry Measurements Protocol

For validation, profilometric measurements of bovine samples were taken for every 6 hours of erosive challenge. A Proscan 2000 non-contact surface profilometer S13/1.1 scan-head with vertical resolution 25 nm (Scantron Industrial Products Ltd, Taunton,

England, UK), was used to acquire topographs of the eroded step height lesion depths. Acquisition of the entire specimen eroded surface (dimensions of approximately 5 x 5 mm) took 40 minutes per sample at 100 μm steps.

The surfaces of the specimen used for profilometry were divided into subdivisions by use of transparent adhesive office tape (RS Component, Corby, UK) to give at least 5 windows of 1 mm on each sample where varying length of erosive challenge was undertaken Figure 22.

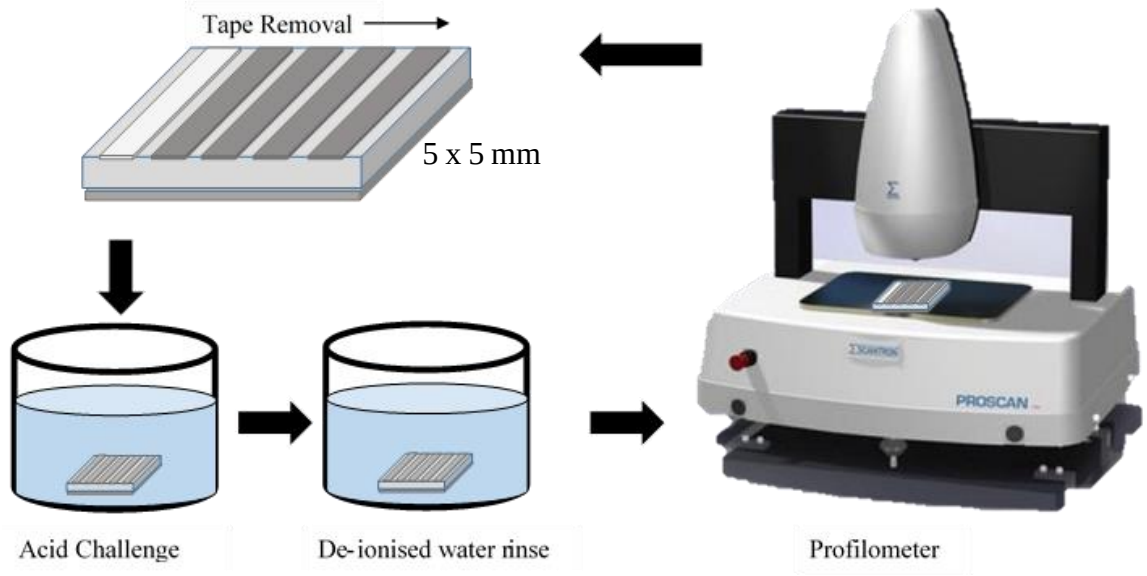

Figure 22 Shows the specimen divided into sections of 1mm thick. Each section is exposed to varying lengths of erosive challenge in 100 ml acid bath. After the challenge the specimen was rinsed in deionised water and dried before surface measurements were taken by the Proscan profilometer.

The tape protecting each section was peeled off in order to expose the enamel surface to the challenge so that the first peeled section represented the longest acid challenge Figure 23.

The specimens were dipped in glass beaker containing 100 ml of acid solution for each sample. After every erosive challenge period, the samples were removed, rinsed with de-ionised water and left to dry for 5 minutes at room temperature. At the end of the challenge, the samples were placed on the profilometer for measurement.

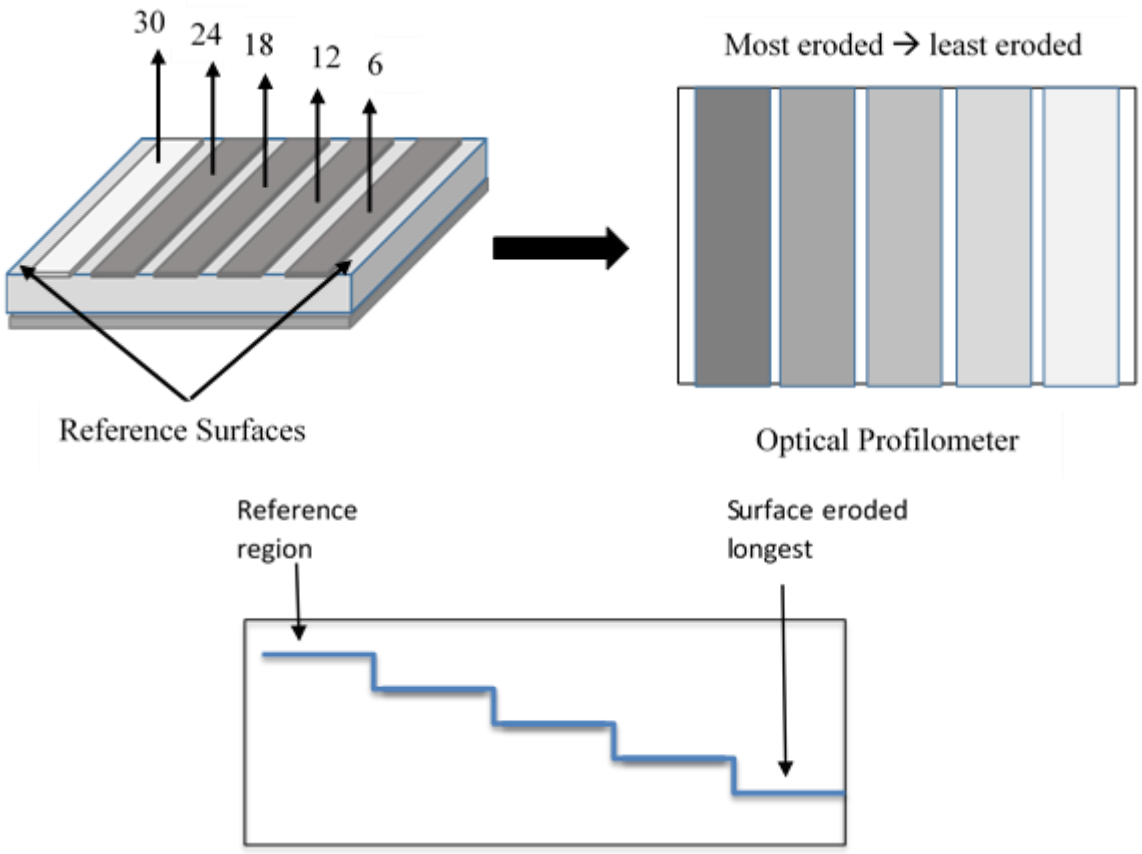

Figure 23 shows the sample surface with the varying length of exposure to acidic challenge. A strip of tape is removed for each erosive challenge so that the first peeled section is exposed to the acid solution for the longest period. An illustration of the expected step height change is shown.

From the profilometry topographs, 5 line profiles were taken (about 1mm spacing) for each sample, in order to measure the step change for each period of erosion. The mean erosion depth was then averaged over all specimens from which the rate of erosion was determined.

7.3.4 OCT System Configuration and Protocol

The instrumentation for this experiment used a super-luminescent light emitting diode (SLD) optical source (SLD1325, Thorlabs, Cambridge, UK), operating with a nominal central wavelength of 1325 nm and bandwidth of approximately 100 nm. The configuration is described in Chapter 6.6.

The OCT measurement protocol was designed to evaluate direct measurement of surface changes from axial pixel displacement on B-Scan similar to the images established on pixel-based measurement reported by (Wilder-Smith et al., 2005). The

receding enamel surface was measured by referencing to fixed points, either the varnished enamel surface or the DEJ.

The samples were placed in the sample holder for OCT imaging under continuous acid challenge Figure 7.5. The samples were mounted orthogonal to the probing beam as described in Chapter 6.6. The solution was continuously refreshed at a rate of 5 ml/minute by a multi-channel pump (323Du/D, Watson Marlow, UK), drawing fresh solution from a 1 litre reservoir and ejecting used solution into a separate container. The acidic challenge was carried out for a period of 40 hours in order to measure progressive bulk material loss.

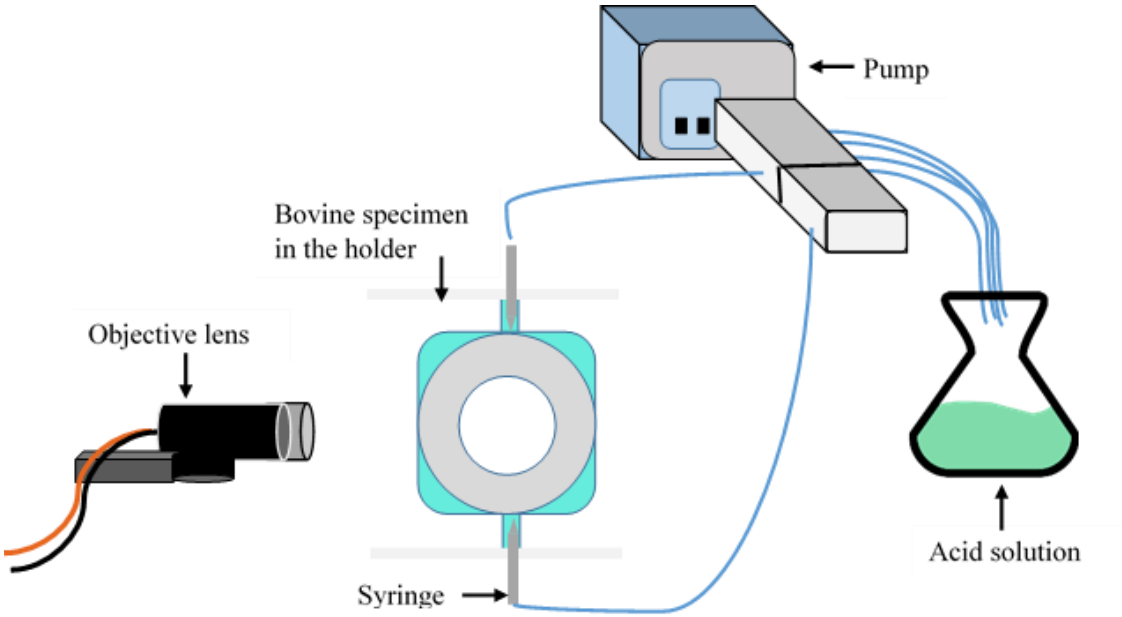

Figure 24 Schematic of the acidic challenge setup with the acid being pumped through the sample holder. The objective lens is focused on the sample which is held in a static position during all measurements.

7.3.5 OCT Analysis

The image analysis software ImageJ was used to read the cross-sectional images from the OCT data (Schneider et al., 2012). To account for mechanical drift in the OCT imaging optics, OCT B-Scans were registered using the ImageJ StackReg plugin (Thevenaz et al., 1998). Following this procedure, the central 100 B-scans were averaged to yield a composite image for each volume dataset. The erosive depth was then measured manually from these composite images, selecting the surface and reference points by eye. This reflected the methodology that was employed in previous clinical reports (Wilder-Smith et al., 2009). Furthermore, this was preferred

to automation which proved unreliable. Erosive depth was measured using two methods, hereon referred to as method A and method B.

Method A measured net surface enamel loss relative to the nail varnish surface Figure 25. For each sample, a region of interest (ROI) from the nail varnished surface extending to the enamel surface was manually selected. The initial dimensions of the ROI were 100 pixels across and approximately 20 pixels in height. The height corresponded to the optical thickness of the nail varnish on the surface of the enamel and the width was chosen such that at least a fifth of the surface of the enamel was covered by this selection. This selection provided an adequate amount of signal averaging but avoided uncertainty due to a non-flat surface.

After each erosive measurement, the height of the ROI selection was increased as a response to the receding enamel surface. This step increase in the height was then recorded in pixels. Ten measurements were made for each specimen and the average used for the analysis.

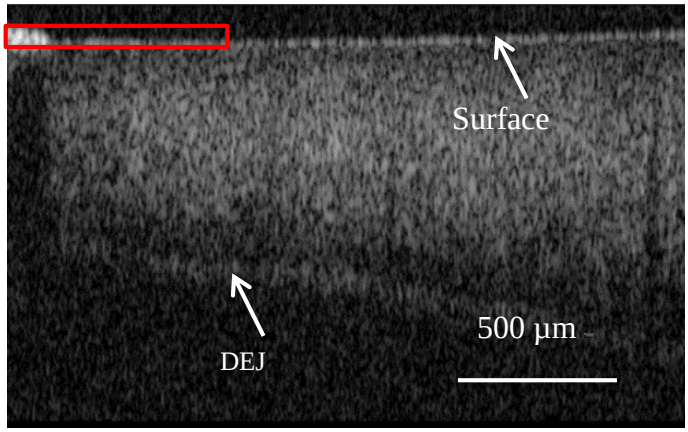

Figure 25 The ROI selected for this measurement method. The height of the ROI bounded in the rectangle increases with increasing loss of enamel.

For method B, the surface enamel loss was measured with reference to the DEJ, effectively monitoring the change in thickness of the enamel. A region of interest (ROI), extending from the top of the exposed enamel surface to the DEJ was manually selected for each sample. Special care was made to avoid the varnished sections of enamel and the intense Fresnel reflections from the surface that saturated the OCT spectrometer.

These regions were selected ensuring that a clear view of the enamel-dentine junction was visible throughout all time points of the measurement. From these regions of

interest, 100 adjacent A-scans were averaged and a mean optical backscattering profile was obtained as a function of depth into the enamel Figure 26a. Plotting the pixel intensities along the selected region produced a smooth line profile plot of the intensity peaks at both the lesion front and DEJ Figure 26b.

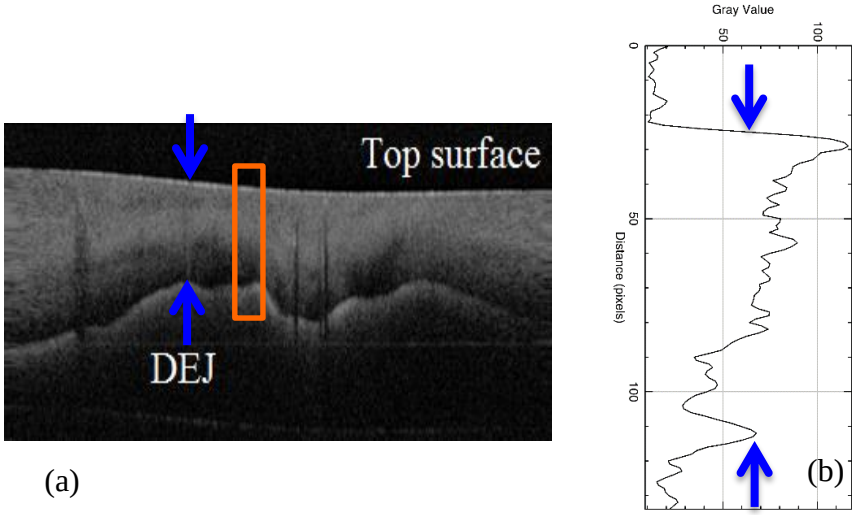

Figure 26 shows an illustration of the enamel surface or lesion front to DEJ analysis (method B). (a) The bounding box indicates the ROI where the A-scans were averaged for analysis. (b) The distance between the highest intensity peaks (indicating top surface of the enamel erosive lesion and another peak for the DEJ) was measured from the line profile plots.

The distance between the highest intensity peaks (indicating top surface of the enamel) and (peak for the DEJ) was calculated and recorded in pixel. These measurements were repeated using data obtained at hourly intervals.

7.4 Results

7.4.1 Profilometry

The step-wise enamel loss from the surface layer was visualised from the profilometry surface profiles shown in Figure 27. The bulk enamel loss for each erosive period can be viewed as a step height change indicated by the arrows.

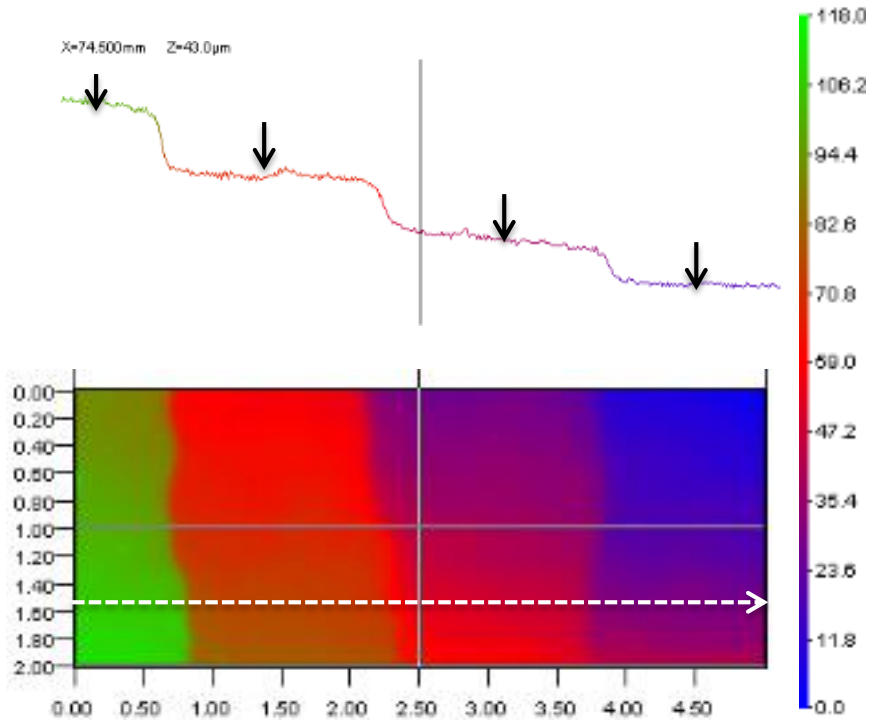

Figure 27 Topographical data of an eroded bovine enamel sample acquired from the Profilometer. The increasing erosion times in each section show an increasing step change in erosion. The white dotted line shows one line profile chosen for measurement while the black arrows show the actual points of measurement on the steps. The scale represents the height in microns.

The results from profilometer step height measurements indicate a mean step height change of 20.18 ± 1.84 µm (95% C.I.) for each of the 6 hours erosion period Table 7.1.

Erosion Time (Hrs)	Average step height for each interval for all samples (µm)	Standard Deviation
6	22	5.28
12	40.75	7.64
18	60.65	6.99
24	82.55	9.61

Table 7.1 Results of the average step height changes from all bovine samples for each 6 hour erosive period.

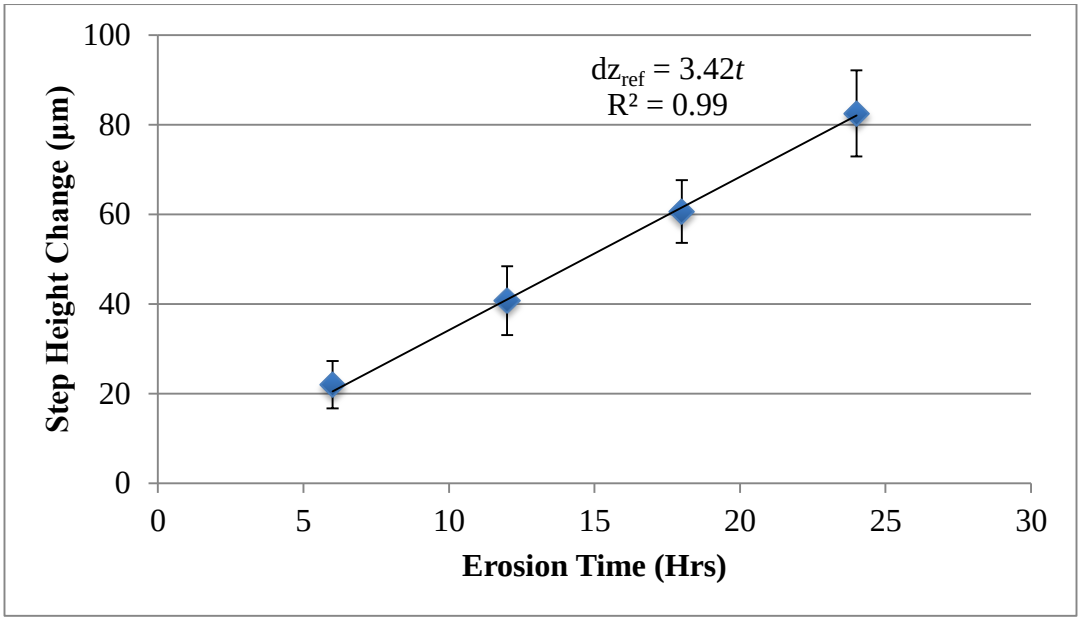

Figure 28 Graph of average step height change for each 6-hour erosive cycle. The R2 value provides an estimate of the % of variation in the data represented by the linear model.

Furthermore, a linear regression through the erosion step height measurements as a function of time yields an erosion rate of 3.42±0.16 µm/hr, with R^2 indicating that the linear model represents 99% of the variation Figure 28.

7.4.2 OCT Imaging of a Developing Erosive Lesion

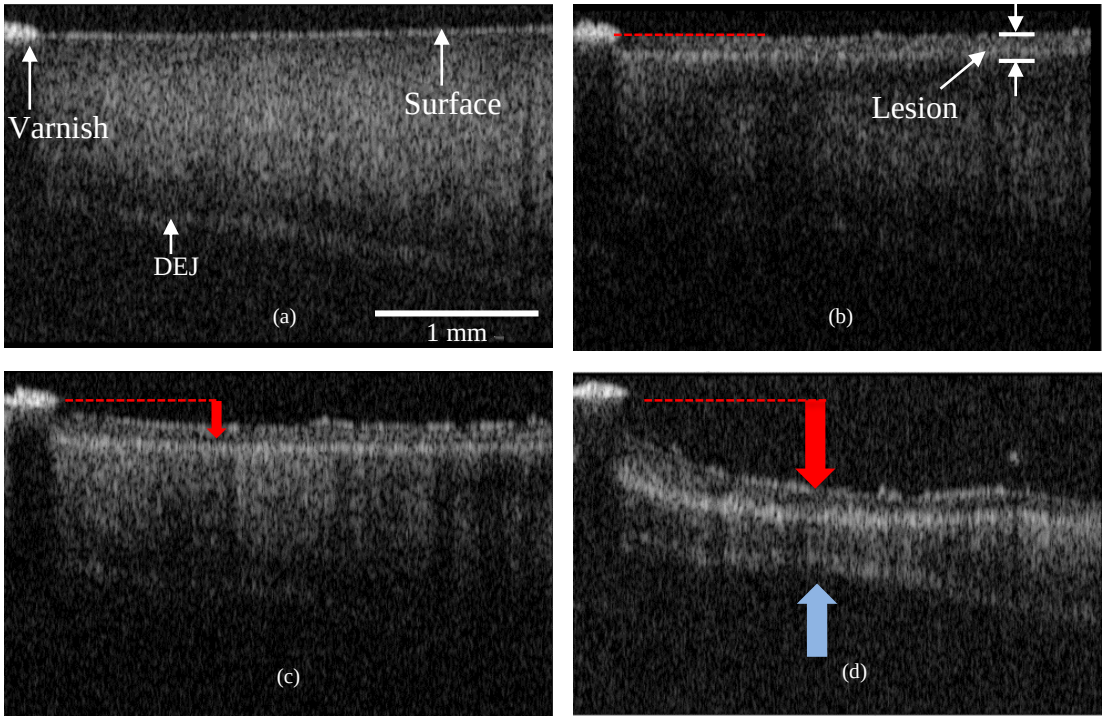

Figure 29 B-Scan images of lesion depth after A) 6 hours, B) 12 hours, C) 18 hours and D) 24 hours of continuous acid challenge. Dotted line indicates enamel surface and red arrow indicates receding enamel surface (method A). Measurement of enamel surface (red arrow) to DEJ (blue arrow) represents method B.

The B-scan images showed a consistent receding surface lesion front due to erosion (red arrows) Figure 29. A band of high backscattering was observed on the surface of the enamel Figure 29b. As the erosion progressed, the lower edge of this band appeared to exhibit a region of higher intensity, compared with the central region of the band Figure 29c. The reference zone, where enamel is masked by the nail varnish, did not exhibited erosion Figure 29d. The visibility of the DEJ was maintained throughout the experiment in most of the samples but visibility of the enamel morphology beneath the lesion varied with different degrees of erosion at different time points. This can be seen as lower pixel intensities beneath the surface of the lesions Figure 29b.

7.4.3 OCT Calibration

The calibration scale factor was determined from both OCT erosion methods A and B using Equation 7.14 and Equation 7.15 as the gradient of a linear regression through

the profilometry measurements of $\Delta z_{\text{erosion}}$ plotted as a function of $\Delta p_{\text{erosion}}$. Results for method A are shown in Table 7.2 and are plotted in Figure 30.

Acid Challenge duration *t*, hours	OCT Measurements $\Delta p_{\text{erosion}}$, pixels	Profilometer $\Delta z_{\text{erosion}}$, µm
24	43.57 (3.62)	82.55 (9.61)
18	37.71 (3.22)	60.65 (6.99)
12	30.14 (2.8)	40.75 (7.65)
6	21.86 (2.41)	22.00 (5.28)

Table 7.2 Mean erosion depths measured using OCT and profilometry on independent batches of specimens after acid challenge durations of 6, 12, 18 and 24 hours. 95% Confidence intervals given in brackets.

Table 7.2 shows the mean erosion step heights measured on separate batches of specimens by OCT (pixels) and profilometry (micrometres). Profilometer steps heights are plotted in Figure 30 as a function of OCT measurements for corresponding acid challenge durations. Error bars represent 95% confidence intervals. The gradient of the linear regression line provided an estimate of the pixel calibration scale factor in the erosion solution, of $\delta z_{\text{erosion}}$ =2.75±0.66 µm pix^{-1}.

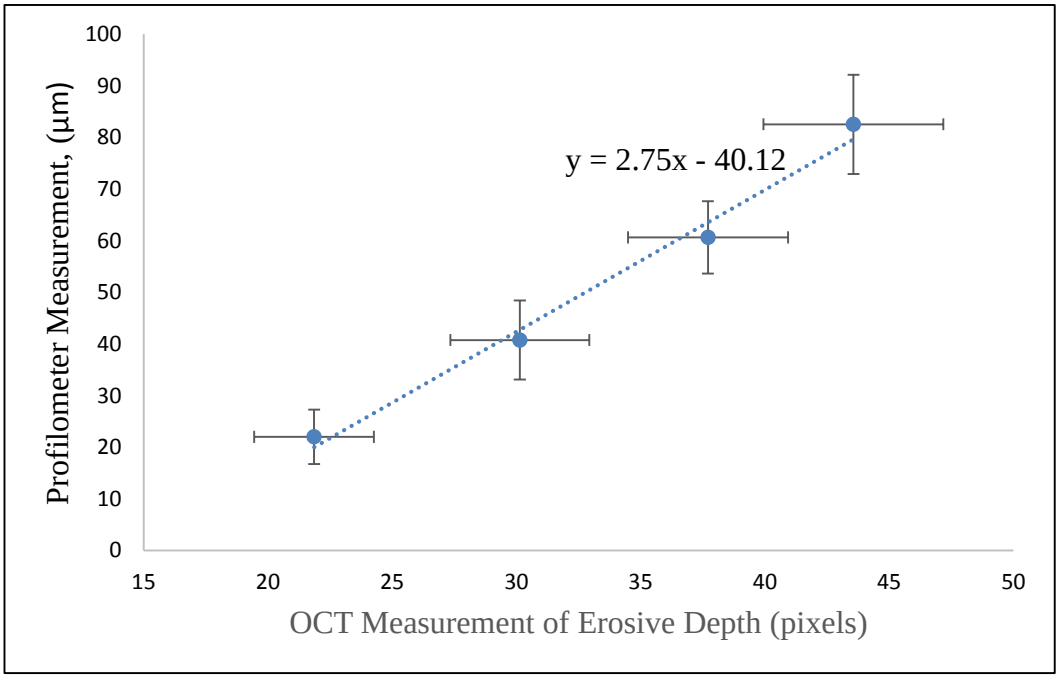

Figure 30 Mean OCT erosion depth measurements plotted with respect to profilometry measurements from Table 7.2. The slope of the regression line gives the calibration factor within the erosive solution.

The enamel thickness varied between specimens leading to a high uncertainty in $\Delta p_{\text{enamel}}(t)$. Dependence upon the total enamel thickness was eliminated by the

subtraction $\Delta p_{\text{enamel}}(t_0) - \Delta p_{\text{enamel}}(t)$. Results for the enamel thickness change, using the DEJ (method B), are shown in Table 7.3 for OCT and profilometer measurements after corresponding durations of acid challenge.

Acid Challenge duration *t*, hours	**OCT Measurements $\Delta p_{\text{enamel}}(t_0) - \Delta p_{\text{enamel}}(t)$, pixels**	**Profilometer $\Delta z_{\text{erosion}}$, µm**
24	27.48 (4.42)	82.55 (9.61)
18	18.72 (4.50)	60.65 (6.99)
12	12.48 (4.05)	40.75 (7.65)
6	5.68 (2.28)	22.00 (5.28)

Table 7.3 Mean enamel thickness change measured using OCT and profilometry on independent batches of specimens after acid challenge durations of 6, 12, 18 and 24 hours. 95% Confidence intervals given in brackets.

The DEJ method resulted in a pixel calibration value in enamel of $\delta z_{\text{erosion}} = 2.80 \pm 1.18$ µm pix^{-1}. This is plotted in Figure 31 showing that the uncertainty of more than 1 micrometre per pixel occurs because of the higher uncertainty associated with measuring enamel thickness compared to measuring the surface displacement.

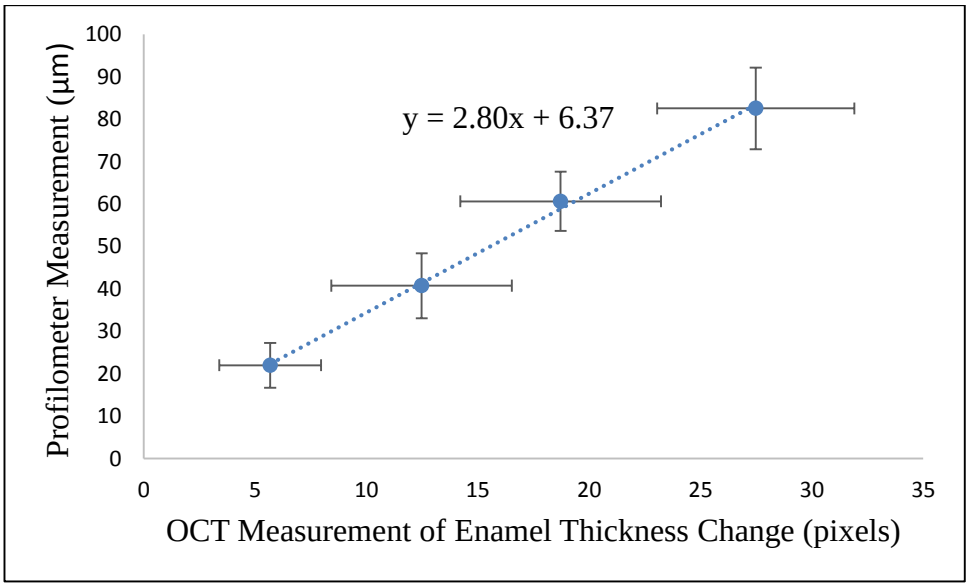

Figure 31 Mean OCT enamel thickness measurements plotted with respect to profilometry measurements from Table 7.3. The slope of the regression line gives the calibration factor within the erosive solution.

Therefore, a statistical calibration of OCT using an independent profilometry experiment provided calibration factors for OCT in the erosion solution of $\delta z_{\text{erosion}} = 2.75 \pm 0.66$ µm pix^{-1} and in enamel, $\delta z_{\text{enamel}} = 2.80 \pm 1.18$ µm pix^{-1}.

7.4.4 Comparison between OCT and Profilometer Measurements

The statistical calibration with profilometer measurements was based upon the assumption that the erosion measured using profilometry was representative of the erosion measured by OCT. However, experimentally the erosion was formed differently for the two techniques. For OCT, the measurements were obtained continuously with the specimens constantly immersed in acidic solution under constant low flow conditions. Specimens measured by profilometry were periodically removed from a static solution for measurement.

Therefore, in order to determine whether the statistical calibration was valid, a similar calibration was carried out using a series of artificial steps of known height. The steps were constructed from a polyurethane substrate doped with titanium dioxide (11 mg/g) and a series of thin layers cut from a similar block. The layer thicknesses were measured 10 times around the location chosen for measurement using a digital micrometre. OCT cross-sections are shown in Figure 32 showing 4 of the scattering layers placed on top of the substrate. The layer was laterally offset to form a step as shown.

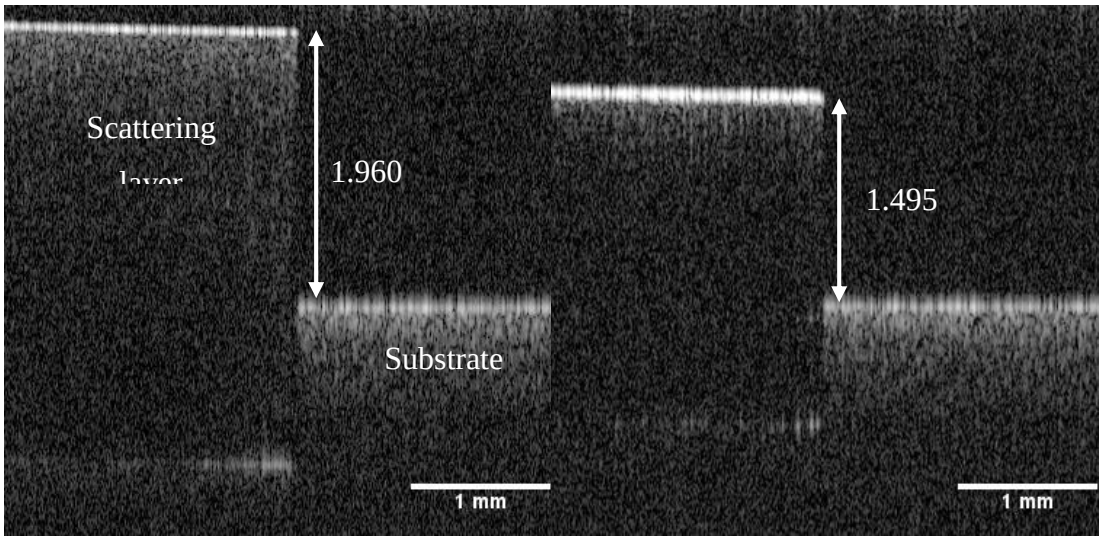

(a) (b)

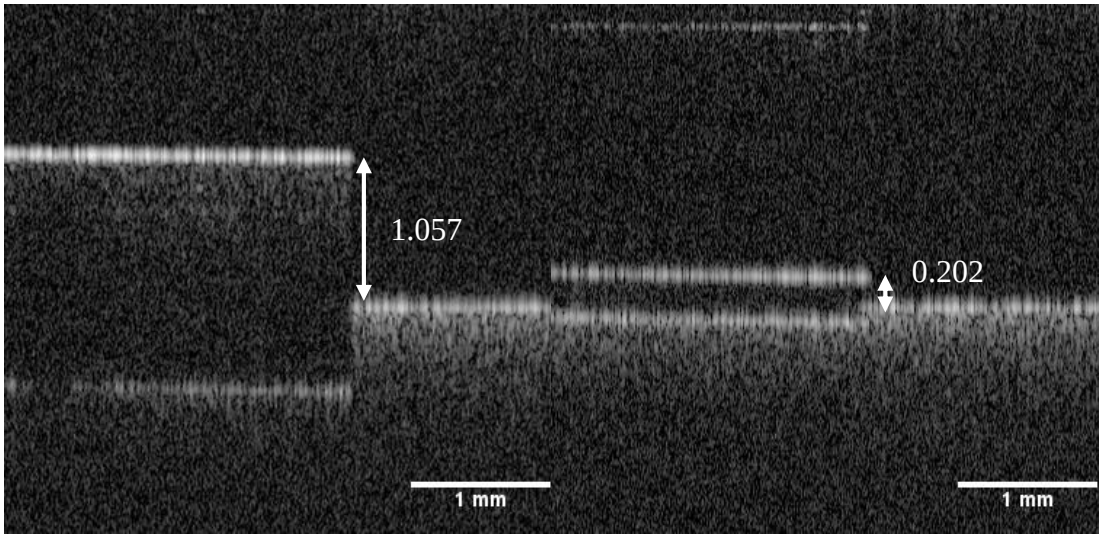

(c) (d)

Figure 32 Steps of different height were created by placing scattering layers of polyurethane on top of a polyurethane scattering substrate. OCT B-Scan images were obtained of each step measuring (a) 1.960±0.003 mm, (b) 1.495±0.003 mm, (c) 1.057±0.003 and (d) 0.202±0.003 mm. Uncertainty represents the 95% confidence interval calculated from 10 independent measurements of each scattering layer with a digital micrometre.

The same method as in the previous section was used to calculate the axial calibration from results shown in Table 7.4.

OCT Measurements of step $\Delta p_{\mathbf{enamel}}$, pixels	**Micrometre Step $\Delta z_{\mathbf{erosion}}$, µm**
206	1960 (3)
157	1495 (3)
111	1057 (3)
42	395 (3)
21	202 (3)

Table 7.4 OCT and micrometre measurements of 5 artificial steps. Measurements were made in air.

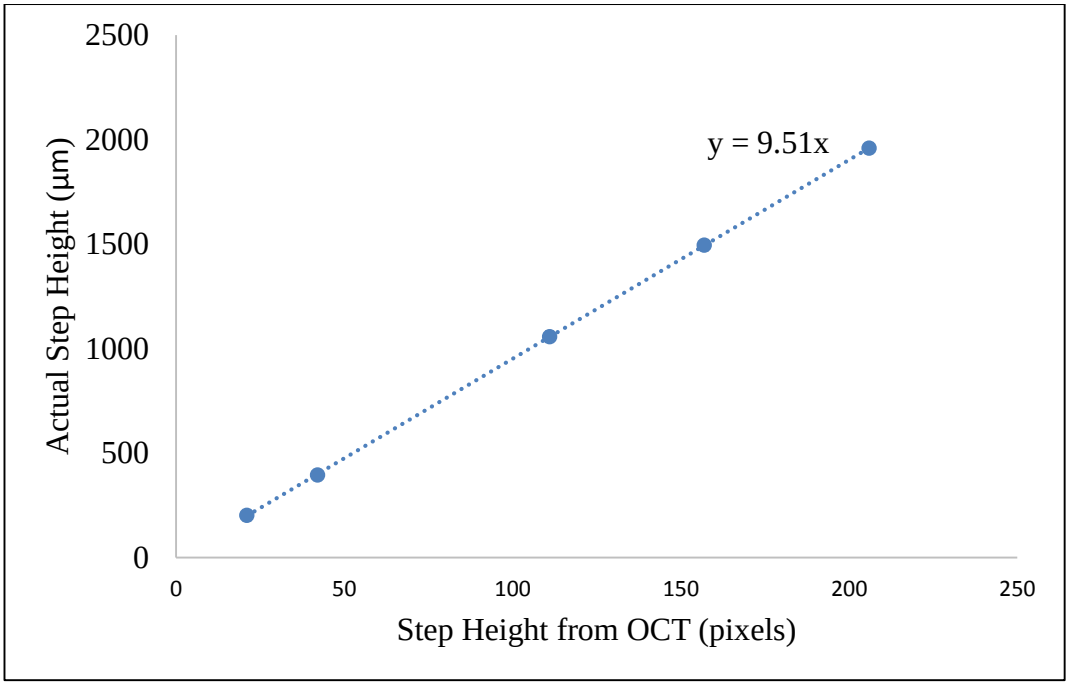

Figure 33 True step height plotted as a function of the step height measured from OCT B-Scans. The gradient of the linear regression indicates a calibration factor of δz=9.52±0.02 µm pix-1 in air.

The known step height measurements gave a calibration factor of $\delta z = 9.52$ µm pix^{-1} in air, Figure 33 True step height plotted as a function of the step height measured from OCT B-Scans. The gradient of the linear regression indicates a calibration factor of δz=9.52±0.02 µm pix-1 in air.r or approximately $\delta z_{\text{erosion}} = 7.30 \pm 0.02$ µm pix^{-1} in the erosion solution and $\delta z_{\text{enamel}} = 6.00 \pm 0.01$ µm pix^{-1} in the enamel. These differences indicate that the results obtained by profilometry are not representative of the lesions formed and measured by OCT under continuous immersion, undisturbed conditions.

7.4.5 Average Rate of Erosion using OCT

Method (A) Erosive Lesion Depth Measurements

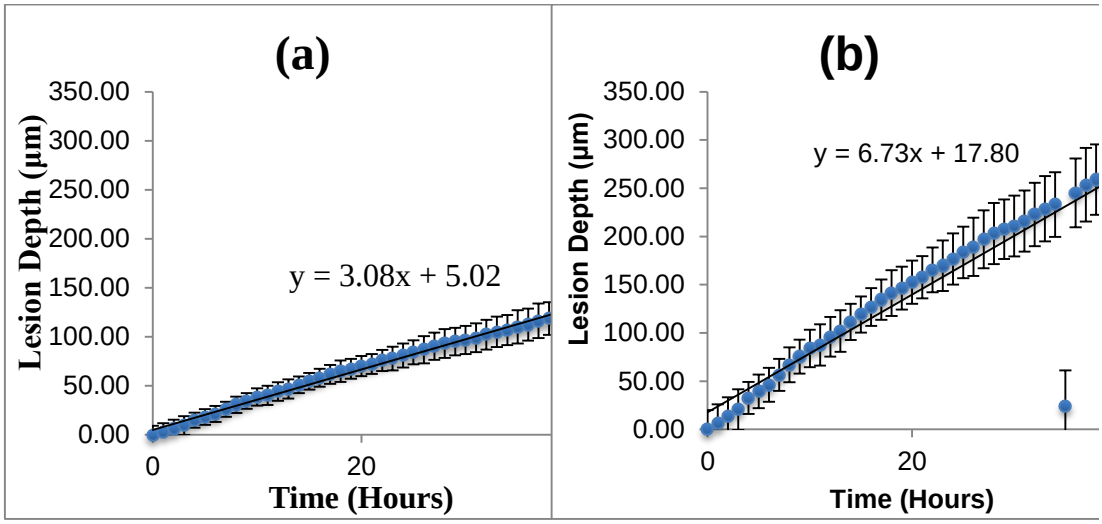

Figure 34 Graph of OCT lesion depth measurement (method A) at hourly intervals up to 40 hours erosive challenge. The OCT pixel depth values have been calibrated using (a) profilometry, of $\delta z_{erosion}$=2.75±0.66 µm pix^{-1} and (b) the known step-height method, $\delta z_{erosion}$=7.30±0.02 µm pix^{-1}

Using the calibrated pixel depth of $\delta z_{\text{erosion}}$ =2.75±0.66 µm pix^{-1}, Figure 34a shows the average erosive lesion depth progression from eight bovine samples. An almost linear increase in the lesion can be seen from the graph using this erosive model (R^2 = 99%) at a rate of 3.08±1.5 µm per hour. For comparison, Figure 34b shows the average erosive lesion depth progression calibrated according to the known step height method such that $\delta z_{\text{erosion}} = 7.3$ µm pix^{-1}, yielding a corresponding erosion rate of 6.73±0.37 µm per hour. The error bars in each figure represent the standard error of the mean for the measurements and the stated uncertainties represent 95% confidence intervals.

Method (B) Enamel Thickness Measurements

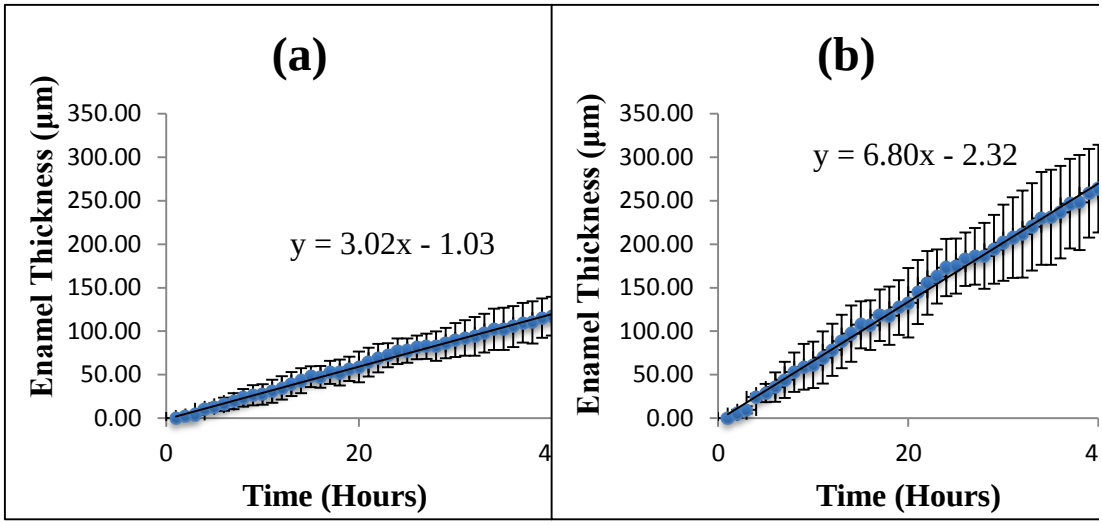

Figure 35 Graph of OCT enamel thickness change measured from the enamel surface to the DEJ. The pixel calibration scale factors used are from (a) profilometry, δz_{enamel}= 2.80±1.18 µm/pixel and (b) from OCT known step height measurements, δz_{enamel}= 6.00±0.10 µm/pixel

Figure 35 shows the enamel thickness changes measured from the receding surface to the DEJ, calibrated from (a) profilometry and (b) OCT known step-height measurements using the corresponding calibration scales. The DEJ was not visible in some of the samples due to poor penetration of light where the enamel layer was thicker, increasing the measurement uncertainty. The error bars in the figure represents the standard error of the mean for total lesion depth, yielding erosions rates of 3.02±1.50 µm per hour using the profilometer calibration and 6.80±0.51 µm per hour based on the OCT step height calibration.

7.4.6 Effect of Flow on the Erosion Rates

The results above reveal an important discrepancy between a known step-height calibration and referencing to profilometry measurements of erosion. This implies that the assumption of equivalence between the erosion obtained for profilometry and OCT is not supported.

One notable experimental difference between the OCT measurements and the profilometry experiments was that for the OCT experiments, the specimens were placed within a flow cell, through which the solution was slowly (5 ml/minute) flowed over the specimens to ensure that it was continuously refreshed. For profilometry

measurements, the solution was static. To rule out flow as contributing to the difference in profilometry and OCT results, an OCT experiment was repeated for a single specimen without flow. Results of these experiments are shown in Figure 36, applying the known-step height calibration values of $\delta z_{\text{erosion}} = 7.3$ µm pix^{-1}. Measurements were made using the surface method (A) over an 18 hour acid challenge at selected durations of 2, 6, 12 and 18 hours.

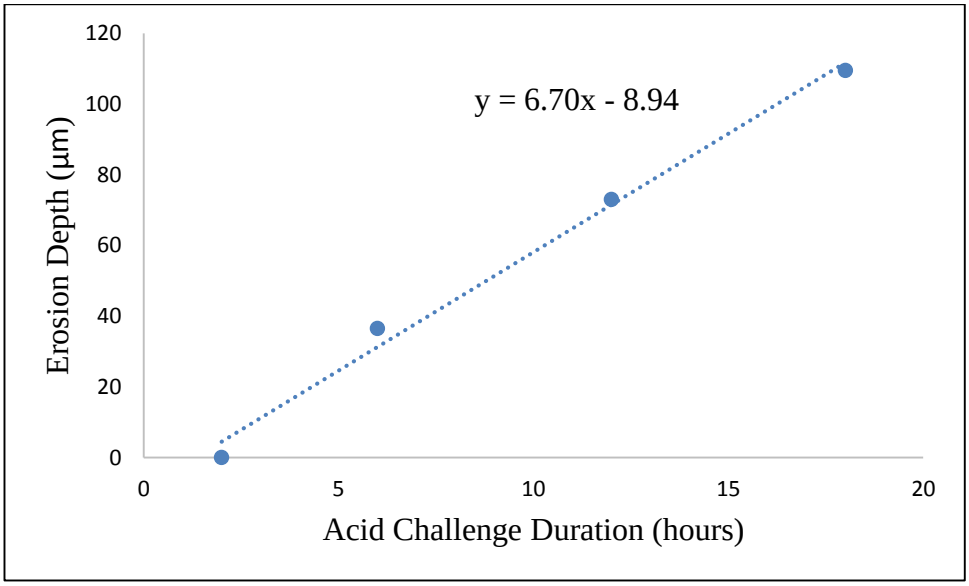

Figure 36 Erosion depth measured with respect to the enamel surface using OCT after an acid challenge duration of 2, 6, 12 and 18 hours.

The erosion rate was 6.70±0.37 µm per hour, agreeing with the erosion rate obtained under flow conditions shown in Figure 34b.

7.5 Discussion

The physical measurement of erosive dental lesions using OCT is hindered by uncertainty. This is mainly because of the dependence of OCT pixel size on the group index of the specimen, which is often unknown for a given specimen. Axial displacements recorded by OCT are optical, being the product of the physical displacement and the group refractive index of the medium. Thus this complicates its use as a physical measurement tool. In this study, an attempt has been made to statistically determine the pixel depth in two important media, i.e. demineralisation solution and bovine dental enamel. This is due to the fact that OCT imaging of demineralisation was carried out in a controlled environment with constant flow

conditions. The axial pixel size (in enamel and solution) was calculated and calibrated from baseline profilometry measurements. The axial pixel size is effectively a calibration scale factor translating between pixel counts obtained from OCT images and physical units. Profilometry measures the bulk tissue loss occurring after erosive impacts and is reported to be Perhaps amongst the most reliable techniques for measuring enamel erosion (Kaur et al., 2015). The step height erosive measurements from profilometry yielded an erosion rate of 3.42±0.16 μm/hr. This erosion rate was lower compared with previous published results (Ganss et al., 2000, Schlueter et al., 2005), but these results are not comparable because the acid challenge was at pH 2.3 compared to 3.8 used in this chapter. Furthermore, these studies used a contact profilometer which may disrupt the delicate surface structure.

Using the calculated calibrated pixel depth of 2.75 and 2.80 μm pix^{-1} for surface and DEJ measurement methods respectively, equivalent erosive rates measured using OCT were found to be approximately 3.0 μm/hr. The DEJ method resulted in a pixel calibration value that showed good agreement to the surface method.

The average erosive lesion depth progression was calibrated using a series of artificial steps of known height using polyurethane scattering calibration phantoms. The values acquired from this varied from the profilometer measurements. Erosion rates were calibrated with rates of 7.30 μm pix^{-1} in the erosion solution and 6.00 μm pix^{-1} in enamel based upon literature values for the group indices of water and enamel. The calibrated values of erosive lesion acquired were more than double the values obtained from profilometry. Furthermore, the ratio of solution and enamel calibration factors is equal to the ratio of the group indices as shown by Equation 7.13. Profilometry yielded a ratio of $dz_{erosion}/dz_{enamel}$ =approx. 1.

This indicated that the results obtained by profilometry were not representative of the lesions formed and measured by OCT under continuous immersion in solution. OCT measurements were obtained continuously with the specimens constantly immersed in acidic solution and under constant flow conditions. Specimens measured by profilometry were periodically removed from a static solution for measurement. To determine whether flow had an effect on the OCT measured erosion rate, the results from the flow-cell experiment were compared with a set of results for which the solution was static. In this case, the measured rate of erosion was within the

uncertainty range of the OCT erosion experiments with flow. Therefore, flow alone cannot account for the discrepancy between the OCT and profilometry results.

It is worth to note that the experimental setup for profilometry measurement dictated that the enamel samples be removed from acid and washed with deionised water between each acid challenge. This was done in order to get the varying erosion times on the subdivision created. However, flushing the enamel surfaces removes the acid thus preventing further erosion. The acid content in the demineralised pores is momentarily replaced with deionised water. Thereafter, placing the specimens back into the acid solution takes a finite time for the acid to diffuse back into the enamel and re-start the erosion process. Perhaps this stop-wash-start procedure causes a decrease on the erosion rate compared to a continuous exposure model.

The hydration phases could affect the elasticity of the organic content within the enamel and underlying dentine, which may result in shrinking of the samples between experiments.

7.6 Conclusion

A laboratory OCT configuration has been developed for measuring real-time lesion depth progression. OCT B-scans images have been used for both visual representation of erosive lesions and for quantitative measurement with the ability to detect erosion steps greater than 6.80 μm per hour. The experiments estimate the reproducibility of these values as ±0.51 expressed as a 95% confidence interval.

The values recorded from the standard profilometric technique was not readily comparable to OCT measurement. The physical reason for the discrepancy between profilometry and OCT erosion measurements remains to be elucidated. However, the findings highlight the difficulty of using comparative techniques to validate OCT measurements when the experimental protocol for both is necessarily different. Therefore, throughout this thesis, unless otherwise stated, the pixel calibration values from OCT step-height measurements have been used as follows:

$\delta z = 9.52$ μm pix^{-1} in air

$\delta z_{\text{erosion}} = 7.3$ μm pix^{-1} in the erosion solution

$\delta z_{\text{enamel}} = 6.0$ μm pix^{-1} in the enamel

8 Characterising Sub-Surface Lesion Depth Dynamics

8.1 Introduction

Clinically, caries lesions are routinely detected using visual/tactile (explorer) methods coupled with radiography. Many caries lesions spread into the underlying dentin while the enamel surface remains intact. These lesions are not obvious under visual examination (Kang et al., 2014). Similarly, radiographic methods have poor sensitivity for carious lesions, and by the time the lesions are radiolucent they have typically progressed deep into the dentin (Fejerskov and Kidd, 2009). New methods are needed to detect such lesions.

Since, optical properties of enamel change during demineralisation (Ko et al., 2000), various optical methods have been explored to detect caries. Using the changes in fluorescence intensity during demineralisation, methods such as DIAGNODent and Quantitative Light-induced Fluorescence (QLF) have been introduced (Al-Khateeb et al., 1997, Amaechi et al., 2003b, Lussi et al., 2004, Hibst et al., 2001). These methods however have their limitations. DIAGNODent for example employs fluorescence from bacteria porphyrin molecules for detecting hidden lesions but the technique suffers from many false positives and it does not measure either the depth or exact position of the lesions (Lussi et al., 1999, Shi et al., 2000, Lussi et al., 2004).

Quantitative depth resolved measurements are valuable for clinical studies and for monitoring the state of early lesions. Many clinicians are only interested in knowing how deep the lesions have actually penetrated into the tooth so that they can decide whether a restoration is necessary (Kang et al., 2014). Moreover, early diagnosis of the enamel lesions may allow the dentist to implement non-invasive strategies to reverse the lesion and to avoid surgical interventions (Ibusuki et al., 2015).

Alternatively, some groups have used OCT and PS-OCT to image dental caries on both smooth surfaces and occlusal surfaces (Colston et al., 1998, Colston Jr et al., 1998, Everett et al., 1999, Feldchtein et al., 1998, Baumgartner et al., 1999). OCT is attractive as it is a non-invasive technique for creating cross-sectional images of

internal biological structure (Bouma, 2001). Therefore, OCT has the added advantage of producing an image showing the spread of demineralisation as opposed to a single reading that does not indicate the depth or area of demineralisation.

Image analysis techniques in correlative OCT studies have been mainly based on the increased signal intensity values to quantify parameters such as depth and mineral loss in demineralised lesions (Natsume et al., 2011). Several studies have demonstrated the use of polarisation-sensitivity as an invaluable tool for providing depth-resolved measurements of the severity of demineralisation both *in vitro* and *in vivo* (Fried et al., 2002, Jones et al., 2004, Ngaotheppitak et al., 2005, Le et al., 2009, Manesh et al., 2008). Similar methods have been applied using conventional OCT systems but the strong surface reflection from the tooth surface greatly interferes with accurate measurement of the lesion making it problematic (Chan et al., 2015). However, to the author's knowledge, only few studies have systematically investigated the objective assessment of non-cavitated lesion depth in a well-controlled *in vitro* setting while avoiding specimen movement and drying. Specimen movement and drying affects accurate measurement of lesions as lesions typically appear deeper in OCT images than they actually are (Chan et al., 2015).

Lesion depth is clearly an important parameter of early enamel lesions extent (Ibusuki et al., 2015). Therefore the aim of this study is to assess subsurface enamel lesions in a well-controlled *in vitro* environment avoiding specimen movement and drying effects. 2D images of the lesion will be used to represent and monitor subsurface demineralised lesion severity on the bovine enamel samples.

8.2 Materials & Methods

8.2.1 Samples Preparation

Eight bovine enamel specimens were prepared into 6 mm diameter discs, sliced in the coronal plane to an approximate thickness of 2.6 mm (Modus Laboratories Ltd, Reading, UK). These were embedded into a 25 mm diameter clear resin substrate.

The enamel surface was exposed by polishing to a flat specular finish, leaving a residual enamel thickness of approximately 0.5 mm on top of the underlying dentine.

8.2.2 Artificial Demineralisation Model

The demineralisation solution was prepared as 10 ml acetic acid in 990 ml distilled water, buffered to pH 4.0 by the addition of NaOH pellets (Sigma Aldrich, UK). The pH of the solution was monitored using a SenTix® 41 electrode pH-meter (WTW GmbH, Germany).

8.2.3 Measurement Protocol

The specimens were initially stored dry in sealed containers at a temperature of 25°C. Prior to demineralisation, a reference three-dimensional x-ray attenuation image of each dry sample was obtained non-invasively using a benchtop X-ray Micro-Tomography (XMT) scanner (uCT40, Scanco Medical, Switzerland). Following XMT measurement, the samples were immersed in de-ionised water for a minimum of 24 hours prior to initiation of demineralisation and OCT measurement. This mitigated against hydration effects influencing the OCT signal during the initial stages of the experiment. A permanent marker pen was used to mark a region of dimension 5x5 mm used for the OCT imaging.

Five hydrated specimens and one reference phantom were placed into each chamber of the transparent 6-chamber sample holder. The reference phantom was a polished epoxy block, loaded with TiO_2 scattering particles having a known scattering coefficient of μ_s=3.5 mm^{-1} (Woolliams and Tomlins, 2011a), thus providing a constant benchmark for the OCT measured light back-scattering intensity. Initially, deionised water was added to each chamber and the central region of the specimen was imaged for alignment and baseline measurements. The deionised water was then drained and replaced with the demineralisation solution. One control specimen was kept in deionised water for the duration of the experiment. The OCT system automatically acquired a 3D image from the same location within each sample at hourly intervals, limited by the positional accuracy of the linear translation stages. Therefore, longitudinally acquired OCT image volumes of each specimen were spatially co-registered. Using this configuration, demineralisation of 8 specimens was measured in two experimental runs. In the first run of the experiment, continuous exposure to

the demineralisation solution was allowed for 48 hours. After reviewing the results, a second experiment was extended to 72 hours. Immediately following completion of the demineralisation experiment, the specimens were removed from the solution, rinsed in distilled water and allowed to dry for at least 24 hours before being re-imaged using XMT.

8.2.4 Lesion Depth Measurement

The OCT system captured 3D volumetric data stored as both raw interference fringes and sequential B-Scan images in 'PNG' image format. The B-Scan images represented the backscattered light intensity, scaled in logarithmic units. Lesion depth was assessed manually by eye from the PNG image B-Scans using ImageJ (Schneider et al., 2012). To obtain the lesion depth measurements, sequential B-Scans (numbers 200 to 300 indicated in Figure 37 were selected and averaged into a single composite B-Scan.

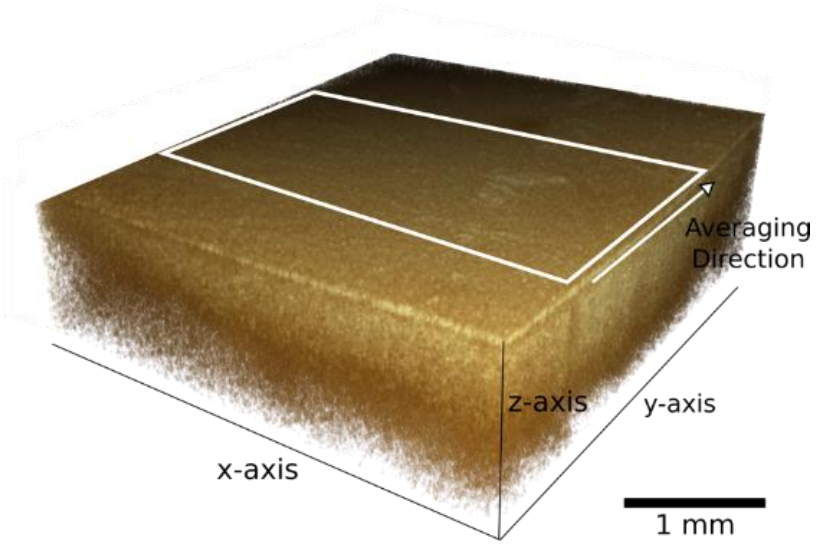

Figure 37 Three-dimensional OCT image of sound bovine enamel. The region of interest selected for averaging (B-Scans 200 - 300) is indicated by the white box on the enamel surface.

This process reduced noise and resulted in a clear visualisation of the effect of demineralisation upon the OCT signal, which is apparent as a band of increased backscattering intensity (bright region), indicated in Figure 38a-f. The thickness of this band was estimated using the ImageJ line tool and converted to optical units using the instrument optical depth scale of 8 μm per pixel, not accounting for the enamel refractive index.

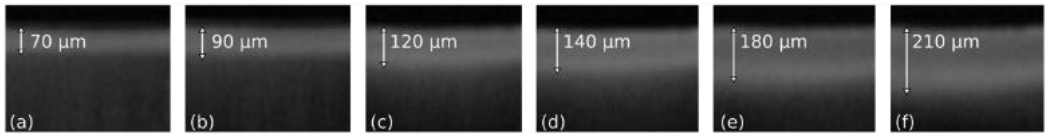

Figure 38 Averages of 100 sequential B-Scans from which the lesion depth was measured for each sample at hourly intervals. Example images (a)-(f) indicate the visual pattern of lesion progression at (a) 6 hours, (b) 12 hours, (c) 18 hours, (d) 24 hours, (e) 36 hours and (f) 48 hours. The arrows indicate the thickness of the band of increased scattering.

This process was repeated for each specimen at the hourly time points acquired. The results from this analysis were plotted for visualisation. The mean average lesion depth progression was also determined by taking the mean of 8 lesion depths (1 per specimen) at each hourly time-point. For each time point a 95% confidence interval was calculated, yielding an estimated uncertainty in the expected bovine lesion depth measured by OCT for this model system.

8.3 Results

8.3.1 Lesion Depth

Volumetric data was acquired for each of the 8 samples at hourly intervals. Each OCT dataset was obtained from the same region of the sample ensuring that corresponding B-Scans at each time point were measured from the same spatial location. The central B-scan image (slice 250) for samples 1 to 4 are shown in Figure 39 at time points 0, 6, 12, 18, 24 and 48 hours. Similarly, the central B-Scan from samples 5 to 8 are shown in Figure 40. The B-Scans show a visually consistent pattern of lesion progression. Notably, by the 6th hour, initial lesion formation produces a region of high backscatter, with the sub-lesional area exhibiting less back-scattering of light compared with the initial baseline measurement. Furthermore, the lower edge of the lesion appears to exhibit a region of high intensity, compared with the central region of the lesion.

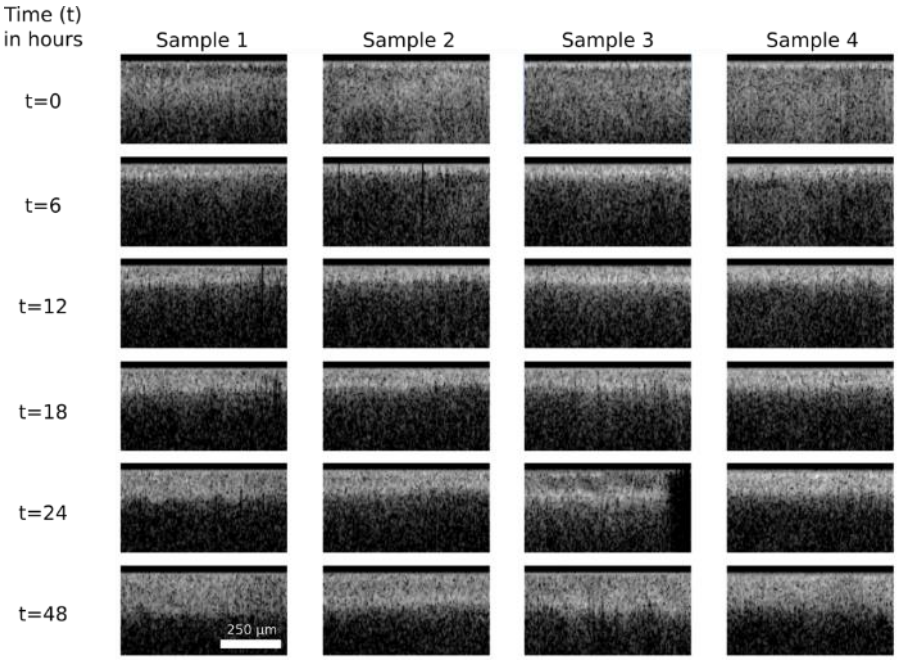

Figure 39 Cross-sectional images (B-Scans) from the centre of the volume (image 250/500). Shown is the central region from samples 1-4. Each image is of the same section of the sample at time points of 0, 6, 12, 18, 24 and 48 hours.

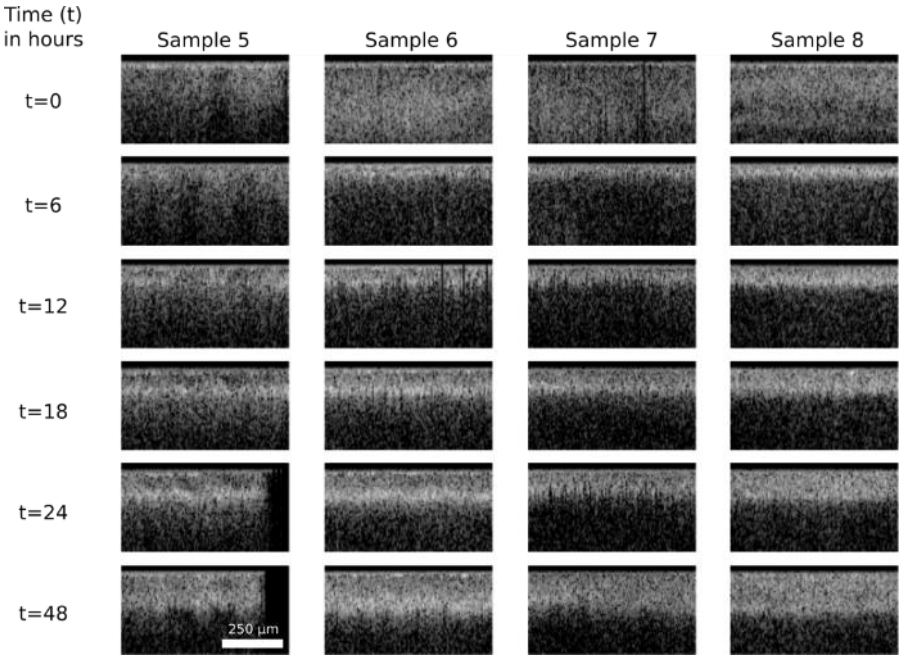

Figure 40 Cross-sectional images (B-Scans) from the centre of the volume (image 250/500). Shown is the central 1 mm wide region from samples 5-8. Each image is of the same section of the sample at time points of 0, 6, 12, 18, 24 and 48 hours.

Samples 5 and 3 exhibit a region of no signal at 24 and 48 hours and 24 hours respectively. This is the consequence of bubble formation on the enamel surface. This

was confirmed by rendering the entire 3D dataset for these samples, as shown in Figure 41 for sample 3 at *t*=24 hours.

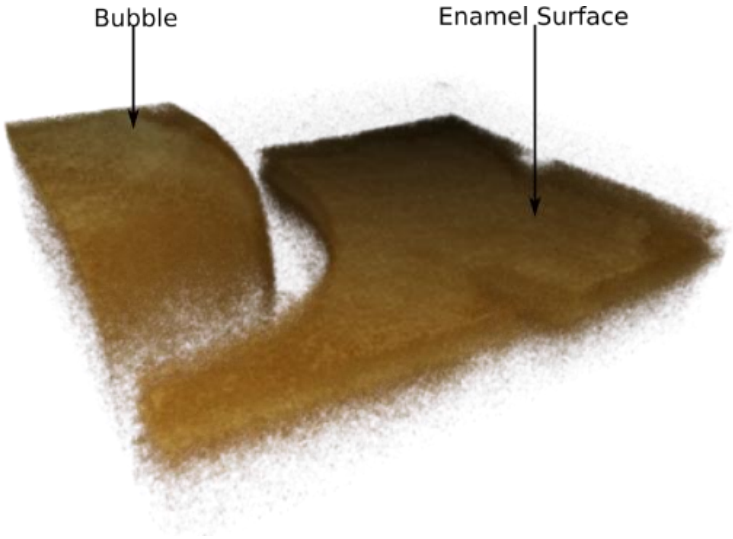

Figure 41 Three-dimensional rendering of sample 3 at t=24 hours. The image shows a bubble that has developed on the enamel surface, thus obscuring the OCT signal below.

Under the assumption that the bright band of intense backscattering is representative of lesion progression, its thickness (in optical units) was measured as described above. The resulting measurements are plotted in Figure 42, showing the pattern of lesion progression in each specimen (a) and the mean of all specimens (b).

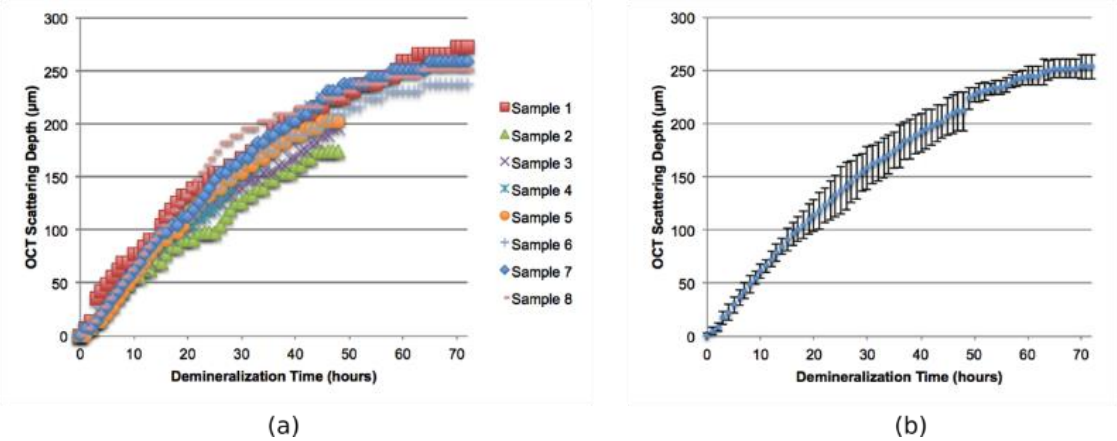

Figure 42 (a) Demineralisation pattern of progression measured by OCT for 8 different bovine enamel samples at hourly time-points for up to 72 hours. (b) Mean OCT scattering depth (points) due to static demineralisation in acetic acid at hourly intervals. Depth is averaged over 8 samples. Error bars represent 95% confidence intervals (n=8) for t <= 48 hours and (n=4) for t>48 hours.

Error bars represent 95% confidence intervals calculated for all contributing samples. Data points up to 48 hours represent all 8 specimens, however only 4 samples were exposed to the demineralisation solution during the period from 48 to 72 hours.

8.3.2 X-Ray Micro-Tomography

XMT measurements obtained before and after the demineralisation cycle provided three-dimensional images of each entire specimen. For example, Figure 43a shows sample 2 following 48 hours of demineralisation. Here, the demineralised surface is evident alongside the 5x5 mm square marked by permanent marker. The marker pen has apparently partially masked the enamel and thus inhibited demineralisation, leaving a corresponding ridge. Within the area demarcated by the ridge is the region scanned by OCT.

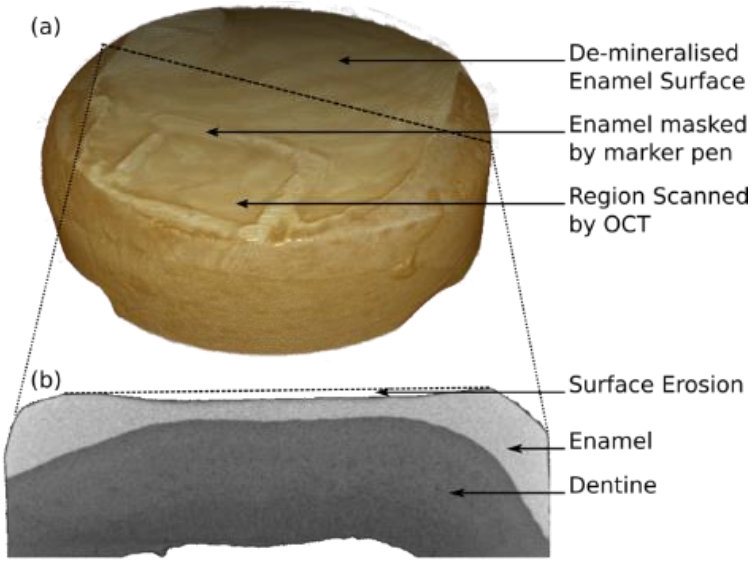

Figure 43 The X-Ray micro-tomography data. (a) A three-dimensional re-construction of sample 2 showing the demineralised surface and the region marked for OCT imaging. A single cross-section (b) taken along the dashed line shows the internal specimen morphology and eroded surfaces.

The XMT cross-section shown in Figure 43b shows the specimen gross morphology and the extent of surface erosion. However, the XMT voxel size (approx. 15 μm^3) substantially limited the visualization of sub-surface lesion extent. Consequently, the sub-surface lesion depth could not be reliably measured for comparison with OCT.

8.4 Discussion

The experiments outlined in this paper aimed to determine the pattern of lesion progression in a simple bovine enamel demineralisation model measured using OCT. Notably, unlike previous studies, this study obtained three-dimensional OCT datasets under computer control at regular (hourly) intervals, keeping the samples in place. Consequently, subsequent image volumes were spatially co-registered and thus comparison at each time-point was made over the same region of the sample.

Consistent with previous reports, the demineralisation process led to the formation of a sub-surface band of intense optical backscatter (Fried et al., 2002). This band extended from the specimen surface to a depth that was shown to be dependent upon the time of exposure to the demineralisation solution. Visually (Figure 39 and Figure 40) the pattern of progression was consistent between specimens. From approximately 12 hours, the progressive lesion manifested in the OCT B-Scans with a distinct morphology comprising an initial intense surface backscatter, presumably dominated by the refractive index mismatch between the demineralisation solution and the dental enamel. Below this the backscattering became less intense but intensified again towards the leading edge of the lesion. Optically, this intra-lesion variation in scattering profile must originate from depth dependent alteration to the enamel structure. However, conclusive explanation of this phenomenon will require a different study design incorporating some high-resolution structural imaging, perhaps using SEM. Quantitatively, the lesion depth exhibited a consistent 95% confidence interval of no more than 20 µm for up to 10 hours of demineralisation. After this time the confidence interval gradually grew to approximately 50 µm. The gradual increase in uncertainty with increasing time may reflect the natural variation in susceptibility to demineralisation of the different bovine tooth specimens. There may also be a degree of uncertainty introduced by the manual method of measurement of the lesion thickness, however this is unlikely to be time dependent. Furthermore, the individual demineralisation curves (Figure 42a) did not exhibit substantial scatter, but each showed a self-consistent progression. This was an important result because for the purpose of this study it ruled out the use of an automated algorithm that was found to be less consistent (results not included in this chapter) than measurement by hand. Nevertheless, an automated approach is favoured for future work because of the inherent objectivity and repeatability, especially with respect to consistent sub-pixel

measurement. This is not considered a major limitation to the present study. However, it is expected to be an important factor for examining the early stages of demineralisation with higher time resolution. For example, the first 5 hours of demineralisation shown in Figure 42b appear to show a subtle sigmoidal shape. Investigation of this will require measurement of the demineralisation band thickness with sub-resolution localization. Arguably, such processing is best performed by an algorithmic curve fit.

The experimental configuration outlined in this chapter provides a platform that can be developed for future controlled OCT experiments to study different aspects of dental demineralisation. However, bubbles were observed to form on the enamel surface during demineralisation. Without further experimentation, it is unclear whether the non-linear lesion depth curves (Figure 42) represent typical lesion development for this model or if this is the product of the demineralisation solution becoming saturated by dissolution of the enamel into a limited volume. Nonetheless, these experimental limits do not invalidate the results or the experimental platform, rather, they provide a useful comparator for future results.

In addition, the measured lesion depths have not been corrected for the enamel refractive index. Therefore the lesion depth results are given in units of optical thickness (physical thickness × refractive index). Potentially, XMT data could provide the physical dimensions required to estimate the enamel refractive index. However, the commercial XMT scanner exhibited ring artifacts at the specimen surface, thus introducing uncertainty into the physical measurements. It was therefore preferred to use optical units. The presence of XMT ring artifacts made visualization and subsequent measurement of the sub-surface lesions ambiguous. To mitigate against this, a high resolution XMT scanner was also used post-demineralisation. Despite the absence of ring artifacts in this data, the voxel size was insufficient to fully view the sub-surface lesions, the depth of which was contained within 2 to 3 pixels. This is a useful finding, because it suggests the complimentary use of both XMT and OCT to measure different aspects of the same specimen. For example, in this study XMT was useful for imaging the whole specimen post-demineralisation. This data could be used to estimate the total volume of mineral dissolution, although this would require further post-processing, which has not been carried out for the present study. The rapid acquisition time of OCT (a few seconds compared to >10 hours for XMT) facilitated

real-time measurement of the demineralisation process and measurement of sub-surface lesions.

8.5 Conclusion

OCT continues to demonstrate substantial potential as an analytical technique for dentistry. Nevertheless, to realize this potential more research is needed to quantitatively understand the manner in which different dental phenomena manifests in OCT data. A Better understanding of the dynamics of different demineralisation lesions is needed.

9 Comparing the Optical Properties of Three Demineralisation Models

9.1 Introduction

Dental hard tissue disease is frequently characterised by mineral loss. Hence, this is a critical factor in its diagnosis and management in terms of carious and erosive lesions. Clinical diagnosis is based upon anatomical site, recurrence, disease progression, extent, tissue involvement and chronology (Garg and Garg, 2010, Ismail et al., 2007). Both acid erosion and caries are driven by acidic pH, either due to external agents (i.e. citrus juices) or naturally occurring metabolites such as lactic acid. Consequently, the two conditions are not necessarily mutually exclusive (Jones and Fried, 2006). However, lesion characteristics are not governed by pH alone, exhibiting dependence on the composition of the demineralising agent (Sperber and Buonocore, 1963). Thus, simplified *in vitro* models have been developed to study dissolution chemistry, aetiological factors and symptomatic features (Sperber and Buonocore, 1963).

Several analytical techniques have found utility for measuring dental mineralisation (Ten Bosch and Angmar-Månsson, 1991). Transverse microradiography (TMR), has been used to assess lesion depth and mineral density (Amaechi et al., 2004, Fontana et al., 1996, Karlsson, 2010), along with micro-hardness testing (Featherstone et al., 1983, Kielbassa et al., 1999) and scanning electron microscopy (SEM) for evaluating structural changes that occur during demineralisation (Cheng et al., 2009b, Faber et al., 2004). X-ray micro-tomography (XMT) has provided quantitative high resolution 3D mapping of dental lesions (Choudhury and Jacques, 2012) and mineral density (Elliott et al., 1998, Cochrane et al., 2012, Davis et al., 2013). These laboratory techniques have contributed to both the understanding of dental lesions and the development of oral healthcare treatments. However, they are not readily translated directly into the clinic for *in vivo* patient examination. Consequently, alternative measurement and imaging technologies have been reported in the dental research literature. These include quantitative light fluorescence (QLF)(Amaechi and Higham, 2002, Amaechi et al., 2003b, Maia et al., 2015, Shi et al., 2001) and optical coherence tomography (OCT)(Amaechi et al., 2003a) which can be used for both laboratory

based *in vitro* experiments and *in vivo* clinical research. OCT is attractive because it non-invasively images backscattered light intensity, which has been shown to be sensitive to changes in dental demineralisation (Colston et al., 1998, Feldchtein et al., 1998).

OCT has been applied by a number of groups to study dental demineralisation in artificial and natural lesions, both *in vitro* and *in vivo* (Fried et al., 2002, Ngaotheppitak et al., 2005). However, OCT measurements are yet to be quantitatively validated. OCT measurements of lesions formed under different demineralising conditions have not previously been compared using a consistent environment. Furthermore, OCT studies have previously been limited by protocols that require specimens to be moved between demineralisation solutions and the imaging equipment. This is a major limitation for longitudinal studies that aim to understand lesion dynamics over time because measurement uncertainty has been associated with specimen re-alignment at each imaging step (Chew et al., 2014).

Therefore, this study reports a 'hands-free' experimental configuration that mitigates against the need for specimen movement at each time point. The primary aim of developing this system was to enable longitudinal OCT measurements of dental mineralisation. This study investigated whether the optical properties of lesions formed using different demineralisation models were distinguishable under OCT.

9.2 Theory

The OCT image-forming signal is the result of optical backscatter from within a specimen. Spatial variations in the scattering properties of materials lead to image contrast, enabling regions with different optical properties, such as different tissue types (Cheong et al., 1990), to be visualised. Furthermore, disease processes have been shown to modify the scattering properties of biological tissue (Papazoglou et al., 2008, Karlsson, 2010, Jacques, 2013). In the single scattering regime, the OCT signal (I) can be approximated by an exponential decay of the form given in Equation 9.1 (Faber et al., 2004, Levitz et al., 2004, Almasian et al., 2015),

$$I(z) = \mu_{\mathrm{B}} \exp[-2\mu_{\mathrm{OCT}}(z - z_0)] \qquad \text{Equation 9.1}$$

Where z_0 represents the axial starting point of a region described by homogeneous optical properties. The optical properties are expressed in terms of the backscattering coefficient μ_B and the signal attenuation constant μ_{OCT}. Light is not guaranteed to scatter equally in all directions, i.e. isotropic scattering. Therefore, the backscattering coefficient is dependent upon the directionality of light scattering, described mathematically by its phase function. The phase function is a probability distribution that statistically relates the intensity of light from an incident direction that couples via single scattering into a given scattered direction. In tissue optics, the phase function is often parameterised in terms of its average cosine, g, known as the anisotropy factor. Thus, g=0 is equivalent to isotropic scattering, g=-1 total backscatter and g=1 total forward scatter. For OCT the incident and collection directions are the same, determined by the numerical aperture of the OCT system optics. Therefore, increasing g necessarily decreases μ_B, leading to a reduced OCT signal (Kodach et al., 2011, Choudhury and Jacques, 2012). It follows that contrast in OCT images can therefore arise from regions exhibiting different degrees of anisotropy and the backscatter coefficient can be written as a function of g, i.e. $\mu_B(g)$.

The signal attenuation constant describes the rate of OCT intensity decrease due to both absorption and scattering. It is a linear combination of the absorption coefficient μ_a and the scattering coefficient μ_s such that $\mu_{OCT} = \mu_a + \mu_s$. The dominance of either scattering or absorption is described by the albedo (Prahl, 1989), $a = \mu_s/(\mu_a + \mu_s)$ such that, $a = 0$ indicates pure absorption and $a = 1$ purely scattering. The operating wave-band of OCT is often chosen to minimise optical absorption, leading to the assumptions that $a \approx 1$ and therefore $\mu_{OCT} \approx \mu_s$.

Statistically, the scattering coefficient can be interpreted as the average number of scattering interactions per unit distance. Therefore, OCT intensity contrast can exist between two regions having identical μ_s providing that their μ_B differs. This is because scattering occurs with the same frequency in both regions, but with different proportions coupled into the backwards direction detected by OCT.

Signal attenuation implies that $\mu_{OCT} > 0$ and that the OCT signal decreases with depth. However, axial increases in signal intensity are observed in practical OCT imaging.

This can be attributed to a relative decrease in g, leading to an increase in $\mu_B(g)$, assuming that axial coupling efficiency variations have been accounted for.

In real OCT systems, the measured OCT signal, I_m, is the product of $I(z)$ with the axial coupling efficiency (T) centred around the focus at z_f and the axial sensitivity roll-off (H).

$$I_m(z) = \alpha T(z - z_f)H(z)I(z) \qquad \text{Equation 9.2}$$

The calibration scale factor, α, facilitates comparison between different specimens and systems by accounting for systematic coupling efficiency differences. Calibration of the axial variations in detection sensitivity and optical coupling efficiency are necessary when comparing measurements of the optical properties obtained from different axial positions. Typically μ_{OCT} and μ_B are obtained from a least squares fit of Equation 9.1 to segments of OCT A-Scans following calibration of the term $\alpha T(z - z_f)H(z)$. Calibration can be achieved by measuring a specimen with a known optical properties (Faber et al., 2004, Almasian et al., 2015). However, even if the anisotropy factor is unknown, a homogeneous scattering phantom with known attenuation coefficient μ_{cal} can still provide a relative intensity calibration. Dividing the OCT A-Scan profile of a specimen I_m by an equivalent calibration A-Scan yields the expression for the corrected signal,

$$I_{corr}(z) = \mu'_B \exp[-2\mu'_{OCT}(z - z_0)] \qquad \text{Equation 9.3}$$

where $\mu'_B = \mu_B(g)/\mu_B(g_{cal})$ and $\mu'_{OCT} = \mu_{OCT} - \mu_{cal}$. The subscript 'cal' denotes the properties of the calibration phantom. Therefore, μ'_{OCT} can be obtained experimentally by fitting Equation 9.3 to a corrected OCT A-Scan. The specimen attenuation coefficient is found from the sum $\mu_{OCT} = \mu'_{OCT} + \mu_{cal}$.

These expressions have facilitated the use of OCT for quantitative evaluation of the optical properties of collagen gel tissue scaffolds (Levitz et al., 2010) and biological tissues (Schmitt et al., 1993) such as atherosclerotic plaques (van der Meer et al., 2005), epithelial pre-cancer (Adegun et al., 2012) and dental caries (Popescu et al., 2008, Shimada et al., 2013). These methods have been extended to the spatial mapping of μ_{OCT}, a technique termed both parametric OCT (McLaughlin et al., 2010) and scattering attenuation microscopy (SAM) (Tomlins et al., 2010).

In general, it is preferred to measure the calibration function, rather than rely upon a theoretical description. However, in the presence of dental erosion, the specimen surface moves with respect to the system objective lens. Refractive index differences between the specimen and its surrounding medium necessarily lead to a shift in the focal plane position, z_f. Dental enamel has a refractive index of approximately 1.63 at a wavelength of 1300 nm (Tearney et al., 1995, Meng et al., 2009) and water 1.32 (Segelstein, 1981). Geometrical optics can be used to estimate the expected focal plane shift due to erosion using the following expression (Zvyagin et al., 2003)

$$\Delta z_f = \frac{r_1 + \tan\theta_1 (z_0 - z_{\text{lens}})}{\tan\theta_2} + z_0 - z'_f \qquad \text{Equation 9.4}$$

The angle, θ_1, denotes the peripheral ray of a focussed beam propagating through a medium having refractive index n_1, where the focusing lens is located at z_{lens} along the optical axis, at which the beam radius is r_1. A specimen, having refractive index n_2 is located such that its surface is perpendicular to the optical axis at z_0. Upon passing into the second medium, the peripheral ray is refracted to a new angle, $\theta_2 = \sin^{-1}\{[n_1 \text{NA}]/n_2\}$. The axial location at which the beam would have come to focus in the absence of the specimen is z'_f.

Assuming an objective numerical aperture of $\text{NA} = \sin\theta_1 = 0.05$, $r_1 = 1.5\,\text{mm}$, $z_{\text{lens}} = 0\text{mm}$, $z_0 = 2\text{mm}$, $n_1 = 1.32$ and $n_2 = 1.63$ and z'_f=30mm, then a 100 μm shift in the surface position, z_0, corresponds with a focal shift of 124 μm. The impact of this on the coupling efficiency is evaluated by inspection of Equation 9.5,

$$T(z - z_{\text{f}}) = \frac{1}{\left[\frac{(z - z_{\text{f}})\lambda_0}{2n_2\pi w_0^2}\right]^2 + 1} \qquad \text{Equation 9.5}$$

Where w_0 is the beam waist at the focus (z_{f}), with illumination wavelength of $\lambda_0 = 1300\text{nm}$. Under these conditions, shifting the focus by ±200 μm leads to a coupling efficiency uncertainty of approximately $\pm 5\%$.

9.3 Materials & Methods

9.3.1 Bovine Enamel Specimens

Twelve bovine incisors were prepared and embedded into 25 mm diameter clear resin substrates. Each tooth was sectioned into a 6 mm diameter disc, sliced in the coronal plane to an approximate thickness of 2.6 mm. The enamel surface was exposed by polishing to a flat specular finish, leaving a residual enamel thickness of approximately 0.5 mm on top of the underlying dentine. The specimens were prepared by Modus Laboratories Ltd, Reading, UK.

9.3.2 Artificial Lesion Models

Artificial lesions were produced by continuous exposure of the enamel to one of three different demineralisation solutions. These were sensitive to longitudinal changes and to describe the differences between three different *in vitro* demineralisation models. 1, 2) and 3)

1) *Citric Acid 'Erosion Model' (pH 3.8)*

A diluted citric acid model previously used for erosion studies (Hughes et al., 2000, Barbour et al., 2003, Young and Tenuta, 2011b) was prepared as 0.05 M citric acid (Sigma Aldrich, UK). The solution was buffered to pH 3.8 using Sodium Hydroxide (NaOH) pellets.

2) *Acetic Acid 'Caries-Like Demineralisation' Model (pH 4.0)*

A diluted acetic acid model, previously reported for demineralisation studies (Anderson and Elliott, 1992), was prepared as 0.17 M acetic acid, buffered to pH 4.0 by the addition of NaOH pellets (Sigma Aldrich, UK).

3) *Acetic Acid 'Caries-like' Model (pH 4.4)*

Caries models typically contain a source of Calcium and Phosphate, enabling a sub-surface lesion to form whilst maintaining an in-tact surface (Ten Cate et al., 1988, Damen et al., 1998, Chan et al., 2013). Thus, the caries-like model solution was prepared as 2.2 mM $CaCl_2$, 2.2 mM KH_2PO_4, 0.05 M acetic acid with the pH adjusted to 4.4 with 1 M NaOH.

9.3.3 OCT System Specification and Configuration

The OCT system used for this study was custom designed and built in-house at Queen Mary University of London. The instrument incorporated a fibre optic Michelson interferometer design (Rollins and Izatt, 1999) utilising a super-luminescent light emitting diode (SLD) optical source (SLD1325, Thorlabs Ltd, Cambridge, UK), operating with a nominal central wavelength of 1310 nm and bandwidth of approximately 100 nm. The axial and transverse resolutions were nominally 8 and 10 µm in air respectively. Interference fringes were detected by a high-speed spectrometer as described in the Materials and Methods chapter 6.5.

The multi-specimen holder comprising 6 isolated flow-cell chambers was used. A typical chamber is shown in Figure 44, each chamber measured 24x24x4 mm (width x height x depth), having an actual volume of 2.3 ml. Solution was flowed through the chambers at a rate of 5 ml/minute by a motorised pump (323Du/D, Watson Marlow, UK). Solution was coupled in and out of the chambers by 21 gauge syringes.

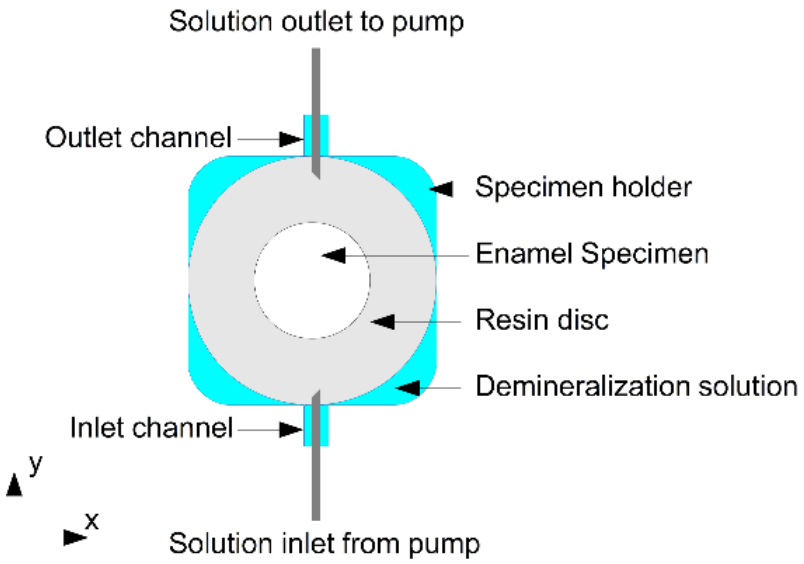

Figure 44 XY plane view of a bovine enamel specimen, mounted in a resin substrate and placed into the specimen holder. The holder and specimen were orientated vertically, immersed in demineralising solution. The solution was continuously refreshed by a pump that introduced fresh solution through an inlet channel at the bottom of the specimen holder and removed solution through an outlet channel at the top.

The OCT probe was mounted onto a linear translation stage (LTS300/M, Thorlabs, Ltd, Cambridge, UK) such that the probe beam propagated horizontally, parallel to the

lab bench. The specimens were mounted vertically in the specimen holder with the exposed enamel face perpendicular to the OCT probe beam. This configuration is shown in Figure 45.

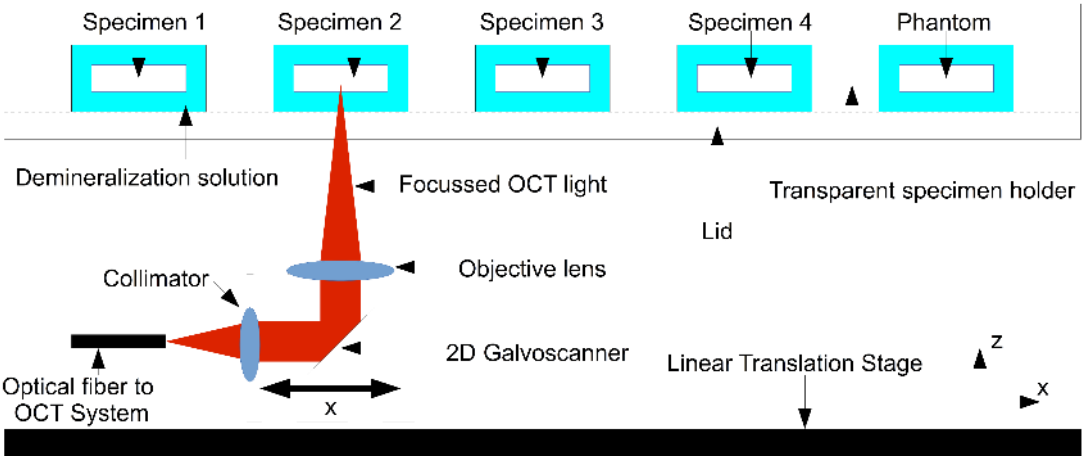

Figure 45 XZ Plane view of the experimental configuration. Four bovine enamel specimens and one scattering phantom were mounted vertically in a transparent specimen holder, through which the demineralising solution was continuously flowed. Three-dimensional OCT *volumes of each were obtained automatically by moving the OCT probe between specimens on a motorized linear translation stage.*

9.3.4 Calibration

The axial collection efficiency of the OCT system and the sensitivity roll-off were calibrated by measuring a weakly scattering phantom (Faber et al., 2004). This has been previously described as a point-spread function (PSF) phantom (Woolliams et al., 2010, Woolliams and Tomlins, 2011b, Tomlins, 2009), comprising a low concentration of FeO nano-particles having an average inter-particle spacing of 50 μm. The well-spaced particles yielded $\mu_{cal} \ll \mu_{OCT}$ and thus the effect of signal attenuation due to scattering was considered negligible. An area of the phantom surface measuring 3x3 mm was measured using the OCT system. The phantom was mounted in the specimen holder and submerged in deionised water in order the match the configuration of the demineralisation experiments. The mean of 250,000 A-Scans was used to represent the average calibration curve by which all subsequent OCT A-Scans of the specimens were divided. The calibration curve is shown in Figure 46. The curve is interrupted by several small sharp peaks that correspond with the spatial frequencies of spurious spectrometer signals and background OCT system reflections.

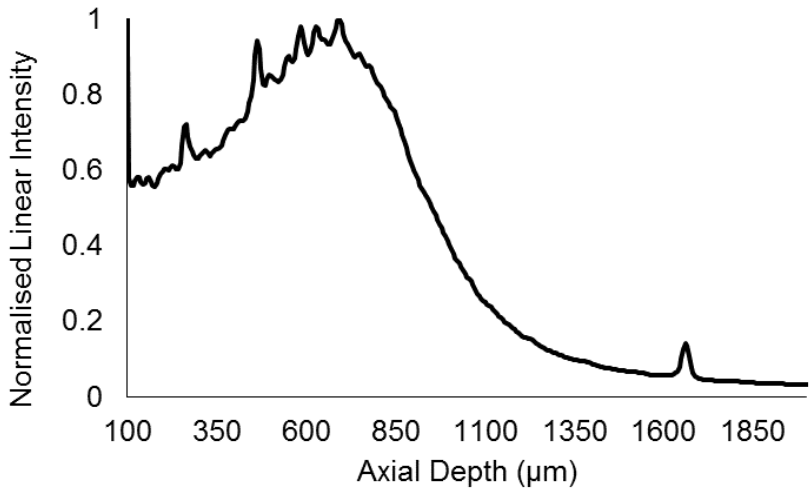

Figure 46 The calibration A-Scan for the OCT system used in this study. Several small sharp peaks are visible which are due to the non-uniform system noise floor.

9.3.5 Measurement Protocol

The specimens were initially stored dry in sealed containers at a temperature of 25°C. The samples were immersed in de-ionised water for 24 hours prior to initiation of demineralisation and OCT measurement. This mitigated against hydration effects influencing the OCT signal during the initial stages of the experiment.

Four hydrated specimens and one reference phantom were placed into each well of the specimen holder. The reference phantom was a polished epoxy block, loaded with TiO_2 scattering particles having a known scattering coefficient of μ_s=3.5 mm^{-1}, thus providing a constant benchmark for the OCT measured light back-scattering intensity. The polished enamel surface was orientated towards the OCT probe beam as shown in Figure 45. Initially, deionized water was pumped into the flow cell and the central region of the specimen imaged using the OCT system. This was accomplished under computer control such that the alignment of the experimental system was not disturbed. The water was then removed from the specimen wells and replaced with demineralisation solution in each chamber using the computer controlled pump. Filling and emptying of the chambers was completed in a few seconds at a flow rate of 5 ml/minute. The solution was not recycled, but drawn from a reservoir of stock demineralisation solution. The OCT system automatically acquired a 3D dataset from a set location within each sample at a minimum of one hour intervals. Therefore, longitudinally acquired OCT image volumes of each specimen were spatially co-

registered. The pH of the solutions was constantly measured using SenTix® 41 electrode pH-meter (WTW GmbH, Germany).

9.3.6 Lesion Depth and Optical Properties Measurement

Quantitative analysis of the OCT measurements was automated from the raw data using a script written in the MATLAB programming language. OCT A-Scans were processed from the detected spectral interference patterns into linear intensity profiles. The approximate specimen surface location was known *a priori* due to the nature of the experimental setup and specimen holder. This information was used to approximately locate the surface reflection peak. The mean of 100 adjacent A-Scans was found, from which the intensity maximum was assumed to represent the specimen surface location.

The lesion depth, d_{lesion}, was estimated by fitting the sum of two Gaussian functions of the form given in Equation 9.6 to the OCT signal intensity region around the lesion, I_{lesion}.

$$I_{\text{lesion}} = A_1 \exp\left[-\frac{(z-z_1)^2}{w_1^2}\right] + A_2 \exp\left[-\frac{(z-z_2)^2}{w_2^2}\right] \qquad \text{Equation 9.6}$$

In Equation 9.6, the two Gaussian functions are denoted by the subscript n = 1,2. The peak height of the functions is given by A, peak location z_n and 1/e half width w. Thus, the lesion depth was estimated as

$$d_{\text{lesion}} = z_2 - z_1 + \frac{1}{2}(w_2 + w_1) \qquad \text{Equation 9.7}$$

Subtracting a systematic offset from the final value to ensure that the lesion thickness was always zero at t=0.

This method was chosen empirically because it proved to be stable for automation, comparing well with manual measurements. A typical fit of Equation 9.6 to a measured lesion mean A-Scan is shown in Figure 47 as a solid line compared to the measured data points (circles). The two Gaussian functions are shown independently as dotted and dashed lines.

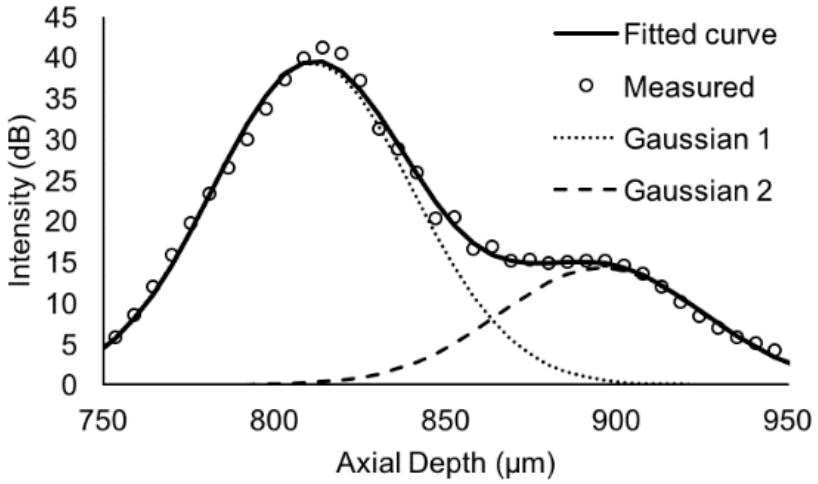

Figure 47 Section of a mean A-Scan for a demineralisation lesion. The circles show the measured data points compared to the fitted sum of Gaussians (solid line). The dotted and dashed lines show the two individual Gaussian functions.

Parameters obtained from the lesion depth fit were also used to define a region of interest (ROI) from which the optical properties were estimated. Typically, the peak reflection was high compared to the backscattered intensity from beneath the surface due to the refractive index mismatch between the demineralising solution and the tooth. Therefore, the peak was filtered out by selecting a ROI from the A-Scan, starting 2 pixels (≈10 μm) below the surface peak and extending across the lesion to z_2. The ROI selection is indicated in Figure 48.

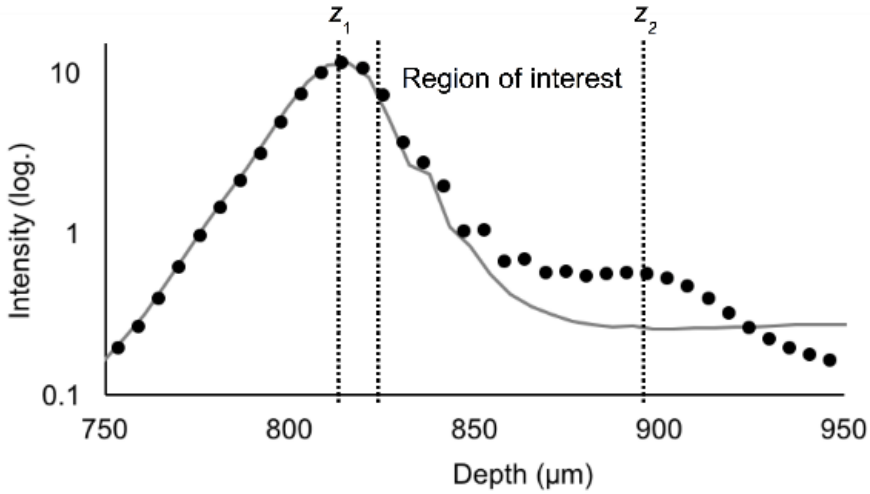

Figure 48 Region of interest (ROI) selection based upon fitted parameters from Equation 9. The ROI started 10 μm below the estimated surface position at z_1.

Equation 9.3 was fitted to the extracted sub-region, providing output estimates of μ'_{OCT} and $\mu'_{\mathrm{B}}(t)$. For each series of longitudinal measurements, the percentage change in $\mu'_{\mathrm{B}}(t)$ was calculated at each measurement time *t* as

$$\Delta\mu'_{\mathrm{B}}(t) = 100\,\frac{\Delta\mu'_{\mathrm{B}}(t) - \Delta\mu'_{\mathrm{B}}(0)}{\Delta\mu'_{\mathrm{B}}(0)}. \qquad \text{Equation 9.8}$$

Assuming $\mu_{\mathrm{cal}} \ll \mu_{\mathrm{OCT}}$ and $a \approx 1$, then $\mu'_{\mathrm{OCT}} \approx \mu_{\mathrm{s}}$. Therefore, from hereon, the measured attenuation coefficient is referred to as the scattering coefficient. The mean scattering coefficient and the corresponding standard error of the mean were calculated at each time-point across all specimens within the model group.

9.4 Results

Central B-Scans from the citric, acetic and caries-like models are shown in Figure 9.6, Figure 9.7 and Figure 9.8 respectively at baseline (a) and following acid challenge of 6 hours (b), 12 hours (c) and 24 hours (d). Visually, all three models followed similar patterns of progression. At baseline, the dentine-enamel junction (DEJ) was visible, but this became increasingly difficult to discern with increasing duration of acid challenge. At and below the surface, a distinct band of high backscatter (lighter region) was observed to form. Following 6 hours of continuous acid challenge, the citric acid model (Figure 49b) showed signs of surface roughening, changing from the smooth profile in Figure 49a. Furthermore, by 24 hours of acid challenge, there was visible erosion of the enamel surface relative to the varnished region.

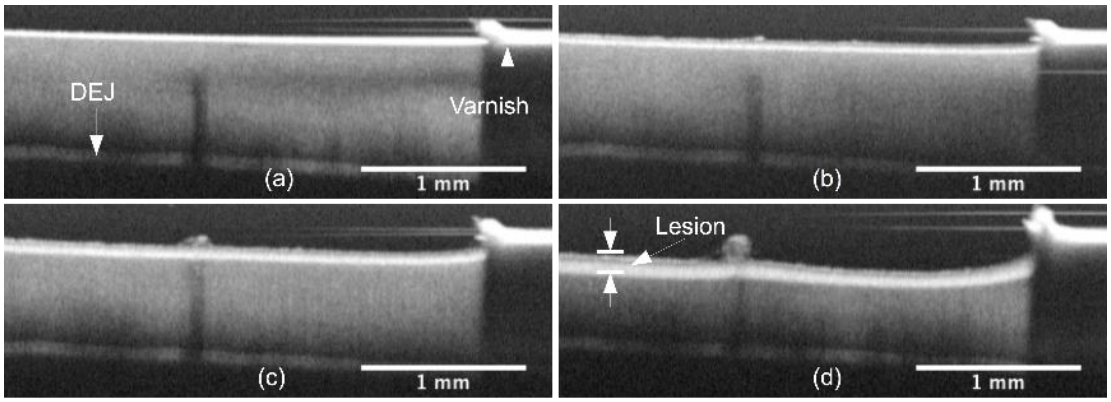

Figure 49 Registered OCT B-Scans of Bovine enamel, (a) hydrated prior to acid challenge and following (b) t=6 hours, (c) t=12 hours and (d) t=24 hours of continuous exposure to a citric acid solution at pH 3.8

The acetic acid model showed less axial erosion. However, the band of intense backscatter extended deeper beneath the surface following 24 hours of acid challenge compared with the citric acid model (see Figure 49d and Figure 50d).

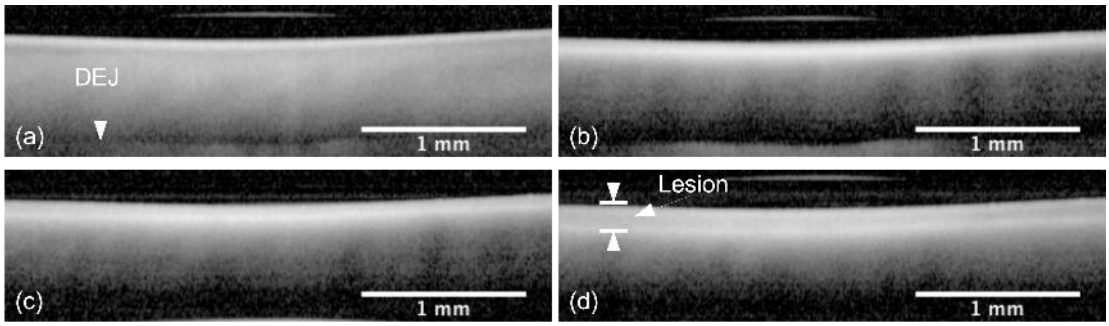

Figure 50 Registered OCT B-Scans of Bovine enamel, (a) hydrated prior to acid challenge and following (b) t=6 hours, (c) t=12 hours and (d) t=24 hours of continuous exposure to an acetic acid solution at pH 4.0.

The caries-like model in Figure 51 similarly developed a band of intense backscatter, increasing in sub-surface depth with acid exposure time. The band itself extended to a similar depth to the citric acid model following 24 hours of acid challenge (Figure 51d). However, there was no perceivable erosion or surface change.

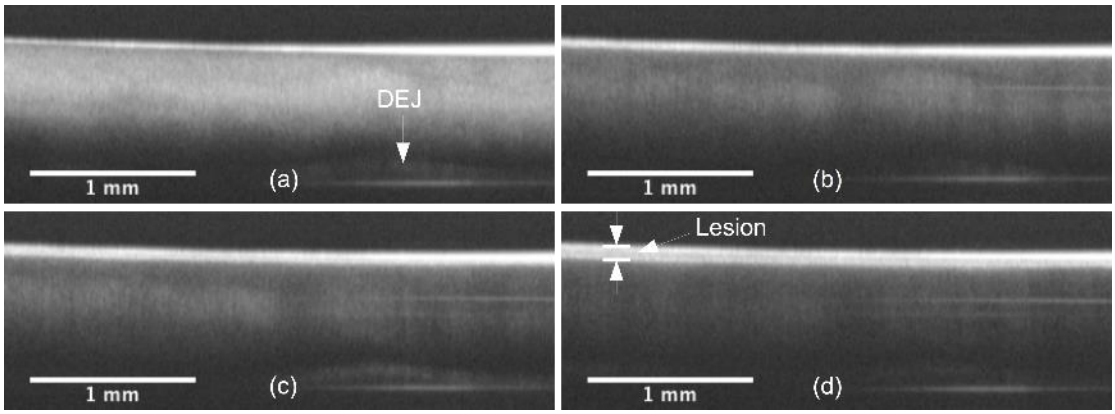

Figure 51 Registered OCT B-Scans of Bovine enamel, (a) hydrated prior to acid challenge and following (b) t=6 hours, (c) t=12 hours and (d) t=24 hours of continuous exposure to an acetic acid/ calcium phosphate solution at pH 4.4.

Visual assessment of the OCT B-Scans was necessarily subjective. However, the advantage of the experimental setup was that it ensured spatio-temporal registration of the images. This facilitated direct comparison of quantitative parameters measured from the OCT data. The sub-surface lesion depth was measured for each specimen. The mean sub-surface lesion depths were compared for each model by plotting their

change throughout the acid challenge, Figure 52a-c, where the error bars represent the standard error of the mean calculated across the 4 specimens in each group. The citric acid model (Figure 52a) yielded a maximum sub-surface lesion depth of 76±4 µm compared with 177±8 µm and 100±4 µm for the acetic (Figure 52b) and caries-like (Figure 52c) models respectively. For all of the models the lesion depth appears approximately logarithmic. However, the citric and acetic acid models exhibit a two stage behaviour in the lesion depth formation. This can be seen in Figure 52a (citric) at t=10 hours and Figure 52b (acetic) at t=24 hours. The lesion depth appears to plateau followed by an instantaneous increase in the growth rate. A similar phenomenon is not clearly evident in Figure 52c for the caries-like model, for which the lesion depth growth rate appears to be linear for t>6 hours. However, there is arguably a subtle increase in the lesion growth rate around 36 hours.

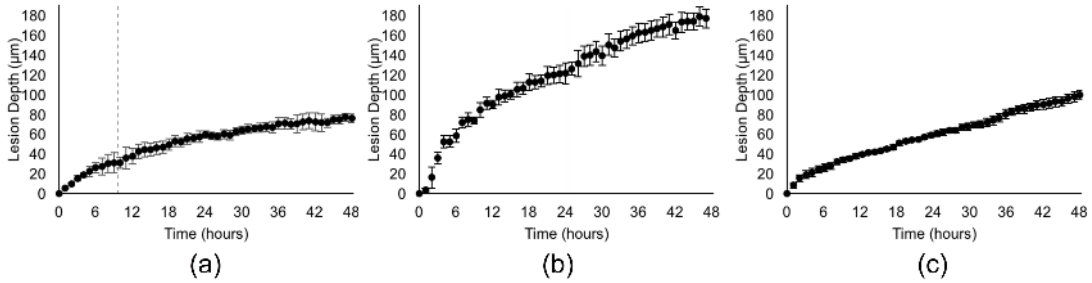

Figure 52 Sub-surface lesion depth measured from mean OCT B-Scans for three different models. (a) Citric acid solution at pH 3.8, (b) Acetic acid solution at pH 4.0 and (c) acetic acid solution containing calcium chloride and potassium phosphate buffered to pH 4.4. The vertical line indicates a discontinuous change in the lesion depth gradient.

The citric and acetic acid solutions are necessarily erosive, albeit with a different pH and ionic composition. Thus, Figure 52 contains only part of the information with regard to lesion depth. The total lesion depth includes the depth of enamel lost from the surface, shown visually in Figure 49d. The sum of surface enamel loss and the sub-surface lesion depth is shown in Figure 53 for all three models at t=24 hours, with error bars representing the standard deviation of the total.

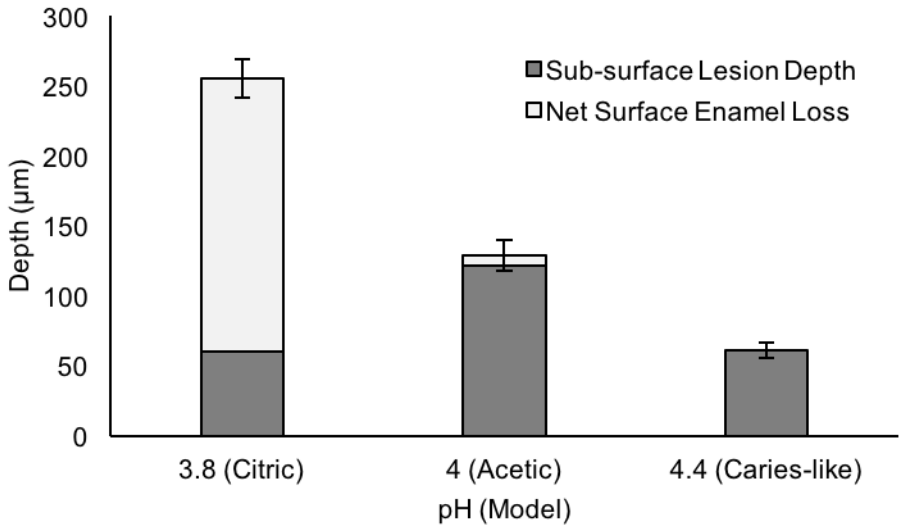

Figure 53 Total lesion depth after 24 hours of continuous acid challenge, representing the sum of the sub-surface lesion depth (dark grey) and the depth of surface enamel loss (light grey). The error bar represents the standard error of the mean for total lesion depth.

The citric acid and caries-like models show statistically similar sub-surface lesion depth measurements (t-test, $p>0.05$). However, the citric model is dominated by surface erosion which is absent from the latter due to the addition of calcium chloride and potassium phosphate to the demineralising solution which served to maintain the enamel surface. The acetic acid model produced a deeper sub-surface lesion, with a relatively small amount of surface erosion. These different lesion characteristics also manifested in terms of the lesion scattering properties, shown in Figure 54a-c. The peak scattering coefficient values are in the range 24±2 to 35±3 mm^{-1}, consistent with values obtained by light transmission measurements (Chan et al., 2014). However, attenuation values were observed to initially increase to these maxima, followed by a decrease to approximately between 0 and 5 mm^{-1}. The acetic acid model Figure 54b shows a drop in the attenuation coefficient to -7±3 mm^{-1}, indicating an axially increasing OCT signal intensity.

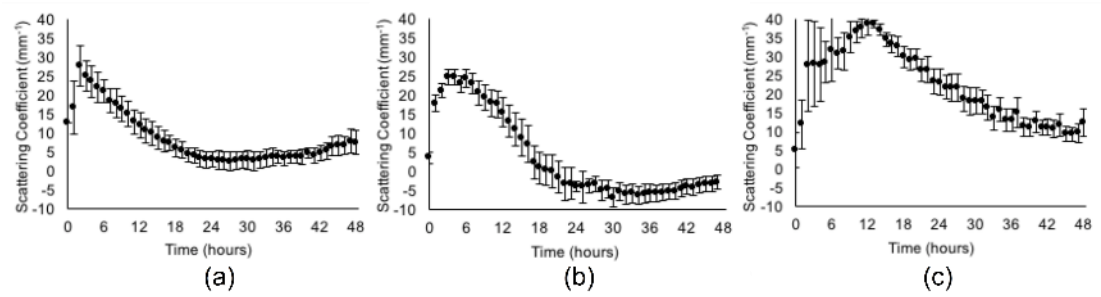

Figure 54 Scattering coefficient, estimated from mean OCT A-Scans for three different models. (a) Citric acid solution at pH 3.8, (b) Acetic acid solution at pH 4.0 and (c) acetic acid solution containing calcium chloride and potassium phosphate buffered to pH 4.4.

Nevertheless, the post-maximum attenuation curves are visually similar between the models, with a few distinct differences. Each of the models produced attenuation curves with different vertical offsets, i.e. citric acid resulted in a range of attenuation values from 2±2 to 27±4 mm^{-1}, acetic a range of -7±3 to 24±2 and the caries-like model a range of 5±5 to 38±1. Similarly, the curves for the different models appear to also be offset in time. Figure 54a appears to be shifted left with respect to Figure 54b and Figure 54c shifted right by approximately 6 hours. The different models also appear to be scaled differently along the time axis.

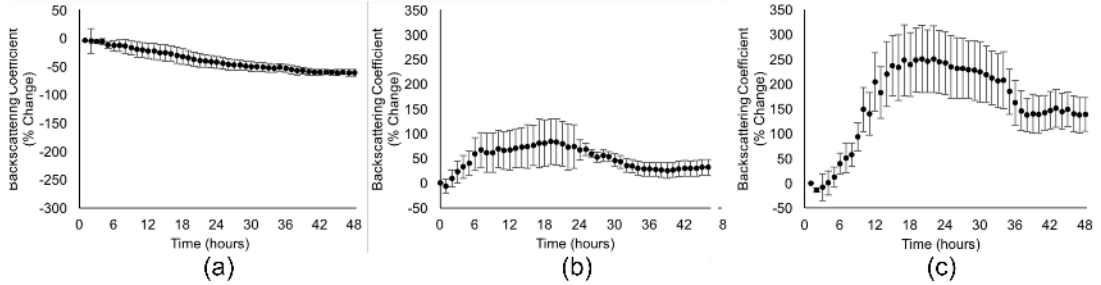

Figure 55 Percentage change in the backscattering coefficient (□B), estimated from mean OCT A-Scans for three different models. (a) Citric acid solution at pH 3.8, (b) Acetic acid solution at pH 4.0 and (c) acetic acid solution containing calcium chloride and potassium phosphate buffered to pH 4.4.

The backscattering coefficient, however, exhibited distinctly different behaviour between the citric model and both acetic acid based models. The citric acid model (Figure 55a) yielded a continuous backscattering coefficient decrease of 61±5% at 48 hours. However, both the acetic (Figure 55b) and caries-like (Figure 55c) models show an initial increase (83±40% and 248±65% respectively) in the backscattering

coefficient followed by a decrease. Notably, after 48 hours of acid challenge the acetic and caries-like models result in a net backscattering coefficient increase of and 31±16% 139±34% respectively.

9.5 Discussion

This work has investigated the temporal dynamics of three bovine enamel demineralisation models using an automated 4D OCT system integrated with a multi-specimen flow cell. This configuration maintained the spatial registration of the OCT image volumes facilitating analysis on the same tissue regions at each acquisition. Furthermore, the specimens were not handled or moved throughout the experiment, thus removing this previously reported source of uncertainty.

Figure 52, Figure 54and Figure 55 all demonstrate that lesion properties vary with time and support the finding that the different models produce detectable differences within the OCT data. The sub-surface lesion depth dynamics are distinct between all models. The citric and caries-like lesions showed statistically similar lesion depths at 24 hours. However, when plotted with time (Figure 52) the lesion progression followed a visually different shape. All models produced a sub-surface lesion. However, in the citric and acetic models the depth to which this extended plateaued. This is consistent with the net removal of surface enamel (Figure 53), which ultimately limited the sub-surface lesion depth. This limit to sub-surface lesion depth is expected because during its formation, the surface also underwent continuous dissolution. Similar rate limiting behaviour has previously been observed in a microradiographic study (Anderson et al., 1998). Furthermore, the same study also reported a secondary increase in the demineralisation rate at 24 hours for a similar pH 4.0 acetic acid models to that used in this work. This coincides with the discontinuous rate of lesion depth formation observed by OCT in Figure 52a and Figure 52b, although the exact reason for this behaviour is yet to be elucidated. In their work, Anderson *et al* attributed it to formation of a surface layer overlying sub-surface demineralisation. This might be supported by the OCT backscattering coefficient measurements in Figure 55b, which indicates a maximum backscatter that occurs shortly before the change in lesion depth rate. A similar change is evident in Figure 55c, which could support a lesion rate change close to 36 hours. However, there is no corresponding backscattering change in Figure 55a. This is possibly due to the rapid formation of such a surface layer

(Margolis et al., 1999). Physically, the backscattering coefficient is associated with the anisotropy *g*. Therefore, an increase in backscattering at the surface is consistent with formation of a surface layer having different microstructure to the underlying lesion. Such a difference was discerned from the B-Scan shown in Figure 50d, where a layer of lower intensity was observed between higher intensity backscatter from the surface and base of the lesion.

Ignoring differences in ionic composition, the lesion depth results indicates that increasing the pH allowed formation of a deeper sub-surface lesion whilst minimising the loss of surface enamel. It was expected (Margolis et al., 1999) that the addition of calcium and phosphate to the demineralisation solution resulted in more caries-like lesion formation, maintaining an in-tact surface. Figure 51 appears to support this, showing little or no change to the surface reflection. However, in this work, the caries-like forming solution has the highest pH at 4.4. The pH scale is logarithmic with respect to hydrogen ion concentration, resulting in a 60% reduction in the caries-like solution compared to the acetic model. Therefore, the results cannot dismiss the possibility that the appearance of an in-tact surface is a consequence of a slower dissolution of surface enamel. Nevertheless, surface changes were not detected in the OCT data for the caries-like model, with the formation of a sub-surface lesion extending 100±4 μm axially after 48 hours of acid challenge. Critically, the lesion depth dynamics differed between each model.

Similarly, the attenuation coefficient measurements produced discernible differences in the dynamics of each lesion type, Figure 54. Visually, there is an arguable time offset between the three models. This makes sense, considering the dissolution rate dependence upon pH (Theuns et al., 1984). Physically, assuming $\mu_{\mathrm{cal}} \ll \mu_{\mathrm{OCT}}$, the change in attenuation coefficient can be attributed to an increase in the mean distance between scattering centres due to the partial dissolution of enamel. As enamel is lost from the prismatic structure, the probability of light interacting with the mineral decreases, thus reducing optical attenuation (the mean distance between scattering events increases). However, within the lesion, the intensity of the backscattered light increases because the corresponding changes in the enamel structure modify the scattering phase function to increase the degree of backscattered light. The initial increase in attenuation coefficient seen in Figure 54b-c may be due to early lesion formation occurring over a distance that is smaller than the axial PSF width.

Consequently, the measurements include both a contribution from the surface changes and from sound enamel. The surface backscatter initially increases, causing the sound enamel to appear less intense in the images. Thus, the apparent attenuation constant increases. However, once the superficial lesion is established, the lesion depth is sufficient that the attenuation slope is measured entirely within the lesion. At this point the attenuation decreases until a minimum is reached. Interestingly, after this the attenuation increases again slowly in Figure 54b. This may be because of the heterogeneity of the lesion structure, evident from the varied backscattering intensity in the OCT B-Scans.

Critically, the OCT based measurements distinguish between the different models. However, the absolute attenuation coefficient values should be interpreted with some caution. The attenuation coefficient estimation is necessarily based upon measurements over a finite depth of the sample. The minimum sampling depth is limited by the width of the axial point-spread function (PSF), which convolves with the optical backscattering intensity. The PSF of the instrument in this study is nominally 8 μm wide. Thus, the PSF inevitably influences attenuation measurements. The relative effects of this have been mitigated in this study by adopting the same measurement and analysis protocol for each set of specimens, thus facilitating direct comparison between the models. However, this methodology has not been validated for comparison with other studies, where the region of interest selection criteria could influence the absolute attenuation values.

Nevertheless, the results in this study are of substantial importance. They demonstrate that OCT can be used to detect the different optical signatures associated with different demineralisation models and track their dynamics. Further study of alternative models with different physiological significance could provide baseline measurements to which clinical OCT data could be compared and physically interpreted.

10 Longitudinal Correlation of 4D OCT to Detect Early Stage Erosion in Bovine Enamel

Presented at the 94th General Session & Exhibition of the IADR

SEOUL, Republic of Korea 22-25 June 2016

10.1 Introduction

The loss of dental hard tissue is multifactorial, contributed to by abrasion between teeth and other materials, attrition and acid erosion. Dental erosion can be defined as an irreversible loss of dental hard tissue due to a chemical process and without bacterial involvement (Zipkin and McClure, 1949).

However, during the early stages of erosion the tooth surface undergoes a superficial partial dissolution of mineral (Arends and Ten Cate, 1981) leaving a partially intact, but softened layer of enamel. The thickness of the softened layer is estimated to be 2-5 μm (Attin et al., 1999, Eisenburger et al., 2000). Detection of erosion at this stage is critical because remineralisation of the softened region is possible, the remaining enamel structure serving as a scaffold for new mineral. Prolongation of the challenge may result in further dissolution, ultimately leading to tissue loss (Addy and Shellis, 2006). The loss of enamel volume is characterized by a persistent softened layer at the surface of the remaining tissue (Hara and Zero, 2008, Cheng et al., 2009b).

One of the major causes of erosion is the consumption of acidic drinks and researchers are keen to quantify the amount of erosion that various beverages may cause (Barbour and Rees, 2004). Quantification of erosion is necessary to provide further insight into the chemical process of erosion, and ways in which erosion can be modified, reduced or prevented.

The gold standard for the measurement of early stage surface softening (ESS) is micro-hardness testing (Schlueter et al., 2011). However, this is typically an *in vitro* technique, reliant upon physical indentation of the specimen. Therefore, various techniques have been proposed for detecting, imaging, monitoring and quantifying dental hard tissue mineralisation dynamics, both *in vitro* and *in vivo* (Elton et al., 2009). Among these techniques, Optical Coherence Tomography (OCT) has been explored for caries detection (Baumgartner et al., 1999, Colston et al., 1998, Everett et al., 1999) and to a lesser extent for erosion measurement (Wilder-Smith et al., 2005, Chew et al., 2014). Notably, ESS has not been widely studied using OCT.

Predominantly, studies have employed two-dimensional OCT B-Scan images to directly monitor lesion formation. For example, *in vivo*, 15.3 μm of erosion was measured over a 3 week period in patients having Gastroesophageal Reflux Disease (GERD) (Wilder-Smith et al., 2009). Enamel thickness was estimated from OCT B-

Scans by measuring the distance from the enamel surface to the enamel dentine junction (DEJ). Similarly, enamel thickness was monitored *in vitro* with OCT (Chan et al., 2013) as a measure of erosive progression. However, the authors reported many challenges in accurately measuring the remaining enamel thickness. They found that if erosion is accompanied by subsurface demineralisation or surface roughness, the strong increase in scattering limits the ability to resolve the DEJ. A well hydrated surface can somewhat mitigate against this by providing a degree of refractive index matching. However, prior to the net loss of enamel, measurement of ESS remains a challenge for OCT. Detection of ESS using OCT cross-sectional B-Scan images is difficult because intense specular reflections from the enamel surface mask information about scattering within the first few micrometres below the tooth surface (Fried et al., 2002). Nevertheless, some progress has been made by measuring changes in the intensity of the backscattered OCT signal, leading to the detection of erosive lesion formation after 10 minutes of continuous acid challenge at pH 3.8 (Chew et al., 2014). However, further development is needed to validate OCT methodologies for monitoring ESS and understanding both experimental repeatability and reproducibility.

OCT is promising because it provides real-time imaging and does not require specimen processing. Moreover, OCT could be developed into a technique for the *in vivo* characterisation of erosive lesions that is both non-ionising and minimally invasive (Huysmans et al., 2011). With OCT, an entire area of the specimen can be measured non-destructively. This is advantageous because it allows for more accurate averaging over specimen heterogeneity compared to measuring a few discrete indentations as with micro-hardness. Furthermore, OCT can re-measure the same area longitudinally. This is not possible with destructive techniques.

Typically, techniques for *in vitro* longitudinal erosion measurement require specimens to be removed from the acidic solution and dehydrated prior to measurement. Such an approach may disrupt the softened region (Shellis and Addy, 2014) and introduce variations in sample hydration (Nazari et al., 2013) that contribute to experimental uncertainty. Repositioning accuracy has previously been addressed by placing control markings to aid realignment of successive measurements (Chew et al., 2014). Nevertheless, manual repositioning limits the accuracy of longitudinal measurements because successive B-Scans are not guaranteed to be spatially co-registered. This can

be a significant limitation where only single B-Scans are acquired for analysis at each time-point (Chew et al., 2014, Chan et al., 2013) and becomes increasingly important for detecting small changes such as in ESS (Attin, 2006). Therefore, a new approach is needed. The design of the present study aimed to avoid specimen movement and drying thus mitigating against the consequent uncertainties. In doing so then the primary aim of this study was to use a novel 4D OCT system to determine whether it could detect ESS and, if so, whether a statistical relationship with a gold standard technique i.e. hardness measurements could be established.

10.2 Theory

Erosion is predominantly a surface effect, with ESS resulting in microscopic changes to surface structure, composition and mineral density. Three-dimensional OCT datasets contain surface information, which can be visualized in the *en face* plane as opposed to the cross-sectional B-Scan view typical of previous studies. Consequently, under acidic challenge, the optical scattering properties of an enamel surface are expected to change. In OCT, changes to the distribution of optical scatterers can lead to two dominant effects i.e. a change in the scattering phase function and an altered speckle pattern.

The scattering phase function provides a measure of the angular dependence of the intensity of scattered light. Thus, changes to it necessarily affect both the intensity of light coupled from the surface into the OCT detection optics and the intensity of light that scatters forward. Consequently, surface changes are expected to yield a change in the intensity of sub-surface light coupled back into the OCT system. Assuming that a polished specular surface has optimal transmission characteristics, then disruption to this through ESS might be expected to decrease the sub-surface OCT signal, i.e. making OCT B-Scan images appear less bright. Therefore, integrating the OCT signal over the full depth to which light penetrates into the specimen would enhance detection sensitivity to small surface changes. Such a projection of the sample can be formed by integrating the OCT linear intensity volume $I(x,y,z)$ over the axial range z_1 to z_2 corresponding with the OCT penetration depth. Mathematically this is expressed as Equation 10.1

$$P(x,y) = \int_{z_1}^{z_2} I(x,y,z)\mathrm{d}z \qquad \text{Equation 10.1}$$

where *x* and *y* represent orthogonal lateral dimensions of the *en face* view and *z* the axial direction into the sample.

Speckle is the visual manifestation of coherent interference between light scattered from closely spaced scattering centres. These effects have previously been exploited in optical coherence elastography (OCE) whereby an applied stress displaces scatterers and consequently modifies the speckle pattern (Kennedy et al., 2014). Furthermore, optical coherence angiography (OCA) is used to image microvasculature (Zhang et al., 2015). Intensity based OCA relies upon changes to the speckle pattern in blood vessels with respect to the surrounding tissue resulting from moving scatterers in the form of red blood cells. Although a number of methods exist for parameterizing speckle and intensity changes, one attractive method is the measurement of statistical correlation (Enfield et al., 2011) because its magnitude is always scaled between 0 and 1.

Specifically, Pearson's product moment correlation coefficient, *r*, is a measure of the linear relationship between two variables, for example $P_0(x,y)$ and $P_t(x,y)$, representing two projection intensities located at *x* and *y* obtained at times 0 and *t* seconds. In this case, the correlation coefficient can be calculated from Equation 10.2 as,

$$r(t) = \frac{\sum_x \sum_y (P_0(x,y) - \overline{P_0})(P_t(x,y) - \overline{P_t})}{\sqrt{\sum_x \sum_y (P_0(x,y) - \overline{P_0})^2 \sum_x \sum_y (P_0(x,y) - \overline{P_0})^2}} \qquad \text{Equation 10.2}$$

where the horizontal bar represents the mean of the quantity beneath it. Then, *r*, is a measure of the strength and direction of the linear relationship between intensities in the two images. OCT images are discretely sampled in *x*, *y* and *z*. Therefore, the projection images comprise discrete pixels. An example is shown in Figure 56a and Figure 56b corresponding to $P_0(x,y)$ and $P_{t=5}(x,y)$. The relationship between pixel intensity values at t=0 minutes and t=5 minutes are shown in the scatter plot, Figure 56c, where the intensity of corresponding pixels is plotted with those from the t=0 minutes image on the horizontal axis and those from the t=5 minutes image on the vertical axis. Visually, image Figure 56b is darker than Figure 56a and higher pixel intensities from $P_0(x,y)$ tend to correspond with higher pixel intensities from $P_{t=5}(x,y)$, although there is some variation from this. Quantitatively, this tendency is quantified by the correlation coefficient, which Figure 56c has been labelled as r=0.77.

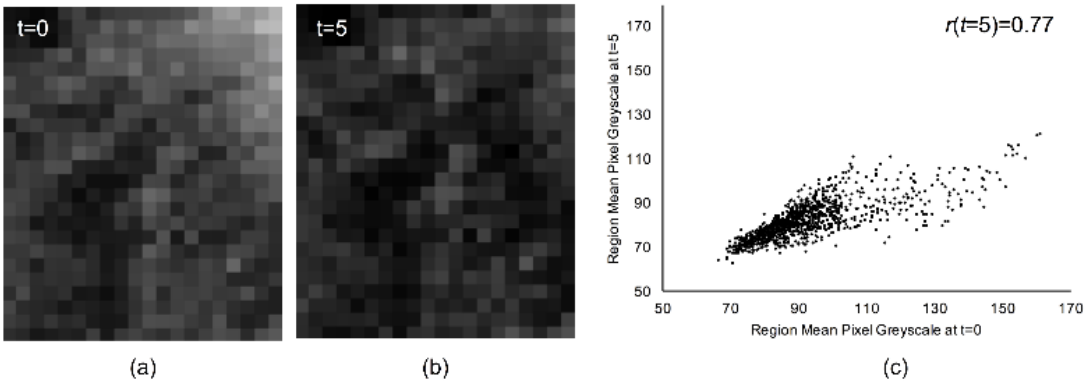

Figure 56 Example of spatially registered projection images at time intervals of (a) t=0 minutes and (b) t=5 minutes expanded to show individual pixels. (c) The intensity of spatially corresponding pixels, plotted such that intensities from t=0 are along the horizontal axis and intensities from t=0 are on the vertical axis.

Therefore, this conveys that whilst the image intensity in Figure 56b appears to have reduced from Figure 56a, the way that the pixel intensities vary is linearly related (r=0.77), although not perfectly (r=1.00). Therefore, correlation is a linear measure of the linear relationship of pixel intensities in two difference images. A correlation coefficient of r=0.00 would indicate no linear relationship.

From Figure 56c, the highest pixel intensity value at t=0 is approximately 160, compared to 120 at *t*=5 minutes. Thus, intensities at *t*=5 minutes can be estimated to be nominally 0.75 (75%) of those at *t*=0 minutes. More objectively, this can be evaluated by finding a straight line the best describes the relationship between intensities at *t*=0 and *t*=5 minutes. The equation for such a straight line is given in Equation 10.3, where the line is constrained to pass through the origin.

$$P_t(i) = bP_0(i) \qquad \text{Equation 10.3}$$

In Equation 10.3, *i* is an index variable enumerated over all pixels in each image. The slope *b* can be estimated by minimising the squared difference between the straight line and measured intensities, Equation 10.4.

$$b(t) = \frac{\sum_x \sum_y P_0(x,y) P_t(x,y)}{\sum_x \sum_y P_0(x,y)^2} \qquad \text{Equation 10.4}$$

Thus, the linear regression slope *b* provides a measure of the fractional intensity change. The correlation coefficient *r* provides a measure of association between the

pixel intensities in two spatially registered by temporally offset images, essentially how well the intensities from the two images sit on the linear regression slope.

10.3 Materials & Methods

10.3.1 Sample Preparation

Sixteen bovine enamel samples from one-year-old calf incisors were sectioned into 5-10mm diameter discs, sliced and polished in the coronal plane to a thickness of 3 mm such that they comprised both dentine and enamel. The samples were then embedded into a 25mm diameter clear resin substrate as described in chapter 6.1. The specimen surfaces were painted with a thin layer of acid-resistant varnish in the form of nail polish, Revlon (570, New York, USA) to prevent erosion except on a 3x3 mm region. The samples were divided into two batches. The first batch of samples (n=8) was used for micro-hardness measurements. The second batch of samples (n=8) were imaged using OCT. Batching of the specimens into OCT and micro-hardness groups enabled the OCT measurements to be conducted without either specimen movement or drying, exploiting its non-invasive advantage. Micro-hardness measurements necessarily required specimen handling between each measurement.

10.3.2 Acidic Challenge

Artificial erosive lesions were induced by exposing the enamel specimens to an acidic solution of 1% citric acid at pH 3.8 (Sigma Aldrich, UK) as described in chapter 6.2. The solution was stored at 25°C for a period of 2 hours prior to use. A custom multiple specimen holder was used for this study. This comprised 6 isolated flow-cell chambers into which individual specimen were placed Figure 15. The bovine samples were hydrated prior to exposure to the erosive agent. After the 24-hour hydration period, the samples were placed in isolated compartments within the sample holder, so that the OCT probe beam was orientated orthogonal to the enamel surface. The specimen holder was mounted vertically such that the enamel surface was perpendicular to the bench.

The citric acid solution was continuously pumped (323Du/D, Watson Marlow, UK) into each chamber of the holder drawing fresh solution from a 1 L reservoir and ejecting used solution into a separate container. Filling of the sample compartments with 0.8 mL solution took less than 10 seconds.

10.3.3 OCT System Specification and Configuration

The custom built OCT system was used for this study. The instrument incorporates a fibre optic Michelson (Rollins and Izatt, 1999) interferometer design utilising a super-luminescent light emitting diode (SLD) optical source (SLD1325, Thorlabs, Ltd, Cambridge, UK), operating with a nominal central wavelength of 1325 nm and bandwidth of approximately 100 nm. Further specification are described in chapter 6.6.

The light was focused approximately 100 µm beneath the sample surface by a scan lens (LSM03, Thorlabs, Ltd, Cambridge, UK). Interference fringes were detected at A-Scan rate of 50 KHz. The system acquired, processed and displayed 3D OCT data in real-time using a General Purpose Graphics Processing Unit (NVIDIA C2070). Three-dimensional OCT volumes were acquired as a series of 500 B-Scan images, each comprising 500 A-Scans, of length 512 pixels. Physically, the lateral pixel spacing between B-Scans and A-Scans was 6.9 µm and the axial pixel spacing was measured to be 9.5 µm in air. The group refractive index of sound enamel is approximately 1.65 (Hariri et al., 2012a), yielding an approximate axial pixel spacing of 5.7 µm within the sample. The system point-spread function and geometric scaling were measured using the method and phantoms described previously (Tomlins et al., 2008, Fouad et al., 2014, Woolliams and Tomlins, 2011b).

The OCT system was configured to automatically measure multiple specimens by mounting the OCT imaging probe onto a motorized linear translation stage (LTS300, Thorlabs, Ltd, Cambridge, UK). The experimental configuration is shown in Figure 57.

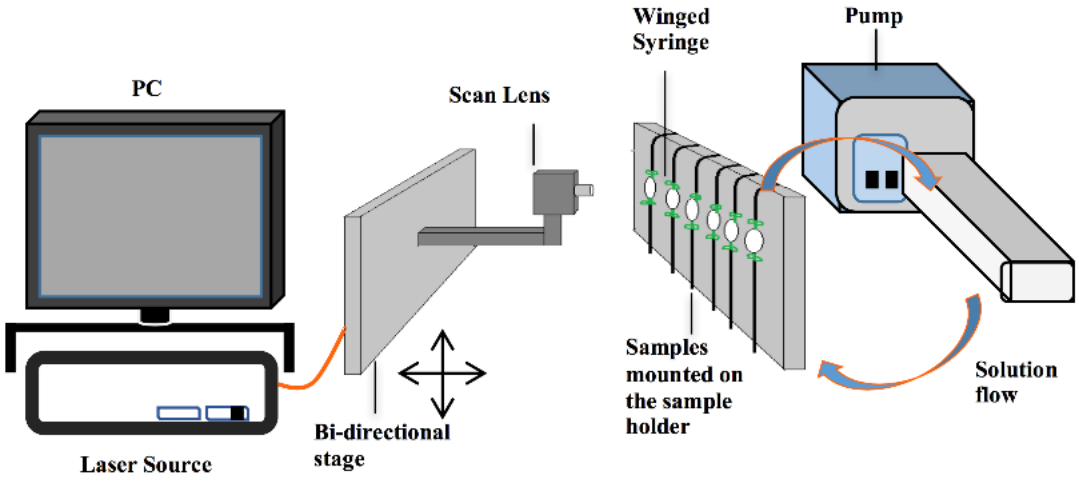

Figure 57 Experimental setup used to capture OCT images during the development of early stage surface softening in bovine enamel. The OCT probe was mounted on a linear translation stage to enable imaging of multiple specimens. The specimens were mounted vertically in a flow-cell through which acidic solution was pumped.

10.3.4 OCT Measurement Protocol

Prior to introducing the acid challenge, the OCT imaging system was aligned such that the top of each specimen was 50 pixels from the top of each B-Scan and the *en face* field of view was adjusted to ensure that a section of the varnished surface was included in each volume as a reference zone. This alignment procedure required that the specimen chambers were filled with deionised water to facilitate the acquisition of initial baseline OCT volume data for each sample. Following alignment, the deionised water was drained from specimen chambers leaving the alignment intact.

Three-dimensional OCT image volumes were acquired from each sample over a square surface area measuring 3x3 mm corresponding to the unvarnished window. To ensure acquisition of images of the first few minutes of erosion, the system was set to acquire the first 20 volumes into computer memory. Acquisition of a single OCT volume and translation between specimens took no more than 20 seconds, enabling OCT image volumes of three different specimens to be imaged at up to once per minute. Once this buffer was full, the subsequent volume imaging rate was limited to 22 OCT volumes over a 2 hour period. This procedure ensured that all specimens had been imaged twice within the first 2 minutes of the acid challenge.

OCT specimens were exposed to acid challenge carried out in four separate experiments. In the first and second experiments, erosion was measured in 3 bovine

enamel specimens each time, moving the OCT measuring probe between specimens as described above. The third and fourth experiments measured single specimens eliminating the need to move the OCT probe between acquisitions.

In the first and second experiments, a scattering reference phantom was measured in its own specimen chamber. The reference phantom comprised a suspensions of Titanium Dioxide powder embedded within a polyurethane matrix with a mass ratio of 6.11 mg g^{-1}, resulting in a scattering coefficient of 3.5 mm^{-1}(Woolliams and Tomlins, 2011a). This was measured automatically before each cycle of specimen measurements, providing a constant baseline for reference. This was preferable as opposed to measuring a control enamel specimen that would be expected to undergo some partial demineralisation in the de-ionised water due to it being under-saturated with respect to hydroxyapatite.

10.3.5 OCT Data Processing & Correlation Analysis

Integrated *en face* projections were generated from each 3D OCT dataset by selecting all C-Scans from the surface to a depth of approximately 500 μm and summing the pixel intensities together to give a single composite image. The depth of 500 μm corresponds with the Rayleigh range of the OCT objective and was chosen to ensure that the ESS region was always within the axial range contributing the highest OCT signal. Furthermore, it was observed that the sections of the bovine enamel were nominally 500 μm thick.

Assuming the *en-face* surface view (C-Scan) to be in the *x,y* plane and the orthogonal axial direction to be in *z*, then the projected image $P(t,x,y)$ acquired at time *t* is given by Equation 10.5.

$$P(t,x,y) = \sum_{z=z_{\text{surface}}}^{500\ \mu\text{m}} I(t,x,y,z) \qquad \text{Equation 10.5}$$

where $I(t,x,y,z)$ represents the volumetric OCT data. Notably, the OCT volumes used in this study were linearly scaled intensities. Thus, these are not the same as post-processed OCT volumes that are typically comprised from a stack of logarithmically scaled B-Scan images.

From the projection image, a region of interest (ROI), measuring (0.65x0.90 mm) was manually selected for each sample to avoid the varnished sections of enamel and

intense Fresnel reflections that saturated the OCT spectrometer. To mitigate against small movements between measurements, the ROI was sub-sampled on a grid of 10x10 pixel regions, replacing the pixel intensities by the mean for that region. This is shown schematically in Figure 58.

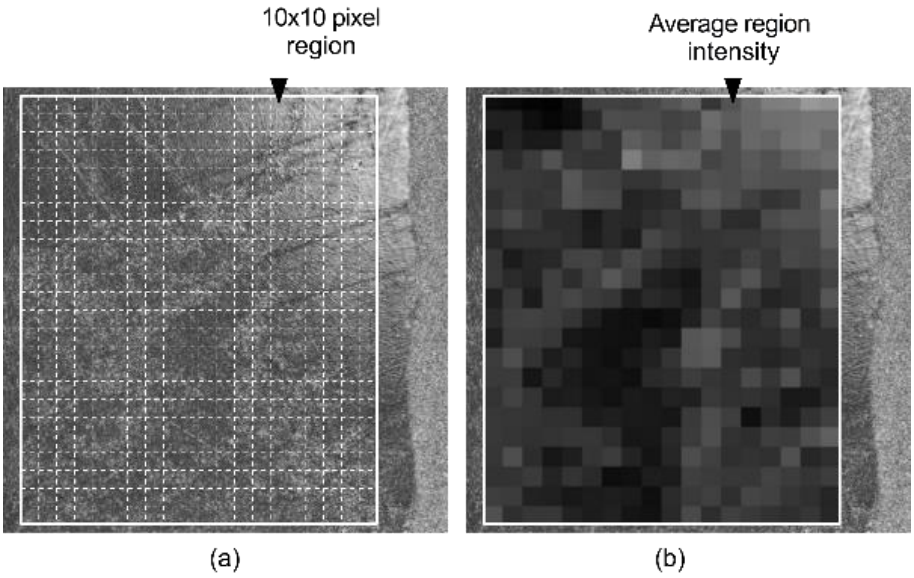

Figure 58 Sub-sampling of an OCT surface projection image. (a) The original projection image overlaid by a region of interest (ROI) comprising a grid of 10x10 pixel regions. (b) Each 10x10 pixel region replaced by its corresponding mean pixel intensity.

Thus, the correlation *r* and regression slope *b* were calculated using the mean region intensities rather than individual pixels. ROI selection and cropping was carried out using ImageJ (Schneider et al., 2012) and calculation of the correlation value and regression slope was achieved using the CorrelationJ plugin (Chinga and Syverud, 2007) and MATLAB.

10.3.6 Surface Microhardness Measurement Protocol

A Vickers micro-indenter (HMV Microhardness Tester, Shimadzu, Japan) was used to measure the enamel surface hardness. Prior to acid challenge, a control region of the enamel surface from each specimen was masked using nail varnish to prevent erosion.

A batch of fresh citric acid (1% w/v) at pH 3.8 was prepared and measured into 100 ml cylindrical glass containers, one for each specimen. Each specimen was submerged in fresh solution, exposing it to an acid challenge for a pre-determined time before being removed and washed thoroughly with de-ionized water. Specimens were left to

dry for 5 minutes at room temperature prior to hardness measurement. Hardness measurements were made following cumulative acid challenge durations of 5, 10, 15, 30, 45 and 60 minutes. The solution was refreshed for each cycle of erosion.

Once dry, the enamel block surface was placed flat on the translation stage, perpendicular to the indenter direction of load. A central area of approximately 1 mm × 1 mm was identified for hardness testing. Indentations were made with a load of 200 g applied for 10 s. The mean of six separate indentations, approximately 100 μm apart, was calculated for each sample. Vickers hardness numbers were calculated for each indentation and averaged for each specimen and time-point.

10.4 Results

Centre B-Scans from each of the measured specimens are shown in Figure 59a-h at time-points *t*=0, 1, 2, 5, 10, 30 and 120 minutes of continuous acid challenge. The B-Scans represent cross-sections of the bovine enamel discs, showing the surface, bulk enamel and nail varnish used to mask regions of enamel from the acid challenge. In addition, DEJ is visible in specimens a)-g). In image Figure 59h, there is a distinct intensity change approximately halfway along the axial dimension. It is possible that this represents the DEJ, however the appearance is not consistent with specimens a)-g). The time sequence images are acquired at exactly the same location within each specimen, thus images from different times can be directly compared. Despite steps taken to normalise the specimens, each has a distinct morphological appearance when imaged by the OCT instrument. In particular there is a variation in the intensity of the images. Nevertheless, some visual consistencies are observed. Firstly, over the duration of the acid challenge, the B-Scan image intensity decreases. However, the B-Scan intensities are logarithmic, leading to compression of intensity variations. Over the initial 10-minute period, no visual changes to the surface are apparent in the B-Scans. Such changes become visible by 30 minutes. However, comparing the enamel surface to the nail varnish, there is no discernable axial loss of enamel.

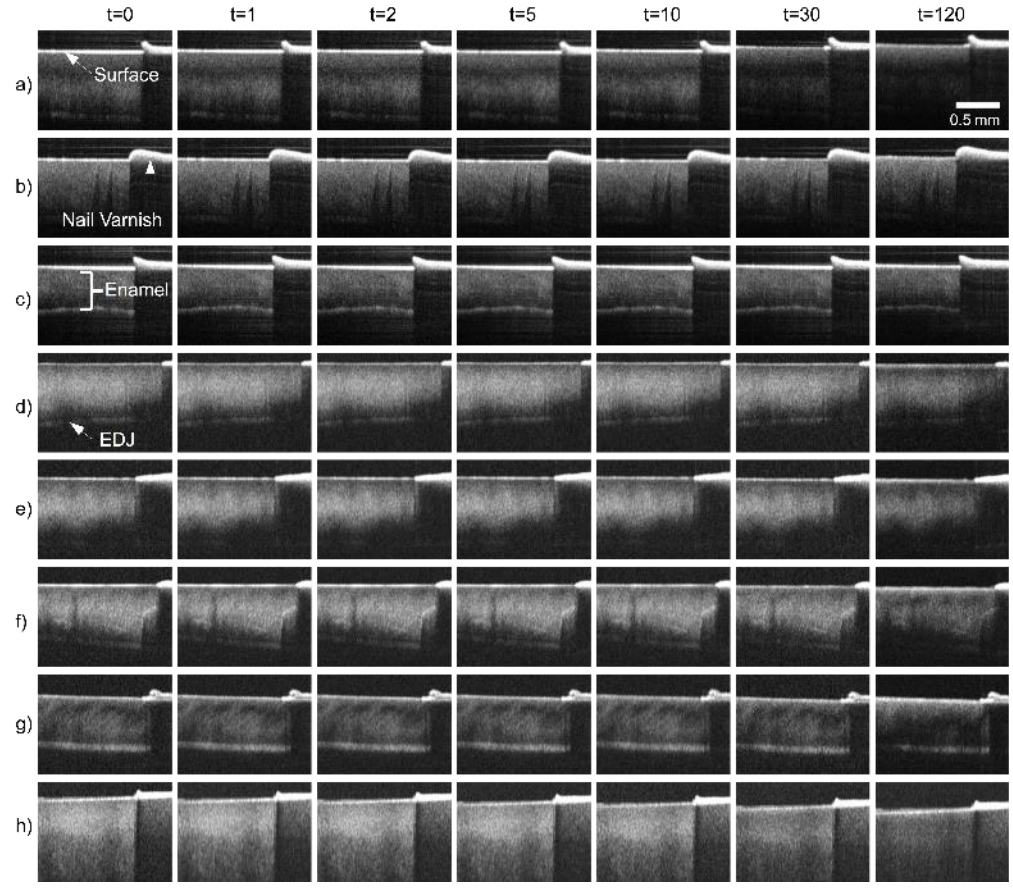

Figure 59 OCT B-Scans (logarithmic intensity) taken from the centre of each specimen at time-points, t=0, 1, 2, 5, 10, 30 and 120 minutes. Rows (a) to (c) correspond to the first experiment, (d) to (g) the second and (h) the third experiment.

The cross-sectional B-Scan view of the 3D OCT volumes is limited in its ability to convey information about ESS, which is necessarily a surface phenomenon. Therefore, projection images were computed for each specimen at all measured time-points from their corresponding 3D OCT datasets. The difference between baseline (P_0) and a subsequent projection image (P_t) acquired at time t, $P_d=P_0-P_t$, were calculated in order to facilitate visualisation of changes due to the acid challenge. Pixel region intensity scatter-plots were produced for each specimen between the baseline and subsequent images and the corresponding correlation coefficient was calculated. Results for t=0, 1, 2, 5, 10, 30 and 120 minutes are shown for specimens from the first (Figure 60), second (Figure 61) repeats of the experiment. The white dashed region in the baseline projection image at t=0 indicates the area selected for correlation analysis.

The projection images (top row) show a superposition of the linear OCT intensity signal backscattered from the specimen surface to a depth of approximately 500 µm below the surface. However, the surface signal dominates due to an approximately exponential signal attenuation axially.

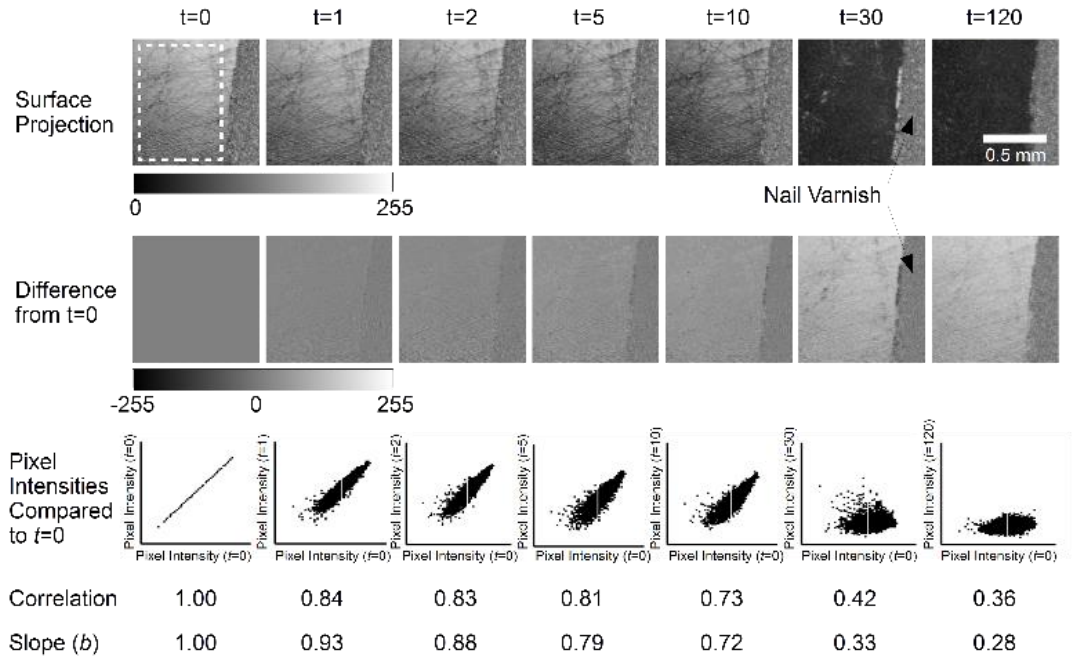

Figure 60 Results for a single specimen from the first experiment at t=0 (baseline) and subsequent time-points t=1, 2, 5, 10, 30 and 120 minutes. Surface projection images are calculated from linear intensity OCT volumes as described in the text. The difference images represent the projection image difference from baseline. The pixel intensity scatter-plots compare the mean intensity of corresponding 10x10 pixel regions in baseline and subsequent images. Correlation values are calculated from each scatter plot.

The results from the first specimen, Figure 60 show some visually subtle darkening of the projection images over the first 10 minutes of the acid challenge, which becomes pronounced after 30 minutes. By 120 minutes there is little visual difference from the projection image at 30 minutes. These changes are reflected in the difference images, which show a progressive intensity difference from baseline. The correlation between baseline and subsequent intensities dropped from r=1.00 to r=0.73 in the first 10 minutes, dropping to r=0.36 by 120 minutes. The nail varnish remained relatively unchanged throughout. The projection image shows surface scratches from the polishing process, these remain evident at 10 minutes, although they are not visible at 30 minutes. The pixel intensity slope shows that the projection image pixel regions at

10 minutes are darker by *b*=0.72 times the baseline pixel regions, i.e. its intensity is 72% that at baseline. This is visually perceivable. However, darkening at *t*=1, 2 and 5 minutes is more subtle, but detectable by pixel intensity slope values of *b*=0.93, 0.88 and 0.79 respectively.

Similarly, the second specimen, Figure 61 shows a consistent projection signal from the varnished region and a progressive intensity decrease. Surface scratches are still evident, however, they appear less prominent than in the first specimen. The temporal intensity decrease appears less than observed in the first specimen, with visual intensity changes up to *t*=10 minutes not clearly visible. Furthermore, whilst it is difficult to subjectively discern an intensity change within the first 5 minutes, objectively the slope reduces as *b*=1.00, 0.98, 0.97, 0.93, 0.89 at corresponding time-points of *t*=0, 1, 2, 5 and 10 minutes. Thus, the projection image at *t*=10 minutes is approximately 89% the intensity of the baseline image. Compared with the specimen shown in Figure 60 the projection exhibits a smaller intensity change over the 120-minute acid challenge, i.e. 71% compared to 28% of baseline intensity.

Notably, the correlation values drop from *r*=1.00 to *r*=0.71 in the initial 10 minute period of acid challenge.

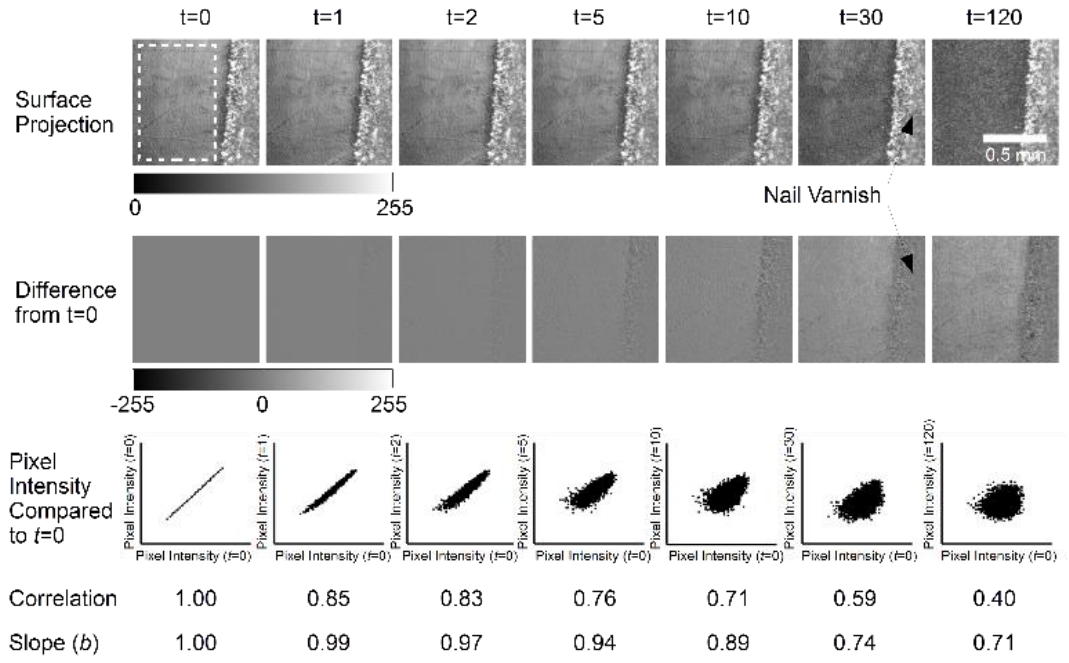

Figure 61 Results for a single specimen from the second experiment at t=0 (baseline) and subsequent time-points t=1, 2, 5, 10, 30 and 120 minutes. Surface projection images are calculated from linear intensity OCT volumes as described in the text. The difference images represent the projection image

difference from baseline. The pixel intensity scatter plots compare the mean intensity of corresponding 10x10 pixel regions in baseline and subsequent images. Correlation values are calculated from each scatter plot.

The inter-sample repeatability of the correlation and slope parameters was assessed by interpolating all of the measurements onto a 2-minute sampling interval. This was necessary because the exact timing of measurements could not be guaranteed to be the same for each sample, but the acquisition time was recorded by the control software. The mean correlation and slope values and their 95% confidence intervals were calculated and plotted in Figure 62a and Figure 62b respectively.

The mean correlation coefficient exhibits a smooth decrease from r=1.00 at baseline to r=0.40±0.05 at t=120 minutes. Similarly, the mean pixel region intensity slope decreases over time from b=1.00 at baseline to b=0.58±0.11 after 120 minutes, indicating that on average, after 120 minutes of acid challenge, the projections images darken to 58% of their original intensity. Furthermore, the linear correspondence between pixel region intensities in the images at the two time points accounts for r^2=16% of the intensity variation. However, the correlation values show three times less sample-to-sample variation, with a median variance of 0.03 compared to 0.09 for the slope measurements. Thus the correlation was a more repeatable measure.

The decreasing correlation values observed in enamel specimens throughout acid challenge were compared to results from a static polyurethane scattering phantom, measured under the same conditions. The variation in the resulting phantom correlation values is plotted as Box and Whisker Diagrams in Figure 63, comparing the range of enamel correlation values from Figure 62a. The Box plots show that the phantom correlation values range from r=1.00 to r=0.95, compared with the minimum enamel mean correlation of r=0.40.

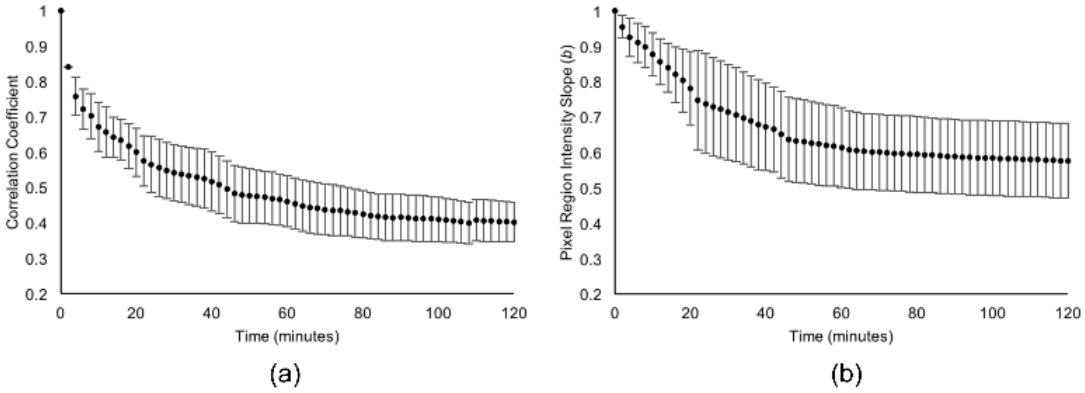

Figure 62 Mean (a) correlation coefficient and (b) image intensity slope at 2-minute intervals measured over a continuous 120 minutes erosive challenge. The mean is calculated over all 8 specimens. The error bars represent 95% confidence intervals.

Furthermore, to quantify the potential impact of axial displacement on the variation of correlation values, a disc of sound bovine enamel was incrementally displaced over an axial range of 120 µm. Zero displacement was taken to be the axial location at which the OCT imaging beam was focussed at the specimen surface. Projection images were generated and compared as described for the main experiment above. The minimum correlation value of r=0.98 was observed at the maximum axial displacement of 120 µm, more than 10 times the expected erosion depth for a 120 minute acid challenge at pH 3.8. Therefore, axial displacement is not expected to contribute to correlation changes measured during ESS formation.

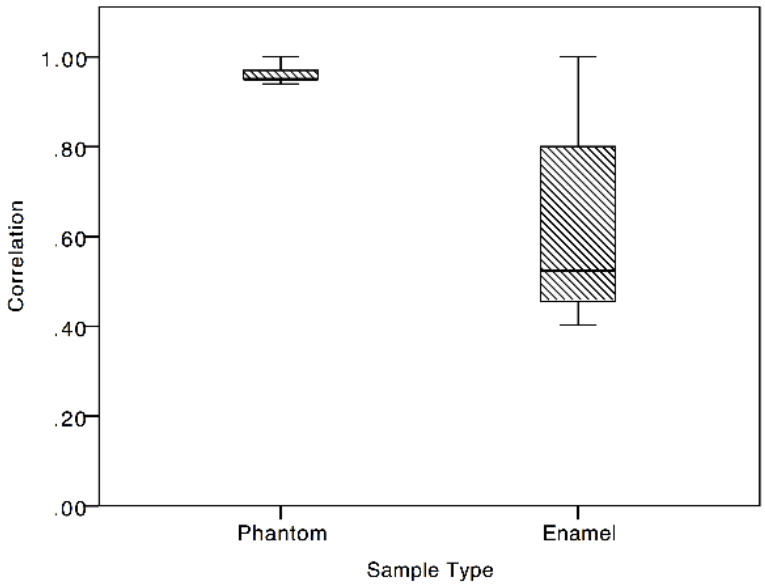

Figure 63 Comparison of the correlation range for the reference phantom and bovine enamel measured in acidic solution over a 120-minute period.

In order to assign physical meaning to the correlation and slope parameters, an independent batch of bovine enamel specimens were subjected to acid challenge and micro-hardness analysis. The mean Vickers hardness (VH) was calculated from all of the measured specimens. The results are plotted in Figure 64, with error bars representing 95% confidence intervals.

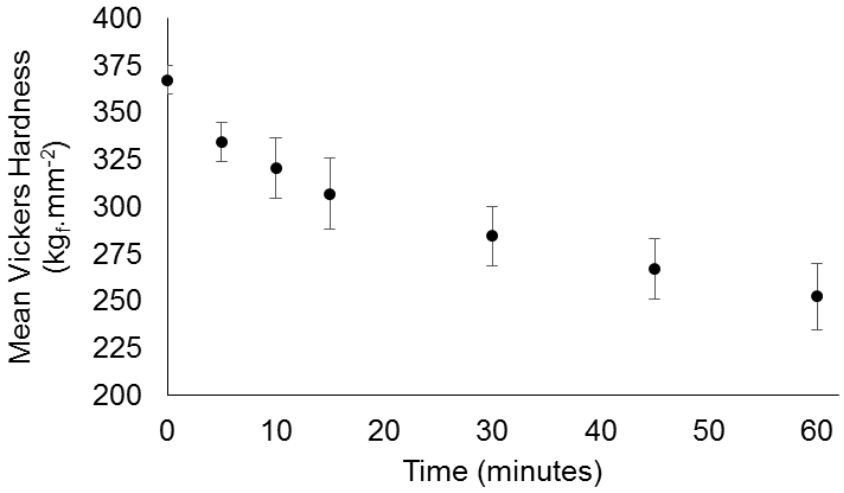

Figure 64 Mean Vickers hardness measurements acquired from a batch of 8 bovine enamel discs each subjected to a total of 1 hour acid challenge. Measurements were carried out at baseline and after 5, 10, 15, 30, 45 and 60 minutes challenge.

The mean Vickers Hardness ranged from 367.1 ± 14.1 $kg_f \cdot mm^2$ at baseline to 252.4 ± 32.8 $kg_f \cdot mm^2$ after 60 minutes of erosive challenge. The average microhardness profile, shown in Figure 64 follows a visually similar trend to that of the correlation and intensity slope curves shown in Figure 62a-b. This relationship is shown in Figure 65 by plotting the correlation coefficients (a) and slope parameter (b) from OCT as a function of measured surface hardness for the two independent batches of specimens.

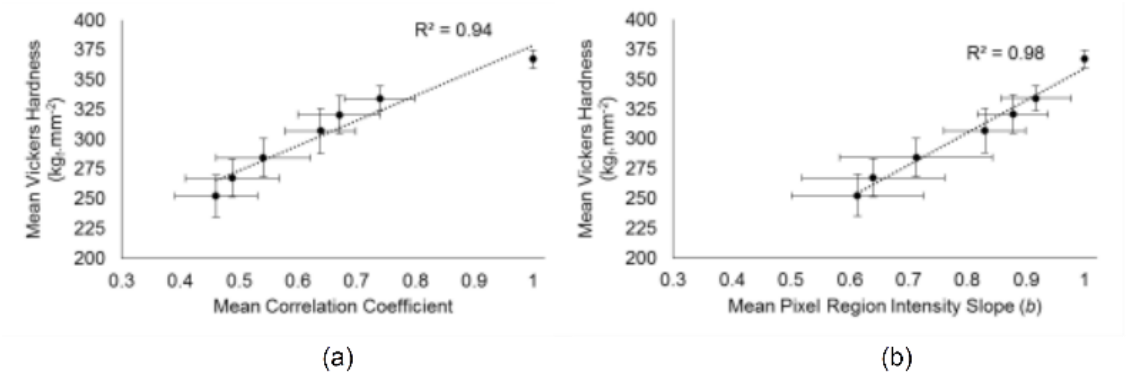

Figure 65 Mean Vickers hardness measurements for 8 bovine enamel specimens following 5, 10, 15, 30, 45 and 60 minutes of acid challenge plotted with the corresponding correlation values (a) and pixel region intensity slope values (b). Error bars represent 95% confidence intervals. A linear regression line is plotted in both.

A linear regression of surface hardness as a function of measured correlation yielded a quantitative relationship between the OCT measurements and surface hardness. The slope parameter demonstrated a higher goodness of fit with r^2=98%, compared with the correlation parameter having r^2=94%. Thus, on average, the regression lines suggest that the experimental conditions employed here, correlation values were related to the surface hardness measurements by the expression HV=209.8r+168.6. Likewise, pixel region mean intensity slope values were related to hardness by HV=269.0b+89.9.

10.5 Discussion

The set of experiments reported in this paper aimed to demonstrate an OCT based measurement and analysis protocol capable of measuring the formation of ESS erosive lesions prior to the net loss of enamel, that were not directly observable as axial change in OCT images. Following 120 minutes of continuous acid challenge (pH 3.8, citric acid) the net loss of surface enamel was approximately 10 µm, corresponding to approximately one axial pixel in the OCT image. Therefore, the net enamel loss was at the limit of what was directly measureable from images, using basic measuring techniques such as ImageJ's line tool. However, more sophisticated techniques such as surface peak fitting or phase sensitive methods could potentially detect substantially smaller changes at the nanometer scale (Wang et al., 2007). Nevertheless, such techniques are sensitive to temporal stability of the specimen and experimental setup and it remains to be shown whether they are sensitive to ESS. In this work, the

specimens were monitored by OCT under continuous acid challenge, without moving or disturbing the samples. In addition to this, three-dimensional volumetric images of the samples were acquired at each measurement. These aspects are important because they ensure that the same enamel locations were longitudinally compared, facilitating assessment of the surface.

ESS and erosive lesion development are fundamentally surface phenomena. This is highlighted by the B-Scans in Figure 59, which show no visible morphological change over time, except to the few rows of pixels corresponding to the surface. These were only visibly modified after 30 minutes of acid challenge. In addition to this, B-Scan visualisation between teeth was not consistent, varying between samples. This is likely due to inter-sample variation, an inherent issue with biological specimens. The formation of surface projection images transforms the OCT data into a more appropriate form for surface analysis. In this rendering, the projections visibly show the surface (i.e. Figure 60 and Figure 61) and the change in back-scattered intensity. Changes to OCT B-Scan intensity under demineralising conditions have been previously studied.

In this work, a new approach to intensity variations was used. The means of local pixel intensities were compared between each time-point and baseline, by regressing a straight line through the origin using Figure 58. The slope of this line describes the fractional intensity of each projection image in terms of the pixel region intensities at baseline. By formulating the data in this way, it is evident that the regression slope contains only part of the available information. The strength of the relationship, or tendency of the pixel intensities to sit on the straight line, is described quantitatively by Pearson's product moment correlation coefficient. Therefore, the correlation coefficient measures how similar projection images are, regardless of intensity scaling. This fact is readily supported by considering that the correlation coefficient of any set of points along a straight line is equal to unity regardless of the slope.

The correlation coefficient (Figure 62a) and slope (Figure 62b) were both observed to follow an approximately exponential decrease with acid challenge time. This is also seen in hardness measurements, whereby the initially rapid softening is explained by an immediate dissolution of mineral from the surface, thus partially exposing deeper enamel to acid challenge and subsequent partial dissolution. This process repeats,

eventually forming a sub-surface lesion that is just evident in the OCT B-Scans (Figure 59) at t=120 minutes. However, dissolution of the initial enamel surface continues, resulting in net erosion. Thus, a sub-surface softened region is constantly formed at depth below the eroding surface. The result is a hardness curve of the form shown in Figure 64. The similar form of both the slope and correlation curves can likewise be explained by the combination of surface and sub-surface changes that are occurring. Initially, changes to the projection images are dominated by the specimen surface. However, once the surface softening is established, sub-surface demineralisation is expected to dominate the projection images. However, the exact mechanism by which chemical and morphological changes affect the OCT measurements remains to be elucidated.

This study has shown that OCT derived measurements are quantitatively sensitive to ESS. Furthermore, correlation between local pixel region intensities was found to be a more reproducible measure of ESS than the intensity slope. This is evidenced by the tighter error bars in Figure 62a compared to Figure 62b indicating less inter-specimen variation for correlation measurements. However, up to 20 minutes acid challenge, the error bars also indicate comparable variation in the slope parameter compared to correlation. This makes sense because demineralisation is a cumulative process. The OCT measurements reference to the specimen at t=0 and therefore, at early time-points the variation between specimens is necessarily limited, i.e. there is a distribution of specimen susceptibility to demineralisation. However, the cumulative effect compounds the variation such that it increases with time until equilibrium is reached. Therefore, once demineralisation is established, the rate of change of OCT projection image intensity tends towards a constant. This theory is supported by the hardness curve, which was linearly related to the surface hardness.

The hardness measurements were obtained from a separate batch of bovine samples to the OCT measurements. This was necessary because the aim of the OCT measurements was to measure *in situ* without disturbing the specimens. Conversely, hardness testing necessarily required specimen handling and preparation. Thus, the correlation and slope relationships shown in Figure 65a and Figure 65b are statistical, relying upon the measurement of multiple different specimens to represent true underlying sample variation sufficiently to show an average relationship between the two experiments. The results indicate a strong linear relationship (r^2=94% and 98%,

$p << 0.05$) and thus support the idea that both backscattered intensity and projection image similarity can be used as non-invasive proxies for hardness, notably this appears to hold within the first 10 minutes of ESS formation thus providing a way to monitor early lesion formation without disturbing the specimen. The quantitative relationships determined from the regression lines between correlation/slope and hardness are necessarily empirical. Therefore, careful calibration would be required in order to use OCT as an optical hardness measuring system. However, these results show the potential for such use.

In this work, the projection images were sub-divided into 10x10 pixel regions, the mean of each being used for all subsequent calculations. The purpose of this was to mitigate against any lateral re-positioning uncertainty that might occur due to imaging multiple specimens and movement of the OCT probe on a linear translation stage. Region sizes were tested from 3x3 to 10x10 pixels. The results of this testing have not been included here, however, the outcome of such tests revealed negligible sensitivity to the region size.

Projection images were formed over a depth of 500 μm, one hundred times the expected depth of the softened layer found in ESS. The rationale for this is as follows. Erosive changes predominantly affect the enamel surface to a depth of 2-5 μm. When the initial surface is polished, as it is here, the initial change is from a specular reflection to a slightly diffuse scattering interaction. Thus, the intensity of light coupled back into the OCT collection optics immediately from the surface is reduced. Furthermore, the intensity of light transmitted into the specimen without interaction and backscattered from within the sample back through the diffuse surface is also modified. The net result of this change is a reduction in the B-Scan image intensity, this is visually apparent in Figure 59.

Whilst it has been shown to be possible to detect erosive changes by concentrating on the intensity of only the surface reflection (Chew et al., 2014, Chan et al., 2013), these approaches ignore the integrated effect at depth that is more than simply a shadowing influence of the surface. When considering this effect, it is important to remember that OCT B-Scan images are typically rendered on a logarithmic scale. In linear units, the axial OCT signal corresponding to a homogeneous scattering medium is typically represented by a strong initial surface reflection peak followed by exponential

intensity attenuation. Thus, integrating the OCT signal over some axial depth is akin to performing an exponential weighted average, with preference for the surface signal. This is expected to increase the sensitivity to subtle surface changes by incorporating the effect of these changes from sub-surface regions.

This study has not attempted to optimise the projection depth. Instead, the Rayleigh range of the objective was chosen as a reasonable estimate over which the collection efficiency is relatively uniform. Further work is required to assess the impact of projection depth on the overall results. However, this work has explicitly integrated over the OCT linear intensity signal that is available from the raw data acquired by the custom OCT system used for this study. Previous studies have utilised the post-processed B-Scan data that is on a logarithmic scale.

The results, protocol and experimental setup described in this study have important implications. For example, ESS is considered to be a reversible change because an enamel framework remains, into which new mineral can be deposited. Therefore, by adopting this setup, not only can ESS formation be monitored non-invasively, but the potential exists by which therapeutic agents could be introduced into the solution and the effects monitored, all without disturbing the samples. Furthermore, should it be necessary to physically apply a treatment to the enamel surface, the specimen holder can be drained and opened without disturbing the specimen position. Thus, spatially registered measurements can be made to assess new interventions.

10.6 Conclusion

This work has demonstrated that pixel region correlation of 4D OCT data can optically detect ESS formation in bovine enamel. Further work is now required to establish how OCT data acquired in this way can be used to measure changes that occur when such lesions are remineralised.

11 Remineralisation Detection using Longitudinal Correlation

11.1 Introduction

Remineralisation is an important natural repair process that counters cariogenic challenges in order to maintain a balance between processes of enamel mineral loss and gain. Remineralisation refers to the process by which lost minerals is recovered and reconstructed on a partially demineralised tooth surface (Arends and Ten Cate, 1981). During demineralisation, the dissolution of calcium and phosphate ions from surface of the crystals roughens the enamel, serving as nucleation sites for remineralisation (Nancollas et al., 1989, Wang and Nancollas, 2008). In the oral environment, the calcium and phosphate ions present in super-saturated saliva reacts with these nucleation sites and results in the repair of the enamel (Cury and Tenuta, 2009).

In the remineralisation process, partially dissolved crystals are induced to grow by deposition of calcium and phosphate ions from saliva or an applied remineralising agent (Wang and Nancollas, 2008). The process is not expected to re-grow lost enamel, but may modify the existing enamel scaffold. The driving force for the remineralisation or 'precipitation' of any new solid phase is the degree of saturation of the fluid environment with respect to the enamel, i.e. the medium at the tooth-plaque interface must be saturated with respect to the tooth mineral (Margolis et al., 1999).

Fluoride is known to promote the remineralisation process (Schemehorn et al., 1999). Several investigators have shown that fluoride in the solution is effective at inhibiting demineralisation (Ten Cate and Featherstone, 1991). However, the presence of fluoride in saliva is generally not sufficient to restore the natural equilibrium between demineralisation and remineralisation, and often this needs to be supplied externally. Fluoride administered in dentifrices and medication is the most common and successful method of inducing remineralisation in practice today. Fluoride promotes enamel remineralisation in demineralised areas, by driving the precipitation of fluoridated apatite from calcium and phosphates in the remineralising agent. The

soluble calcium-phosphate phases present in the enamel lattice are converted to a more stable and more acid resistant form known as fluorapatite (FAP). The FAP crystals are then deposited either as new crystals or on the surface of existing demineralised crystals. Fluorapatite is considered to be relatively less soluble and a more stable compound.

The present knowledge about the mechanisms of dental caries development, fluoride effect and preventive measures on caries is due mainly to *in vitro* studies. Consequently, several models have been developed, and among these models, those mimicking *in vitro* caries processes (pH-cycling), previously reported (Ten Cate and Duijsters, 1982) have been used for different purposes. The most important application has been the evaluation of fluoride effect on caries. Different pH-cycling models have been developed to evaluate the fluoride effect in either reducing enamel demineralisation (Featherstone et al., 1986) or enhancing remineralisation (White, 1987). However, *in vitro* testing protocols show limitations, and one of the limitations is the inability to study the effect of fluoride on all stages of the caries process, mainly the early stage. At the early stages, the surface layer appears unaltered because it is continuously regenerated. Recent studies ascertain that exposure to high fluoride concentrations at one time leads to remineralisation and thickening of the surface, hindering the penetration of fluorides along the depth of the lesion (Al-Khateeb et al., 1997).

Considering the importance of the surface layer in caries progression and arrest, the evaluation of changes in this region is relevant and OCT lends itself as a potentially suitable technique for this purpose. OCT has been widely used in the assessment of demineralisation based on increased light scattering in the porous partially demineralised tissue (Fried et al., 2002, Amaechi et al., 2003a). Demineralisation leads to partial dissolution of the enamel, leaving a porous structure, greater local variation in refractive index and hence increased scattering of light.

However, there are fewer studies on the assessment of remineralisation by conventional OCT. Previous OCT studies have measured the optical changes in artificial caries undergoing remineralisation (Jones et al., 2006b, Kang et al., 2012a, Mandurah et al., 2013). The remineralisation of enamel caries can lead to distinct optical changes within a lesion. It is hypothesized that the restoration of mineral

volume would result in a measurable decrease in the depth-resolved reflectivity of OCT light from the lesion. Jones et al. showed that an increase in mineral volume from the fluoride-enhanced remineralisation significantly decreased the optical reflectivity of artificial lesions within an enlarged surface zone (Jones et al., 2006b). The authors also observed that the lesion body did not remineralise to the same level as the surface zone. It was observed that slight changes or increase in the signal intensity from the surface zone made it difficult to perform objective analysis (Kang et al., 2012b). Similarly, other groups used OCT signal attenuation analysis in an attempt to monitor changes of enamel lesions during remineralisation (Mandurah et al., 2013).

The study assumed a simple single-scattering event during light propagation in the tissue (Huang et al., 1991, Schmitt et al., 1994). However, results observed cannot rule out changes to the surface reflectivity due to deposition of minerals only at the surface. It is arguable where the source of attenuation originates from and if there were any changes beyond the very surface.

From these studies, no consensus has been formed on how this process manifests in the OCT images. The intensity of the band of backscatter that corresponds with demineralised tissue has been reported to change, but the changes are subtle, making it difficult to perform objective analysis on the results obtained (Mandurah et al., 2013). The specific effects of surface changes on the tooth, time dependent changes in the lesion, spatial variations and environmental effects on the OCT signals are yet to be quantified. Correlation analysis introduced in chapter 10 offers the potential to detect the subtle changes in the samples during the remineralisation process.

Longitudinal correlation assessment of 3D OCT images can potentially provide a repeatable means of tissue characterisation. This approach demonstrated that OCT volumes could be used to detect subtle changes in enamel that were not visible in B-Scan cross-sections. Consequently, it was shown to be sensitive to changes during early stage erosion prior to the net loss of tissue. Remineralisation is likewise expected to manifest as subtle changes to light scattering due to the nucleation and growth of new apatite crystals predominantly at the surface. Therefore, the primary aim of the work reported in this chapter was to determine whether longitudinal correlation was

sensitive to enamel remineralisation and also to ascertain whether demineralisation and remineralisation could be discriminated by calculating the correlation coefficient.

11.2 Materials and Methods

11.2.1 Sample preparation

Bovine tooth samples were acquired from Modus Laboratories, Kent, U.K. as previously discussed in chapter 6.1. To acquire uniform specimen thickness, specimens were ground and polished to a thickness of 3mm with p180 abrasive paper using a Kemet 40 automatic lapping unit (Kemet International Ltd. Maidstone, UK). The specimen surfaces were painted with a thin layer of acid-resistant nail varnish, Revlon (570, New York, USA) to create a 3x3 mm window for demineralisation and remineralisation.

11.2.2 Demineralisation and Remineralisation

1 litre of demineralisation solution was prepared as 0.05 M acetic acid, 2.2mM of $CaCl_2$, and 2.2mM KH_2PO_4 in deionized water with pH adjusted to 4.4 using NaOH (Ten Bosch and Angmar-Månsson, 1991). The pH of the solution was monitored throughout the experiments using SenTix® 41 electrode pH-meter (WTW GmbH, Germany). The demineralisation cycle was carried out for 48 hours in order to produce caries-like lesions while maintaining an intact surface.

After an initial 48-hour period of demineralisation, the specimens were exposed to a remineralisation solution reported by (Jones et al., 2006b, Yamazaki and Margolis, 2008). 1 litre solution was prepared by adding 2mmol $CaCl_2$, 1.2mmol KH_2PO_4, 150mmol NaCl and 2 ppm NaF in deionised water. The pH of the remineralisation solution was adjusted to pH 4.9. The pH of the solution was monitored throughout the experiments using SenTix® 41 electrode pH-meter (WTW GmbH, Germany). The remineralisation cycle was carried out for 168 hours.

11.2.3 OCT System Specification and Configuration

The OCT system used for this study was a custom designed lab-based instrument as described in chapter 6.5. The OCT system was configured to automatically measure multiple specimens by mounting the OCT imaging probe onto a motorized linear

translation stage with a repositioning accuracy of 2.0±1.7 μm (LTS300, Thorlabs, UK). Acquisition of a single OCT volume and translation between specimens took no more than 20 seconds for each sample, enabling OCT image volumes of different specimens to be imaged at the desired hourly intervals. The experimental configuration is shown in chapter 6.

11.2.4 Measurement Protocol

In order to investigate the remineralisation process as manifested in OCT images, the samples were setup in a longitudinal experiment that acquired hourly scans. Both demineralisation and remineralisation cycles were carried out on the same untouched specimens.

Firstly, the samples were immersed in 100 ml of deionised water for 24 hours prior to exposure to the demineralising solution. After the 24-hour hydration period, the samples were placed in isolated compartments within the custom sample holder, orientated with the enamel surface orthogonal to the OCT probe beam. The O-rings were placed in position then the holder was fastened using screws to ensure the setup was watertight. The chambers were designed such that they could accommodate approximately 2.3 ml of solution with the specimen and resin disc occupying a volume of 1.5 ml and the remaining volume 0.8 ml was solution. The demineralisation solution was introduced into each chamber of the holder through an inlet channel located below each specimen and ejected through an outlet channel located above. The solution was continuously refreshed at a rate of 5 ml/minute by a multi-channel pump (323Du/D, Watson Marlow, UK), drawing fresh solution from a 1 litre reservoir and ejecting used solution into a separate container. A fresh batch of solution was replenished when the reservoir was depleted.

Once the solution had filled the chambers, hourly measurements were automatically acquired by moving the OCT measuring probe between specimens. Three-dimensional OCT image volumes were acquired from each sample over a square surface area measuring 3x3 mm corresponding to the unvarnished window. After the 48 hours of demineralisation cycle, a buffer solution was pumped through the flow cell to flush the demineralisation solution. Then the remineralisation solution was pumped through to replace the buffer. This step was all accomplished within an hour

window between measurements so that the image acquisition was not stopped at any time.

11.2.5 Processing

ImageJ was used for the processing of both cross-sectional B-scan images and for the *en face* correlation coefficients calculations. The central cross-sectional B-Scan images (B-scan 250) were used to measure and compare the lesion depths before and after the demineralisation and remineralisation phases. These images were aligned using the StackReg plugin on ImageJ (Thevenaz et al., 1998) in order to fit all the specimen surfaces on the same plane on the OCT images.

En face projections generated from each 3D OCT dataset were used for the correlation analysis. These were by processed by selecting all C-Scans from the surface to a depth of approximately 500 μm and summing the pixel intensities together to give a single composite image as described in chapters 10.3.5. From the projection images, a region of interest (ROI), measuring (1.5x1.5 mm) was manually selected. These were chosen from regions where least amount of specular reflections from the surface were observed. ROI selection and cropping was carried out using ImageJ. The correlation coefficient was calculated using the mean region intensities (10x10 pixel grid) rather than individual pixels. Calculation of the correlation value was achieved using the CorrelationJ plugin (Chinga and Syverud, 2007).

11.3 Results

OCT cross-sectional images of a sound, demineralised and remineralised bovine enamel of one of the samples are presented in Figure 66. The images represent a single B-scan taken at the same location at different time intervals. Each image shows a cross-section of the enamel structure and demineralised region.

As the demineralised region developed, visibility of the underlying enamel structure decreased (0Hours - 12Hours). At 12 hours of demineralisation, a band of increased backscattering is seen developing under the sample surface (Figure 66). This is representative of a developing subsurface lesion having an intact surface. The band of high backscattering increases in depth with the progression of demineralisation, indicative of progression of enamel demineralisation with time.

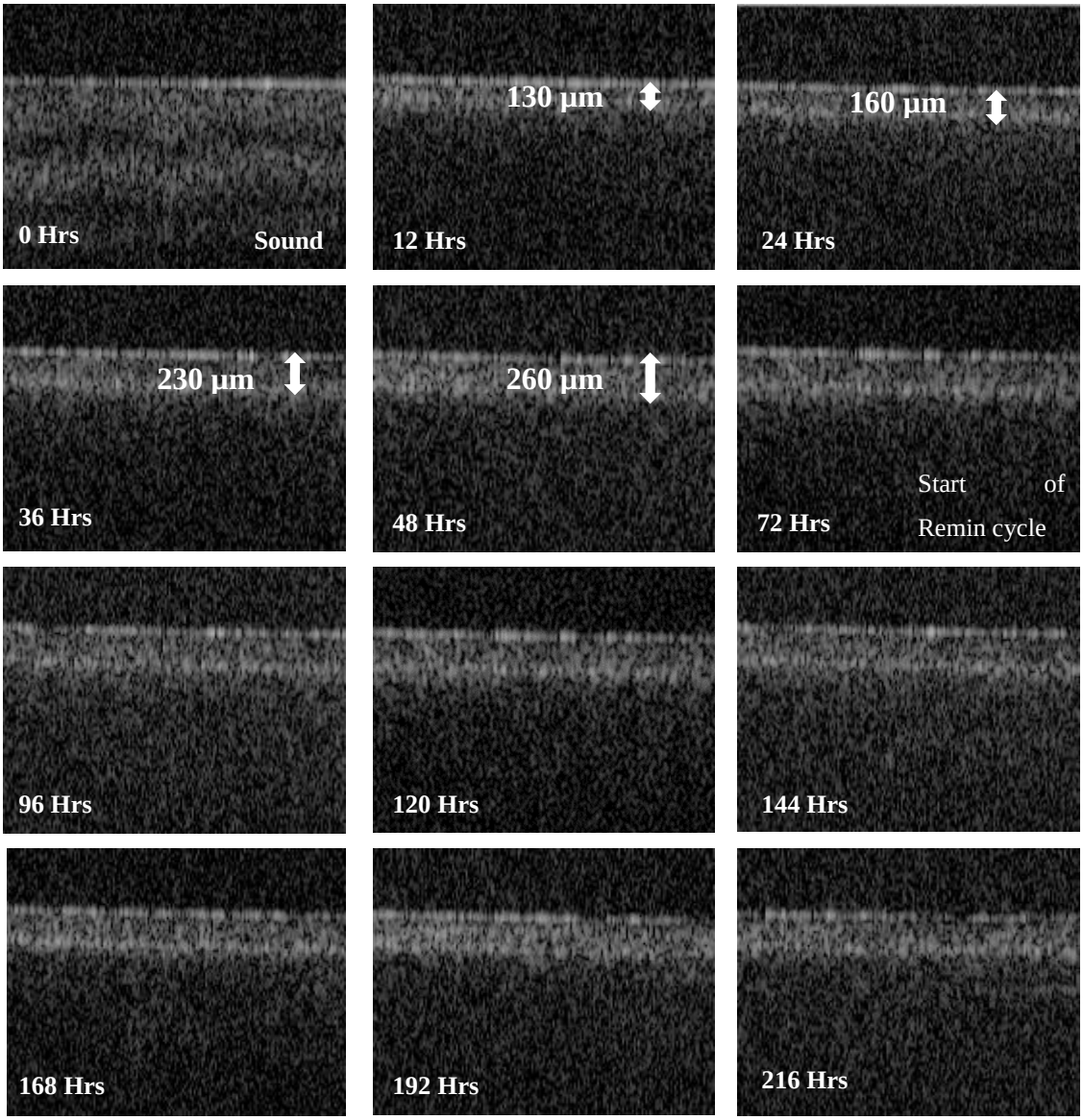

Figure 66 Time series OCT B-scans of a bovine sample undergoing 2-day demineralisation (0-48 hours) and 7-day remineralisation (72-216 hours) cycle. Each OCT B-Scan image represent 12 hours intervals. Arrows show the thickness of the high backscattering band of light that is indicative of demineralisation. The band is maintained even after the remineralisation phase.

Moreover, the cross-sectional images revealed that the band of high backscatter, associated with the demineralised region, persisted throughout the remineralisation period (72 Hours – 216 hours) (Figure 66). No apparent change was noticed between the end of demineralisation and remineralisation phases, making it difficult to discern any differences through cross-sectional images.

Quantitatively, this was assessed by measuring the sub-surface lesion depth before and after the remineralisation period. The results are plotted in the box plot Figure 67.

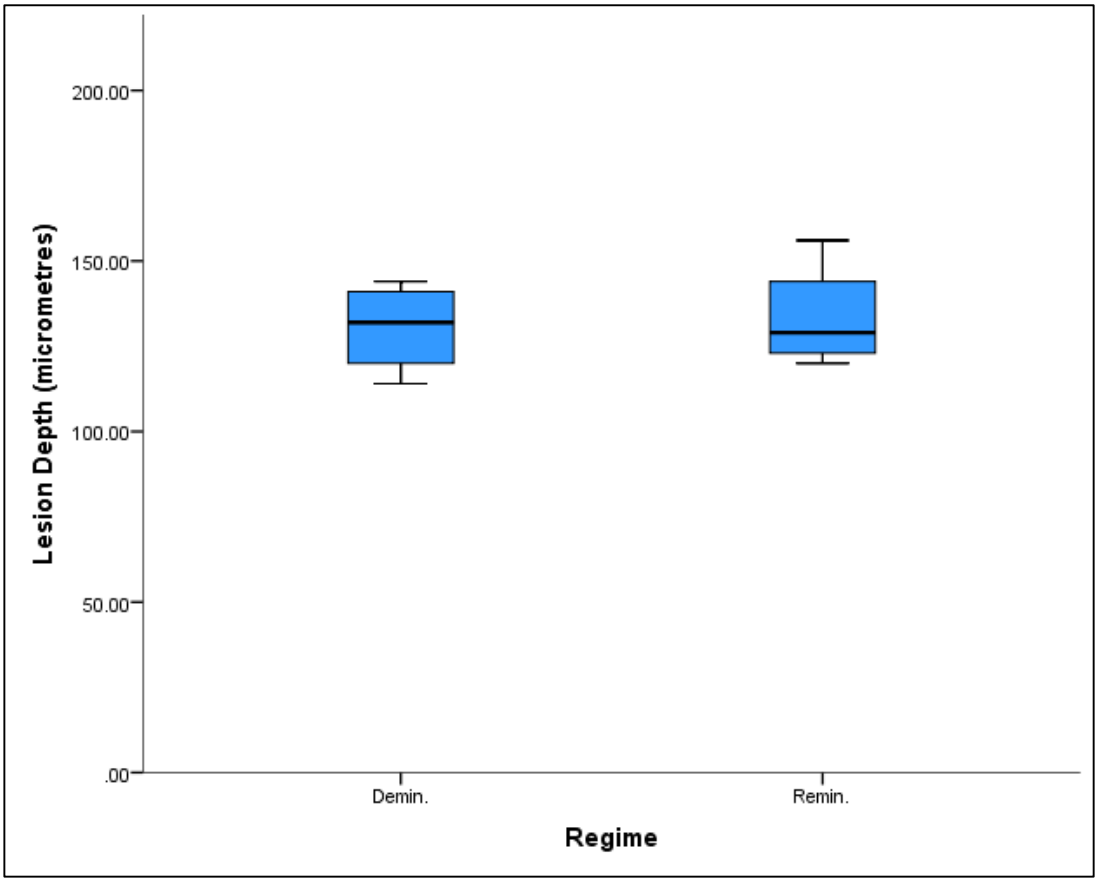

Figure 67 The mean lesion depths of samples before and after remineralisation measured from the thickness of high backscatter band on the OCT images that correspond to lesion depth progression. No change is observed.

Using an independent samples T-Test, the mean lesion depth between the demineralised and remineralised phases were found to be statistically similar (p=0.89). Therefore, OCT was unable to detect any change to the sub-surface lesion depth following a 168-hour period of remineralisation.

En face composite images form the volumetric dataset were processed. Visual changes were apparent on the surface of the samples at the end of the experiment. Examples from samples 2 and 4 are shown Figure 68 for sound enamel, the same enamel following 48 hours of continuous demineralisation and later following a further 7 days continuous remineralisation. The *en face* images show the surface changes during the remineralisation phase, which was not readily visualised on the cross-sectional images. Visually, the surface does not appear to change substantially during the demineralisation phase. However, following remineralisation, dark spots

are apparent on the surface indicative of a change in texture. More subtle changes are visible in Figure 68c compared to Figure 68f.

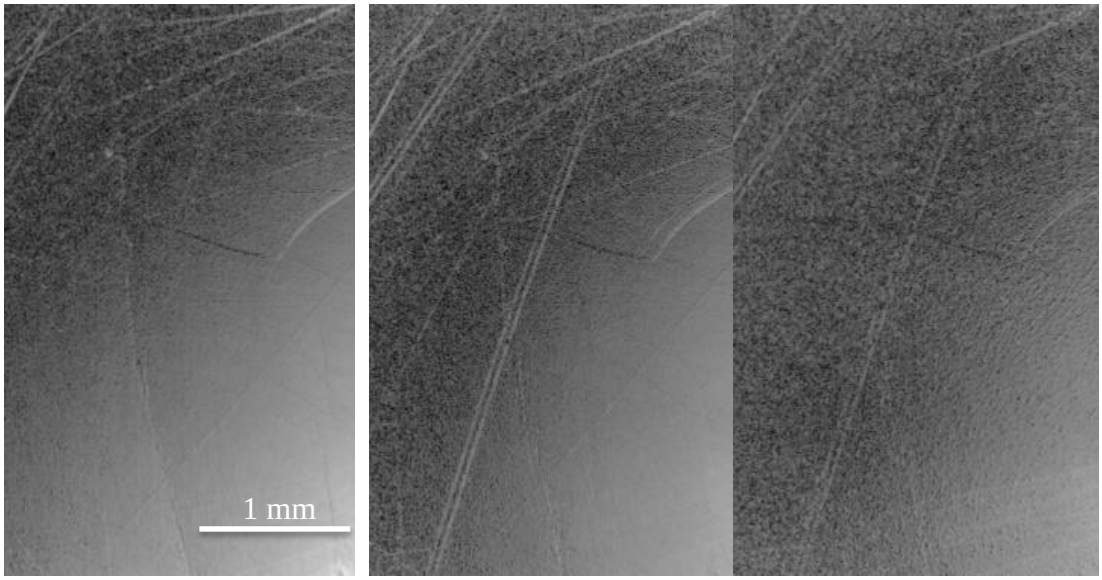

(a) (b) (c)

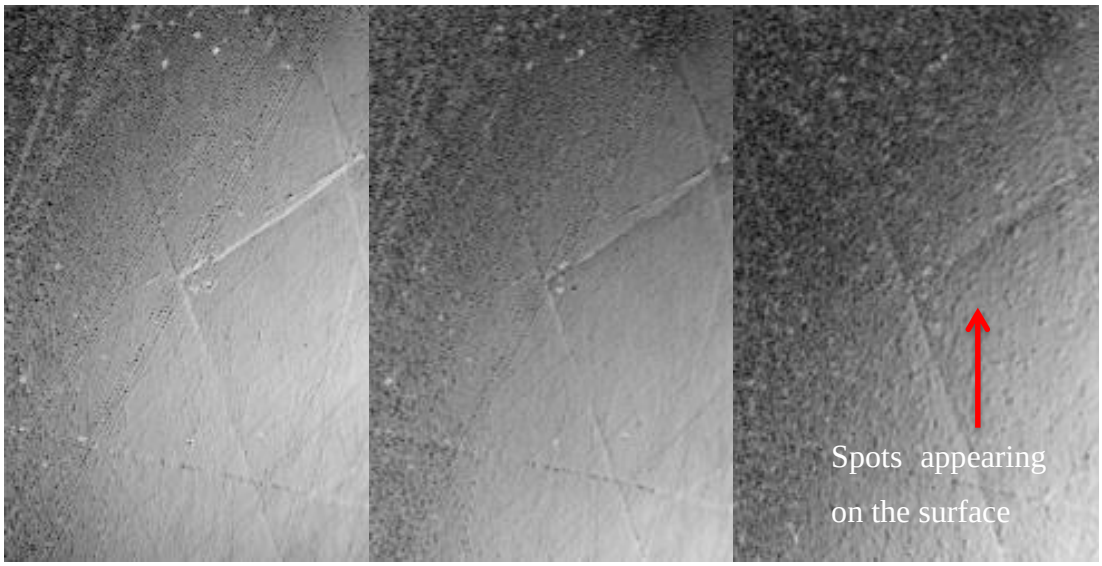

(d) (e) (f)

Figure 68 Sample 2 (a-c) and sample 4 (d-f) surface images extracted from the OCT volumetric images of sound enamel. (a,d), same surfaces after 48 hours of continuous demineralisation (b,e) and then following a further 7 days continuous remineralisation (c,f). Little change in surface is observed after the demineralisation phase however surface changes visible after remineralisation phase.

From these images, the Pearson's product moment correlation coefficients were calculated over the specimen surfaces. The correlation coefficient was calculated between the baseline image at t_0 and all subsequent surface volume projections

including both demineralisation and remineralisation cycles (0-216 hours) as shown in **Error! Reference source not found.**.

Figure 69 Graph of correlation coefficient values against time of remineralised bovine samples. Initial phase of demineralisation (0- 48 hours) is indicated in red colour followed by remineralisation phase (49- 216 hours) in blue. After a drop of correlation values during the demineralisation phase, a small recovery in correlation is seen in the initial phases of remineralisation which later plateaus.

The correlation coefficient values are seen to 'de-correlate' during the demineralisation cycle and a slight recovery in correlation is observed during the first 24 hours of the remineralisation cycle. This is then seen to plateau for the rest of the remineralisation period.

11.4 Discussion

The recent outlook in dentistry is focused on preventative measures rather than surgical interventions (Pitts, 2004). However, therapeutic intervention is hindered by the fact that lesions are not clinically observable at the early stages of the caries process. At this stage, the intervention has potential in inhibiting further caries

development. Therefore, a good understanding of the early changes on the surface of enamel during *in vitro* demineralisation process is essential.

The ability to image the surface zone on an early enamel lesion holds particular significance for both lesion development and arrest. Since caries lesions remineralise from the outside surfaces inwards, the nature of such a surface zone can potentially provide information about the activity of the lesion (Ngaotheppitak et al., 2005). In the current study, the internal structure of early caries lesions with surface zone was reproduced and imaged.

Recent studies have suggested that restoration of mineral volume would result in a measurable decrease in the depth-resolved reflectivity of light from the lesion (Jones et al., 2006b, Kang et al., 2012b). The signal intensity would decrease when porosities are filled by mineral aggregation as a result of the precipitation of calcium and phosphate ions with fluoride on nucleation sites of the pores and micro-interfaces created during demineralisation. However, this phenomenon was not readily visible on the cross-sectional images of demineralised lesions produced in the current study. The visual and statistical assessment of lesion depth did not detect any evidence of change, either decrease or increase, associated with remineralisation duration. This added to the fact that previous studies (Chew et al., 2014) involve movement of the samples from the acid challenge to the imaging equipment; means accurate analysis of levels of remineralisation is problematic.

Alternative analysis methods are necessary in order to quantify early changes. Correlation analysis was demonstrated in chapter 10 to be sensitive to early stage erosion showed a quantifiable method of assessing erosive lesions. The potential for this analysis method to quantify remineralisation was investigated in the current study.

Using the integrated projection images, subtle changes on the surface of enamel were observed. The sample surfaces exhibited no change after the demineralisation phase but visible surface changes were noted after the remineralisation phase. Visible dark spots were apparent on the surface indicative of a change in texture. Since remineralisation is more likely to be a surface effect, these textural changes could be due to precipitation of minerals on the nucleation sites on the roughened demineralised enamel.

Image correlation analysis showed a consistent 'de-correlation' of images of demineralised enamel to those of sound enamel. The correlation values also seemed to exhibit a recovery during the initial phase of remineralisation phase and plateau after 24 hours of remineralisation. These subtle observations could be attributed to the composition of enamel structure.

It has been documented that one of the fluoride effects on white spot lesions is a preferential deposition of minerals in the surface layer of the enamel, resulting in arrestment of these lesions (Arends and Ten Cate, 1981). However, this relatively thick and highly mineralised surface layer might act as a barrier, and, thus, has also been suspected to inhibit remineralisation. Mineral aggregation at the superficial zone may result in a decreased rate of mineral deposition in the deeper areas due to blockage of diffusion pathways (Kang et al., 2013). This effect depends on several factors including size of the remineralising compound, surface zone characteristics and pore size throughout the lesion and demineralised depth. Perhaps this was the mechanism behind the observed correlation coefficient values. Consequently acidic remineralisation regimes have been suggested (Yamazaki and Margolis, 2008).

Furthermore, it is hypothesized that during remineralisation, the mineral is precipitated, but the ordering is quite different to that of the sound enamel. It was showed that remineralisation showed partial recovery of the enamel prism ordering (Siddiqui et al., 2014). Therefore, light scattering is altered, but the speckle pattern continues to evolve in such a way that it is increasingly different to that of demineralised enamel but not quite the same as sound enamel. Perhaps this explains the textural dark spots that are visible on the surface images (Figure 68c and Figure 68f). Initially it was questionable whether these effects were as a consequence of the cumulative pixel intensity differences from the generated integrated volume images compared between sound/baseline images and demineralised/remineralised images. This could be ruled out as investigation of surface images after the demineralisation (Figure 68b and Figure 68e) show little or no change on the *en face* images. If the dark sport were caused by the image process techniques their effect would also be apparent on the demineralised images. Furthermore, repair of the surface during remineralisation is expected to affect the propagating light as mineral deposited act as scattering centres improving signal propagation. The increase in signal propagation can be seen to visualise more subsurface structures within the lesion and perhaps in

the body of the enamel. Hence the subtle changes in correlation values observed during remineralisation could be validated.

In this case, perhaps, correlation analysis appears to be a promising approach for monitoring remineralisation of enamel lesion. The method of longitudinal assessment of remineralisation, with the use of volumetric images as opposed to single cross-section images of the specimens showed utility in this study.

Remineralisation is a slow process since precipitation is a much slower process than dissolution (Ten Cate, 1990). The apatite crystals require a prolonged period to complete crystallization during remineralisation (Kitasako et al., 2011). Although the largest change to the remineralisation correlation signal was in the first 24 hours, future studies will benefit from observations over longer period of remineralisation are necessary to test the efficacy of this method. Furthermore, in order to validate this technique, comparisons with other gold standard techniques such as Nano-indentation, chemical analysis or Transverse Microradiography are necessary. These will provide an objective measure of an actual physical property for example hardness or mineral density of enamel structure that would enable a significant correlation between optical and mechanical findings. However, validation with other techniques requires careful experimental design to ensure that both techniques are measuring the same phenomenon (as described in Chapter 7).

11.5 Conclusion

Monitoring of enamel lesions based on the OCT longitudinal correlation coefficient evaluation appears to be a promising approach. OCT has shown potential for non-destructive measurement of the surface zone of caries lesions *in vivo*. Furthermore, this method could provide a unique tool for the assessment of new outcomes of non-surgical therapies, which would in turn increase the overall understanding of the remineralisation of enamel caries.

The technique employed in this study show potential as a potential alternative that would be a useful utility for monitoring lesion recovery *in vivo*. However, this technique will be sensitive to patients' movement.

12 Discussion

The studies presented in this thesis aimed to understand the effects of enamel demineralisation on OCT measurements. Furthermore, different methods of making quantitative measurements from OCT data have been explored and developed. To achieve this, certain steps were necessarily taken; In order to objectively study the multi-factorial nature of dental hard tissue lesions, simplified *in vitro* models were adopted (Featherstone, 2000). Many variables such as salivary pellicle and dental biofilm that influence the development and progression of dental caries *in vivo* were eliminated in order to assess only the direct physical effect of demineralisation of enamel on the OCT images. Various laboratory-based studies have been reported in the OCT research literature using these *in vitro* models and so the results in this thesis can, to some extent, be compared.

All of the work reported in this thesis was underpinned by a substantial effort to create a controlled laboratory based environment and experimental setup to maximise the accuracy and reproducibility of the results. Furthermore, the experimental setup was uniquely configured to study lesion dynamic without disturbing the specimens. Whilst this does not replicate the *in vivo* natural environment, it provides a stable foundation from which to evaluate new OCT analysis protocols. Therefore, a custom-built sample holder was used to ensure the samples were static whilst subject to continuous acid challenge. This enabled the localisation of samples ensuring they were imaged at the same location and orientation each time at each measurement. Time-lapse OCT measurements were obtained in real-time through the transparent lid of the specimen holder, eliminating the need to move specimens for measurement. This configuration was used to obtain all of the OCT results in this thesis. Additionally, a custom-built laboratory-based OCT system was used for this research enabling access to raw data and control of all processing steps.

Critically, to the author's knowledge, no similar 'hands free' experimental configuration has been used elsewhere in dental OCT research. However, the stability advantage gained does introduce complications when comparing to other, more invasive techniques. This was made evident by the work presented in Chapter 7, which showed that the continuous acid challenge used in OCT produced different

erosive lesions when compared with profilometry. Therefore, OCT results obtained under continuous acid challenge must be interpreted carefully with respect to more established methods that require removal of specimens from the acid challenge.

Bovine Enamel Samples Justification

The work presented was carried out using bovine enamel substrates. Bovine enamel samples have been used extensively in dental research. Whilst bovine enamel is not identical to human dental enamel (Yassen et al., 2011) it serves as a useful platform from which to develop new experimental and analytical techniques, whilst retaining some natural biological variation.

Some disadvantages and limitations associated with the use of human teeth in dental research exist. Human tooth samples are often difficult to obtain in sufficient quantity and with adequate quality, because teeth are usually extracted due to extensive caries lesions and other defects (Mellberg, 1992). It can also be challenging to control the source and age of the collected human teeth, which may lead to larger variations in the outcome measures of the study. Furthermore, the relatively small and curved surface area of human teeth may also be a limitation for specific tests requiring flat surfaces of uniform thickness (Zero, 1995).

Whilst a number of alternative substrates have been proposed for use in dental research (Yassen et al., 2011), bovine teeth are considered a good alternative (Laurance-Young et al., 2011). Bovine teeth are easy to obtain in large quantities, in good condition and with a more uniform composition than that of human teeth. Furthermore, bovine teeth have a relatively large flat surface, and do not have caries lesions and other defects that make them desirable in artificial carious models. Therefore, they are the most broadly utilised substitute for human teeth in dental erosion studies (Yassen et al., 2011).

Concerning dental erosion, bovine teeth can serve as a model alternative for *in vitro* studies, accepting that they do not perfectly mimic real-life, *in vivo* lesions (Wegehaupt et al., 2008). Furthermore, human and bovine enamel hardness changes have been found to be comparable (Turssi et al., 2010).

Accurate data from the published literature regarding the comparative properties of human and bovine hard dental tissue remain inconclusive, but consensus appears to

accept the continuing use of bovine enamel as a substitute for human enamel (Laurance-Young et al., 2011). Yet, from the perspective of clinical relevance, human teeth are preferred (Yassen et al., 2011). However, regardless of substrate, it is widely acknowledged that *in vitro* lesions to not match the complexity of natural lesions. Nevertheless, they enable systematic and controlled study of specific aspects of dental lesion development and provide a controlled target for measurement.

Bovine enamel has been reported to have a more uniform composition than human enamel and thus provides a less variable response to both cariogenic challenge and anti-caries treatments (Mellberg, 1992).

Simulation of Demineralisation

Owing to its diverse presentation, unique multifactorial origin and intricate microstructure, natural caries has been difficult to study and understand. To be able to study the origin of caries and nature of its progression, it is necessary to be able to establish and define all the factors suspected to play a role in the aetiology. Therefore, simplified models have been developed that produce artificial caries-like lesions *in vitro*, focussing upon specific chemical or morphological factors. From a biological perspective, it is virtually impossible for *in vitro* models to adequately simulate the complex and diverse intra-oral conditions contributing to caries development (White, 1995). However, artificial caries models allow for the control of the extension of the lesion among other factors including origin (microbial or external acid), severity, pH and exposure time.

Numerous studies have observed demineralisation induced by artificial lesions produced in teeth (Ten Cate et al., 1988, Argenta et al., 2003) and more recently using OCT (Sadr et al., 2013, Nazari et al., 2013, Nakajima et al., 2014). For the purpose of this study, simplified *in vitro* erosion and caries models have been adopted. Various *in vitro* demineralisation models including citric acid solutions, acetic models that excluded additional calcium or phosphate ions and buffered acetic acid solutions to simulate erosive and cariogenic challenge were used. However, the automated experimental framework and analysis techniques developed in this thesis are not restricted to the study of these models or bovine substrates.

Custom Sample holder

A major part of the experimental framework was the development of a specimen holder to hold the specimens in a static position during the demineralisation process. Specimen movement during experimentation can introduce uncertainties in the results. The sample holder also allowed for precisely controlled flow rates and changing of solutions without disturbing the specimens.

The setup used in this study proved to be particularly useful in ensuring that the same sample position was imaged at each repeat of OCT acquisition. Young et al. observed that the re-positioning of the specimens must not vary to an extent that it will influence the results between specimens (Young and Tenuta, 2011b). This was crucially important for the sensitive real-time monitoring of lesion formation using the longitudinal assessment of OCT image correlation analysis of early stage surface erosion. Whilst some repositioning error does remain, due to the finite accuracy of the translation stages, this is within the OCT instrument resolution.

The main disadvantage of using the sample holder was that the lid of the sample holder can create a shadow effect on the OCT images therefore masking the surfaces under investigation. To mitigate against this, the samples were polished to uniform thickness so that after the alignment of the path lengths, the shadow would not interfere with sample surfaces.

Hydration effects on the OCT measurements

Studies have shown that the hydration state of the samples affects the OCT signal intensity from enamel lesions thus affecting the OCT images (Fried et al., 2002, Natsume et al., 2011). A recent OCT study comparing the reflectivity of sound and demineralised enamel under hydrated and dry conditions (Nazari et al., 2013) reported that significant differences were found between sound and demineralised enamel, and between different periods of demineralisation evaluation of the OCT signals at hydrated and dry conditions. Sound enamel exhibited very similar images regardless of the hydration state of the specimens, but demineralised enamel at hydrated and dry conditions showed different images.

Other studies have investigated the application of high refractive index fluids on the samples to study how they influence performance of the OCT system. The study

showed that these liquids increased the effective imaging depth and lesion contrast (Kang et al., 2014).

Therefore the decision was made in this study to image the samples under constant hydration avoiding any uncertainties that may arise due to subtle contrast changes during hydration effects. Some OCT hydration results are shown in Appendix A (Figure A1). These results guided the protocol which ensured a minimum hydration time of 2 hours.

Calibration Protocol

In order to address some of the measurement uncertainties associated with OCT, a calibration protocol was developed to ensure that the voxel dimensions, 3D geometric distortion and detected scattering intensity were all normalised between experiments. Without this calibration step it is impossible to compare OCT results between studies. This is one of the potential limitations of dental OCT results published to date.

In this study, the methods and phantoms described by (Tomlins, 2009) were employed. The use of the reference phantoms that are loaded with TiO_2 scattering particles having a known scattering coefficient (Woolliams and Tomlins, 2011a), provided a constant benchmark for the OCT measured light back-scattering intensity. The axial and transverse resolutions in air, the system point-spread function and geometric scaling were acquired for each experiment in order to describe system's performance during measurements and ensure result across experiments were comparable. The axial collection efficiency of the OCT system and the sensitivity roll-off were calibrated by measuring a weakly scattering phantom (Faber et al., 2004) previously described as a point-spread function (PSF) phantom (Tomlins, 2009). These phantoms were particularly useful when applying longitudinal correlation analysis. Incorporation of phantoms within the experimental setup allowed for a constant benchmark for comparison. For erosion studies monitoring the image correlation changes over erosive time, the tissue phantoms were used to show only 5% change in correlation over the experiment while correlation coefficient values changed over time for the enamel samples.

Validation with other techniques:

Gold standard techniques such as microhardness measurements (Arends et al., 1980, Attin et al., 1997, Featherstone et al., 1983, de Cara et al., 2012) used to measure early stage softening, and profilometry (Schlueter et al., 2005, Heurich et al., 2010) for advanced dissolution of bulk enamel were used in this study. Using profilometric measurements, the OCT pixel depth was calibrated assuming that the erosion measured in profilometry was, on average, equal to the erosion observed in OCT. A comparison with OCT measurements of a known step height invalidated the assumption of equivalence. This is an important result because it reveals the dependence of the measured quantity (erosion depth) on the experimental protocol. This does not invalidate OCT as a measurement tool in dental research, but manages the expectation that it should produce results that agree with previously established techniques.

Nevertheless, in chapter 11 microhardness measurement was used to measure hardness values of demineralised early erosive lesions, which were compared and shown to agree with OCT correlation analysis values from the analysis employed. However, in this case it was the linearity of both quantities that was compared, rather than an absolute measure because OCT does not directly measure hardness. Instead it measures optical changes that were shown to relate linearly to expected hardness changes. Hence, the results from chapter 11 do not mean that the actual hardness of the specimens measured by OCT was the same as the hardness of the micro-hardness measurement group. Rather it indicates that if the specimens measured by OCT had been subjected to the microhardness protocol, then they might be expected to have the hardness indicated by the linear relationship.

X-ray Micro-Tomography (XMT) was also used to visualise subsurface lesion depth and severity in artificial caries models. The superior measuring range of the XMT system enabled visualisation of whole bovine specimens used in this study, with some results shown in Chapter 8. However, this technique was not used extensively because the pixel size was such that lesions were difficult to discern from the images. Furthermore, XMT imaging took considerably longer than OCT, of the order of several hours. OCT volumes were obtained within 30 seconds to 1 minute. Therefore, XMT was not able to provide an adequate reference for the OCT data. Nevertheless, in future work, the correlation technique developed in this thesis may be equally applicable to XMT as it has been in OCT.

Clinical Implication

OCT is particularly attractive because it non-invasively images backscattered light intensity, which has been shown to be sensitive to changes in dental demineralisation (Feldchtein et al., 1998, Amaechi et al., 2001). OCT is based on techniques that use non-ionising radiation making it attractive clinically when compared to conventional X-ray techniques.

OCT is attractive because of its superior acquisition times, which lends it to clinical use. However, one of the main challenges associated with the application of OCT *in vivo* is patients' movement during image acquisition. Acquisition speeds have greatly increased in recent years, encouraging various *in vivo* studies (Brandenburg et al., 2003, Feldchtein et al., 1998, Lenton et al., 2012, Ibusuki et al., 2015). However, none of the studies provide a true measure of the challenges associated with patient's movement during image acquisition. Any slight movements during measurements are expected to cause artefacts in the OCT images that would make objective analysis of lesion activity problematic.

OCT has been traditionally used *in vitro* for imaging smooth surfaces. Acquiring optimal images of other surfaces for example the occlusal surface, is problematic due to the varying optical penetration and surface reflectivity and the complex morphology of the fissures (Terrer et al., 2009). This issues need to be addressed before OCT can be used objectively clinically.

In vitro study therefore provides the fundamental basis for development, preceding *in vivo* or *in situ* studies that are necessary before OCT can be adopted confidently clinically.

However, *in vivo* studies remain beneficial. This is especially true for the study and validation of new treatments protocols and therapeutic agents. Furthermore, using OCT as a laboratory based tool may be beneficial when translating any treatment to the clinic, since OCT can potentially continue to be used *in vivo* verification.

Mechanism of enamel dissolution

Earlier studies for example (White and Nancollas, 1977) and (Higuchi and Connors, 1965), describe the dissolution of HAp as a diffusion-controlled process. Other more

recent studies suggest that the dissolution of HAp is not limited purely by diffusion and that surface processes play an important role in controlling the overall reaction kinetics (Anderson et al., 2004).

Studies at the crystal structure level using high-resolution microscopic technologies show evidence for the development of tiny holes (etch pits) in the central region of the enamel rods during the initial stages of enamel dissolution (Featherstone et al., 1979, Takuma, 1980). Many studies have observed the preferential dissolution of enamel crystallites in the central rod areas to proceed with the formation of holes with approximately hexagon symmetry (Scott et al., 1974, Yanagisawa and Miake, 2003). Prolonged treatments of enamel to acid results in the 'hollowing' of the enamel rod structure (Poole and Johnson, 1967), revealing the keyhole shape of a rod which is comprised of rounded heads and narrow tails.

OCT has been widely used in assessment of demineralisation based on two main principles; increased light scattering in the porous demineralised tissue, and depolarisation of the incident light by the demineralised tissue (Mandurah et al., 2013). In caries lesions, the signal generally increases and the demineralised region appears brighter on the grayscale OCT images, because of the formation of numerous sub-micrometre size defects resulting from demineralisation in carious lesions (Bakhsh et al., 2011, Natsume et al., 2011). The increase is attributed to scattering at the numerous micro-interfaces created in the hard tissue between media of different refractive indices, due to increased porosity by such causes as the dissolution of minerals (Ibusuki et al., 2015). For OCT, the visible boundary between bright and dark areas on the grayscale OCT image was reported to be associated with the depth of lesion (Nazari et al., 2013). Several studies have confirmed demineralised lesions manifesting as regions of high back scattering underneath the enamel surfaces (Sadr et al., 2013, Nakajima et al., 2014) similar to natural caries images under OCT (Manesh et al., 2008).

Refractive index considerations

Refractive index is an important parameter of light propagation in biological tissues including teeth; indeed, scattering is the end result of local refractive index variation (Knu et al., 2004). OCT image contrast relies upon consequent differences in the backscattering characteristics of different materials.

In addition, refractive index bears diagnostic information as dental demineralisation induces local changes in the refractive index (Houwink, 1974). However, the 3D refractive index distribution of any given tooth will be unknown. OCT based measurements can utilise statistical estimates of refractive indices. However, interpretation of OCT results must take into account this ambiguity. Furthermore, care must be taken not to mistake shadowing, caused by strong surface scattering, for real morphology. Nevertheless, the correlation of surface projection images (Chapters 10 and 11) appears to work because of shadowing. Demineralisation decreases the visibility of the sub-lesional enamel, resulting in de-correlation of the surface volume projections. Remineralisation may partially increase the light transmission through the lesion by decreasing the refractive index mismatch. Thus, the sub-lesional enamel region regains some of its visibility and contributes to the projection image. Because the sub-lesional enamel remains unchanged, the correlation between sound and remineralised specimens increases. However, this is a working hypothesis and remains to be confirmed.

Characterisation of Erosive Lesions Depth

Some studies have used algorithms to automatically calculate the depth from the lesion area (Le et al., 2010). The researchers have tried various mathematical functions or algorithms to automatically process the signal or the image and determine the boundary on OCT B-scans. However, there has been little success in development of an optimized method that could work properly on the wide range of lesion depths for specimens (Natsume et al., 2011). For example, Le et al. tried to use an edge finding algorithm by computer processing for determining the lesion depth on enamel by using a constant value as a cut-off point in the signal intensity for the lesion depth. They defined the depth as a location where the intensity decreased to a dB value of ($1/e^2$) from the peak intensity; however, they mentioned that this approach was not always reliable. (Le et al., 2009).

Hence for the current study, lesion depth was measured using a manual measurement approach that involved measuring the erosive lesions from B-scan images using a simple line tool to measure the number of image pixels over which erosive depth and the enamel thickness extended.

This manual method was sufficient for measuring lesion depths of advanced erosive lesions but was not sensitive to very early stage lesions.

Correlation Analysis

Identification of erosion is difficult and most eroded teeth are not identified whilst the condition is still reversible. The most important part of erosive lesion management is to establish the diagnosis and control progression of the lesion.

Frequently, *in vitro* studies are conducted on advanced subsurface lesions rather than evaluating the early surface changes in the enamel. During the early lesion formation, The OCT signal is intimately related to functional disturbances in the tissue, which usually precede morphological changes (Podoleanu, 2014).

After the conclusion that direct physical measurement of erosive lesion depth were not sufficient for measuring early stage surface softening, a new approach was proposed based upon correlation of sequential OCT surface volume projections. This approach showed encouraging results, being capable of detecting early stages of demineralisation when remineralisation is still possible.

OCT can detect demineralisation because it is sensitive to light scattering. Light scattering is modified by changes to the microscopic tissue structure within the specimen. Therefore anything that causes change to the microstructure will be detected in OCT. However, OCT images are traditionally viewed in B-Scan cross-sections. In this view, surface changes are only represented by a thin line of pixels across the image. It is more efficient to utilise the 3D OCT data that represents that surface volume region. Integrating over the surface volume depth produces a projection image containing surface and sub-surface information. These projection images were compared sequentially on all images acquired during the acid challenge.

Changes to the enamel surface during early stage softening are subtle and challenging to measure. As mineral is lost from the apatite crystals, the signal propagation are expected to change. The location of erosion is different from that of caries. Erosion occurs at the surface. Therefore, optical changes in appearance of sub-surface structures, such as the DEJ, are due to physical changes occurring at the surface. The correlation of OCT images under erosion therefore showed a ‘de-correlation’ trend.

Carious lesions form a sub-surface lesion, whilst the surface remains is intact. Furthermore, a clear lesion boundary is formed, exhibited as a band of high backscatter. Additionally, beyond the lesion, the OCT signal is considerably attenuated and no subsurface structures are visible. As previously mentioned, the remineralisation process may have decreased the optical density of the lesion, thus revealing more sub-surface structure and increasing correlation with the sound enamel surface volume projection. The remineralised surface volume projection images show evidence of mineral deposition. However, the images are integrated over depth, so it is not possible to determine whether this is deposition at the surface of whether some component of the new mineral exists within the lesion body. To determine this would require further study, perhaps using SEM or FIB-SEM. However, even by using FIB-SEM to etch away the lesion structure, care must be taken not to misinterpret damage from sectioning as effects due to the demineralisation/remineralisation process.

Results from remineralisation are preliminary. They show that OCT is sensitive to changes that occur in the remineralisation experiment. However, more work is required to establish what physical changes are taking place and how these manifest in the correlation result.

Concluding remarks

OCT is a useful technique for visualising scattering materials at high resolution. This makes it attractive in clinical diagnostics. Dental enamel mineral loss is multi-factorial and is consequently explored using a variety of *in vitro* models. The simplified *in vitro* models used in this thesis were not intended to replicate the complex conditions in the oral environment, rather they allowed a strategic approach for controlling individual variables of a multi-factorial disease process. The focus of this thesis was to investigate the efficacy of using OCT to quantify enamel demineralisation in a controlled experimental framework. OCT based characterisation and comparison of demineralisation model dynamics is challenging without a consistent experimental environment. By eliminating various physiological factors it was possible to successfully determine the effects of different demineralisation solution dynamics on the enamel demineralisation process and show how different models exhibit differently under OCT analysis.

Further studies are required to investigate the corresponding effects of a dynamic pH cycling system in order to mimic the demineralisation and remineralisation equilibrium that takes place in the *in situ* environment.

OCT is a promising tool that could play a major role as dental practice realises a paradigm shift from dental disease intervention to dental disease prevention and management – known as minimally invasive dentistry. Clinical translation of the techniques developed in this thesis could facilitate the objective measurement of teeth at regular intervals using OCT to investigate whether the caries or erosion has been arrested and to monitor the effectiveness of treatments.

REFERENCES

ADDY, M. & SHELLIS, R. 2006. Interaction between attrition, abrasion and erosion in tooth wear.

ADEGUN, O. K., TOMLINS, P. H., HAGI-PAVLI, E., MCKENZIE, G., PIPER, K., BADER, D. L. & FORTUNE, F. 2012. Quantitative analysis of optical coherence tomography and histopathology images of normal and dysplastic oral mucosal tissues. *Lasers in medical science,* 27**,** 795-804.

AL-KHATEEB, S., TEN CATE, J., ANGMAR-MÅNSSON, B., DE JONG, E. D. J., SUNDSTRÖM, G., EXTERKATE, R. & OLIVEBY, A. 1997. Quantification of formation and remineralization of artificial enamel lesions with a new portable fluorescence device. *Advances in Dental Research,* 11**,** 502-506.

ALMASIAN, M., BOSSCHAART, N., VAN LEEUWEN, T. G. & FABER, D. J. 2015. Validation of quantitative attenuation and backscattering coefficient measurements by optical coherence tomography in the concentration-dependent and multiple scattering regime. *Journal of biomedical optics,* 20**,** 121314-121314.

ALTSHULER, G. B., GRISIMOV, V. N., ERMOLAEV, V. S. & VITYAZ, I. V. Human tooth as an optical device. Optics, Electro-Optics, and Laser Applications in Science and Engineering, 1991. International Society for Optics and Photonics, 95-104.

AMAECHI, B. & HIGHAM, S. 2001. In vitro remineralisation of eroded enamel lesions by saliva. *Journal of Dentistry,* 29**,** 371-376.

AMAECHI, B., HIGHAM, S., PODOLEANU, A., ROGERS, J. & JACKSON, D. 2001. Use of optical coherence tomography for assessment of dental caries: quantitative procedure. *J Oral Rehabil,* 28**,** 1092-1093.

AMAECHI, B., PODOLEANU, A. G., KOMAROV, G., ROGERS, J., HIGHAM, S. & JACKSON, D. 2003a. Application of optical coherence tomography for imaging and assessment of early dental caries lesions. *LASER PHYSICS-LAWRENCE-,* 13**,** 703-710.

AMAECHI, B. T. & HIGHAM, S. M. 2002. Quantitative light-induced fluorescence: a potential tool for general dental assessment. *Journal of biomedical optics,* 7**,** 7-13.

AMAECHI, B. T., HIGHAM, S. M. & EDGAR, W. M. 1999. Factors influencing the development of dental erosion in vitro: enamel type, temperature and exposure time. *J Oral Rehabil,* 26**,** 624-30.

AMAECHI, B. T., PODOLEANU, A., HIGHAM, S. M. & JACKSON, D. A. 2003b. Correlation of quantitative light-induced fluorescence and optical coherence tomography applied for detection and quantification of early dental caries. *J Biomed Opt,* 8**,** 642-7.

AMAECHI, B. T., PODOLEANU, A. G., KOMAROV, G., HIGHAM, S. M. & JACKSON, D. A. 2004. Quantification of root caries using optical coherence tomography and microradiography: a correlational study. *Oral Health Prev Dent,* 2**,** 377-382.

ANDERSON, P., BOLLET-QUIVOGNE, F., DOWKER, S. & ELLIOTT, J. 2004. Demineralization in enamel and hydroxyapatite aggregates at increasing ionic strengths. *Archives of oral biology,* 49**,** 199-207.

ANDERSON, P. & ELLIOTT, J. 1992. Subsurface demineralization in dental enamel and other permeable solids during acid dissolution. *Journal of dental research,* 71**,** 1473-1481.

ANDERSON, P., ELLIOTT, J., BOSE, U. & JONES, S. 1996. A comparison of the mineral content of enamel and dentine in human premolars and enamel pearls measured by X-ray microtomography. *Archives of oral biology,* 41**,** 281-290.

ANDERSON, P., LEVINKIND, M. & ELLIOTT, J. 1998. Scanning microradiographic studies of rates of< i> in vitro</i> demineralization in human and bovine dental enamel. *Archives of Oral Biology,* 43**,** 649-656.

ARENDS, J., SCHUTHOF, J. & JONGEBLOED, W. 1980. Lesion depth and microhardness indentations on artificial white spot lesions. *Caries research,* 14**,** 190-195.

ARENDS, J. & TEN BOSCH, J. 1992. Demineralization and remineralization evaluation techniques. *J Dent Res,* 71.

ARENDS, J. & TEN CATE, J. 1981. Tooth enamel remineralization. *Journal of Crystal Growth,* 53**,** 135-147.

ARGENTA, R. M. O., TABCHOURY, C. P. M. & CURY, J. A. 2003. A modified pH-cycling model to evaluate fluoride effect on enamel demineralization. *Pesquisa Odontológica Brasileira,* 17**,** 241-246.

ATTIN, T. 2006. Methods for assessment of dental erosion. *Monographs in Oral Science,* 20**,** 152.

ATTIN, T., BUCHALLA, W., GOLLNER, M. & HELLWIG, E. 1999. Use of variable remineralization periods to improve the abrasion resistance of previously eroded enamel. *Caries research,* 34**,** 48-52.

ATTIN, T., KOIDL, U., BUCHALLA, W., SCHALLER, H., KIELBASSA, A. & HELLWIG, E. 1997. Correlation of microhardness and wear in differently eroded bovine dental enamel. *Archives of oral biology,* 42**,** 243-250.

ATTIN, T., MEYER, K., HELLWIG, E., BUCHALLA, W. & LENNON, A. 2003. Effect of mineral supplements to citric acid on enamel erosion. *Archives of oral biology,* 48**,** 753-759.

ATTIN, T., WEISS, K., BECKER, K., BUCHALLA, W. & WIEGAND, A. 2005. Impact of modified acidic soft drinks on enamel erosion. *Oral diseases,* 11**,** 7-12.

AZZOPARDI, A., BARTLETT, D., WATSON, T. & SHERRIFF, M. 2001. The measurement and prevention of erosion and abrasion. *Journal of dentistry,* 29**,** 395-400.

BADER, J. D., SHUGARS, D. A., ROZIER, G., LOHR, K. N., BONITO, A. J., NELSON, J. P. & JACKMAN, A. M. 2001. Diagnosis and Management of Dental Caries: Summary.

BAKHSH, T. A., SADR, A., SHIMADA, Y., TAGAMI, J. & SUMI, Y. 2011. Non-invasive quantification of resin–dentin interfacial gaps using optical coherence tomography: validation against confocal microscopy. *dental materials,* 27**,** 915-925.

BARBOUR, M. & REES, J. 2004. The laboratory assessment of enamel erosion: a review. *Journal of dentistry,* 32**,** 591-602.

BARBOUR, M. E., PARKER, D. M., ALLEN, G. C. & JANDT, K. D. 2003. Human enamel dissolution in citric acid as a function of pH in the range 2.30≤ pH≤ 6.30–a nanoindentation study. *European journal of oral sciences,* 111**,** 258-262.

BARDSLEY, P., TAYLOR, S. & MILOSEVIC, A. 2004. Epidemiological studies of tooth wear and dental erosion in 14-year-old children in North West England. Part 1: The relationship with water fluoridation and social deprivation. *British Dental Journal,* 197**,** 413-416.

BARTLETT, D. W., ANGGIANSAH, A., OWEN, W., EVANS, D. F. & SMITH, B. G. 1994. Dental erosion: a presenting feature of gastro-oesophageal reflux disease. *European Journal of Gastroenterology & Hepatology,* 6**,** 895-900.

BASHIR, E., EKBERG, O. & LAGERLÖF, F. 1995. Salivary clearance of citric acid after an oral rinse. *Journal of dentistry,* 23**,** 209-212.

BAUMGARTNER, A., DICHTL, S., HITZENBERGER, C., SATTMANN, H., ROBL, B., MORITZ, A., FERCHER, A. & SPERR, W. 1999. Polarization–Sensitive Optical Coherence Tomography of Dental Structures. *Caries research,* 34**,** 59-69.

BORN, M. & WOLF, E. 2000. *Principles of optics: electromagnetic theory of propagation, interference and diffraction of light*, CUP Archive.

BOUMA, B. 2001. *Handbook of optical coherence tomography,* Informa Health Care.

BOYDE, A. & LESTER, K. 1967. Electron microscopy of resorbing surfaces of dental hard tissues. *Zeitschrift für Zellforschung und mikroskopische Anatomie,* 83**,** 538-548.

BRANDENBURG, R., HALLER, B. & HAUGER, C. 2003. Real-time in vivo imaging of dental tissue by means of optical coherence tomography (OCT). *Optics communications,* 227**,** 203-211.

BREZINSKI, M. E. 2006. *Optical coherence tomography: principles and applications*, Academic press.

CAN, A. M., DARLING, C. L., HO, C. & FRIED, D. 2008. Non‐destructive assessment of inhibition of demineralization in dental enamel irradiated by a λ = 9.3‐μm CO2 laser at ablative irradiation intensities with PS‐OCT. *Lasers in Surgery and Medicine,* 40**,** 342-349.

CARLSTRÖM, D., GLAS, J.-E. & ANGMAR, B. 1963. Studies on the ultrastructure of dental enamel: V. The state of water in human enamel. *Journal of ultrastructure research,* 8**,** 24-29.

CASA, D. J., CLARKSON, P. M. & ROBERTS, W. O. 2005. American College of Sports Medicine roundtable on hydration and physical activity: consensus statements. *Current sports medicine reports,* 4**,** 115-127.

CAUFIELD, P. W. & GRIFFEN, A. L. 2000. Dental caries: an infectious and transmissible disease. *Pediatric Clinics of North America,* 47**,** 1001-1019.

CHAN, A. C., DARLING, C. L., CHAN, K. H. & FRIED, D. Attenuation of near-IR light through dentin at wavelengths from 1300-1650-nm. SPIE BiOS, 2014. International Society for Optics and Photonics, 89290M-89290M-5.

CHAN, K. H., CHAN, A. C., DARLING, C. L. & FRIED, D. Methods for monitoring erosion using optical coherence tomography. SPIE BiOS, 2013. International Society for Optics and Photonics, 856606-856606-6.

CHAN, K. H., CHAN, A. C., FRIED, W. A., SIMON, J. C., DARLING, C. L. & FRIED, D. 2015. Use of 2D images of depth and integrated reflectivity to represent the severity of demineralization in cross‐polarization optical coherence tomography. *Journal of biophotonics,* 8**,** 36-45.

CHENG, R., YANG, H., SHAO, M.-Y., HU, T. & ZHOU, X.-D. 2009a. Dental erosion and severe tooth decay related to soft drinks: a case report and literature review. *Journal of Zhejiang University SCIENCE B,* 10**,** 395-399.

CHENG, Z.-J., WANG, X.-M., CUI, F.-Z., GE, J. & YAN, J.-X. 2009b. The enamel softening and loss during early erosion studied by AFM, SEM and nanoindentation. *Biomedical Materials,* 4**,** 015020.

CHEONG, W.-F., PRAHL, S. A. & WELCH, A. J. 1990. A review of the optical properties of biological tissues. *IEEE journal of quantum electronics,* 26**,** 2166-2185.

CHEW, H., ZAKIAN, C., PRETTY, I. & ELLWOOD, R. 2014. Measuring Initial Enamel Erosion with Quantitative Light-Induced Fluorescence and Optical Coherence Tomography: An in vitro Validation Study. *Caries research,* 48**,** 254-262.

CHINGA, G. & SYVERUD, K. 2007. Quantification of paper mass distributions within local picking areas. *NORDIC PULP & PAPER RESEARCH JOURNAL,* 22**,** 441-446.

CHONG, S. L., DARLING, C. L. & FRIED, D. 2007. Nondestructive measurement of the inhibition of demineralization on smooth surfaces using polarization‐sensitive optical coherence tomography. *Lasers in surgery and medicine,* 39**,** 422-427.

CHOUDHURY, N. & JACQUES, S. L. Extracting scattering coefficient and anisotropy factor of tissue using optical coherence tomography. SPIE BiOS, 2012. International Society for Optics and Photonics, 822111-822111-5.

COCHRANE, N. J., ANDERSON, P., DAVIS, G. R., ADAMS, G. G., STACEY, M. A. & REYNOLDS, E. C. 2012. An X-ray Microtomographic Study of Natural White-spot Enamel Lesions. *J Dent Res,* 91**,** 185-191.

COLSTON, B., SATHYAM, U., DASILVA, L., EVERETT, M., STROEVE, P. & OTIS, L. 1998. Dental oct. *Optics Express,* 3**,** 230-238.

COLSTON JR, B. W., EVERETT, M. J., DA SILVA, L. B., OTIS, L. L., STROEVE, P. & NATHEL, H. 1998. Imaging of hard-and soft-tissue structure in the oral cavity by optical coherence tomography. *Applied Optics,* 37**,** 3582-3585.

CÔRTES, D., ELLWOOD, R. & EKSTRAND, K. 2003. An in vitro comparison of a combined FOTI/visual examination of occlusal caries with other caries diagnostic methods and the effect of stain on their diagnostic performance. *Caries research,* 37**,** 8-16.

CURY, J. A. & TENUTA, L. M. A. 2009. Enamel remineralization: controlling the caries disease or treating early caries lesions? *Brazilian oral research,* 23**,** 23-30.

DAMEN, J., BUIJS, M. & TEN CATE, J. 1998. Fluoride–Dependent Formation of Mineralized Layers in Bovine Dentin during Demineralization in vitro. *Caries research,* 32**,** 435-440.

DARLING, A. 1956. Studies of the early carious lesion with transmitted light, polarised light and radiography. *Brit. dent. J.,* 101**,** 289-297.

DARLING, A. 1961. The Selective Attack of Caries on the Dental Enamel: Charles Tomes Lecture delivered at the Royal College of Surgeons of England on 21st July 1961. *Annals of the Royal College of Surgeons of England,* 29**,** 354.

DARLING, C. L., HUYNH, G. D. & FRIED, D. 2006. Light scattering properties of natural and artificially demineralized dental enamel at 1310nm. *Journal of Biomedical Optics,* 11**,** 034023-034023-11.

DAVIS, G., DOWKER, S., ELLIOTT, J., ANDERSON, P., WASSIF, H., BOYDE, A., GOODSHIP, A., STOCK, S. & IGNATIEV, K. 2002. Non-destructive 3D structural studies by X-ray microtomography. *Advances in X-ray Analysis. Newtown Square, International Centre for Diffraction Data,* 45**,** 485-490.

DAVIS, G. R., EVERSHED, A. N. & MILLS, D. 2013. Quantitative high contrast X-ray microtomography for dental research. *Journal of dentistry,* 41**,** 475-482.

DE CARA, A. C. B., ZEZELL, D. M., ANA, P. A., DEANA, A. M., AMARAL, M. M., VIEIRA JR, N. D. & DE FREITAS, A. Z. Comparative analysis of optical coherence tomography signal and microhardness for demineralization evaluation of human tooth enamel. SPIE Photonics Europe, 2012. International Society for Optics and Photonics, 84271H-84271H-10.

DE JONG, E. D. J., VAN DER LINDEN, A. & TEN BOSCH, J. 1987. Longitudinal microradiography: a non-destructive automated quantitative method to follow mineral changes in mineralised tissue slices. *Physics in medicine and biology,* 32**,** 1209.

DE JOSSELIN DE JONG, E., SUNDSTRÖM, F., WESTERLING, H., TRANAEUS, S., TEN BOSCH, J. & ANGMAR-MÅNSSON, B. 1995. A new method for in vivo quantification of changes in initial enamel caries with laser fluorescence. *Caries research,* 29**,** 2-7.

DEVLIN, H., BASSIOUNY, M. & BOSTON, D. 2006. Hardness of enamel exposed to Coca‐Cola® and artificial saliva. *Journal of Oral Rehabilitation,* 33**,** 26-30.

DOWKER, S., ANDERSON, P., ELLIOTT, J. & GAO, X. 1999. Crystal chemistry and dissolution of calcium phosphate in dental enamel. *Mineralogical Magazine,* 63**,** 791-791.

DOWKER, S. E., DAVIS, G. R. & ELLIOTT, J. C. 1997. X-ray microtomography: nondestructive three-dimensional imaging for in vitro endodontic studies. *Oral Surgery, Oral Medicine, Oral Pathology, Oral Radiology, and Endodontology,* 83**,** 510-516.

DREXLER, W. & FUJIMOTO, J. G. 2008. *Optical coherence tomography: technology and applications*, Springer.

EHLEN, L. A., MARSHALL, T. A., QIAN, F., WEFEL, J. S. & WARREN, J. J. 2008. Acidic beverages increase the risk of in vitro tooth erosion. *Nutrition Research,* 28**,** 299-303.

EISENBURGER, M., ADDY, M., HUGHES, J. & SHELLIS, R. 2001. Effect of time on the remineralisation of enamel by synthetic saliva after citric acid erosion. *Caries research,* 35**,** 211-215.

EISENBURGER, M., HUGHES, J., WEST, N., JANDT, K. & ADDY, M. 2000. Ultrasonication as a method to study enamel demineralisation during acid erosion. *Caries research,* 34**,** 289-294.

ELLIOTT, J., WONG, F., ANDERSON, P., DAVIS, G. & DOWKER, S. 1998. Determination of mineral concentration in dental enamel from X-ray attenuation measurements. *Connective tissue research,* 38**,** 61-72.

ELLIOTT, J. C. 2013. *Structure and chemistry of the apatites and other calcium orthophosphates*, Elsevier.

ELTON, V., COOPER, L., HIGHAM, S. M. & PENDER, N. 2009. Validation of enamel erosion in vitro. *Journal of Dentistry*, 37**,** 336-341.

ENFIELD, J., JONATHAN, E. & LEAHY, M. 2011. In vivo imaging of the microcirculation of the volar forearm using correlation mapping optical coherence tomography (cmOCT). *Biomedical optics express*, 2**,** 1184-1193.

EVERETT, M. J., COLSTON JR, B. W., SATHYAM, U. S., DA SILVA, L. B., FRIED, D. & FEATHERSTONE, J. D. Noninvasive diagnosis of early caries with polarization-sensitive optical coherence tomography (PS-OCT). BiOS'99

International Biomedical Optics Symposium, 1999. International Society for Optics and Photonics, 177-182.
FABER, D. J., VAN DER MEER, F. J., AALDERS, M. C. & VAN LEEUWEN, T. G. 2004. Quantitative measurement of attenuation coefficients of weakly scattering media using optical coherence tomography. *Optics express,* 12**,** 4353-4365.
FEATHERSTONE, J. 2004. The continuum of dental caries—evidence for a dynamic disease process. *Journal of dental research,* 83**,** C39-C42.
FEATHERSTONE, J. 2008. Dental caries: a dynamic disease process. *Australian dental journal,* 53**,** 286-291.
FEATHERSTONE, J., DUNCAN, J. & CUTRESS, T. 1979. A mechanism for dental caries based on chemical processes and diffusion phenomena during in-vitro caries simulation on human tooth enamel. *Archives of oral biology,* 24**,** 101-112.
FEATHERSTONE, J., O'REILLY, M., SHARIATI, M. & BRUGLER, S. 1986. Enhancement of remineralization in vitro and in vivo. Factors relating to demineralisation and remineralisation of the teeth. IRL Press. Oxford and Washington.
FEATHERSTONE, J., TEN CATE, J., SHARIATI, M. & ARENDS, J. 1983. Comparison of artificial caries-like lesions by quantitative microradiography and microhardness profiles. *Caries research,* 17**,** 385-391.
FEATHERSTONE, J. D. 2000. The science and practice of caries prevention. *The Journal of the American dental association,* 131**,** 887-899.
FEJERSKOV, O. & KIDD, E. 2009. *Dental caries: the disease and its clinical management*, John Wiley & Sons.
FELDCHTEIN, F., GELIKONOV, V., IKSANOV, R., GELIKONOV, G., KURANOV, R., SERGEEV, A., GLADKOVA, N., OURUTINA, M., REITZE, D. & WARREN, J. 1998. In vivo OCT imaging of hard and soft tissue of the oral cavity. *Optics Express,* 3**,** 239-250.
FERCHER, A. F., DREXLER, W., HITZENBERGER, C. K. & LASSER, T. 2003. Optical coherence tomography-principles and applications. *Reports on progress in physics,* 66**,** 239.
FERCHER, A. F., HITZENBERGER, C. K., DREXLER, W., KAMP, G. & SATTMANN, H. 1993. In-Vivo Optical Coherence Tomography. *American Journal of Ophthalmology,* 116**,** 113-115.
FERNANDES, C. P. & CHEVITARESE, O. 1991. The orientation and direction of rods in dental enamel. *The Journal of prosthetic dentistry,* 65**,** 793-800.
FIELD, J., WATERHOUSE, P. & GERMAN, M. 2010. Quantifying and qualifying surface changes on dental hard tissues in vitro. *journal of dentistry,* 38**,** 182-190.
FONTANA, M., LI, Y., DUNIPACE, A., NOBLITT, T., FISCHER, G., KATZ, B. & STOOKEY, G. 1996. Measurement of enamel demineralization using microradiography and confocal microscopy. *Caries research,* 30**,** 317-325.
FOUAD, A., PFEFER, T. J., CHEN, C.-W., GONG, W., AGRAWAL, A., TOMLINS, P. H., WOOLLIAMS, P. D., DREZEK, R. A. & CHEN, Y. 2014. Variations in optical coherence tomography resolution and uniformity: a multi-system performance comparison. *Biomedical optics express,* 5**,** 2066-2081.
FRIED, D., GLENA, R. E., FEATHERSTONE, J. D. & SEKA, W. 1995. Nature of light scattering in dental enamel and dentin at visible and near-infrared wavelengths. *Applied optics,* 34**,** 1278-1285.

FRIED, D., XIE, J., SHAFI, S., FEATHERSTONE, J. D., BREUNIG, T. M. & LE, C. 2002. Imaging caries lesions and lesion progression with polarization sensitive optical coherence tomography. *Journal of Biomedical Optics,* 7**,** 618-627.

FUJIMOTO, J. 2003a. Optical coherence tomography: principles and applications. *REVIEW OF LASER ENGINEERING-LASER SOCIETY OF JAPAN,* 31**,** 635-642.

FUJIMOTO, J. G. 2003b. Optical coherence tomography for ultrahigh resolution in vivo imaging. *Nature biotechnology,* 21**,** 1361-1367.

GANSS, C., KLIMEK, J. & SCHWARZ, N. 2000. A comparative profilometric in vitro study of the susceptibility of polished and natural human enamel and dentine surfaces to erosive demineralization. *Archives of oral biology,* 45**,** 897-902.

GARG, N. & GARG, A. 2010. *Textbook of operative dentistry,* Boydell & Brewer Ltd.

GOMEZ, J. 2015. Detection and diagnosis of the early caries lesion. *BMC oral health,* 15**,** S3.

GOMEZ, J., ZAKIAN, C., SALSONE, S., PINTO, S., TAYLOR, A., PRETTY, I. & ELLWOOD, R. 2013. In vitro performance of different methods in detecting occlusal caries lesions. *Journal of dentistry,* 41**,** 180-186.

GOODHEW, P. J., HUMPHREYS, J. & BEANLAND, R. 2000. *Electron microscopy and analysis,* CRC Press.

GROENEVELD, A., JONGEBLOED, W. & ARENDS, J. 1974. The mineral content of decalcified surface enamel. *Caries research,* 8**,** 267-274.

HALL, A., SADLER, J., STRANG, R., DE JONG, E. D. J., FOYE, R. & CREANOR, S. 1997. Application of transverse microradiography for measurement of mineral loss by acid erosion. *Advances in dental research,* 11**,** 420-425.

HANNIG, M. & HANNIG, C. 2010. Nanomaterials in preventive dentistry. *Nature nanotechnology,* 5**,** 565-569.

HARA, A. T. & ZERO, D. T. 2008. Analysis of the erosive potential of calcium‐containing acidic beverages. *European Journal of Oral Sciences,* 116**,** 60-65.

HARIRI, I., SADR, A., NAKASHIMA, S., SHIMADA, Y., TAGAMI, J. & SUMI, Y. 2012a. Estimation of the enamel and dentin mineral content from the refractive index. *Caries research,* 47**,** 18-26.

HARIRI, I., SADR, A., SHIMADA, Y., TAGAMI, J. & SUMI, Y. 2012b. Effects of structural orientation of enamel and dentine on light attenuation and local refractive index: An optical coherence tomography study. *Journal of Dentistry,* 40**,** 387-396.

HENRIQUES, R., GRIFFITHS, C., HESPER REGO, E. & MHLANGA, M. M. 2011. PALM and STORM: Unlocking live‐cell super‐resolution. *Biopolymers,* 95**,** 322-331.

HEURICH, E., BEYER, M., JANDT, K. D., REICHERT, J., HEROLD, V., SCHNABELRAUCH, M. & SIGUSCH, B. W. 2010. Quantification of dental erosion—a comparison of stylus profilometry and confocal laser scanning microscopy (CLSM). *Dental Materials,* 26**,** 326-336.

HIBST, R., PAULUS, R. & LUSSI, A. 2001. Detection of occlusal caries by laser fluorescence: basic and clinical investigations. *Medical Laser Application,* 16**,** 205-213.

HIGUCHI, T. & CONNORS, A. 1965. Phase-solubility techniques.

HONÓRIO, H., RIOS, D., SANTOS, C., MAGALHÃES, A., BUZALAF, M. & MACHADO, M. 2008. Effects of erosive, cariogenic or combined erosive/cariogenic challenges on human enamel. *Caries research,* 42**,** 454-459.

HOUWINK, B. 1974. The index of refraction of dental enamel apatite. *British dental journal,* 137**,** 472-475.

HUANG, D., SWANSON, E. A., LIN, C. P., SCHUMAN, J. S., STINSON, W. G., CHANG, W., HEE, M. R., FLOTTE, T., GREGORY, K. & PULIAFITO, C. A. 1991. Optical coherence tomography. *Science,* 254**,** 1178-1181.

HUGHES, J., WEST, N., PARKER, D., VAN DEN BRAAK, M. & ADDY, M. 2000. Effects of pH and concentration of citric, malic and lactic acids on enamel, in vitro. *Journal of Dentistry,* 28**,** 147-152.

HUYSMANS, M.-C. & LONGBOTTOM, C. 2004. The challenges of validating diagnostic methods and selecting appropriate gold standards. *J Dent Res,* 83**,** C48-C52.

HUYSMANS, M. C., CHEW, H. P. & ELLWOOD, R. P. 2011. Clinical studies of dental erosion and erosive wear. *Caries Res,* 45 Suppl 1**,** 60-8.

IBUSUKI, T., KITASAKO, Y., SADR, A., SHIMADA, Y., SUMI, Y. & TAGAMI, J. 2015. Observation of white spot lesions using swept source optical coherence tomography (SS-OCT): in vitro and in vivo study. *Dental materials journal,* 34**,** 545-552.

IMAI, K., SHIMADA, Y., SADR, A., SUMI, Y. & TAGAMI, J. 2012. Noninvasive Cross-sectional Visualization of Enamel Cracks by Optical Coherence Tomography< i> In Vitro</i>. *Journal of endodontics,* 38**,** 1269-1274.

ISMAIL, A., SOHN, W., TELLEZ, M., AMAYA, A., SEN, A., HASSON, H. & PITTS, N. 2007. The International Caries Detection and Assessment System (ICDAS): an integrated system for measuring dental caries. *Community dentistry and oral epidemiology,* 35**,** 170-178.

JACQUES, S. L. 2013. Optical properties of biological tissues: a review. *Physics in medicine and biology,* 58**,** R37.

JAEGGI, T. & LUSSI, A. 2006. Prevalence, incidence and distribution of erosion. *Dental Erosion.* Karger Publishers.

JOHANSSON, A. K., LINGSTRÖM, P. & BIRKHED, D. 2002. Comparison of factors potentially related to the occurrence of dental erosion in high‐and low‐erosion groups. *European journal of oral sciences,* 110**,** 204-211.

JONES, R. & FRIED, D. 2006. Remineralization of enamel caries can decrease optical reflectivity. *J Dent Res,* 85**,** 804-808.

JONES, R. S., DARLING, C. L., FEATHERSTONE, J. D. & FRIED, D. 2006a. Imaging artificial caries on the occlusal surfaces with polarization-sensitive optical coherence tomography. *Caries Res,* 40**,** 81-9.

JONES, R. S., DARLING, C. L., FEATHERSTONE, J. D. & FRIED, D. 2006b. Remineralization of in vitro dental caries assessed with polarization-sensitive optical coherence tomography. *J Biomed Opt,* 11**,** 014016.

JONES, R. S., STANINEC, M. & FRIED, D. 2004. Imaging artificial caries under composite sealants and restorations. *Journal of Biomedical Optics,* 9**,** 1297-1304.

KANG, H., CHAN, K., DARLING, C. L. & FRIED, D. Monitoring the remineralization of early simulated lesions using a pH cycling model with CP-OCT. SPIE BiOS, 2013. International Society for Optics and Photonics, 85660J-85660J-6.

KANG, H., DARLING, C. L. & FRIED, D. 2012a. Nondestructive monitoring of the repair of enamel artificial lesions by an acidic remineralization model using polarization-sensitive optical coherence tomography. *Dental Materials,* 28**,** 488-494.

KANG, H., DARLING, C. L. & FRIED, D. Nondestructive monitoring of the repair of natural occlusal lesions using cross polarization optical coherence tomography. SPIE BiOS, 2012b. International Society for Optics and Photonics, 82080X-82080X-7.

KANG, H., DARLING, C. L. & FRIED, D. Enhancing the detection of hidden occlusal caries lesions with OCT using high index liquids. SPIE BiOS, 2014. International Society for Optics and Photonics, 89290O-89290O-7.

KARLSSON, L. 2010. Caries detection methods based on changes in optical properties between healthy and carious tissue. *International journal of dentistry,* 2010.

KAUR, S., MAKKAR, S., KUMAR, R., PASRICHA, S. & GUPTA, P. 2015. Comparative evaluation of surface properties of enamel and different esthetic restorative materials under erosive and abrasive challenges: An in vitro study. *Indian journal of dentistry,* 6**,** 172.

KENNEDY, B. F., KENNEDY, K. M. & SAMPSON, D. D. 2014. A review of optical coherence elastography: fundamentals, techniques and prospects. *Ieee Journal of Selected Topics in Quantum Electronics,* 20**,** 272-288.

KHOLODNYKH, A. I., PETROVA, I. Y., LARIN, K. V., MOTAMEDI, M. & ESENALIEV, R. O. 2003. Precision of measurement of tissue optical properties with optical coherence tomography. *Applied optics,* 42**,** 3027-3037.

KIDD, E., GIEDRYS-LEEPER, E. & SIMONS, D. 2000. Take two dentists: a tale of root caries. *Dental update,* 27**,** 222-230.

KIELBASSA, A. M., WRBAS, K.-T., SCHULTE-MÖNTING, J. & HELLWIG, E. 1999. Correlation of transversal microradiography and microhardness on in situ-induced demineralization in irradiated and nonirradiated human dental enamel. *Archives of oral biology,* 44**,** 243-251.

KILCAST, D. & SUBRAMANIAM, P. 2011. *Food and beverage stability and shelf life,* Elsevier.

KITASAKO, Y., TANAKA, M., SADR, A., HAMBA, H., IKEDA, M. & TAGAMI, J. 2011. Effects of a chewing gum containing phosphoryl oligosaccharides of calcium (POs-Ca) and fluoride on remineralization and crystallization of enamel subsurface lesions in situ. *Journal of dentistry,* 39**,** 771-779.

KNU, A., BONEV, S. & KNAAK, W. 2004. New method for evaluation of in vivo scattering and refractive index properties obtained with optical coherence tomography. *Journal of biomedical optics,* 9**,** 265-273.

KO, C., TANTBIROJN, D., WANG, T. & DOUGLAS, W. 2000. Optical scattering power for characterization of mineral loss. *J Dent Res,* 79**,** 1584-1589.

KODACH, V., FABER, D., VAN MARLE, J., VAN LEEUWEN, T. & KALKMAN, J. 2011. Determination of the scattering anisotropy with optical coherence tomography. *Optics express,* 19**,** 6131-6140.

LANDIS, E. N. & KEANE, D. T. 2010. X-ray microtomography. *Materials characterization,* 61**,** 1305-1316.

LARSEN, M. & PEARCE, E. 2003. Saturation of human saliva with respect to calcium salts. *Archives of Oral Biology,* 48**,** 317-322.

LAURANCE-YOUNG, P., BOZEC, L., GRACIA, L., REES, G., LIPPERT, F., LYNCH, R. & KNOWLES, J. 2011. A review of the structure of human and

bovine dental hard tissues and their physicochemical behaviour in relation to erosive challenge and remineralisation. *Journal of dentistry,* 39**,** 266-272.

LE, M. H., DARLING, C. L. & FRIED, D. Methods for calculating the severity of demineralization on tooth surfaces from PS-OCT scans. SPIE BiOS: Biomedical Optics, 2009. International Society for Optics and Photonics, 71620U-71620U-7.

LE, M. H., DARLING, C. L. & FRIED, D. 2010. Automated analysis of lesion depth and integrated reflectivity in PS‐OCT scans of tooth demineralization. *Lasers in surgery and medicine,* 42**,** 62-68.

LEE, C., DARLING, C. L. & FRIED, D. 2009. Polarization-sensitive optical coherence tomographic imaging of artificial demineralization on exposed surfaces of tooth roots. *Dent Mater,* 25**,** 721-8.

LENTON, P., RUDNEY, J., CHEN, R., FOK, A., APARICIO, C. & JONES, R. S. 2012. Imaging in vivo secondary caries and ex vivo dental biofilms using cross-polarization optical coherence tomography. *Dent Mater,* 28**,** 792-800.

LEVITZ, D., HINDS, M. T., CHOUDHURY, N., TRAN, N. T., HANSON, S. R. & JACQUES, S. L. 2010. Quantitative characterization of developing collagen gels using optical coherence tomography. *Journal of biomedical optics,* 15**,** 026019-026019-11.

LEVITZ, D., THRANE, L., FROSZ, M., ANDERSEN, P., ANDERSEN, C., ANDERSSON-ENGELS, S., VALANCIUNAITE, J., SWARTLING, J. & HANSEN, P. 2004. Determination of optical scattering properties of highly-scattering media in optical coherence tomography images. *Optics express,* 12**,** 249-259.

LOESCHE, W. J. 1982. *Dental caries: a treatable infection*, University of Michigan School of Dentistry.

LOWE, N., AUTY, J. & ROBINSON, C. Changes in Protein of Mineralizing Enamel. Journal of Dental Research, 1971. AMER ASSOC DENTAL RESEARCH 1619 DUKE ST, ALEXANDRIA, VA 22314, 693-&.

LUSSI, A., HIBST, R. & PAULUS, R. 2004. DIAGNOdent: an optical method for caries detection. *Journal of Dental Research,* 83**,** C80-C83.

LUSSI, A., IMWINKELRIED, S., PITTS, N., LONGBOTTOM, C. & REICH, E. 1999. Performance and reproducibility of a laser fluorescence system for detection of occlusal caries in vitro. *Caries research,* 33**,** 261-266.

LUSSI, A. & JAEGGI, T. 2008. Erosion—diagnosis and risk factors. *Clinical oral investigations,* 12**,** 5-13.

LUSSI, A., SCHLUETER, N., RAKHMATULLINA, E. & GANSS, C. 2011. Dental erosion--an overview with emphasis on chemical and histopathological aspects. *Caries Res,* 45 Suppl 1**,** 2-12.

MAIA, A. M. A., FREITAS, A. Z., L CAMPELLO, S., GOMES, A. S. L. & KARLSSON, L. 2015. Evaluation of dental enamel caries assessment using Quantitative Light Induced Fluorescence and Optical Coherence Tomography. *Journal of biophotonics.*

MANDURAH, M. M., SADR, A., SHIMADA, Y., KITASAKO, Y., NAKASHIMA, S., BAKHSH, T. A., TAGAMI, J. & SUMI, Y. 2013. Monitoring remineralization of enamel subsurface lesions by optical coherence tomography. *Journal of Biomedical Optics,* 18**,** 046006-046006.

MANESH, S. K., DARLING, C. L. & FRIED, D. Imaging natural and artificial demineralization on dentin surfaces with polarization sensitive optical

coherence tomography. Biomedical Optics (BiOS) 2008, 2008. International Society for Optics and Photonics, 68430M-68430M-7.

MARGOLIS, H. & MORENO, E. 1992. Kinetics of hydroxyapatite dissolution in acetic, lactic, and phosphoric acid solutions. *Calcified tissue international,* 50**,** 137-143.

MARGOLIS, H., ZHANG, Y., LEE, C., KENT, R. & MORENO, E. 1999. Kinetics of enamel demineralization in vitro. *Journal of dental research,* 78**,** 1326-1335.

MCLAUGHLIN, R. A., SCOLARO, L., ROBBINS, P., SAUNDERS, C., JACQUES, S. L. & SAMPSON, D. D. 2010. Parametric imaging of cancer with optical coherence tomography. *Journal of biomedical optics,* 15**,** 046029-046029-4.

MELLBERG, J. 1992. Hard-tissue substrates for evaluation of cariogenic and anti-cariogenic activity in situ. *Journal of dental research,* 71**,** 913-919.

MENG, Z., YAO, H., LIANG, Y., LI, Y., LAN, S., WANG, G., LIU, T. & YAO, X. S. 2009. Measurement of the refractive index of human teeth by optical coherence tomography. *Journal of biomedical optics,* 14**,** 034010-034010-4.

MEREDITH, N., SHERRIFF, M., SETCHELL, D. & SWANSON, S. 1996. Measurement of the microhardness and Young's modulus of human enamel and dentine using an indentation technique. *Archives of Oral Biology,* 41**,** 539-545.

NAKAGAWA, H., SADR, A., SHIMADA, Y., TAGAMI, J. & SUMI, Y. 2013. Validation of swept source optical coherence tomography (SS-OCT) for the diagnosis of smooth surface caries in vitro. *Journal of dentistry,* 41**,** 80-89.

NAKAJIMA, Y., SHIMADA, Y., SADR, A., WADA, I., MIYASHIN, M., TAKAGI, Y., TAGAMI, J. & SUMI, Y. 2014. Detection of occlusal caries in primary teeth using swept source optical coherence tomography. *Journal of biomedical optics,* 19**,** 016020-016020.

NANCI, A. 2007. *Ten Cate's oral histology: development, structure, and function*, Mosby.

NANCOLLAS, G., LORE, M., PEREZ, L., RICHARDSON, C. & ZAWACKI, S. 1989. Mineral phases of calcium phosphate. *The Anatomical Record,* 224**,** 234-241.

NATSUME, Y., NAKASHIMA, S., SADR, A., SHIMADA, Y., TAGAMI, J. & SUMI, Y. 2011. Estimation of lesion progress in artificial root caries by swept source optical coherence tomography in comparison to transverse microradiography. *Journal of biomedical optics,* 16**,** 071408-071408-8.

NAZARI, A., SADR, A., CAMPILLO‐FUNOLLET, M., NAKASHIMA, S., SHIMADA, Y., TAGAMI, J. & SUMI, Y. 2013. Effect of hydration on assessment of early enamel lesion using swept‐source optical coherence tomography. *Journal of biophotonics,* 6**,** 171-177.

NGAOTHEPPITAK, P., DARLING, C. L. & FRIED, D. 2005. Measurement of the severity of natural smooth surface (interproximal) caries lesions with polarization sensitive optical coherence tomography. *Lasers in surgery and medicine,* 37**,** 78-88.

NOVOTNY, L. & HECHT, B. 2012. *Principles of nano-optics*, Cambridge university press.

ONGOLE, R. & PRAVEEN, B. 2014. *Textbook of oral medicine, oral diagnosis and oral radiology*, Elsevier Health Sciences.

OTIS, L. L., COLSTON, B. W., JR., EVERETT, M. J. & NATHEL, H. 2000. Dental optical coherence tomography: a comparison of two in vitro systems. *Dentomaxillofac Radiol,* 29**,** 85-9.

PAPAZOGLOU, E. S., WEINGARTEN, M. S., ZUBKOV, L., NEIDRAUER, M., ZHU, L., TYAGI, S. & POURREZAEI, K. 2008. Changes in optical properties of tissue during acute wound healing in an animal model. *Journal of biomedical optics,* 13**,** 044005-044005-11.

PETERSEN, P. E. 2003. The World Oral Health Report 2003: continuous improvement of oral health in the 21st century – the approach of the WHO Global Oral Health Programme. *Community Dentistry and Oral Epidemiology,* 31**,** 3-24.

PITTS, N. 2004. Modern concepts of caries measurement. *J Dent Res,* 83**,** C43-C47.

PITTS, N. & STAMM, J. W. 2004. International Consensus Workshop on Caries Clinical Trials (ICW-CCT)—final consensus statements: agreeing where the evidence leads. *Journal of Dental Research,* 83**,** C125-C128.

PODOLEANU, A. G. 2014. Optical coherence tomography. *The British journal of radiology*.

POOLE, D. & JOHNSON, N. 1967. The effects of different demineraliz1ng agents on human enamel surfaces studied by scanning electron microscopy. *Archives of oral biology,* 12**,** 1621IN471633IN49-1632IN481634IN50.

POPESCU, D. P., SOWA, M. G., HEWKO, M. D. & CHOO-SMITH, L. P. 2008. Assessment of early demineralization in teeth using the signal attenuation in optical coherence tomography images. *Journal of Biomedical Optics,* 13.

PRAHL, S. A. 1989. *Light transport in tissue.* University of Texas at Austin.

PRETTY, I., EDGAR, W. & HIGHAM, S. 2002. Detection of in vitro demineralization of primary teeth using quantitative light‐induced fluorescence (QLF). *International Journal of Paediatric Dentistry,* 12**,** 158-167.

PRETTY, I., EDGAR, W. & HIGHAM, S. 2004. The effect of dehydration on quantitative light‐induced fluorescence analysis of early enamel demineralization. *Journal of oral rehabilitation,* 31**,** 179-184.

PRETTY, I. A. 2006. Caries detection and diagnosis: novel technologies. *Journal of Dentistry,* 34**,** 727-739.

RASAKANTHAN, J., SUGDEN, K. & TOMLINS, P. H. 2011. Processing and rendering of Fourier domain optical coherence tomography images at a line rate over 524 kHz using a graphics processing unit. *Journal of Biomedical Optics,* 16**,** 020505-020505-3.

ROBINSON, C., SHORE, R., BROOKES, S., STRAFFORD, S., WOOD, S. & KIRKHAM, J. 2000. The chemistry of enamel caries. *Critical Reviews in Oral Biology & Medicine,* 11**,** 481-495.

ROBINSON, C., WEATHERELL, J. & HALLSWORTH, A. 1971. Variation in composition of dental enamel within thin ground tooth sections. *Caries research,* 5**,** 44-57.

ROBINSON, C., WEATHERELL, J. & HALLSWORTH, A. 1983. Alterations in the composition of permanent human enamel during carious attack. *Demineralisation and remineralisation of the teeth. IRL Press, Oxford, UK,* 209.

ROLLINS, A. M. & IZATT, J. A. 1999. Optimal interferometer designs for optical coherence tomography. *Optics letters,* 24**,** 1484-1486.

SADR, A., MANDURAH, M., NAKASHIMA, S., SHIMADA, Y., KITASAKO, Y., TAGAMI, J. & SUMI, Y. Monitoring of enamel lesion remineralization by optical coherence tomography: an alternative approach towards signal analysis. SPIE BiOS, 2013. International Society for Optics and Photonics, 856602-856602-8.

SALAS, M., NASCIMENTO, G., VARGAS-FERREIRA, F., TARQUINIO, S., HUYSMANS, M. & DEMARCO, F. 2015. Diet influenced tooth erosion prevalence in children and adolescents: Results of a meta-analysis and meta-regression. *Journal of dentistry,* 43**,** 865-875.

SCHEMEHORN, B., ORBAN, J., WOOD, G., FISCHER, G. & WINSTON, A. 1999. Remineralization by fluoride enhanced with calcium and phosphate ingredients. *Journal of Clinical Dentistry,* 10**,** 13-16.

SCHEUTZEL, P. 1996. Etiology of dental erosion–intrinsic factors. *European journal of oral sciences,* 104**,** 178-190.

SCHLUETER, N., GANSS, C., DE SANCTIS, S. & KLIMEK, J. 2005. Evaluation of a profilometrical method for monitoring erosive tooth wear. *European journal of oral sciences,* 113**,** 505-511.

SCHLUETER, N., HARA, A., SHELLIS, R. P. & GANSS, C. 2011. Methods for the measurement and characterization of erosion in enamel and dentine. *Caries Res,* 45 Suppl 1**,** 13-23.

SCHMITT, J., KNÜTTEL, A. & BONNER, R. 1993. Measurement of optical properties of biological tissues by low-coherence reflectometry. *Applied Optics,* 32**,** 6032-6042.

SCHMITT, J. M. 1999. Optical coherence tomography (OCT): a review. *Selected Topics in Quantum Electronics, IEEE Journal of,* 5**,** 1205-1215.

SCHMITT, J. M., KNUTTEL, A., YADLOWSKY, M. & ECKHAUS, M. 1994. Optical-coherence tomography of a dense tissue: statistics of attenuation and backscattering. *Physics in medicine and biology,* 39**,** 1705.

SCHNEIDER, C. A., RASBAND, W. S. & ELICEIRI, K. W. 2012. NIH Image to ImageJ: 25 years of image analysis. *Nat methods,* 9**,** 671-675.

SCOTT, D. B., SIMMELINK, J. W. & NYGAARD, V. 1974. Structural aspects of dental caries. *Journal of dental research,* 53**,** 165-178.

SEGELSTEIN, D. J. 1981. *The complex refractive index of water*. University of Missouri--Kansas City.

SHAFFNER, T. & VAN VELD, R. 1971. 'Charging'effects in the scanning electron microscope. *Journal of Physics E: Scientific Instruments,* 4**,** 633.

SHELLIS, R. & ADDY, M. 2014. The interactions between attrition, abrasion and erosion in tooth wear. *Erosive Tooth Wear*. Karger Publishers.

SHI, X. Q., TRANAEUS, S. & ANGMAR-MANSSON, B. 2001. Comparison of QLF and DIAGNOdent for quantification of smooth surface caries. *Caries research,* 35**,** 21-26.

SHI, X. Q., WELANDER, U. & ANGMAR-MANSSON, B. 2000. Occlusal caries detection with KaVo DIAGNOdent compared with bite-wing radiography. *J Dent Res,* 79**,** 1297-1297.

SHIMADA, Y., NAKAGAWA, H., SADR, A., WADA, I., NAKAJIMA, M., NIKAIDO, T., OTSUKI, M., TAGAMI, J. & SUMI, Y. 2013. Noninvasive cross‐sectional imaging of proximal caries using swept‐source optical coherence tomography (SS‐OCT) in vivo. *Journal of biophotonics*.

SHIMAMURA, Y., MURAYAMA, R., KUROKAWA, H., MIYAZAKI, M., MIHATA, Y. & KMAGUCHI, S. 2011. Influence of tooth-surface hydration

conditions on optical coherence-tomography imaging. *Journal of dentistry,* 39**,** 572-577.
SIDDIQUI, S., ANDERSON, P. & AL-JAWAD, M. 2014. Recovery of crystallographic texture in remineralized dental enamel. *PloS one,* 9**,** e108879.
SILVERSTONE, L. 1967. Observations on the dark zone in early enamel caries and artificial caries-like lesions. *Caries research,* 1**,** 261-274.
SILVERSTONE, L. 1968. The surface zone in caries and in caries-like lesions produced in vitro. *British dental journal,* 125**,** 145-157.
SPERBER, G. H. & BUONOCORE, M. G. 1963. Effect of different acids on character of demineralization of enamel surfaces. *J. dent. Res.,* 42**,** 707-723.
SPIJKER, A. V. T., RODRIGUEZ, J. M., KREULEN, C. M., BRONKHORST, E. M., BARTLETT, D. W. & CREUGERS, N. H. 2009. Prevalence of tooth wear in adults. *International Journal of Prosthodontics,* 22.
STAINES, M., ROBINSON, W. & HOOD, J. 1981. Spherical indentation of tooth enamel. *Journal of materials science,* 16**,** 2551-2556.
STANINEC, M., DOUGLAS, S. M., DARLING, C. L., CHAN, K., KANG, H., LEE, R. C. & FRIED, D. 2011. Non‐destructive clinical assessment of occlusal caries lesions using near‐IR imaging methods. *Lasers in surgery and medicine,* 43**,** 951-959.
STOOKEY, G. K. & GONZÁLEZ-CABEZAS, C. 2001. Emerging methods of caries diagnosis. *Journal of Dental Education,* 65**,** 1001-1006.
TAKUMA, S. 1980. Demineralization and Remineralization of Tooth Substance- An Ultrastructural Basis for Caries Prevention. *Journal of Dental Research,* 59**,** 2146-2156.
TEAFORD, M. F., SMITH, M. M. & FERGUSON, M. W. 2007. *Development, function and evolution of teeth,* Cambridge University Press.
TEARNEY, G., BREZINSKI, M., BOUMA, B., HEE, M., SOUTHERN, J. & FUJIMOTO, J. 1995. Determination of the refractive index of highly scattering human tissue by optical coherence tomography. *Optics Letters,* 20**,** 2258-2260.
TEARNEY, G. J., BREZINSKI, M. E., BOUMA, B. E., BOPPART, S. A., PITRIS, C., SOUTHERN, J. F. & FUJIMOTO, J. G. 1997. In vivo endoscopic optical biopsy with optical coherence tomography. *Science,* 276**,** 2037-2039.
TEN BOSCH, J. & ANGMAR-MANSSON, B. 2004. Characterization and validation of diagnostic methods.
TEN BOSCH, J. & ANGMAR-MÅNSSON, B. 1991. Invited Review: A Review of Quantitative Methods for Studies of Mineral Content of Intra-oral Incipient Caries Lesions. *J Dent Res,* 70**,** 2-14.
TEN CATE, J. 1990. In vitro studies on the effects of fluoride on de-and remineralization. *J Dent Res,* 69.
TEN CATE, J. & DUIJSTERS, P. 1982. Alternating demineralization and remineralization of artificial enamel lesions. *Caries research,* 16**,** 201-210.
TEN CATE, J. & FEATHERSTONE, J. 1991. Mechanistic aspects of the interactions between fluoride and dental enamel. *Critical Reviews in Oral Biology & Medicine,* 2**,** 283-296.
TEN CATE, J., TIMMER, K., SHARIATI, M. & FEATHERSTONE, J. 1988. Effect of timing of fluoride treatment on enamel de-and remineralization in vitro: a pH-cycling study. *Caries research,* 22**,** 20-26.
TERRER, E., KOUBI, S., DIONNE, A., WEISROCK, G., SARRAQUIGNE, C., MAZUIR, A. & TASSERY, H. 2009. A new concept in restorative dentistry: light-induced fluorescence evaluator for diagnosis and treatment. Part 1:

Diagnosis and treatment of initial occlusal caries. *J Contemp Dent Pract,* 10**,** E086-094.

THEUNS, H., VAN DIJK, J., DRIESSENS, F. & GROENEVELD, A. 1984. Effect of the pH of buffer solutions on artificial carious lesion formation in human tooth enamel. *Caries research,* 18**,** 7-11.

THEVENAZ, P., RUTTIMANN, U. E. & UNSER, M. 1998. A pyramid approach to subpixel registration based on intensity. *IEEE transactions on image processing,* 7**,** 27-41.

THRANE, L., YURA, H. T. & ANDERSEN, P. E. 2000. Analysis of optical coherence tomography systems based on the extended Huygens–Fresnel principle. *JOSA A,* 17**,** 484-490.

TOMLINS, P. H. 2009. *Point-spread function phantoms for optical coherence tomography,* National Physical Laboratory.

TOMLINS, P. H., ADEGUN, O., HAGI-PAVLI, E., PIPER, K., BADER, D. & FORTUNE, F. 2010. Scattering attenuation microscopy of oral epithelial dysplasia. *Journal of Biomedical Optics,* 15**,** 066003-066003-8.

TOMLINS, P. H. & WANG, R. 2005. Theory, developments and applications of optical coherence tomography. *Journal of Physics D: Applied Physics,* 38**,** 2519.

TOMLINS, P. H., WOOLLIAMS, P., TEDALDI, M., BEAUMONT, A. & HART, C. Measurement of the three-dimensional point-spread function in an optical coherence tomography imaging system. Biomedical Optics (BiOS) 2008, 2008. International Society for Optics and Photonics, 68472Q-68472Q-8.

TURSSI, C. P., MESSIAS, D. F., CORONA, S. M. & SERRA, M. C. 2010. Viability of using enamel and dentin from bovine origin as a substitute for human counterparts in an intraoral erosion model. *Brazilian dental journal,* 21**,** 332-336.

UHLHORN, S. R., BORJA, D., MANNS, F. & PAREL, J.-M. 2008. Refractive index measurement of the isolated crystalline lens using optical coherence tomography. *Vision research,* 48**,** 2732-2738.

VAN DER MEER, F. J., FABER, D. J., SASSOON, D. B., AALDERS, M. C., PASTERKAMP, G. & VAN LEEUWEN, T. G. 2005. Localized measurement of optical attenuation coefficients of atherosclerotic plaque constituents by quantitative optical coherence tomography. *IEEE transactions on medical imaging,* 24**,** 1369-1376.

WANG, L. & NANCOLLAS, G. H. 2008. Calcium orthophosphates: crystallization and dissolution. *Chemical reviews,* 108**,** 4628.

WANG, R. K., KIRKPATRICK, S. & HINDS, M. 2007. Phase-sensitive optical coherence elastography for mapping tissue microstrains in real time. *Applied Physics Letters,* 90**,** 164105.

WANG, X.-J., MILNER, T. E., DE BOER, J. F., ZHANG, Y., PASHLEY, D. H. & NELSON, J. S. 1999. Characterization of dentin and enamel by use of optical coherence tomography. *Applied Optics,* 38**,** 2092-2096.

WEGEHAUPT, F., GRIES, D., WIEGAND, A. & ATTIN, T. 2008. Is bovine dentine an appropriate substitute for human dentine in erosion/abrasion tests? *Journal of Oral Rehabilitation,* 35**,** 390-394.

WEIDMANN, S., WEATHERELL, J. & HAMM, S. M. 1967. Variations of enamel density in sections of human teeth. *Archives of oral biology,* 12**,** 85-97.

WEST, N. X., DAVIES, M. & AMAECHI, B. T. 2011. In vitro and in situ erosion models for evaluating tooth substance loss. *Caries Res,* 45 Suppl 1**,** 43-52.

WHITE, D. 1987. Reactivity of fluoride dentifrices with artificial caries. *Caries research,* 21**,** 126-140.
WHITE, D. 1995. The application of in vitro models to research on demineralization and remineralization of the teeth. *Advances in dental research,* 9**,** 175-193.
WHITE, W. & NANCOLLAS, G. H. 1977. Quantitative study of enamel dissolution under conditions of controlled hydrodynamics. *Journal of dental research,* 56**,** 524-530.
WIEGAND, A., STOCK, A., ATTIN, R., WERNER, C. & ATTIN, T. 2007. Impact of the acid flow rate on dentin erosion. *Journal of Dentistry,* 35**,** 21-27.
WILDER-SMITH, C., HAMMER-WILSON, M., NGUYEN, V., LE, A., NGUYEN, K., ZHANG, J., JUNG, W., CHEN, Z. & WILDER-SMITH, P. Detection of GERD-induced dental erosion and demineralization using optical coherence tomography. Gastroenterology, 2005. WB SAUNDERS CO INDEPENDENCE SQUARE WEST CURTIS CENTER, STE 300, PHILADELPHIA, PA 19106-3399 USA, A391-A391.
WILDER-SMITH, C. H., WILDER-SMITH, P., KAWAKAMI-WONG, H., VORONETS, J., OSANN, K. & LUSSI, A. 2009. Quantification of dental erosions in patients with GERD using optical coherence tomography before and after double-blind, randomized treatment with esomeprazole or placebo. *Am J Gastroenterol,* 104**,** 2788-95.
WOJTKOWSKI, M. 2010. High-speed optical coherence tomography: basics and applications. *Applied Optics,* 49**,** D30-D61.
WONG, F., ANDERSON, P., FAN, H. & DAVIS, G. 2004. X-ray microtomographic study of mineral concentration distribution in deciduous enamel. *Archives of Oral Biology,* 49**,** 937-944.
WOOLLIAMS, P. & TOMLINS, P. 2011a. The modulation transfer function of an optical coherence tomography imaging system in turbid media. *Physics in medicine and biology,* 56**,** 2855.
WOOLLIAMS, P. D., FERGUSON, R. A., HART, C., GRIMWOOD, A. & TOMLINS, P. H. 2010. Spatially deconvolved optical coherence tomography. *Applied optics,* 49**,** 2014-2021.
WOOLLIAMS, P. D. & TOMLINS, P. H. 2011b. Estimating the resolution of a commercial optical coherence tomography system with limited spatial sampling. *Measurement Science and Technology,* 22**,** 065502.
YAMAZAKI, H. & MARGOLIS, H. 2008. Enhanced enamel remineralization under acidic conditions in vitro. *Journal of dental research,* 87**,** 569-574.
YANAGISAWA, T. & MIAKE, Y. 2003. High-resolution electron microscopy of enamel-crystal demineralization and remineralization in carious lesions. *Journal of electron microscopy,* 52**,** 605-613.
YASSEN, G. H., PLATT, J. A. & HARA, A. T. 2011. Bovine teeth as substitute for human teeth in dental research: a review of literature. *Journal of oral science,* 53**,** 273-282.
YOUNG, A. & TENUTA, L. 2011a. Initial erosion models. *Caries research,* 45**,** 33-42.
YOUNG, A. & TENUTA, L. M. 2011b. Initial erosion models. *Caries Res,* 45 Suppl 1**,** 33-42.
ZERO, D. 1995. In situ caries models. *Advances in Dental Research,* 9**,** 214-230.
ZHANG, A., ZHANG, Q., CHEN, C.-L. & WANG, R. K. 2015. Methods and algorithms for optical coherence tomography-based angiography: a review and comparison. *Journal of biomedical optics,* 20**,** 100901-100901.

ZIJP, J., TEN BOSCH, J. & GROENHUIS, R. 1995. HeNe-laser light scattering by human dental enamel. *Journal of dental research,* 74**,** 1891-1898.

ZIMNYAKOV, D. A. & TUCHIN, V. V. 2002. Optical tomography of tissues. *Quantum Electronics,* 32**,** 849.

ZIPKIN, I. & MCCLURE, F. 1949. Inhibitory effect of fluoride on tooth decalcification by citrate and lactate in Vivo. *Journal of dental research,* 28**,** 151-159.

ZVYAGIN, A., SILVA, K. B., ALEXANDROV, S., HILLMAN, T., ARMSTRONG, J., TSUZUKI, T. & SAMPSON, D. 2003. Refractive index tomography of turbid media by bifocal optical coherence refractometry. *Optics Express,* 11**,** 3503-3517.

Appendix A. Hydration of Bovine Enamel

In order to understand how water hydration affected OCT images of Bovine enamel a specimen was imaged continuously over a 24 hour period, from dry to fully hydrate. This information was used to determine the minimum hydration time for specimens prior to OCT measurement. OCT image results are shown below. Based on these results, a minimum 24 hour hydration time was used throughout this project.

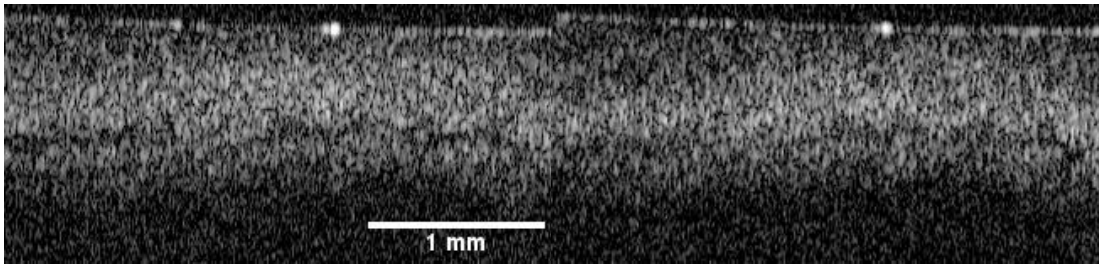

0 hours 1 hour

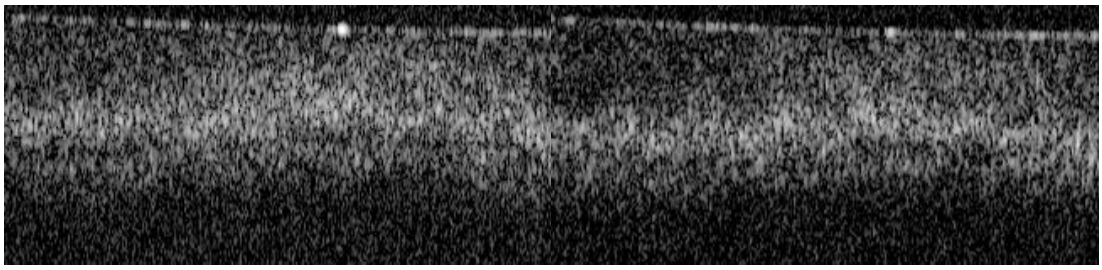

2 hours 6 hours

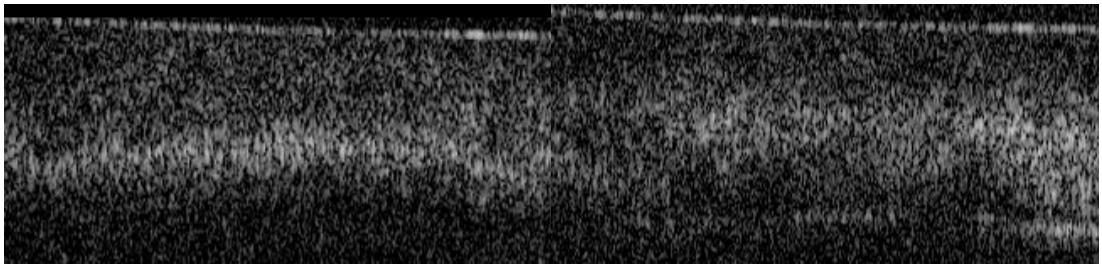

12 hours 16 hours

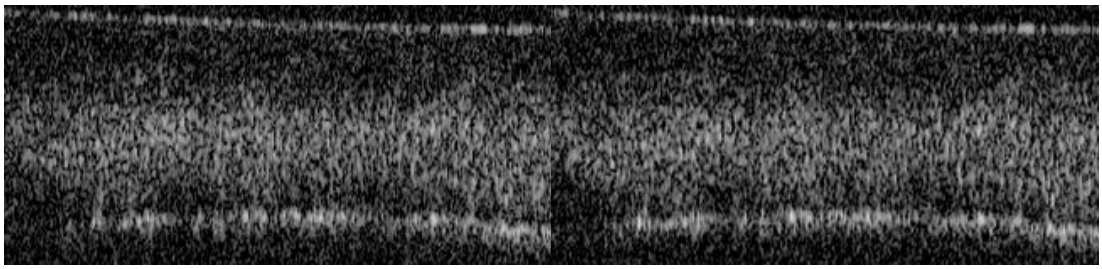

T=18 hours 24 hours

Figure A1 Cross-sectional B-Scan image of a bovine enamel sample under 24-hour hydration with deionised water.

Appendix B: OCT Based Surface Roughness Measurements

The optical profilometer, used in Chapter 7 to measure erosion, is based upon white-light interferometry, similar to OCT. Therefore, the OCT data from the demineralisation study was post-processed to estimate the surface roughness and how it developed with time. An existing MATLAB script was used that worked by fitting a Gaussian function to localise the surface in each A-Scan of logarithmically scaled B-Scan images. The roughness parameter, R_a, was calculated as follows:

$$R_a = \frac{1}{N}\sum_{n=1}^{N} |z_0 - z_n| \qquad \text{Eq. 1}$$

Where z_0 represents the mean axial height of the surface measured from the OCT image and z_n is the axial height of the nth point on the surface. R_a was computed using all available N points on the surface, typically N was of the order 10^4.

The surface topography of each specimen was determined from the OCT data at all time points as described above. The resulting surface profile of sample 1 is shown in **Error! Reference source not found.**B1(a)-(h) as greyscale images at 1, 2, 3, 4, 5, 6, 24 and 48 hours. The greyscale represents the surface height relative to a polynomial surface fitted through the acquired surface points.

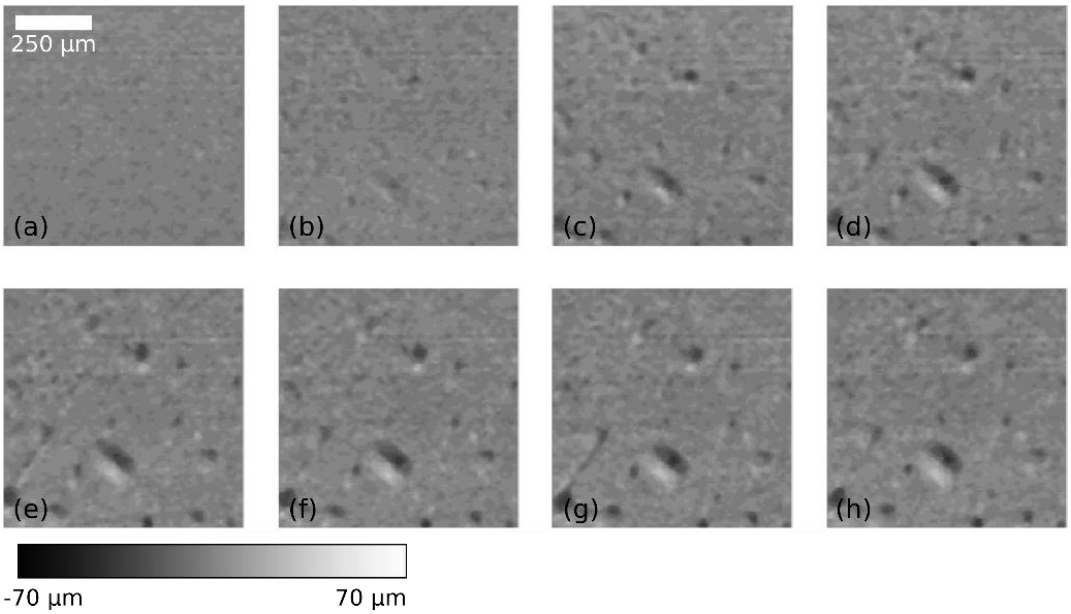

Figure B 1 Central 1 mm2 region of the change in the enamel surface of sample 1 at time points (a) 1 hour, (b) 2 hours, (c) 3 hours, (d) 4 hours, (e) 5 hours, (f) 6 hours, (g) 24 hours and (h) 48 hours

The images show visually little change after 4 hours of demineralisation. Quantitatively, R_a was measured over the same area and the mean for all specimens is plotted in **Error! Reference source not found.** as a function of time. The error bars represent the 95% confidence interval calculated over all 8 specimens.

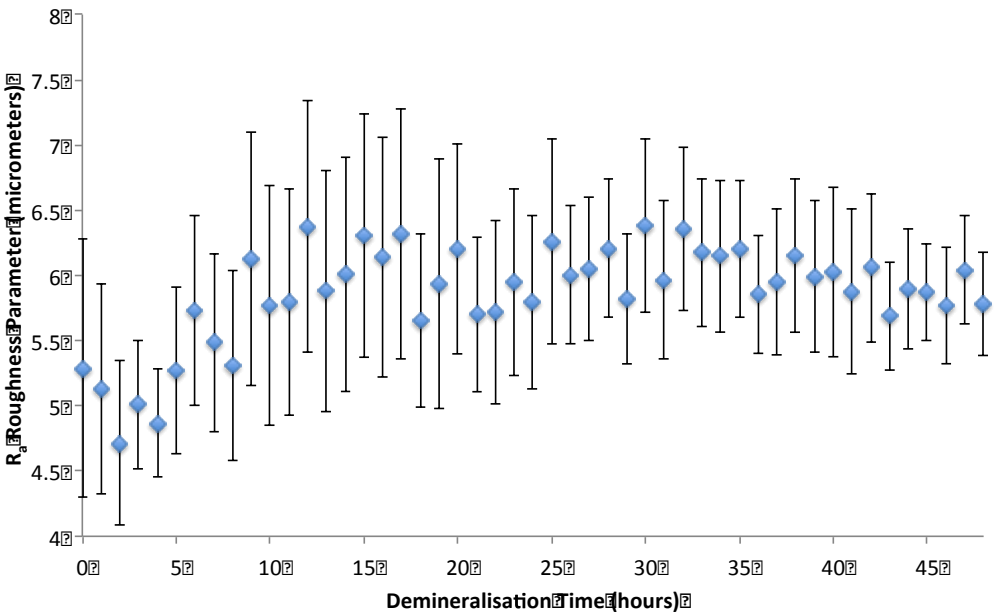

Figure B 2 Roughness parameter Ra plotted as a function of time. Each point represents the value of Ra measured from all 8 specimens and the error bars are the 95% confidence intervals

Appendix C. SEM Images of bovine samples eroded under erosive challenge

The specimen used in the experiments carried out for erosive lesion depth measurements were placed under the SEM to evaluate the resulting structures. The loss of bulk enamel can viewed on the SEM images.

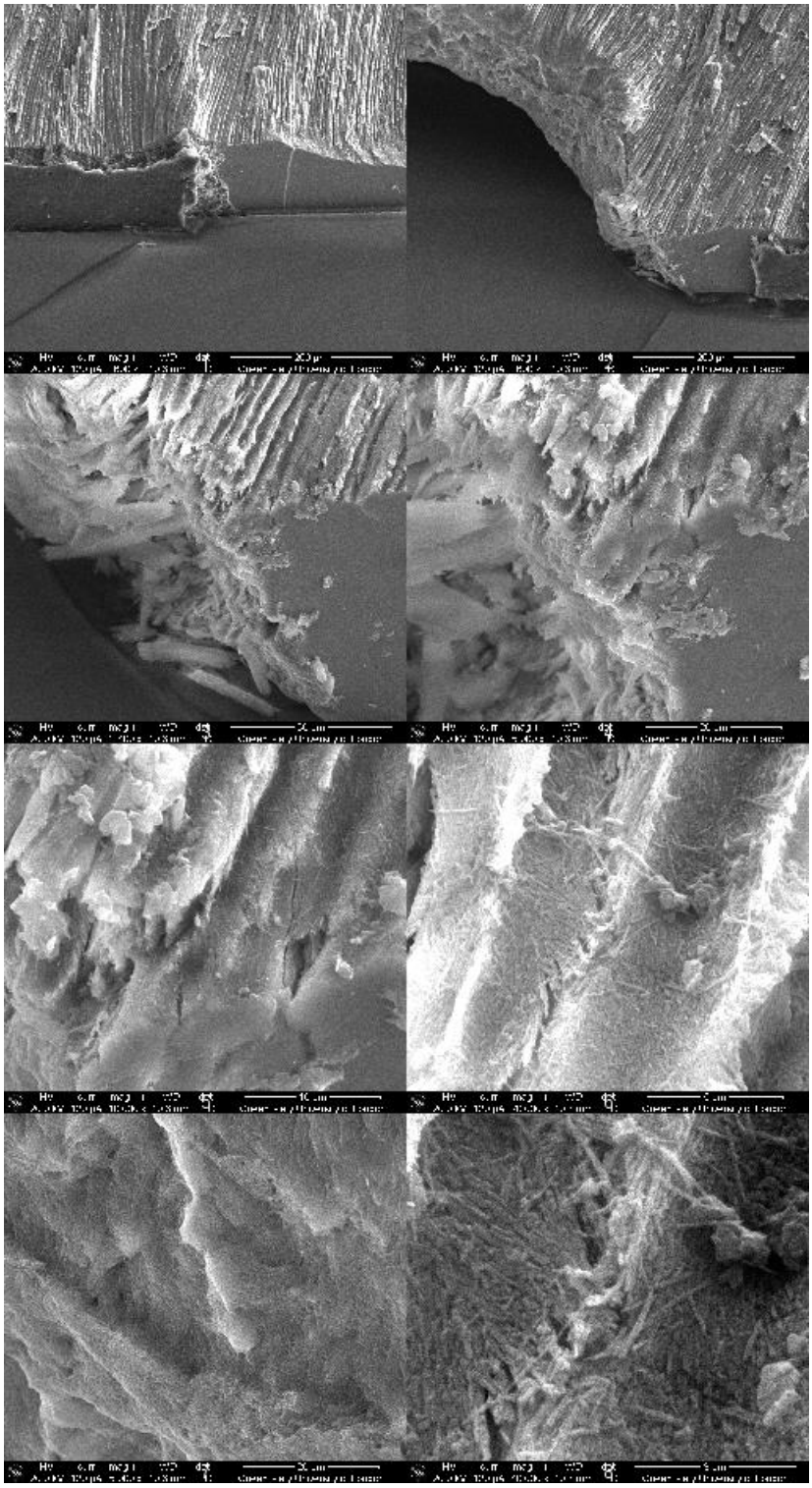

Figure C 1 Images of remaining structures of an erosive lesion on bovine enamel. imaged with a FIB-SEM (QMUL) at increasing structural resolutions (50x50 microns – 10x10 microns).